Ab initio exploration of materials for the detection and selective capture of iodine species and nitrogen oxide

Ayoub Daouli

Ayoub Daouli. Ab initio exploration of materials for the detection and selective capture of iodine species and nitrogen oxide. Physics [physics]. Université de Lorraine; Université Sultan Moulay Slimane (Beni Mellal, Maroc), 2023. English. NNT : 2023LORR0023 . tel-04321129

HAL Id: tel-04321129
https://hal.univ-lorraine.fr/tel-04321129v1

Submitted on 4 Dec 2023

En cotutelle avec l'Université de Sultan Moulay Slimane

Thèse

Présentée et soutenue publiquement pour l'obtention du titre de

DOCTEUR DE l'UNIVERSITE DE LORRAINE

Mention : Physique

par Ayoub DAOULI

Sous la direction de Prof. BADAWI et Prof. HASNAOUI

Ab initio exploration of materials for the detection and selective capture of iodine species and nitrogen oxide

---

Le 06 janvier 2023

Membres du jury :

Directeurs de thèse :	**Mr Michaël BADAWI**	**Prof, Université de Lorraine, Saint-Avold**
	Mr Abdellatif HASNAOUI	**Prof, Université de Sultan Moulay Slimane, Khouribga**
Président de jury :	**Mr Said OUASKIT**	**Prof, Université Hassan II, Casablanca**
Rapporteurs :	**Mr Jean-Marc SIMON**	**Dr, Université de Bourgogne, Dijon**
	Mr Hafid ANANE	**Prof, Université Cadi Ayad, Marrakech**
	Mr Soufiane El HOUSSAME	**Prof, Université de Sultan Moulay Slimane, Khouribga**
Examinateurs :	**Mme Sabine DEVAUTOUR-VINOT**	**Dr, Université de Montpellier, Montpellier**
	Mr Sébastien LEBEGUE	**Directeur de recherches, CNRS & Université de Lorraine, Nancy**

Acknowledgements

After three long years of research, it is not surprising that so many hands and hearts have helped me throughout this research adventure, and a few words of appreciation are insufficient but absolutely deserved.

First, I would like to thank my supervisors BADAWI Michael and HASNAOUI Abdellatif for offering me this lifetime opportunity. They have contributed with valuable knowledge, which has inspired me greatly in my work. I also wish to express my deep gratitude to you for your support and availability throughout these three years and for your scientific direction which I greatly benefited from. It has been a real privilege to work together, and it has been a precious source of scientific research!

Over these years, I have learned a lot from our meetings and personal conversations. I would also like to thank you for trusting me and handing me the freedom and its responsibilities to lead and collaborate with other groups. This has allowed me to build my self-esteem and effectively navigate this journey to the finish line of my PhD with many personal and professional skills.

I would also like to thank marie-antoinette Dziurla; for her help to comments on the final manuscript, and her participation at our meetings for interesting discussions.

A special thanks should also be addressed to Pr. Guillaume Maurin, for giving me the opportunity to join his research group “**The Dream Team**” during a research internship. It is thanks to him that I was able to happily combine new aspects of theoretical research into this thesis. These researchers have strongly inspired some applications related to the present thesis.

My ultimate thanks go to my family and colleagues who have helped and supported me in all that I have accomplished. And to all those who made my thesis years in such an amazing experience, and more than just books and studying. It’s been a great time!

Finally, the majority of the work in this thesis was achieved thanks to a funding within the "Toubkal N° TBK/20/106" project. We therefore address our special gratitude to all the PHC Toubkal representatives for having provided and secured these funds and thus made this thesis possible.

Résumé

Les isotopes radioactifs de l'iode, tels que ^{129}I et ^{131}I, sont susceptibles d'être disséminés dans l'environnement sous forme d'espèces gazeuses hautement volatiles, I_2 et ICH_3, après un accident nucléaire grave ou une fuite dans des installations de retraitement de combustible. Ces molécules ont des conséquences dramatiques sur l'environnement, la santé des écosystèmes, et des êtres humains. Il convient donc de détecter précisément ces molécules et de développer des filtres passifs pour les piéger. Tout l'enjeu est aujourd'hui de trouver une solution efficace et applicable dans les conditions nucléaires. En particulier, la présence d'autres espèces gazeuses appelées contaminants, telles que CO, H_2O et O_2, peut affecter la performance des matériaux utilisés pour détecter ou piéger ces espèces volatiles de manière pérenne. Les méthodes de simulation à l'échelle moléculaire permettent une compréhension fondamentale des phénomènes observés, en apportant des connaissances approfondies au niveau atomique qui sont souvent difficiles à obtenir par des méthodes expérimentales. Dans ce travail, des calculs utilisant la théorie de la fonctionnelle de densité (DFT) et des simulations de Monte Carlo grand canonique (GCMC) ont été déployés pour identifier des matériaux prometteurs pour la détection et la capture des gaz. En ce qui concerne la détection, le graphène et les matériaux carbonés bi-dimensionnels (BC_3, C_3N, BCN_6-2) sont des candidats prometteurs. Pour le graphène, nos résultats révèlent qu'en termes de sélectivité thermodynamique, PG (graphène pristine), Cu_PG (graphène pristine dopé en cuivre) et dans une moindre mesure Ag_MG (Graphene mono-lacunaire dopé en argent) sont clairement les monocouches de graphène les plus intéressantes pour la capture sélective de I_2, ICH_3 en présence de CO, H_2O et O_2. En ce qui concerne les matériaux carbonés 2D, les résultats de l'adsorption sur C_3N semblent très prometteurs dans la mesure où la différence entre les énergies d'adsorption de (I_2, ICH_3) vs (CO, H_2O) est très significative. Ces conclusions sont renforcées par des simulations à des températures finies. En outre, une discussion sur les calculs de structure électronique est également fournie. En matière de piégeage, notre choix s'est porté sur une classe de matériaux poreux nommée Metal-Organic Frameworks (MOFs). Notre évaluation systématique de la performance d'adsorption du M-MOF-74 où M = Mg, Zn, Cu, Fe, Co, Ni et Mn a montré que d'un point de vue thermodynamique, les Fe-MOF-74 et Cu-MOF-74 sont clairement les structures les plus intéressantes pour la capture sélective de composés iodés.

Une seconde application abordée dans cette thèse, toujours dans le contexte des gaz nocifs, vise l'adsorption des émissions de NO_x. Ces émissions représentent une préoccupation majeure dans un environnement de travail confiné sans ventilation ni traitement. Des études récentes ont révélé que les zéolithes peuvent permettre une capture efficace des NO_x. Dans ce contexte, nos résultats démontrent que parmi une série de zéolites échangées par des cations divalents (Be^{2+}, Mg^{2+}, Ca^{2+}, Sr^{2+}, Ba^{2+}, Fe^{2+}, Cu^{2+}, Zn^{2+}, Pd^{2+}, Pt^{2+}), la Faujasite Y-Pt^{2+}, est un matériau intéressant pour

l'adsorption sélective des NO_x issus des gaz d'échappement des moteurs diesel en présence de vapeur d’eau. Nous avons ensuite étendu notre exploration aux MOFs en intégrant les mêmes cations en tant que métaux dans le ligand catécholate avant son incorporation dans l'UiO-66 en forme de cage. Des simulations GCMC mettant en œuvre un champ de force NO_x/MOF ont été déployées pour comprendre en profondeur le mécanisme microscopique en jeu. Nos simulations moléculaires indiquent que l'UiO-66-CatFe(II) nanoporeux serait un excellent adsorbant pour la capture des NO_x, même à une très faible concentration de quelques ppm. Ceci vient compléter le portefeuille de matériaux poreux qui, jusqu'à présent, ont été presque exclusivement testés dans des conditions de fonctionnement impliquant une concentration plus élevée de NO_x (>1000 ppm).

Abstract:

Radioactive isotopes of iodine, such as ^{129}I and ^{131}I, are likely to be disseminated in the environment after a serious nuclear accident or a leak in fuel reprocessing facilities, under the form of highly volatile gaseous species, I_2 and ICH_3, resulting in dramatic consequences. It is therefore necessary to accurately detect these molecules and develop passive filters for trapping them. The challenge today is to find an effective solution that can be applied in nuclear conditions. In particular, the presence of other gaseous species called contaminants, such as CO, H_2O and O_2 can affect the performance of materials used to detect or trap these iodine volatile species in a perennial manner. Molecular scale simulation methods provide a fundamental understanding of the observed phenomena, providing in-depth knowledge at the atomic level that is often difficult to obtain by experimental methods. In this work, density function theory (DFT) calculations and grand canonical Monte Carlo (GCMC) simulations have been used to identify promising materials for the detection and capture of gaseous molecules. Regarding sensing, graphene, and two-dimensional carbon materials (BC_3, C_3N, BCN_6-2) are promising candidates. For graphene, our results reveal that in terms of thermodynamic selectivity, PG (pristine graphene), Cu_PG (copper-doped pristine graphene) and to a lesser extent Ag_MG (silver-doped monolayer graphene) are clearly the most interesting graphene monolayers for the selective capture of I_2, ICH_3 in the presence of CO, H_2O and O_2. As far as 2D carbon materials are concerned, results of adsorption on C_3N seem very promising insofar the difference between the adsorption energies of (I_2, ICH_3) vs (CO, H_2O) is very significant. These findings are strengthened by simulations at finite temperatures. In addition, a discussion of electronic structure calculations is also provided. For trapping, we have selected a class of porous materials named Metal-Organic Frameworks (MOFs). Our systematic evaluation of the adsorption performance of M-MOF-74 where M = Mg, Zn, Cu, Fe, Co, Ni and Mn showed that from a thermodynamic point of view, Fe-MOF-74 and Cu-MOF-74 are clearly the most interesting structures for the selective capture of iodine compounds.

A second application addressed in this thesis, still in the context of noxious gases, is the adsorption of NO_x emissions. These emissions in a confined work environment without ventilation or treatment represent a major concern. Recent studies have revealed that zeolites can provide effective capture of NO_x. In this context, our results reveal that from a series of divalent cations-exchanged zeolite (Be^{2+}, Mg^{2+}, Ca^{2+}, Sr^{2+}, Ba^{2+}, Fe^{2+}, Cu^{2+}, Zn^{2+}, Pd^{2+}, Pt^{2+}), Faujasite Y-Pt^{2+}, is an interesting material for the selective adsorption of NOx from diesel engine exhaust in the presence of water vapor. We then have extended our explorations to MOFs by integrating the same cations as metals into the catecholate ligand prior to its incorporation into the cage-like UiO-66. GCMC simulations implementing a new NO_x/MOF force field were deployed to gain an in-depth understanding of the microscopic mechanism involved. Our molecular simulations indicate

that the nanoporous UiO-66-CatFe(II) would be an excellent adsorbent for NO_x capture, even at very low concentrations of a few ppm. This complements the portfolio of porous materials that, to date, have been almost exclusively tested under operating conditions involving higher NO_x concentrations (>1000 ppm).

Contents

Avant-propos

La présente thèse de doctorat traite de l'adsorption de gaz avec des matériaux solides par des approches computationnelles de modélisation moléculaire, dans le cadre de deux applications environnementales, visant à protéger la santé des humains et des écosystèmes.

La première application concerne le piégeage et la détection d'espèces radioactives, en particulier l'iode et l'iodométhane pouvant émaner de centrales au cours des conditions nucléaires. Dans ce cadre, des matériaux carbonés bi-dimensionnels (BC_3, C_3N, BCN_6-2) et le graphène pristine (parfait), ou dopé à l'argent ou au cuivre ont été étudiés pour la détection d'espèces iodées radioactives volatiles, tandis que des matériaux poreux tels que les réseaux organo-métalliques (metal-organic frameworks (MOFs)) ont été sélectionnés pour assurer un piégeage stable.

La seconde application est destinée, toujours dans le même contexte de gaz nocifs, à la problématique du piégeage des émissions des espèces NO_x par des matériaux poreux (zéolithes types faujasite et MOFs type UiO-66).

Résumé général de la thèse

Depuis la création du Commissariat à l'énergie atomique (CEA) en 1945, l'énergie nucléaire est progressivement devenue le premier mode de production d'électricité en France.

Cependant, bien que présentant des avantages et permettant de pallier l'intermittence des énergies renouvelables, l'énergie nucléaire comme toute autre activité industrielle reste dangereuse et ne pourra jamais être exploitée en toute sécurité. En effet, ce développement a conduit à une augmentation du risque de contamination par des gaz radioactifs, parmi lesquels les composés iodés nécessitent une attention particulière car ils entraînent de graves conséquences sanitaires et des impacts environnementaux à long terme. Deux radioisotopes de l'iode sont particulièrement dangereux, ^{131}I et ^{129}I. L'isotope ^{131}I, volatil et à courte durée de vie (demi-vie de ~8,02 jours), est un substrat spécifique des récepteurs thyroïdiens responsable du développement à long terme de cancers de la thyroïde. L'isotope ^{129}I, très volatil à durée vie longue (demi-vie de ~15 millions d'années), peut endommager les cellules humaines et provoquer des mutations génétiques. De plus, dans l'environnement, l'iode radioactif I_2 peut réagit avec des hydrocarbures comme le méthane CH_4 ou d'autres composés organiques volatils pour produire de l'iodure de méthyle ICH_3 qui est également très volatil. Toute fuite de matière radioactive constitue un réel danger et un risque majeur pour la population environnante exposée à ces rejets.

Il existe deux principales sources d'exposition à la radioactivité :

- **L’accident nucléaire grave** qui génère l'isotope ^{131}I en très grande quantité
- La fuite de déchets radioactifs lors d’opérations de retraitement de déchets nucléaires, qui génère l'isotope ^{129}I, signature des déchets radioactifs.

Les conséquences liées à l’exposition d’iode radioactif, très néfastes pour l’environnement et la population, pourraient être considérablement atténuées par l’utilisation de filtres d’éventage spécifiques et efficaces vis-à-vis des espèces radioactives ayant le plus fort impact radiologique. La ligne de dépressurisation des centrales nucléaires françaises n’étant pas adaptée à la rétention d’espèces iodées gazeuses, et ces espèces représentant un grave danger pour les personnes exposées, il serait extrêmement bénéfique de piéger les radioisotopes de l’iode. Leur piégeage est une étape essentielle pour assurer la sécurité nucléaire et la protection de la santé des personnes potentiellement exposées à la contamination. Il faut également ajouter que, même en petites quantités, ces espèces présentent les mêmes dangers de contamination, ce qui démontre la réelle nécessité de mettre en place des capteurs d'iode puissants afin de détecter toute dissémination ou fuite ultérieure, qui puisse nous avertir et nous alerter d'un danger aussi grave.

Tout l’enjeu est aujourd’hui de trouver une solution efficace et applicable dans les conditions drastiques d’un accident nucléaire, pour piéger et détecter ces espèces volatiles de manière pérenne.

Au regard de ces aspects et parmi une large sélection de matériaux existant pour la détection de gaz, notre choix s’est porté sur le graphène et les matériaux carbonés bi-dimensionnels. Les capteurs actuels présentent de vraies limites de performance pour l’application envisagée, à savoir une mauvaise sélectivité (la couche sensible peut réagir de la même manière sous l'influence de différents gaz), une mauvaise stabilité, une température de fonctionnement limitée, et un temps d'analyse long à cause des nombreux points de mesure. Ces limitations actuelles sont de véritables points négatifs pour un capteur nécessitant des performances bien spécifiques. Par conséquent, plusieurs facteurs doivent être pris en compte pour décider de la pertinence d'un capteur de gaz. Les plus significatifs sont la sélectivité qui est liée à la capacité de reconnaissance d’un gaz spécifique parmi d'autres, la sensibilité qui indique la plus petite quantité absolue de changement détectable, le temps de réponse qui est le temps nécessaire à un capteur pour changer transmettre le signal d’un changement de paramètre d'entrée du capteur, et la réversibilité qui indique la capacité du système à revenir à son état initial après une détection. Enfin, un autre facteur crucial qui dénote la sensibilité et la sélectivité d'un capteur est son affinité à interagir avec un gaz toxique, peut être affectée par sa capacité d'adsorption. Tous ces facteurs ont suscité depuis plusieurs décennies un engouement considérable pour le développement de nouveaux capteurs toujours plus performants.

Les matériaux carbonés ont attiré une attention considérable en raison de leur grande disponibilité, leur excellente conductivité électrique et thermique, leur stabilité chimique et leur fonctionnalisation ou hybridation relativement facile. En effet, les capteurs bi-dimensionnels (2D) à base de carbone (**Figure R.2**) sont des capteurs de gaz, innovants et révolutionnaires.

Depuis la synthèse du graphène, un matériau carboné hybride sp^2 découvert en 2004, les matériaux à base de graphène ont suscité un déploiement exponentiel d'activités de recherche/développement pour la détection de gaz toxiques et explosifs, en raison de leurs caractéristiques remarquables, telles qu'une extraordinaire conductivité thermique, une conductivité électrique incomparable, une très grande surface spécifique (jusqu'à 2630 $m^2.g^{-1}$), une résistance mécanique exceptionnelle et une excellente biocompatibilité. Bien que le graphène soit très sensible, il manque de sélectivité par rapport à plusieurs gaz réducteurs. Par conséquent, sa fonctionnalisation, son dopage et la création de défauts sont nécessaires pour améliorer sa sélectivité. Pour le dopage, une petite quantité de métaux nobles est ajoutée à la couche sensible du capteur. Cela modifie la morphologie de la couche (taille des grains, rugosité...) et améliore la sensibilité du capteur. Les métaux les plus utilisés sont le palladium, le platine, l'indium, le ruthénium et les oxydes métalliques.

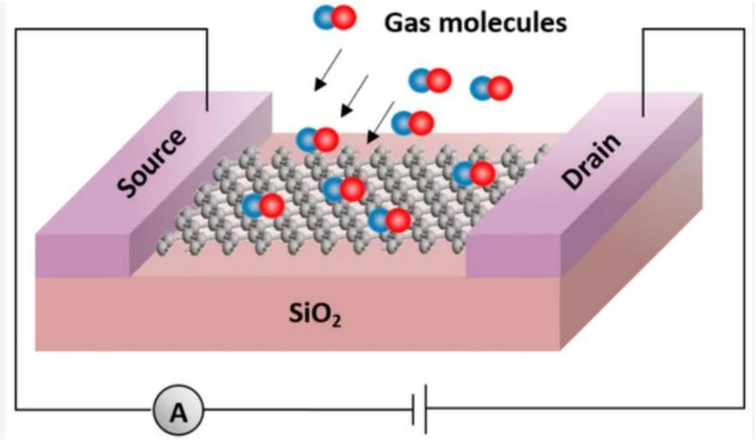

Figure R.2: Schéma d'un capteur de gaz graphène de type transistor à effet de champ.

En matière de piégeage de gaz, les techniques existantes sont principalement basées sur les adsorbants poreux, à savoir les charbons actifs et les zéolithes échangées à l'argent (notamment Ag-MOR). Cependant, ces matériaux présentent des inconvénients et d'autres alternatives doivent être trouvées. En effet, les charbons actifs se sont avérés inflammables, trop sensibles à l'humidité et aux températures élevées (>150°C), et ne sont donc pas adaptés aux conditions d'un accident nucléaire grave. En outre, en raison de leur nature hétérogène, ces matériaux n'ont pas de sites de piégeage bien définis, ce qui rend difficile l'ajustement et le contrôle de certaines caractéristiques telles que la porosité ou la chimie de surface. Parallèlement, la zéolithe mordénite à l'argent Ag-

MOR, très stable à la température et à l'oxydation, s'est révélé être l'un des adsorbants les plus intéressants pour le piégeage de composés iodés. Malheureusement, le coût élevé de l'argent a encouragé les scientifiques à chercher des matériaux alternatifs. D'autres zéolithes échangées avec métaux moins chères (plomb, cadmium, thallium, palladium, manganèse, mercure et cuivre) ont été évaluées comme une alternative possible à la zéolithe à base d'argent pour la capture des espèces iodées. Cependant, bien que certaines aient donné des résultats prometteurs pour l'élimination de l'iode, toutes ont présenté une efficacité de capture insatisfaisante et/ou un faible capacité d'adsorption de l'iodure de méthyle.

Nous avons donc choisi d’accorder une attention particulière aux réseaux organo-métalliques MOFs qui peuvent être envisagés afin d'éviter tout risque de propagation de produits radioactifs dans l'environnement et d’éviter toute probabilité de contamination. En effet, les MOFs sont des matériaux hybrides cristallisés, constitués de clusters inorganiques liés entre eux par des ligands organiques (**Figure R.3**). Cette organisation de faible densité offre une grande porosité et des surfaces spécifiques élevées (jusqu'à 7000 $m^2.g^{-1}$), bien supérieures à celles des solides poreux habituels comme les zéolithes.

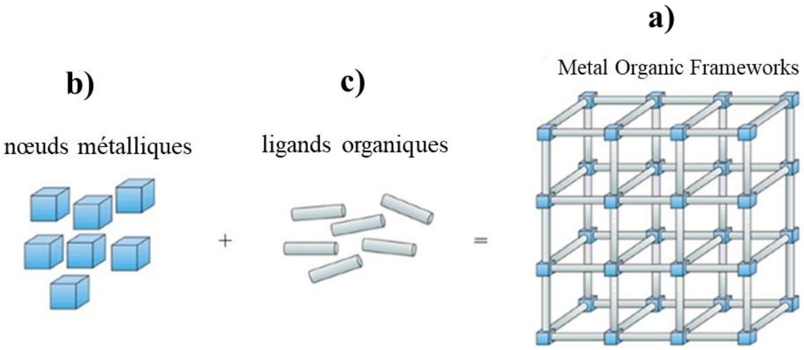

Figure R.3 : Schématisation de la structure des MOF, représentant des nœuds métalliques, reliés entre eux par des ligands organiques.

Notre seconde application mentionnée dans l’avant-propos vise l'adsorption des émissions de NO_x qui sont également des gaz nocifs. Ces émissions des moteurs diesel (300-1000 ppm pour le NO et le NO_2), en particulier dans un environnement de travail confiné sans ventilation ni traitement des gaz d'échappement, représentent une préoccupation majeure en matière de santé et de sécurité professionnelles (risque de cancer des poumons et attaque de la circulation sanguine). En France, près de 800 000 travailleurs sont exposés à ces émissions. Par conséquent, la réduction des émissions de NO_x dans les gaz d'échappement des véhicules non routiers est une priorité actuelle en matière de prévention des risques professionnels. Il est nécessaire de développer des technologies efficaces pour se conformer aux normes sanitaires (les exigences réglementaires de l'UE prévoient une valeur limite d'exposition professionnelle au NO et NO_2 émis par les moteurs dans un environnement de travail, de 2 et 0,5 ppm, respectivement), pour améliorer la santé et la sécurité dans les environnements de travail confinés. Plusieurs stratégies telles que la réduction par stockage des NO_x (NSR) et la réduction catalytique sélective (SCR) ont été proposées au cours de cette dernière décennie pour limiter les émissions de NO_x dans les moteurs à mélange pauvre. Efficaces à haute température, elles ont déjà été mises en œuvre dans les véhicules légers où la température du moteur augmente rapidement en raison du fonctionnement continu. Cependant, ces techniques sont confrontées à plusieurs problèmes. En particulier, leur efficacité à réduire les NO_x devient limitée dans les équipements de construction qui fonctionnent de manière intermittente et qui sont donc soumis à de multiples démarrages à froid, ce qui entraîne des températures de gaz d'échappement basses. Par conséquent, un adsorbant efficace pour la capture sélective de faibles concentrations de NO et NO_2 doit être conçu.

Des études récentes ont révélé que les adsorbants inorganiques tels que les zéolithes peuvent permettre la capture des NO_x. En effet, sur la base de 200 zéolithes existantes, les architectures mordénite (MOR), MFI (ZSM5), et faujasite (FAU) ont été proposées comme des candidats prometteurs pour l'élimination des NO_x. Les zéolithes sont constituées d'un arrangement de tétraèdres TO_4 reliés par leurs sommets, où T est un atome de silicium ou d'aluminium. Cet arrangement régulier de tétraèdres crée un réseau de cavités dont la forme et le diamètre varient en fonction de la structure cristalline du matériau (**Figure R.4)**. Il s'agit d'un matériau microporeux doté de propriétés physico-chimiques remarquables, notamment une stabilité thermique élevée, une capacité d'échange d'ions élevée, une surface spécifique et une porosité élevée. Elles sont l'un des matériaux les plus utilisés pour l'adsorption des gaz et s'avèrent être des candidats excellents et prometteurs pour cette application.

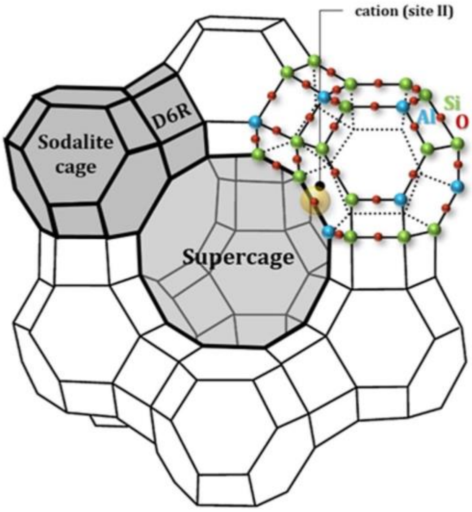

Figure R.4 : Schéma de la cellule conventionnelle de la faujasite avec trois types de cavités. Le prisme hexagonal (D6R), la cage sodalite (cage β) et la supercage (cage α)

D'une manière générale, cette thèse est organisée de la façon suivante :

Le chapitre I est classiquement consacré à l'état de l'art. En effet, afin de savoir comment les radionucléides iodés sont formés, il est tout d'abord primordial d'avoir une meilleure connaissance du cycle nucléaire. Par conséquent, la première partie sera consacrée à la description du contexte (production d'électricité nucléaire et aperçu sur l'iode radioactif). Une deuxième partie sera consacrée à l'état de l'art des méthodes de piégeages existantes (liquide et solide) et de détection (différents types de capteurs), afin de souligner leurs performances et leurs inconvénients. Au vu des lacunes existantes dans la littérature, une conclusion sera établie pour justifier le travail réalisé et le choix des matériaux sélectionnés dans le cadre de cette thèse. Une troisième partie sera consacrée à l'étude bibliographique des matériaux promoteurs sélectionnés : graphène et matériaux 2D pour la détection de l'iode radioactif, puis MOFs pour le piégeage de l'iode.

Le deuxième chapitre sera consacré à la présentation des méthodologies de calcul utilisées pour l'étude du piégeage et de la détection d'iode, en particulier la théorie de la fonctionnelle de la densité DFT (pour Density Functional Theory) sera utilisée pour évaluer quantitativement les performances de piégeage et de détection de I_2 et ICH_3 qui seront décrits tout en déduisant leurs mécanismes par la suite. Cette partie présentera quelques bases sur la théorie DFT appliquée aux systèmes périodiques, et les différents outils utilisés dans nos calculs. La DFT nous permettra de comprendre d'une façon approfondie la nature des interactions adsorbant/substrat au niveau moléculaire, et les mécanismes de piégeage et de détection en termes de structure, propriétés électroniques, et transfert de charges.

Les troisième et quatrième chapitres rapporteront nos investigations de recherche théorique portant sur un capteur capable de détecter sélectivement et efficacement les espèces iodées I_2 et ICH_3 pouvant être relâchées de centrales nucléaires ou d'installations de retraitement de combustible nucléaire. Le graphène et d'autres matériaux carbonés 2D (BC_3, C_3N, BCN_6-2) seront étudiés, en présence d'inhibiteurs (contaminants) d'adsorption de l'iode présents dans l'air (CO, H_2O, O_2).

Dans **le troisième chapitre**, les performances de détection du graphène pristine (parfait) et contenant des défauts, ainsi que des monocouches de graphène dopées à l’argent ou au cuivre, ont été évaluées à l'aide de calculs DFT périodiques avec correction des forces de dispersion, sur la base de quatre critères de détection importants (sélectivité, sensibilité, stabilité et temps de régénération).

Les résultats (**Figure R.5**) ont révélé que la monocouche de graphène pur (PG) présente une affinité plus élevée pour I_2 et ICH_3 que pour CO, H_2O et O_2, ce qui indique que ce matériau est adapté à une adsorption sélective des espèces iodées. Les défauts (lacunes) sur le graphène (mono-lacunaire MG et bi-lacunaire DG) conduisent à une interaction favorable avec CO et O_2, avec une dissociation des deux atomes pendant l'adsorption suivie d’un remplissage du site vide du défaut. Par conséquent, les monocouches de graphène MG et DG présentent une affinité plus élevée pour le CO et l'O_2 que pour I_2 et ICH_3, ce qui indique que ces monocouches sont inadaptées à la détection des espèces iodées.

Si l'on considère les monocouches de graphène dopé à l'argent, les monocouches Ag_PG (graphène pristine dopé en argent) et Ag_MG (Graphene mono-lacunaire dopé en argent) présentent une affinité plus élevée ou équivalente pour O_2 et H_2O que pour ICH_3 respectivement, mais une affinité beaucoup plus élevée pour I_2 que pour les autres molécules de gaz. Cela signifie que l'eau et l'oxygène devraient jouer un rôle néfaste sur l'adsorption de ICH_3. Par conséquent, les monocouches de PG et MG dopées à l'Ag ne pourraient être appropriées que pour l'adsorption sélective de I_2 en présence d'autres contaminants. D'autre part, Ag_DG (Graphene bi-lacunaire dopé en argent) présente une affinité plus élevée pour le CO que pour I_2 et ICH_3, ce qui montre que cette surface est inadaptée à la détection des espèces iodées en présence de contaminants. Cu_PG (graphène pristine dopé en cuivre) est la seule monocouche qui présente une affinité plus élevée pour I_2 et ICH_3 que pour tous les autres contaminants. Dans ce cas, CO, H_2O et O_2 ne devraient pas inhiber l'adsorption de ces deux espèces iodées. Cu_MG (Graphene mono-lacunaire dopé en cuivre) interagit plus fortement avec CO et O_2 qu'avec ICH_3, mais présente une affinité plus élevée pour I_2 que pour les autres molécules de gaz. Cu_DG (Graphene bi-lacunaire dopé en cuivre) présente une affinité plus élevée pour CO que pour I_2 et ICH_3. Ces résultats révèlent qu'en termes de sélectivité thermodynamique, PG, Cu_PG et dans une moindre mesure Ag_MG sont clairement les monocouches de graphène les plus intéressantes pour la capture sélective de I_2, ICH_3 en présence de CO, H_2O et O_2.

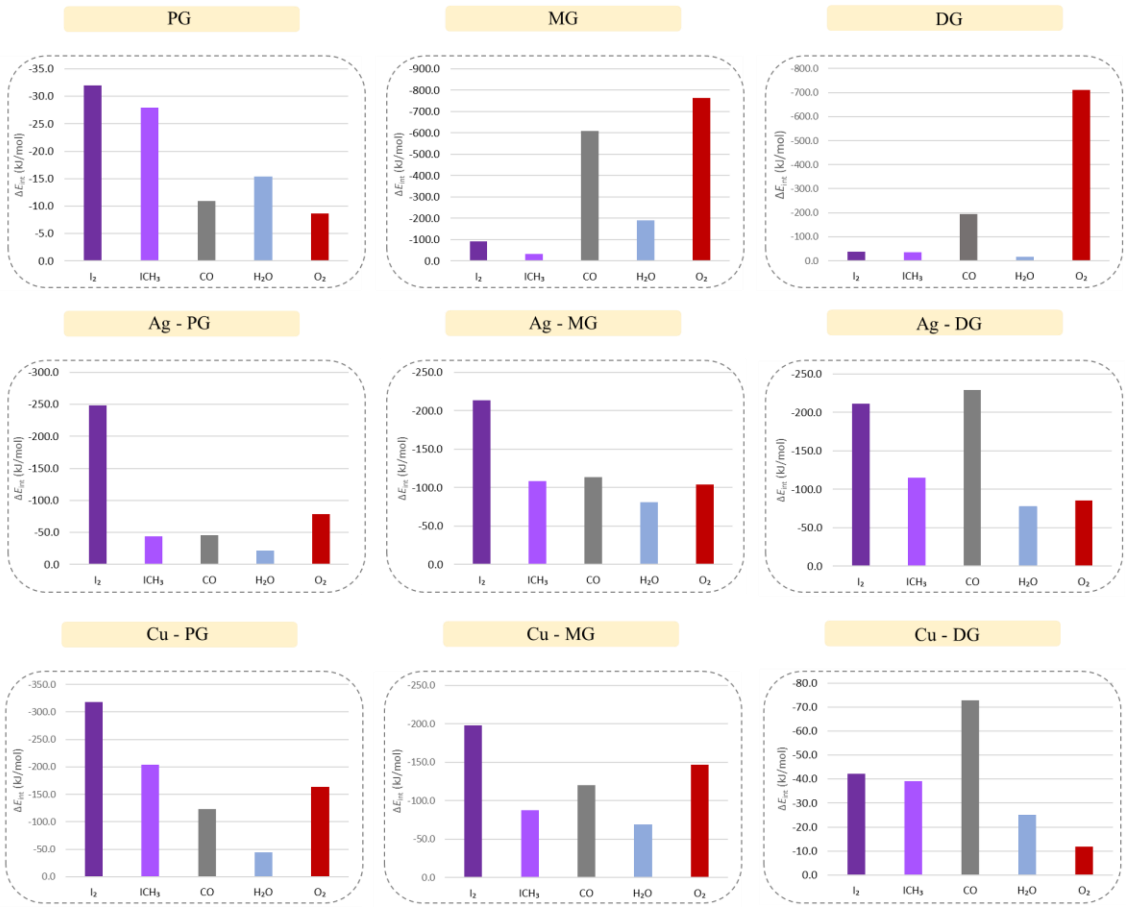

Figure R.5 : Les énergies totales d'interaction de I_2, ICH_3, CO, H_2O et O_2 avec les monocouches de graphène, calculées en utilisant le niveau de théorie PBE + D3(BJ).

Ces mesures d'affinité ont été suivies d'une simulation de la dynamique moléculaire *Ab initio* (AIMD) dans le but de déterminer la stabilité thermique des systèmes sélectionnés (soit PG, Ag_MG et Cu_MG) à température ambiante (300K). La **Figure R.6** montre les variations des fluctuations de l'énergie potentielle totale au cours du temps (de 1 à 20 ps avec un pas de temps de 1 fs), en indiquant les structures géométriques à la fin des simulations AIMD (après 20 ps) pour I_2 et ICH_3 adsorbés sur les trois monocouches de graphène. Ces résultats montrent qu'il n'y a pas de rupture significative des liaisons ou de distorsion structurelle. La structure planaire du graphène est bien maintenue et aucun décalage atomique dans la direction z n'est observé. De plus, toutes nos configurations finales précédentes révélées par les calculs DFT (0K) ont été préservées à 300K ce qui indique la stabilité thermique des trois monocouches de graphène à température ambiante.

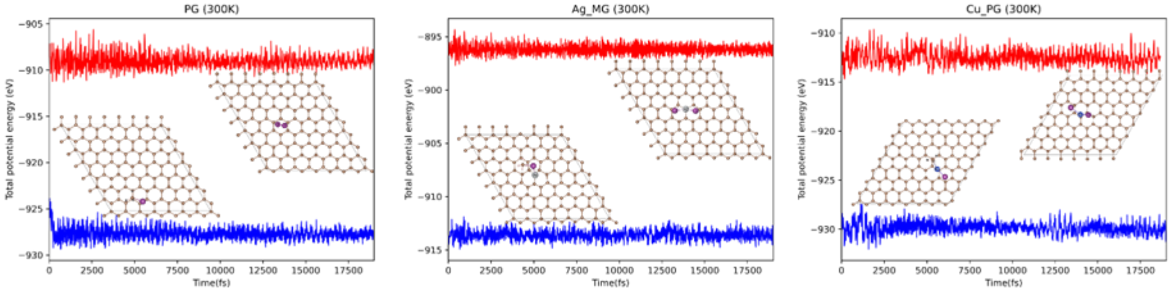

Figure R.6 : Fluctuations de l'énergie potentielle totale de I_2 (rouge) et ICH_3 (bleu) adsorbés sur PG, Ag_MG et Cu_PG pendant les simulations AIMD de 20ps à 300 K. Les encarts représentent les instantanés de l'adsorption de I_2 (en haut) et ICH_3 (en bas) à la fin des simulations.

Enfin, nous avons déduit de l'équation ci-dessous, le temps de récupération (τ) ou temps nécessaire pour désorber les molécules de gaz de la surface des feuilles de graphène, pour prédire les performances de récupération des capteurs.

$$\tau = \frac{1}{\vartheta_0} \exp\left(\frac{-E^*}{K_B T}\right)$$

Où T est la température en K, ϑ_0 est la fréquence, K_B est la constante de Boltzmann et $-E^*$ est la barrière d'énergie de désorption qui est équivalente à l'énergie d'adsorption.

Nos résultats ont révélé que PG se régénère après adsorption de I_2 et ICH_3 en un temps très court, de l'ordre de la micro et nanoseconde pour les deux molécules à température ambiante. Pour Ag_MG, le temps de récupération calculé pour l'adsorption de ICH_3 est de plusieurs jours sous vide à température ambiante. Avec une irradiation UV à la même température (T=300K), le temps de récupération prédit a été réduit à 2 heures. De plus, l'augmentation de la température à 500K sous vide a permis d'obtenir un temps de récupération approprié de 0,1 seconde. Pour I_2@Cu_PG et ICH_3@Cu_PG, étant donné qu'une dissociation moléculaire spontanée et de fortes énergies d'interaction ont été observées, le temps de récupération est de supérieur à 10^{14} s. Il reste trop élevé ($>10^9$ s) à 500 K.

Bien que ces matériaux (Cu_PG et Ag_MG) aient montré un temps de récupération élevé, nos résultats les classent comme des capteurs à usage unique (jetables) attrayants, et des matériaux prometteurs pour les applications de capture de l'iode, en raison de leur haute sélectivité et sensibilité. Ils sont donc une alternative pratique aux capteurs réutilisables. À ce jour, les capteurs jetables à base de graphène ont été largement utilisés dans de nombreuses applications industrielles et seront extrêmement utiles dans les domaines de la manipulation de matières nocives en fournissant une protection supplémentaire.

Le **quatrième chapitre** est consacré à l'exploration des matériaux bidimensionnels BC_3, borophène, BC_6N-2 et C_3N dans le même but que le chapitre 3: trouver un détecteur qui adsorberait facilement I_2 et ICH_3 et non CO et H_2O. Les matériaux BC_3 et borophène, bien que suggérés par certaines études, ne se sont pas révélés prometteurs dans ce contexte (**Tableau R.2**).

Tableau R.2: Energies d'adsorption calculées et distances d'interaction minimales pour les molécules sur les substrats

	Energie d'interaction (eV)				**La distance d'interaction (Å)**			
Substrat	**I_2**	**ICH_3**	**CO**	**H_2O**	**I_2**	**ICH_3**	**CO**	**H_2O**
BC_3	−0.491	−0.437	−0.746	−0.207	3.20	2.54	1.53	2.33
8−Pmmn borophene	−0.663	−0.351	−0.651	−0.236	2.51	1.79	1.40	2.41
BC_6N-2	−0.400	−0.265	−0.122	−0.172	3.08	3.29	3.06	2.41
C_3N	−0.801	−0.335	−0.152	−0.194	3.38	2.53	2.95	2.41

Le problème majeur réside dans le fait qu'une forte liaison covalente se forme entre la molécule de CO, entraînant ainsi une "contamination" du capteur potentiel. Dans le matériau BC_6N-2, la présence d'atomes d'azote empêche la formation de la liaison covalente avec le CO; cependant, la différence d'énergie entre les énergies d'adsorption de I_2 et ICH_3, d'un côté, et celles de CO et H_2O, de l'autre côté, n'est pas convaincante (**Tableau R.2**); par conséquent, même si ce système peut, en principe, être utilisé pour détecter les gaz I_2 et ICH_3, sa sélectivité nécessiterait d'être améliorée. Enfin, les résultats de l'adsorption sur C_3N semblent très prometteurs dans la mesure où la différence entre les énergies d'adsorption de (I_2, ICH_3) vs (CO, H_2O) est significative (**Tableau R.2**). Conscients des limites de l'approche "statique" (à température zéro), nous avons effectué des simulations de dynamique moléculaire pour deux systèmes, I_2 et ICH_3 sur C_3N, qui ont renforcé la conclusion sur la stabilité thermique de ces monocouches. Cependant, sur la base des résultats obtenus jusqu'à présent, on peut suggérer la validation de nos résultats par l'expérience, en vue de l'utilisation pratique du C_3N pour la détection de l'iode.

Le cinquième chapitre présente nos travaux effectués sur les MOFs pour un piégeage sélectif des espèces iodées. Dans ce chapitre, nous avons réalisé une évaluation systématique de la performance d'adsorption du M-MOF-74 où M = Mg, Zn, Cu, Fe, Co, Ni et Mn. Les modes et les énergies d'adsorption des espèces iodées (I_2, ICH_3) et des contaminants (H_2O, CO) sur la série M-MOF-74 ont été systématiquement examinés à l'aide de calculs DFT périodiques afin de déterminer le métal (II) optimal pour la capture sélective de I_2 et ICH_3. Les meilleures séries ont été ajustées en remplaçant leur liants ("dobdc") par une molécule plus petite ("dhfuma") afin d'améliorer l'affinité du site métallique pour les composés iodés adsorbés (**Figure R.7**).

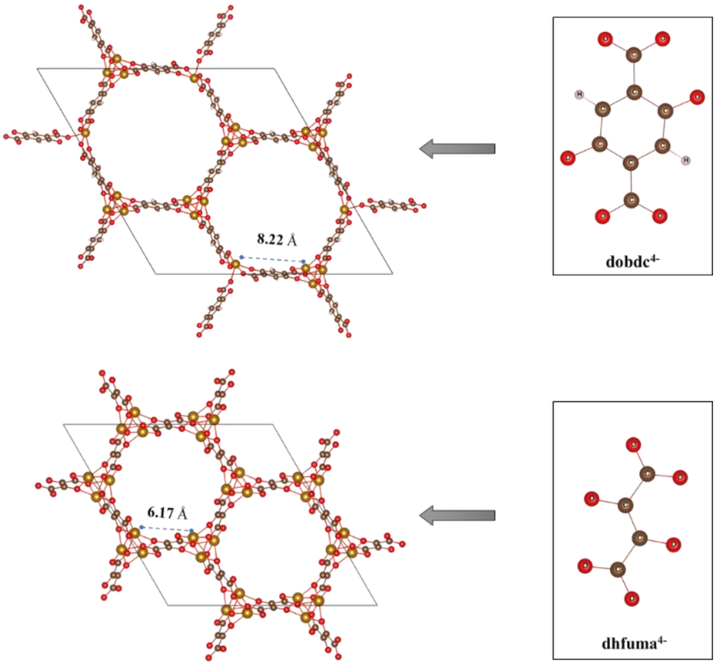

Figure R.7 : Le ligand organique "dobdc" est visuellement comparé au ligand "dhfuma", ainsi que leurs cadres MOF-74 correspondants : haut) M_2(dhfuma) et bas) M_2(dobdc).

Les résultats (**Figure R.8)** ont révélé que Mg et Zn, bien que présentant une énergie de liaison de I_2 et ICH_3 plus élevée que celle du CO, affichent tous les deux une affinité beaucoup plus élevée pour l'eau que pour le reste. D'autre part, Ni et Mn montrent une bonne affinité pour I_2 en présence de CO et d'eau, mais présentent simultanément une affinité similaire pour H_2O et ICH_3, ce qui indique une forte probabilité d'adsorption compétitive entre les deux molécules. Comme le montre la **Figure R.8**, en raison de la forte interaction du cobalt avec la molécule de CO, on s'attend à ce que le CO joue un rôle inhibiteur dans l'adsorption des composés iodés, en particulier pour ICH_3. Le cuivre (Cu) et le fer (Fe) sont les seuls sites métalliques du MOF-74 montrant une affinité plus élevée pour I_2 et ICH_3 que pour H_2O et CO. La plus grande différence I_2-H_2O et I_2-CO a été rapportée pour le fer avec des valeurs de 53 et 63 kJ/mol respectivement, tandis que pour ICH_3-H_2O et ICH_3-CO, le cuivre était en tête par 17.6 et 33.8 kJ/mol respectivement. D'un point de vue thermodynamique, ces résultats révèlent que Fe-MOF-74 et Cu-MOF-74 sont clairement les structures de MOF-74 les plus intéressantes pour la capture sélective de composés iodés à partir de monoxyde de carbone et de l'eau.

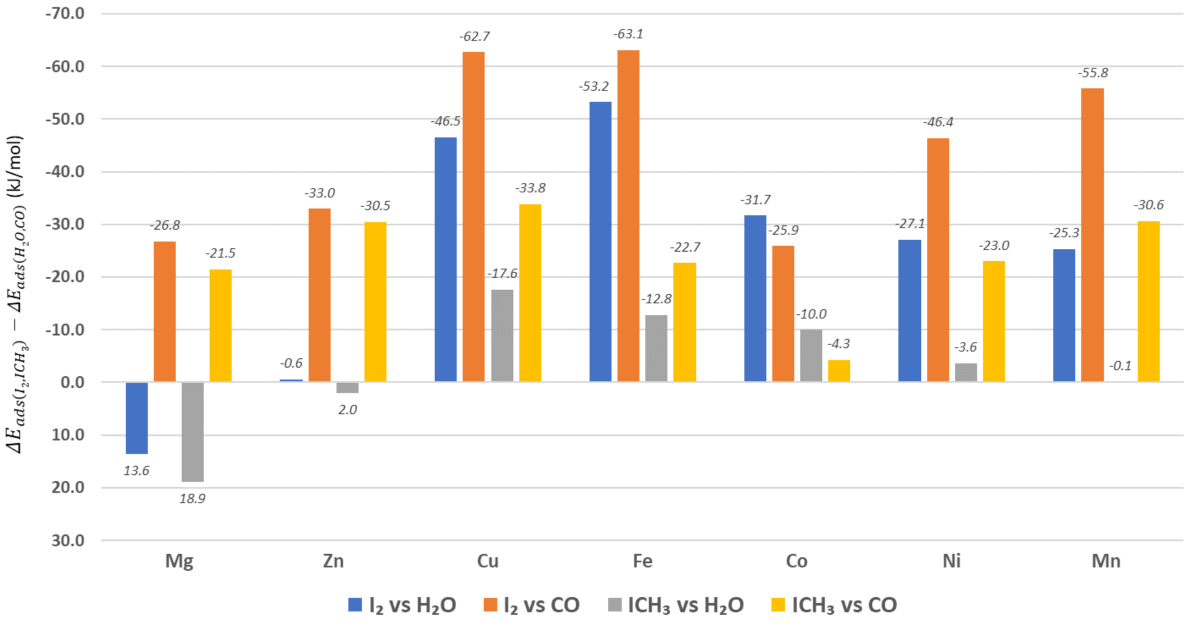

Figure R.8 : La différence des énergies d'interaction totales entre (I_2, et ICH_3) et (H_2O, et CO) dans la série M_2(dobdc) (M=Mg, Zn, Cu, Fe, Co, Ni, et Mn,) calculée en utilisant le niveau de théorie PBE + D2.

Afin de poursuivre notre exploration de matériaux MOFs d’une façon pertinente pour capturer sélectivement les composés iodés en présence d'eau et de CO, nous avons posé l'hypothèse qu'une plus grande sélectivité pourrait être obtenue dans ces matériaux M-MOF-74 prometteurs en changeant l'affinité du site métallique pour les composés iodés adsorbés. Pour cette raison nous avons modifié le ligand. Les énergies d'interaction calculées de I_2, ICH_3, H_2O et CO sur le nouveau matériau MOF M_2(dhfuma) étaient en moyenne 18.2, 6.0, 3.0 et 2.9 kJ/mol plus fortes que sur M_2(dobdc). Le remplacement du ligand dobdc par le ligand dhfuma a raccourci la distance métal-métal, rendant possible l'adsorption croisée (c'est-à-dire l'interaction avec deux sites métalliques en même temps) de molécules plus grandes comme I_2 et ICH_3 avec les sites métalliques du MOF, augmentant ainsi leur affinité pour les composés iodés. Comme pour les M_2(dobdc), Ni_2(dhfuma) et, dans une moindre mesure, Co_2(dhfuma) présentent une faible affinité pour ICH_3 en présence d'eau et de monoxyde de carbone, respectivement. En revanche, l'affinité du cuivre s'est encore améliorée grâce à l'utilisation de ce ligand alternatif et a fait ressortir la structure MOF Cu_2(dhfuma) comme un matériau prometteur. Lors de l'adsorption sur le Mn-MOF et le Fe-MOF, la molécule d'iode semble conserver les mêmes tendances des modes d’adsorption que dans le M_2(dobdc), I_2 se dissociant en deux atomes I liés à deux sites métalliques distincts du MOF à une distance égale à Mn···I = 2.9 Å et Fe···I = 2.67 Å. Les énergies d'adsorption calculées les plus élevées pour I_2 sont observées pour Mn et Fe parmi tous les métaux étudiés, soit -130.1 et -125.4 kJ/mol, respectivement. L'interaction des contaminants (H_2O et CO) sur le Mn-MOF et le Fe-MOF est significativement plus faible que celle de la molécule d'iode gazeux. La **Figure R.9** indique que l'interaction de I_2 sur le Mn-MOF et le Fe-MOF est en moyenne 62 et 83 kJ/mol plus forte que celle de H_2O et de CO, ce qui est plus élevée que celle déjà rapportée sur M_2(dobdc). L'eau et le monoxyde de carbone ne devraient donc pas jouer un rôle préjudiciable sur l'adsorption des molécules de radionucléides gazeux volatils (I_2, ICH_3) dans ces structures MOF M_2(dhfuma). Contrairement à I_2, la molécule ICH_3 ne montre aucune dissociation lors de l'adsorption sur Fe et Mn. Leurs énergies calculées étaient plus de 20 kJ/mol plus fortes que celle de CO, alors qu'elles étaient seulement 6.3 et 9.5 kJ/mol plus favorables que celles de H_2O, respectivement.

D'un point de vue pratique, la forte chimisorption observée avec le Fe et le Mn sera extrêmement utile dans les domaines de la manipulation des matières nocives (par ex. les centrales nucléaires) en fournissant une protection supplémentaire. Par ailleurs, l'interaction du Cu est principalement contrôlée par la dispersion à longue portée, ce qui offre la possibilité d'un matériau régénérable de capture de l'iode qui peut être très intéressant comme pré-concentrateur chimique pour la détection des espèces iodées.

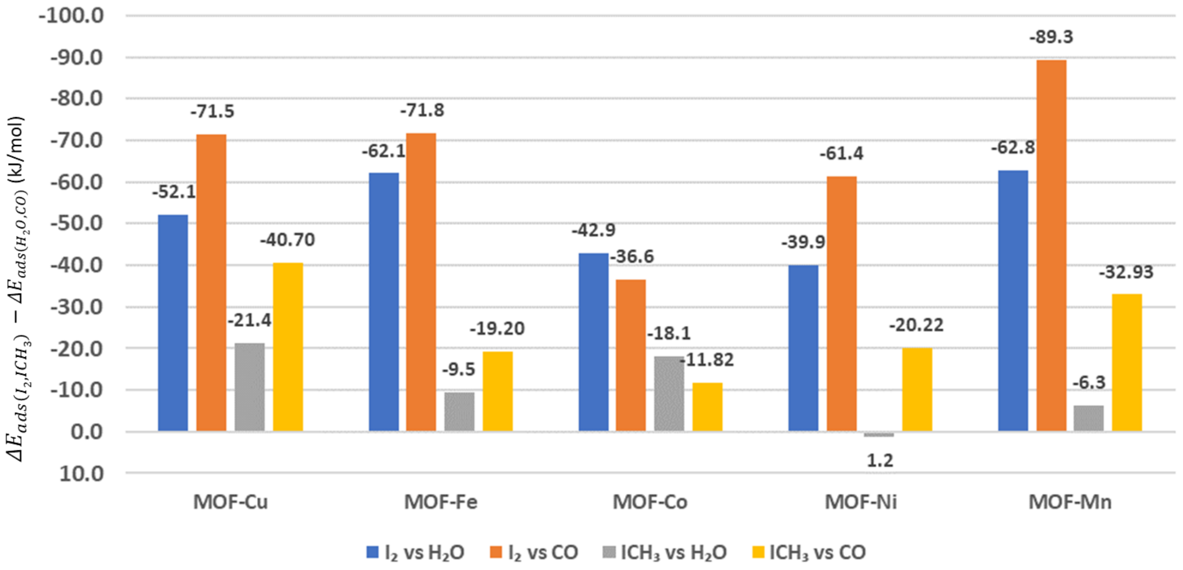

Figure R.9 : La différence des énergies d'interaction totales entre (I_2, et ICH_3) et (H_2O, et CO) dans la série M_2(dobdc) (M=Mg, Zn, Cu, Fe, Co, Ni, et Mn,) calculée en utilisant le niveau de théorie PBE + D2.

Les chapitres 6, 7 et 8 sont orientés vers la seconde application envisagée dans cette thèse qui concerne la capture des gaz nocifs NO_x. Le $6^{ème}$ chapitre sera introduit par une étude bibliographique sur les NO_x, leurs effets sur la santé humaine et les méthodes existantes pour réduire leurs émissions, pour lesquelles les matériaux zéolithiques de type faujasite ont été choisis comme un matériau adsorbant prometteur, pour cette application exigeante.

Le potentiel de la zéolithe de type faujasite (FAU) pour l'application de capture sélective des NO_x en présence d'eau est exploré dans le **septième chapitre**. Avec un rapport Si/Al=23, les FAU échangés par $Be^{2+,}$ $Mg^{2+,}$ $Ca^{2+,}$ $Sr^{2+,}$ $Ba^{2+,}$ Zn^{2+} et Cu^{2+}, présentent une affinité supérieure ou équivalente pour l'eau que pour les NO_x (**Figure R.11**). NO et NO_2 ont presque la même énergie d'interaction sur un cation donné, leur interaction diminue en valeur absolue de $Mg^{2+,}$ (49 kJ/mol) à Ba^{2+} (23.5kJ/mol). Cela indique que ces matériaux seront de mauvais adsorbants pour les NO_x, et qu'ils ne sont pas adaptés à l'application de contrôle de la pollution prévue.

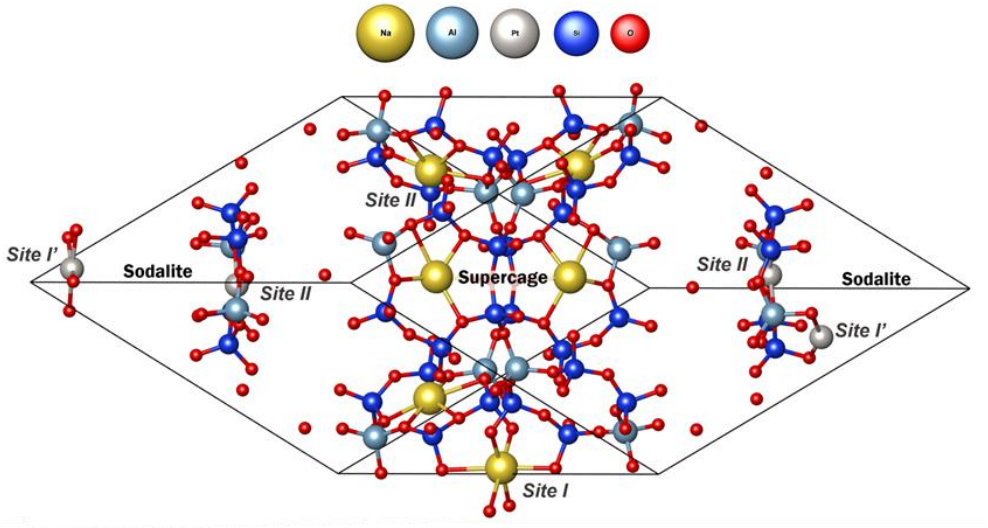

Figure R.10 : la cellule primitive de la zéolithe Pt-NaY représentée en cellule à boule et bâton, avec trois sites accessibles. Site II (Supercage), site I (Prisme hexagonal) et site I'(Cage de sodalite).

Comme le montre la **Figure R.11**, FAU échangé par Fe^{2+} présente une affinité similaire pour l'eau et le NO_2 (-56,3, -53,7 kJ/mol, respectivement), mais une affinité beaucoup plus élevée pour le NO (-155 kJ/mol). Cela signifie que l'eau devrait jouer un rôle négatif sur l'adsorption de NO_2. Cependant, la molécule de NO_2 semble être très réactive avec l'eau dans les zéolithes, conduisant à la formation de NO, par conséquent Fe^{2+} pourrait être un cation approprié pour piéger sélectivement les NOx en présence d'eau en raison de sa haute affinité pour NO.

Le palladium et le platine sont les seuls cations montrant une affinité plus élevée pour NO et NO_2 que pour l'eau (**Figure R.11**). NO présente une forte affinité pour les deux cations (-145,6 et -168,7 kJ/mol, respectivement), suivi par NO_2 (-84,7 et -74,2 kJ/mol). Ces énergies d'interaction sont significativement plus élevées que pour l'eau (-33,2 et -48,2 kJ/mol, pour $Pd^{2+,}$ et $Pt^{2+,}$ respectivement). Par conséquent l'eau ne devrait pas jouer un rôle négatif sur l'adsorption des NO_x dans ces zéolithes.

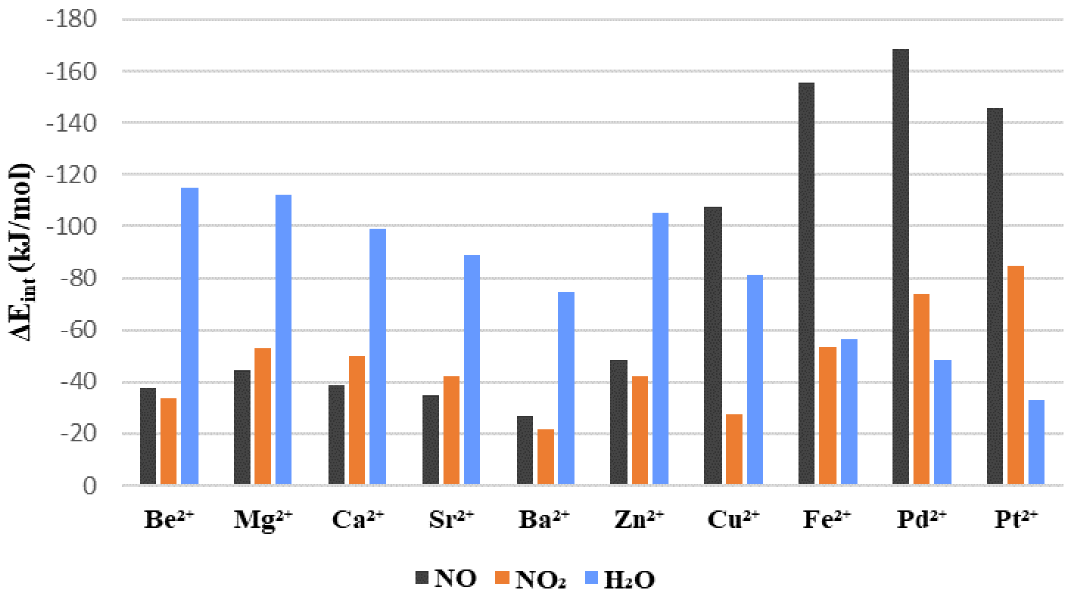

Figure R.11: Les énergies d'interaction totales de NO, NO_2, et H_2O avec la faujasite échangée par des cations divalents, calculées en utilisant le niveau de théorie PBE + TS/HI.

Ces résultats révèlent qu'en terme de sélectivité thermodynamique, les formes Pd^{2+}, Pt^{2+}, et dans une moindre mesure Fe^{2+} sont clairement les faujasites les plus intéressantes pour la capture sélective des NO_x en présence d'eau. Néanmoins, l'analyse de l'activation des liaisons a écarté Fe^{2+} de la liste des cations appropriés, car une activation importante des liaisons N-O est observée lors de l'adsorption de NO_2 sur Fe^{2+}, ce qui peut entraîner la formation de sous-produits indésirables, alors qu'une variation négligeable de la longueur des liaisons est observée pour $Pd^{2+,}$ et Pt^{2+}. Par la suite, le cation Pt^{2+} a été incorporé et étudié dans la zéolithe Y (Si/Al = 2.4) (**Figure R.10**). Les résultats mettent en évidence que la Faujasite Y-$Pt^{2+,}$ est un matériau intéressant pour l'élimination des NO_x des gaz d'échappement des moteurs diesel.

Le huitième chapitre traitant toujours de la capture des NO_x est une extension vers les MOFs en intégrant les cations prometteurs identifiés dans le chapitre 7 en tant que métaux dans le ligand catécholate avant son incorporation dans l'UiO-66 en forme de cage. Des simulations Monte Carlo dans l'ensemble Grand Canonique (GCMC) mettant en œuvre un champ de force NO_x/MOF nouvellement dérivé ont ensuite été réalisées pour évaluer les performances d'adsorption du MOF fonctionnalisé correspondant et comprendre en profondeur le mécanisme microscopique en jeu. Nos simulations moléculaires indiquent que l'UiO-66-CatFe(II) nanoporeux serait un excellent adsorbant pour la capture des NO_x, même pour une très faible concentration de quelques ppm, en raison de fortes interactions Fe(II)/NO_x qui conduisent à des isothermes d'adsorption très pentues pour les deux NO_x. Ce MOF, qui présente un comportement d'adsorption intéressant à une très faible concentration de NO_x, vient compléter le portefeuille de matériaux poreux qui, jusqu'à présent, ont été presque exclusivement testés dans des conditions de fonctionnement impliquant une concentration plus élevée de NO_x (>1000 ppm). Cela devrait guider l'élaboration de l'UiO-66-CatFe(II) pour des tests d'adsorption expérimentaux.

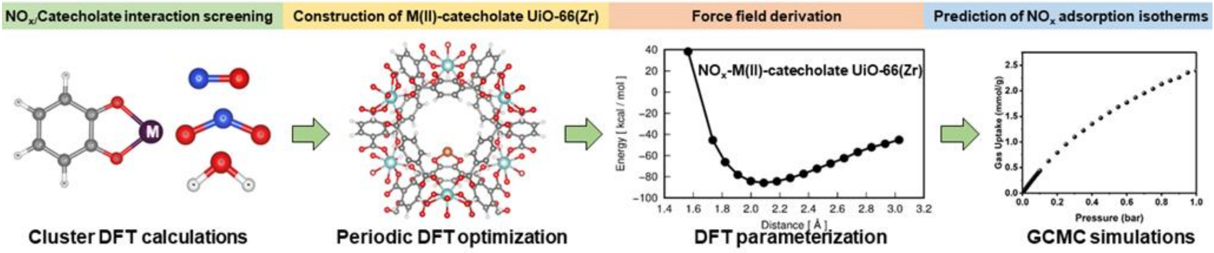

Figure R.12 :Vue d'ensemble de la stratégie globale de calcul avec étape 1 : calculs DFT pour évaluer l'énergie d'interaction entre NO_x et une série de modèles de M-catécholate (M= métaux divalent listées); étape 2 : incorporation des meilleurs catécholates comme ligand dans la structure cristalline périodique de UiO-66 optimisée par DFT ; étape 3 : dérivation des paramètres du champ de force NOx/catécholate métallique UiO-66(Zr) pour les UiO-66(Zr) fonctionnalisés par le catécholate et, étape 4 : prédictions GCMC de leurs isothermes d'adsorption.

General Introduction

The worldwide amount of electricity generated through the nuclear power plant fluctuates considerably from one country to another. Nevertheless, two major countries can be identified as being leaders regarding nuclear power generation: The United States and France, which accounts for half of the EU's production. Since the creation of the French Atomic Energy Commissariat (CEA) in 1945, nuclear energy has gradually become the primary method of electricity production in France.

However, although its advantages and allow to compensate for the intermittence of renewable energies, nuclear energy like any other industrial activity remains dangerous and can never be operated in complete safety. Indeed, this development has led to an increase in the risk of contamination by radioactive gas wastes, among them, iodine compounds require special attention because they lead to serious health consequences and long-term environmental impacts. Two iodine radioisotopes are particularly dangerous, ^{131}I and ^{129}I. The volatile and short-life isotope ^{131}I (half-life of ~8.02 days) is a specific substrate of thyroid receptors and responsible for the long-term development of thyroid cancers. The highly volatile long-life isotope ^{129}I (half-life of ~15 million years) can damage human cells and cause genetic mutations. Additionally, in the environment, radioactive iodine I_2 interacts with hydrocarbons (methane CH_4) and other volatile organic compounds to produce methyl iodide ICH_3. Any leakage of radioactive material constitutes a real danger and a major risk for the surrounding population exposed to these releases. There are two major sources of radioactive exposure:

- Iodine can be generated in very high amounts during a **severe nuclear accident**, especially the isotope 131.
- In the case of leakage of radioactive waste during **nuclear reprocessing operations**, potentially the isotope 129 is produced, which is considered as a nuclear waste signature.

On the other hand, with a view to opening up towards trapping other hazardous gases by means of adsorbents. A second application will be aimed specifically within NO_x capture. Especially in a confined working area without ventilation and without exhaust gas treatment, NO_x emissions from engines (300-1000 ppm for NO and NO_2) are a major health (with frightening effects such as lung cancer and blood circulation attack) and safety concern. In France, nearly 800,000 workers are exposed to these emissions. The reduction of NO_x emissions from non-road vehicles is therefore a current priority in the prevention of occupational risks.

This thesis aims to develop efficient and prompt materials to detect and trap the volatile radionuclides during severe nuclear accidents or nuclear fuel reprocessing, in order to reduce the risks associated to the presence of radioactive iodine compounds in the atmosphere. Among the potential means of detection, we can firstly mention graphene and other 2D carbon materials, which are promising candidates for ensuring the sustainable detection of the main volatile iodine species (I_2 and ICH_3). Secondly, radioactive iodine sorbents such as Metal Organic Frameworks (MOFs) can be considered in order to avoid any risk of propagation of radioactive products in the environment and to avoid any probability of contamination. In the case of capturing NO_x. Zeolites were selected as one of the most widely used materials for gas adsorption, as previously revealed, and are proving to be excellent and promising candidates for this challenging application.

To achieve this goal, a theoretical approach was applied where periodic DFT calculations were carried out. The results obtained using this approach provide atomic level insight into the interaction of gas molecules with the listed materials and understand the detection/trapping mechanism of iodine compounds. These insights are expected to guide the experimental effort towards the synthesis of the optimum sensors/sorbents in order to avoid a tedious and time-consuming trial-error approach.

Following, we detail the structure of this manuscript, giving a brief description of the content of each chapter.

The first chapter is classically dedicated to the state of the art. It will serve in a first part to provide a better knowledge of the source of these volatile radionuclides, then in a second part will be devoted to a bibliography of the existing detection techniques (different types of sensors) and trapping technologies (liquid and solid) in order to evaluate their performances and to underline their drawbacks. In view of the existing gaps in the literature, a conclusion will finally be given to justify the work done and the choice of materials surveyed in this thesis.

Supported by the density functional theory (DFT), the second chapter presents the theoretical approach adopted to study these newly outlined aspects. Briefly, we will present some basics of the DFT theory applied to periodic systems and the different tools used in our calculations.

The third and fourth chapters are devoted to our theoretical investigations for an efficient sensor suitable for detecting iodine species (I_2 and ICH_3) mainly formed in nuclear power plants and nuclear fuel reprocessing facilities. In the third chapter, the detection performance of pristine and defected graphene, as well as Ag- and Cu-doped graphene monolayers, was examined using periodic density function theory calculations and Grimme's D3(BJ) dispersion correction scheme, based on four important detection criteria (selectivity, sensitivity, stability, and recovery time). Similarly, in fourth chapter, we perform a comparative study of the potential detection performance of four promising 2D materials (borophene 8-Pmmn, BC_3, C_3N, and BC_6N) against the above-mentioned iodine-containing gases and, for selectivity verification purposes, against common inhibitory gases in the containment atmosphere (H_2O and CO).

The fifth chapter will be devoted to present the findings regarding MOFs for stable trapping of iodinated species. In this chapter, we have performed a systematic evaluation of the adsorption performance of M-MOF-74 where M = Mg, Zn, Cu, Fe, Co, Ni and Mn. The adsorption modes and energetics of iodine species (I_2, ICH_3) and contaminants (H_2O, CO) on the M-MOF-74 series were systematically examined using periodic DFT calculations to determine the optimal metal (II) for selective capture of I_2 and ICH_3. The best Cu-, Mn- and Fe-MOF-74 series were tuned by replacing their linker ("dobdc") with a smaller molecule ("dhfuma") to improve the affinity of the metal site for the adsorbed iodine compounds.

Chapters 6, 7 and 8 will be oriented to the second application envisaged in this thesis, as previously outlined, and which concerns the capture of harmful NO_x gases. The 6th chapter will be introduced by a bibliographical survey on NO_x, their effects on human health and the existing methods to reduce their emissions, among which faujasite-type zeolite materials have been chosen as a promising sorbent material for this challenging application.

To this end, in the seventh chapter, a periodic density functional theory (DFT) calculations along with a recent dispersion correction scheme, namely Tkatchenko-Scheffler coupled with iterative Hirshfeld partitioning TS/HI, were performed to investigate the interactions between NO, NO_2, H_2O and a series of divalent cations (Be^{2+}, Mg^{2+}, Ca^{2+}, Sr^{2+}, Ba^{2+}, Fe^{2+}, Cu^{2+}, Zn^{2+}, Pd^{2+}, Pt^{2+}) exchanged faujasites. This enabled to identify the optimum zeolites to selectively capture NO_x in presence of H_2O, with respect to two important criteria, thermodynamic affinity, and regeneration.

The eighth chapter will be a rational and dedicated continuation of this zeolite study in which density functional theory (DFT) calculations and grand canonical Monte-Carlo (GCMC) simulations were combined to systematically assess the adsorption performance of M(II) = Mg(II), Mn(II), Fe(II), Co(II), Ni(II), Cu(II), Zn(II), Pd(II) and Pt(II) metals into the catecholate ligand for an efficient NO_x capture prior to its incorporation into the cage-like UiO-66.

Finally, conclusions were drawn regarding the theoretical results obtained in this work, and their importance in this field. In addition, some perspectives for future studies have been listed.

Chapter 1 : State of the Art

"*Nuclear energy, in terms of an overall safety record, is better than other energy.*"

– Bill Gates

1.1 Introduction

Electricity, one of the world's socio-economic pillars, has become essential in all life areas, domestic and industrial.[1,2] Its consumption, intimately linked to the improvement of the life quality and the wealth of countries has not stopped increasing. In France, electricity consumption has tripled between 1973 and 2010.[3] In 2018, the world electricity consumption was 22,315 TWh, in total 4% higher than in 2017.[3] During the same year, 10 countries accounted for nearly 70% of total global electricity consumption. Particularly, China (6,880.1 TWh), the United States (4,288.5 TWh) and India (1,309.4 TWh) alone accounted for more than the half of it.[3] Electricity production depends on the availability of energy resources, which are mainly fossil fuels, renewable energies, and uranium:[4]

- Fossil fuels (oil, natural gas, and coal), which are made of hydrogen and carbon, are highly energy-efficient substances allowing the production of electricity in thermal power plants.
- Renewable energies (sun, wind, heat, water, organic matter, etc.) allow the production of "green" electricity through specific devices or installations, such as solar panels, windmills, hydro-electric power stations, biogas plants...
- Uranium, a natural radioactive ore is used for producing electricity through nuclear fission.

France does not have sufficient energy resources (gas, oil, or coal) to produce its own electricity. The country has therefore decided to develop nuclear energy to ensure both security of supply and energy independence. Thanks to nuclear power, the country is now able to generate continuous electricity and adapt to electricity demand variations. In addition, nuclear power is one of the cheapest sources of electricity to produce, allowing France to have one of the lowest electricity prices in Europe.[5]

Although these benefits are well appreciated, however, like any industrial activity, the production of electricity from nuclear sources generates gaseous, liquid, or solid wastes. These liquid and gaseous wastes are radioactive, and they can be dispersed in the environment.

That is the main motivation for this Ph.D. In the present thesis, we focus on the capture and sensing of radioactive iodine present in the gaseous and liquid effluents of nuclear power plants and waste reprocessing plants. Firstly, a general description is given on the economic importance of uranium in France and the whole world for the production of nuclear electricity. Then, particular attention will be given to the phenomenologies of the release of radioactive fission products potentially dangerous for the population and the environment and all the remediation possibilities.

1.2 Economic value of uranium in France and around the world

Nuclear electricity represents about 10% of the world's electricity production.[6] Amongst the 33 countries that operate nuclear power plants worldwide, France has 18 nuclear power plants currently in service with a total of 56 nuclear power reactors.[7] On this aspect, France is in the lead, generating around 78% of its power from nuclear (Figure 1.1).

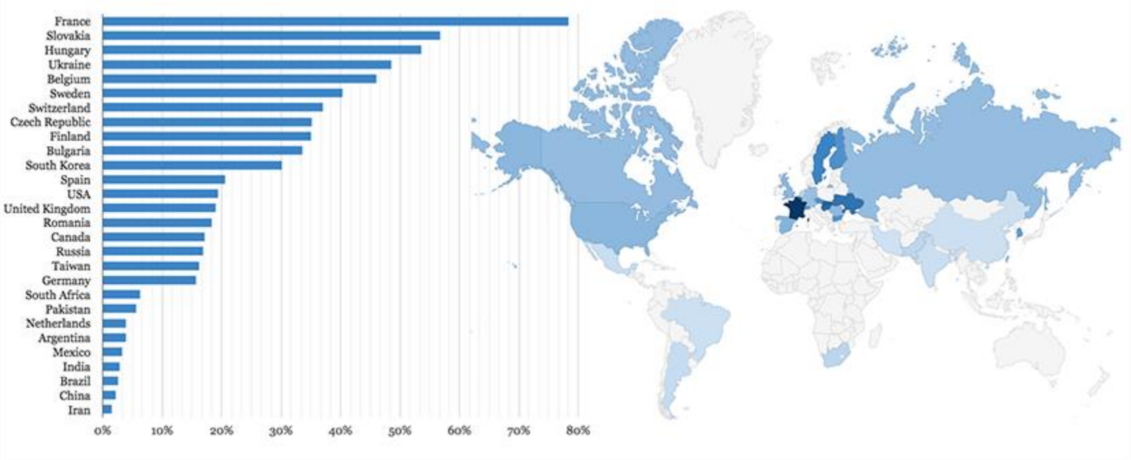

Figure 1.1: Countries of the world according to the share of their electricity generated from nuclear power. Source: BP statistical review of world energy.[8]

Each plant has two to six operational reactors with different power levels, such as 900, 1300 and 1450 MW (Table 1.1). As an example, a 900 MW reactor produces an average of 500,000 MWh per month, which corresponds to the consumption of about 400,000 houses.

Table 1.1: Number of nuclear reactors in France by power. Source: EDF 2020.[7]

Power	Number of reactor units
1 450 MW	4
1 300 MW	20
900 MW	32

More specifically in France, almost all electricity reserves are from nuclear power plants. Other energy sources, notably fuel oil, coal, and gas, are occasionally used to meet electricity consumption peaks. Moreover, in 2016, nuclear energy provided 72.3% of the electricity produced in the country.[9]

Considering the importance of nuclear energy in the world, it is essential to know how it is produced in order to precisely identify its associated constraints.

1.3 Nuclear energy generation process at the atomic scale

Nuclear energy generation cycle starts with uranium ore extraction (Figure 1.2), conversion and concentration into nuclear fuel required for power plants.[10] This process generates spent fuel which contains radioactive elements (i.e., the nuclear residual materials: uranium and plutonium; Actinides (neptunium, americium, curium…etc.); and the fission products), some of which are released into the atmosphere or/and in liquid effluents. In addition, this spent fuel and various radioactive wastes generated by the process require reprocessing (Figure 1.2), which is also accompanied with radioactive releases.

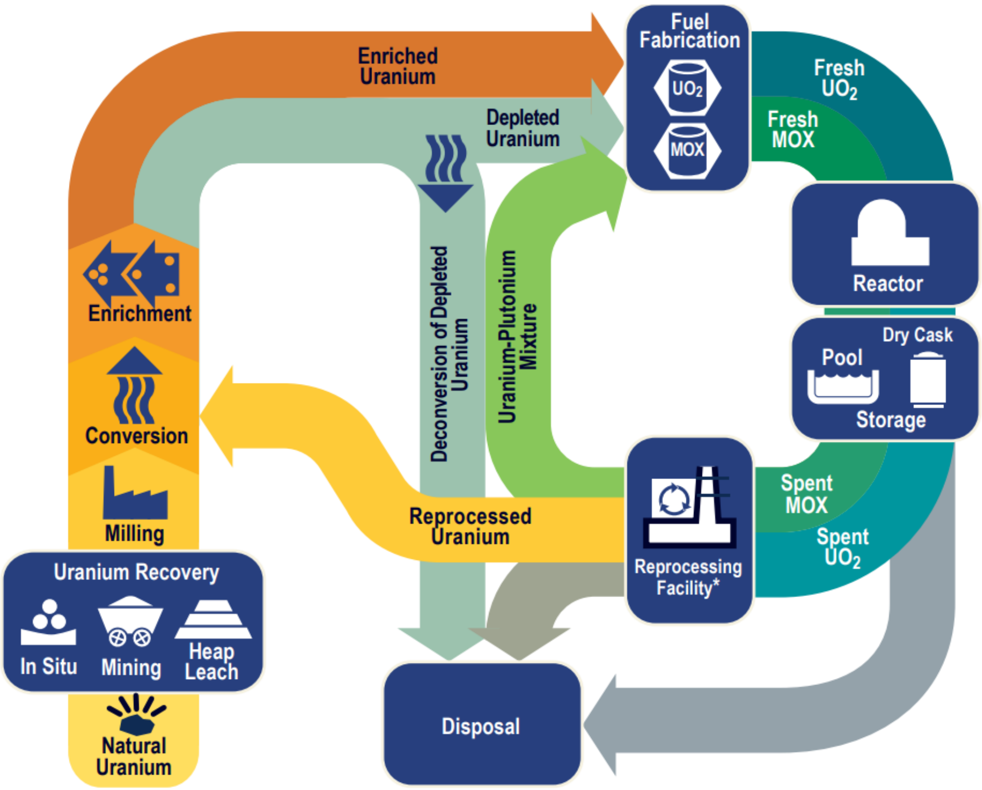

Figure 1.2: The nuclear fuel cycle. Source: United States Nuclear Regulatory Commission.[11]

The radioactive uranium (isotope 235) content of natural uranium is about 0.7%, while most reactors use enriched uranium at levels up to 2 to 4%. Therefore, extracted uranium ores are concentrated/purified for producing uranium hexafluoride (UF6) gas,[12] which is further used for producing uranium oxide fuels UO_2[10] (Figure 1.2). Pellets made of UO_2 are coated to form rods, which are joined together to produce fuel assemblies. These assemblies are then introduced into the core of the nuclear reactors where they deliver energy by fission of uranium 235 nuclei using neutrons. When a uranium nucleus is hit by a neutron, the fission releases energy and produces 2 or 3 more neutrons (Figure 1.3). Fission reactions are controlled and maintained at constant rate thanks to the control rods that regulate the number of neutrons.

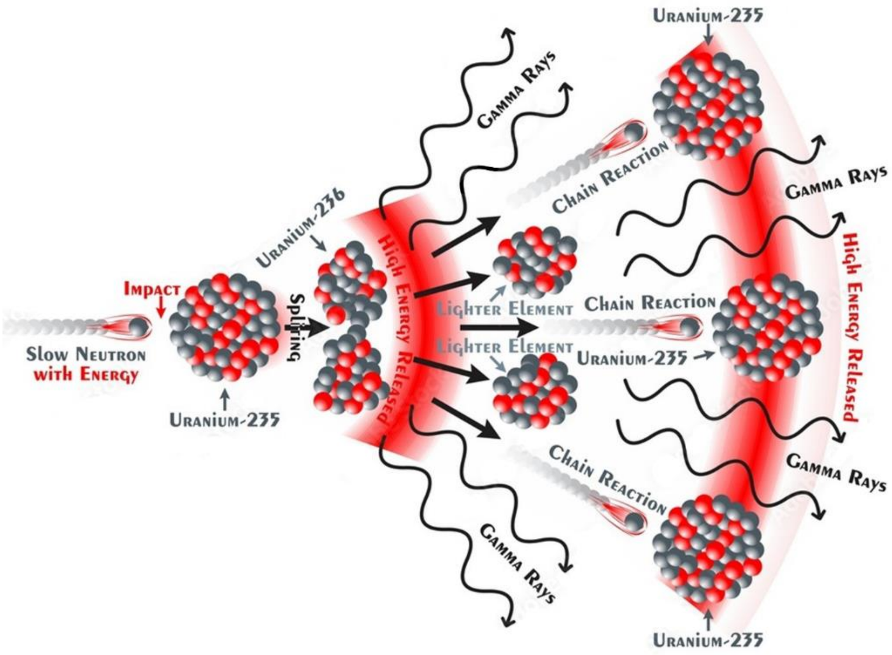

Figure 1.3: Fission of uranium 235 and chain reaction.

These reactions lead to the consumption of uranium 235, and the formation of radioactive products called fission products, which in turn release a significant amount of energy in the form of heat. This latter is recovered by the coolant (gas or liquid) flowing around uranium rods and is transferred to a turbine to produce electricity. The excess steam is condensed by a cooling system that depends on the geographical location of the installation (river water, sea water, or a cooling tower). The entire primary circuit is confined in a concrete enclosure called the containment.

At the atomic scale, uranium 235 fission occurs by the absorption of one neutron, and every neutron emitted, can cause the fission of another nucleus which itself will emit neutrons likely to produce new fissions by chain reactions (Figure 1.3). This leads to the formation of two unstable nuclei, most often one nucleus with a mass number close to $A = 95$ (bromine, krypton, zirconium, strontium...) and the other one with a mass number around $A = 139$ (iodine, xenon, barium, cesium...). The fission products include more than 400 nuclides at the exit of the reactor, over 300 of which are radioactive. Among these, more than 100 will still be active after a few years of cooling. These nuclei can be present in gas, liquid, or solid state, and are responsible for almost all of the fuel's radioactivity. They are highly radioactive, volatile, and are accumulated and stored in reactors.

Any radioactive leak represents a major risk for the surrounding population. Even at low levels, these dangerous substances cause cancers that are probably responsible for numerous deaths.[13] Food, water, soil, and buildings can be severely contaminated, requiring people's evacuation from the area close to the radioactive release.

1.4 Radioactive pollutants

Generally, the exposure risks to radioactive products occur in two major cases:

- During a **severe nuclear accident,** an event that may lead to an excessive release of radioactive elements (iodine, Krypton, Xenon, etc.) in the environment.[13]
- In the case of radioactive leakage during **reprocessing facilities of radioactive waste**.[14,15]

1.4.1 Iodine, its isotopes, and emitted radiations

The atom I of atomic number 53 belongs to the family of halogens. It is mainly present as I_2 with a boiling temperature of +184.4 °C.[**16**] Among its various oxidation states (-1, +1, +3, +5 and +7), -1 is the most stable. Considering organic chemistry, iodine is involved in two main types of reactions: 1) saturation reactions of multiple bonds (addition reactions with organic compounds in soils for example) and 2) substitution reactions.[17]

Iodine has 37 isotopes with masses ranging from 117 to 141 (u).[18] Except for iodine 127 (stable) all other isotopes are radioactive fission products. Isotopes ^{123}I (half-life of 13 hours) and ^{125}I (half-life of 59 days) are used for nuclear imaging of kidneys and thyroid, as well as for monitoring thyroid uptake.[18] ^{129}I and ^{131}I represent the main iodine isotopes signature in nuclear releases with the first being a highly volatile long-lived isotope with half-life of ∼15 million years, and the second with a very short half-life of 8,0 days (Table 1.2), both considered from radioecological point of view as of the most feared fission products of nuclear waste since they are the only released iodine isotopes with a half-life greater than one day.[18]

Table 1.2: Radioactive Properties of key Iodine Isotopes.

Isotope	Half-Life	Specific Activity (Ci/g)	Decay Mode	Radiation Energy *(MeV)*		
				Alpha (α)	**Beta (β)**	**Gamma (γ)**
^{129}I	16 million yr	0.00018	β	-	0.064	0.025
^{131}I	8 days	130,000	β	-	0.19	0.38

Ci = curie, g = gram, and MeV = million electron volts; a dash means the entry is not applicable.

Iodine 131 decays with β^- radioactivity to ^{131}Xe, and is therefore a γ-ray emitter. [13]

$$^{131}_{53}I \rightarrow {}^{131}_{54}Xe + {}^{0}_{-1}\beta$$

Iodine 129 decays with β^- emissions to ^{129}Xe analogously.[19]

Beta radiations, positively (β^+ called positron), or negatively charged (β^- which is an electron) interact easily with matter, requiring few millimeters thick protections (e.g., aluminum foil) since they can penetrate a 0.6 to 2.0 mm thick tissue. Gamma radiations are high-energy electromagnetic radiations (i.e., photons) without mass and charge. They interact poorly with matter but are extremely penetrating and require very heavy protections such as several centimeters of lead.[20] Because of the high energy β radiations, ^{131}I is the most carcinogenic of the iodine's isotopes. Once released in the environment, ^{131}I isotope hits its target, the thyroid, where it concentrates, and causes long-term health problems.[20] ^{129}I contaminate humans through the food chain, particularly through the air-plant-dairy-human chain. Inside the body, β^- emissions from ^{129}I can damage cells, and cause genetic mutations.

The major forms of radioactive iodine present in a nuclear cycle are as follows:[21]

- Molecular iodine (I_2) present in gaseous form: I_2 gas can rapidly adsorb onto the paintings on the walls of the containment and react with these paints to create organic iodine gas.
- Organic iodine, commonly methyl iodide (ICH_3), present in gaseous form: which in turn can be transformed, under the effect of radiation, into iodine oxides, which are assimilated to very fine aerosols that can be deposited in the air.
- Particulate iodine (aerosols) with variable particle diameter (with the possibility of aggregation.

1.4.2 Radioactive pollutants released during nuclear accidents

The handling of any industrial equipment is not always perfectly controllable. Sometimes, a loss of control or improbable leaks can lead to disasters and catastrophes. These include nuclear accidents. In general, these accidents occur in the part of the reactor where the fuel is severely degraded by a melting of the core caused by a significant rise in temperature. This is the consequence of a prolonged absence of cooling, normally provided by the coolant.[22] This failure can be due either to a human factor, to electricity loss, to a material dysfunction (as it happened at Chernobyl[23] and Three Mile Island[23]), or to an insufficient protection against natural disasters such as the accident at Fukushima Daiichi on March 11, 2011.[23]

From these sever nuclear accidents, large quantities of radioactive products (fission products and noble gases) have been released into the atmosphere with disastrous consequences. The activity due to iodine-131 released during the Chernobyl accident was estimated at 300,000 TBq (tera-becquerels). In mass, this activity would correspond to the dispersion of 65 grams of iodine-131, a hint of the extreme radioactivity of these nuclear elements.[24]

Consequently, these accidents have given new importance to the criteria of nuclear safety and to the structure of the organizations in charge for its control. The exposure to radioactivity can have serious consequences on the population and the environment. Concentrated radioactive species in particular iodine, depending on their physicochemical properties, present various degrees of danger and risks.

In general, nuclear accidents generate two types of radioactive pollutants:

- Iodine 131. Following nuclear accidents, this iodine isotope disperses rapidly in air (as gaseous iodine I_2 and ICH_3) and water (CsI, I_xO_y) producing aerosols (iodine aerosols).[25] In the Fukushima nuclear disaster (2011), the level of radioactive iodine reached 1850 times the legal standard in a water sampled taken from several meters away from the power plant.[26]

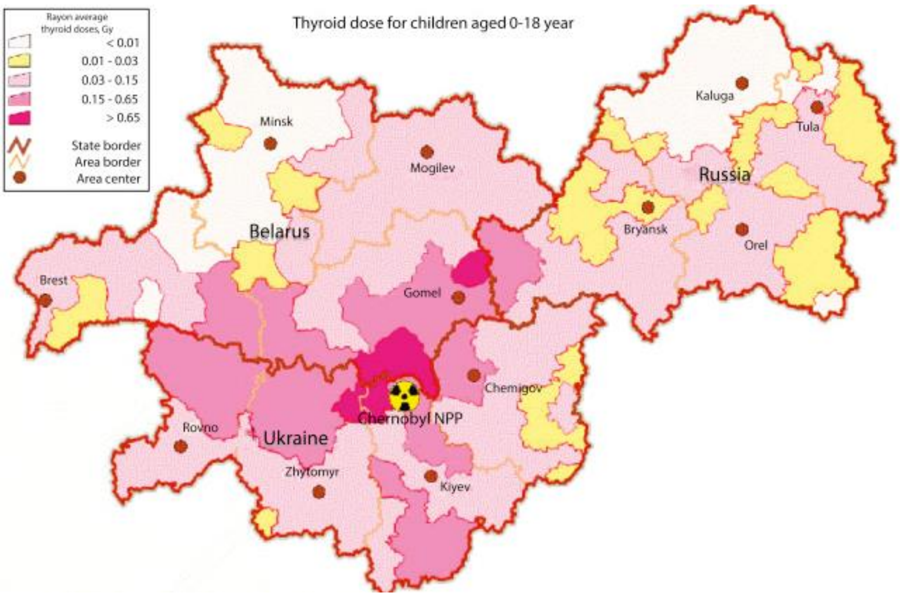

Figure 1.4: Average thyroid doses of children and adolescents living at the time of the accident in the most affected regions of Belarus, Russia, and Ukraine. [27]

Ingestion of ^{131}I-contaminated food has resulted in significant thyroid intakes for non-evacuated residents of the contaminated zones of Belarus, Russia, and Ukraine after the Chernobyl accident (Figure 1.4). Due to their small thyroid mass, children have received a significantly higher average thyroid dose than adults. This is a major reason why so many children subsequently developed thyroid cancer.

- Inert rare gases (neon, xenon, krypton) which disappear in the atmosphere without being captured by the body.

1.4.3 Reprocessing of radioactive waste and resulting pollutants

Power plant effluents are collected, treated, and recycled, leaving only a small proportion to be discharged according to regulatory requirements.[28] Gaseous effluents arise from process equipment and, secondarily, from workshop ventilation.

Radioactive and non-radioactive gaseous fission products present in spent fuel are mainly recovered during shearing and dissolution of spent fuel.[29] The majority of krypton 85 and part of the tritium, carbon-14, and iodine 129 are thus found there. Reprocessing centers release the ^{129}I, in gaseous form or in liquid effluents, into the environment (Table 1.3).

Table 1.3: Inventory of ^{129}I in reprocessing facilities.

Source	**^{129}I (Kg)**		**^{129}I (Bq)**		**Ref**
	Liquide	Gas	Liquide	Gas	
Hague (1966-2004) France	3119	68	20.27	0.44	**Lopez-Gutiérrez et al. 2004**[30]
Marcoule (1998-1997) France	N/A[a]	68	N/A	0.44	**Cogema 1997**[31]
Sellafield (1952-2004) UK	1371	182	8.91	1.18	**Aldahan et al. 2007**[32]
Savannah river (1954-1989) USA	N/A	42	N/A	0.27	**Reithmeier et al. 2010**[33]
Mayak (1948-1986) Russia	N/A	162	N/A	1.05	**Reithmeier et al. 2010**[33]
Seversk (1956-1995) Russia	N/A	35	N/A	0.23	**Reithmeier et al. 2010**[33]
Zhelesnogorsk (1964-1995)	N/A	22	N/A	0.14	**Reithmeier et al. 2010**[33]

After three to five years activity for sustaining the nuclear chain reaction, spent fuel is removed from the reactor core, recycled, and reprocessed. Once out of the reactor, it is deactivated in pools close to the reactor core,[34] that is because water is an effective radiation barrier and helps cooling the fuel that continues to emit heat. At the end of this period (six months to one year) its activity decreases, and the fuel is sent therefore to reprocessing facilities, as *Areva's La Hague* in France. There, it will be stored for three to five years in a water pool, to carry on its deactivation and help its subsequent handling. Four meters water are present on the top of the fuel to ensure biological protection. Reprocessing in the context of a nuclear fuel cycle has the potential to be employed both to recover uranium and plutonium, and to stabilize radioactive fission products in the form of sustainable waste.

1.4.3.1 Shearing and Dissolving

After its deactivation in the pool, spent fuel is transferred to shearing workshops (Figure 1.5) where fuel rods are cut into 35 mm long sections called clams, which fall by gravity into a dissolving wheel (dissolver).[35,29]

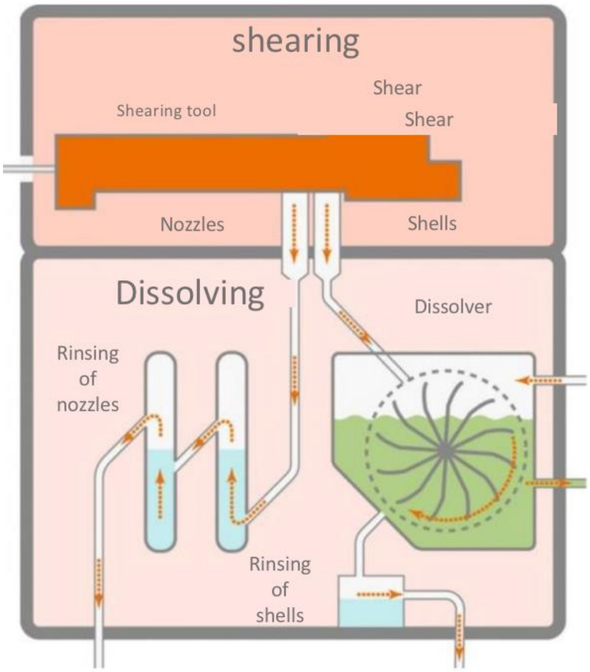

Figure 1.5: Shearing and dissolving process.

Nozzles are treated separately through rinsing as they don't contain nuclear substances, and then stored along with Shells before being compacted. While radioactive substances present in fuel rods are extracted by solubilization using boiling concentrated nitric acid in the dissolver and then sent to gas treatment and clarification.

1.4.3.2 Clarification

Clarification (Figure 1.6) allows the separation by centrifugation, of shearing fines and fission products which are insoluble in acid. The acid solution contains uranium, plutonium, nitric acid, and soluble fission products.[35,29]

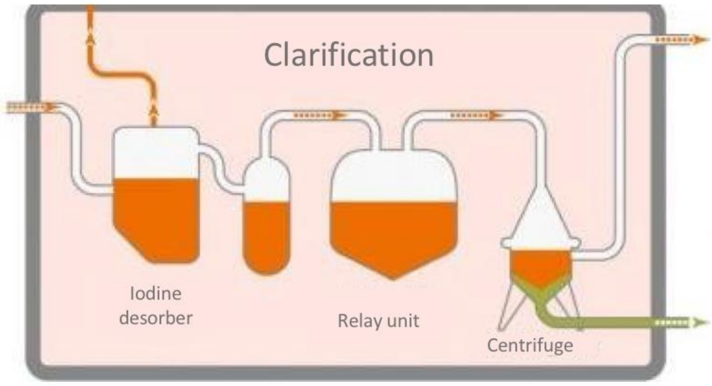

Figure 1.6: Clarification Process.

The clarified solution has the following composition: [29]

- 200 g/L Uranium.
- 2.5 g/L Plutonium.
- 3.5 mol/L Nitric acid.
- 6 to 7 g/L Fission products.

The separated fission products are then concentrated by evaporation and stored in tanks waiting for vitrification. The clarified solution is transferred to the extraction and concentration plants for separation of nuclear materials. The different steps of extraction allow the separation of plutonium, uranium, and fission products.

1.4.3.3 Packaging and storage of shells and tips

Shells and tips are packed (Figure 1.7) in shuttle drums after which they are sent to the compacting workshop. Fission products and actinides which are unrecyclable are final waste products. For permanent and stable immobilization, they are vitrified in glass, since the latter is insoluble in water and remains inert towards physico-chemical agents.[35,29]

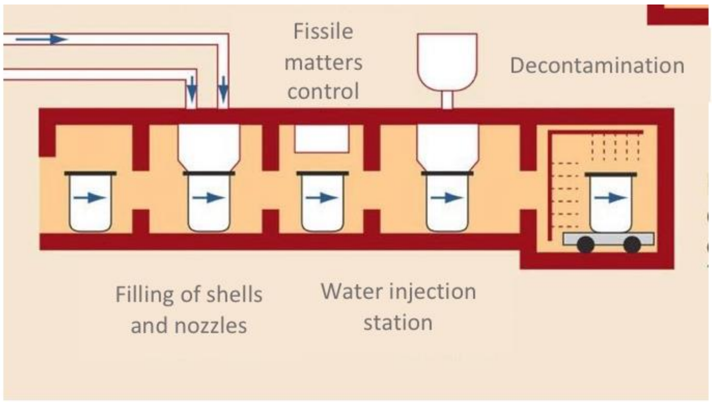

Figure 1.7: Packaging and storage Process.

1.4.3.4 Gas treatment

Dissolution of irradiated fuels produces gaseous effluents which are treated, washed, and filtered in specific units before their release in the atmosphere through the plant chimney, while the acid solution is clarified (Figure 1.8). Gaseous effluents contain NO and NO_2 produced from the reaction of nitric acid with fuel, gaseous or volatile fission products (iodine, krypton, xenon), carbon 14 (mainly in the form of CO_2) and radioactive aerosols.[35-29]

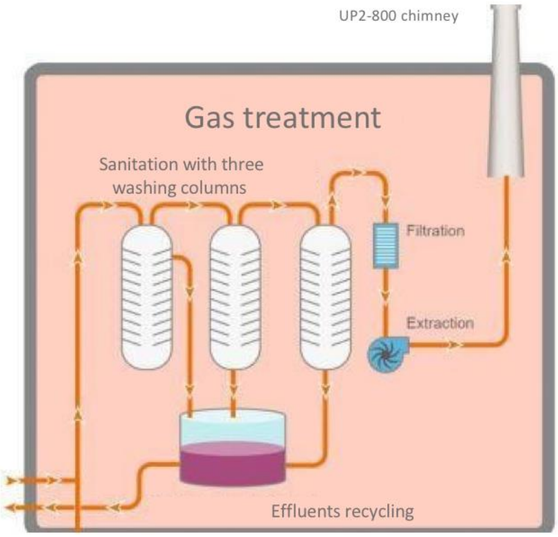

Figure 1.8: Gas treatment Process.

Treatments consist of recombining nitrogen oxides to produce nitric acid, which is further recycled. The main effort is focused on iodine 129. During dissolution, iodine is desorbed and released in dissolution gases, this concerns more than 97% of iodine present in the fuel from *La Hague* plants.[36] Iodine released in gases will then be trapped almost quantitatively, after recombination with nitrous vapors, in the form of sodium iodide $NaIO_3$ by a sodium scrubber, and then released into the sea. A second trap by adsorption on solid supports (mineral support based on silica or alumina impregnated with silver nitrate) ensures a complementary gas purification.[36] Two other iodine trapping devices on solid supports ensure the immobilization of the desorbed iodine in the workshop's downstream dissolution. With those trapping units, 0.5% of ^{129}I present in the fuel is released into the atmosphere through hundred-meter-high stacks. Residual iodine can be carried throughout the rest of the plant and desorbed in the various workshops.

In summary, radioactive releases can be issued from several nuclear accidents or reprocessing plants. In particular, radioactive iodine species are among the most dangerous elements, presenting two distinct isotopes. The ^{129}I being a signature of nuclear waste from reprocessing plants and the ^{131}I isotope, the most dangerous fission products in case of severe nuclear accidents. Recognizing the serious dangers of radioactive iodine species, and the severe thyroid diseases suffered by contaminated people. Trapping them is an essential need to ensure nuclear safety and the health protection of persons potentially in risk of contamination. We must also add that even in small quantities, these species still present the same dangers of contamination, which explains the real need to introduce powerful iodine sensors in order to detect any further dissemination or leakage and warn and alert us to such a serious danger. The real challenge is to find an effective solution that can be adopted on an industrial scale to trap and detect these volatile species.

It seems therefore very relevant to first develop a complete bibliography on these sensing and trapping methods currently used in the nuclear industry while exploring their efficiencies and performances for this challenging application. Then, the most promising trapping/detection materials for radioactive iodine species will be outlined, making it the main objective of this thesis.

1.5 Sensing of radioactive iodine

As discussed earlier, detection of volatile radioisotopes in nuclear power plants is necessary for the health of humans, and ecosystems for environmental protection. Indeed, several incidents can occur as was the case when radioactive gaseous effluents from the *Penly* nuclear power plant (France) were released on June 21, June 27, and July 9, 2001, without iodine being filtered. The iodine traps were not in operation during the release of radioactive gaseous effluents. Following an error of interpretation, the manufacturer wrongly considered that filtration through iodine traps was not technically feasible.[37]

1.5.1 Definition of a gas sensor

A gas sensor is a device that transforms at least one of its physical characteristics when subjected to a change in the gas environment. More generally, a sensor is built up with two main elements: the sensitive element and the transducer to which it is associated. The sensitive element is the heart of the sensor allowing gas recognition. The transducer is the device that converts the reaction between the gas and the sensitive element into an electrical signal. Sometimes the sensitive element and the transducer are confused, as for example in the Metal oxides sensors (MOS).

Generally, a sensor is chosen considering the object to detect, the environment, and the type of detection. Several large families of gas sensors are identified according to the type of measurements performed, as follows:

- ***Electrochemical sensors.***[38–40] Based on redox reactions, such sensors allow gases to diffuse across a porous membrane to an electrode where they are either reduced or oxidized. The electrochemical sensors operate through a chemical reaction between the gas and the oxygen contained in the gas sensor. This electrochemical reaction with the target gas generates a current flow between the sensing electrode and the counter electrode. The electrolyte is responsible for transporting these ionic charges (Figure 1.9). This sensor displays a good sensitivity and selectivity (the metal oxide detects 175 ppb ozone at operating temperatures between 200°C and 400°C), wide operating temperature range, multiple ranges, and linear output but a limited lifetime and low reproducibility. In addition, a high humidity or dryness will adversely influence the sensor's lifetime. Instantaneous changes in pressure can produce a sensor transient output and/or a false alarm.

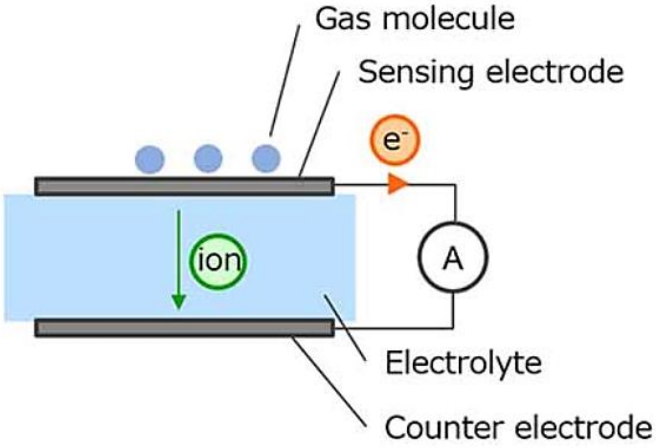

Figure 1.9: Electrochemical gas sensor.

- ***Catalytic sensors.***[41–43] This type of sensor typically includes a catalyst surface being heated to a very high temperature through a platinum resistor that is coated onto the catalyst (Figure 1.10), thereby giving any flammable gas molecules a chance to ignite. Gas concentrations can be detected by monitoring the change in platinum resistance resulting from the increase in temperature. These gas sensors have accurate measurement, fast response, and long life, making them a leading sensor in the field of safety detection. However, they are non-selective in the flammable gas range and susceptible to poisoning. Moreover, in case of fire, the risk of explosion increase.

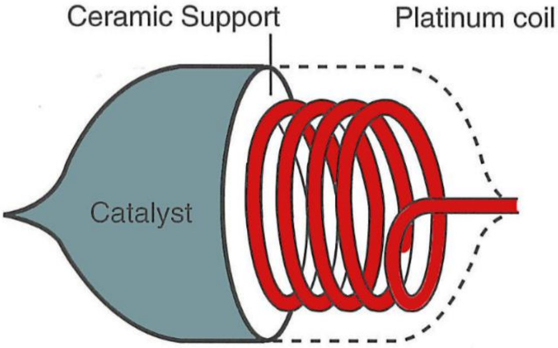

Figure 1.10: Catalytic gas sensor

- ***Optical sensors.***[44,45] Consists of a light emitting element, a photodetector element, and a gas detector element, based on the modification of light propagation in the presence of the gas to be detected (Most gases have characteristic absorption peaks in the mid-infrared region). Optical sensors work on the following principle: light from a laser or other super luminescent source is transmitted through an optical fiber. The changes of its parameters in the optical fiber or in the Bragg gratings are transmitted to a detector which measures these changes. Although these sensors are widely used for their ease of operation in the absence of oxygen, they can still be affected by interference from ambient light. The infrared gas sensors are one of the most common optical gas sensors offering the advantage of long life and high precision response, good selectivity, no toxicity, and no oxygen dependency. However, fiber optic gas sensors can be affected by ambient light interference, while infrared requires more expertise and suffers from the limited number of gas types to detect (not all gases have infrared absorption).

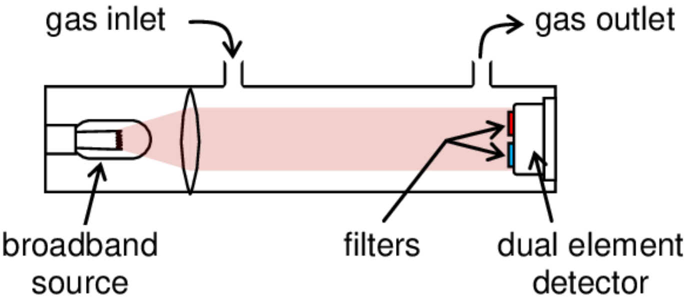

Figure 1.11: Optical Sensor.[44]

- ***Thermal Conductivity sensor.***[46] Based on the measured heat loss from a warmer body to the cold element through the thermal conductivity. These gas sensors are generally used for the detection of gases with a higher thermal conductivity than that of air, e.g., H_2 and CH_4, while the gas with a conductivity close to that of air cannot be detected (e.g., NH_3 and CO). Gases with a thermal conductivity lower than that of air are difficult to detect by this method because of interferences (e.g., CO_2 and butane) resulting to narrow the application range and many limiting factors of these gas sensors.

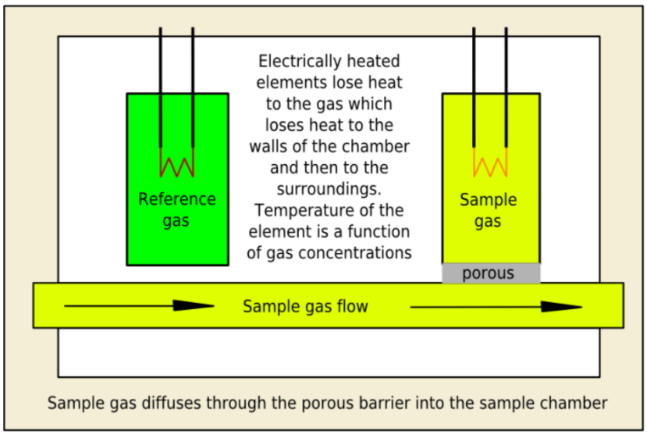

Figure 1.12: Thermal conductivity gas sensor.

- ***Piezoelectric sensors.***[47,48] Based on the measurement of the characteristic resonance frequency of the system, these sensors consist of a sensitive element that generally absorbs the gas to be detected. This recognition film is deposited between the two electrodes in the path of a wave. The adsorption of the target gas compound modifies the propagation of the wave due to a change of mass for example and thus of its frequency (Figure 1.13). These sensors are very sensitive, in the ppm range for ammonia. This class of sensors involves different types of sensors: quartz crystal microbalances (QMB),[49] surface acoustic waves (SAW),[50] etc.

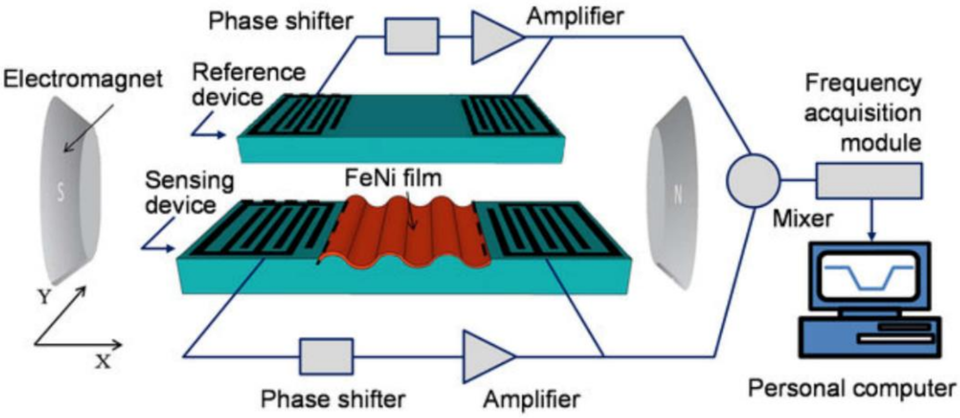

Figure 1.13: Piezoelectric type Surface acoustic wave (SAW) sensor[50].

- ***Semiconductor sensors.***[51–53] Consist of a metal oxide semiconductor material (MOS) (e.g., SnO_2 and ZnO). This material is deposited between two metallic contacts, a heating resistor that raises the temperature of the sensor between 200°C and 500°C. When the gas reaches the surface of the active material, the resistance between the metal electrodes changes proportionally with the gas concentration (Figure 1.14). They are sensitive to humidity, and susceptible to poisoning by sulfur compounds present in the gas to be detected, the semiconductor gas sensors are configured in single and dual electrode configurations. MOS sensors offer low cost and high sensitivity can detect gases at much lower ppm levels, but their operating temperatures need to be quite high making them expensive to employ and to maintain.[54] In addition, the sensor operation at elevated temperatures may degrade the long–term stability, reduce the sensitivity, and even modify the morphology of the sensor. [55]

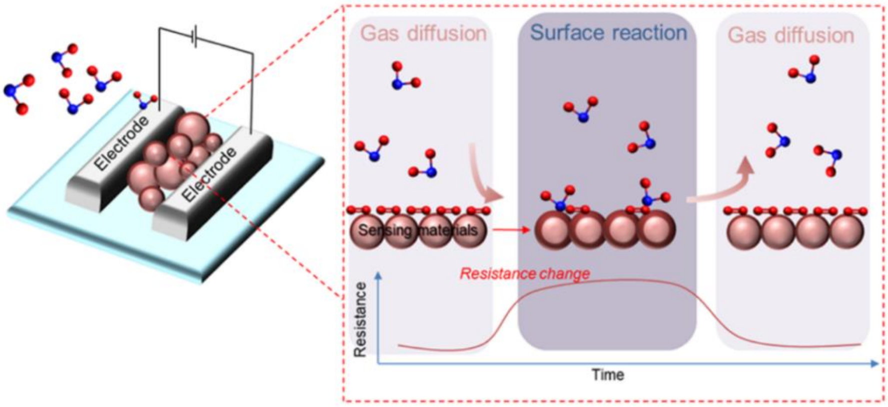

Figure 1.14: Metal oxide semiconductors showing dual electrode configuration.[56]

A summary of the different gas sensors reviewed is shown in Table 1.4, citing their main advantages and drawbacks.

Table 1.4: Summary and Comparison of gas detection sensor technologies.

Sensor Type	Advantages	Disadvantages
Catalytic	• Simple, measures flammability of gases having low cost	• Non-selective in the flammable gas range • Susceptible to explosion during fire • Requires air oxygen to work, can be poisoned.
Thermal	• Simple construction, easy to operate in absence of oxygen.	• Reaction due to heating wire
Electrochemical	• Measures toxic gases in relatively low concentrations	• low reproducibility • Sensitive to high humidity, dryness, and changes in pressure.
Optical	• no toxicity, and no oxygen dependency	• Can be affected by ambient light interference
Piezoelectric **(Surface Acoustic Wave)**	• Detect nerve and blister agents Battery-less and could be used for wireless applications. • Could be placed in harsh and rotating parts	• Due to its small size, there is difficulty in handling during fabrication process.
Semiconductors	• Mechanically robust, works well at constant high humidity condition.	• Susceptible to contaminants and changes due to environmental conditions. Non-linear response effects complexity.

The diversity of materials that can be used in gas sensors is remarkable. However, many of these gases sensors still have performance limits that play a real negative role for the development of sensors. Therefore, several factors need to be considered for deciding of the suitability of a gas sensor. These include selectivity which is related to the ability to recognize a specific gas among others, the sensitivity which indicates the smallest absolute amount of detectable change, the response time which is the time needed for a sensor to change the output state when a change of input parameter occurs, and the reversibility which indicates the ability of the system to return to its original state after a detection. Lastly, an additional crucial factor that denotes the sensitivity and selectivity of a sensor is its affinity to interact with a toxic gas, which can be affected by its adsorption capacity. This is what has generated for several decades such an enthusiasm for the development of novel sensors always more efficient.

With this in mind, we have chosen a class of materials, the 2D carbon materials (i.e., graphene-like materials), which are ideally promising in the field of sensors. In the following section, we will describe some of their interesting properties, and we will also provide some background literature on previous investigations in order to confirm the validity of the chosen materials.

1.5.2 2D carbon-based sensor materials

Carbon, a key ingredient for most life on Earth. This chemical element has different orbital hybridizations allowing it to generate different chemical bonds with different orientations. As a result, carbon owns different allotropic forms (e.g., graphite and diamond) and can generate a list of materials, namely single sheets of graphene, carbon nanotubes, carbon fibers, fullerenes, etc. In addition, carbon can bind to almost any chemical element, generating an unlimited variety of 2D carbon-based materials with a number of different chemical and physical properties.

Initiated by Filip Braet who has raised the question, “Should you use nanotubes or graphene as carbon nanomaterial in biosensors?”.[57] Carbon-based nanomaterials have become one of the dominant materials in many sensor applications. A survey on the Science Web has so far revealed more than 2,200 publications related to nanomaterials and sensing, of which about 50% concern carbon nanomaterials.[58] Further investigation reveals that nearly half of the carbon materials belong to the so-called graphene family.

2D carbon-based sensors are innovative and revolutionary gas sensors that have attracted considerable attention due to their wide availability, excellent electrical and thermal conductivity, chemical stability and relatively easy functionalization or hybridization. The preparation and application of 2D carbon materials, have been widely studied, and remarkable progress has been made after showing some good detection results.

1.5.2.1 Carbon isotopes and hybridizations

Carbon occurs naturally as isotope 12C (with a nuclear spin I = 0) which makes up almost 99% of overall carbon atoms; carbon-13 (with a nuclear spin of 1/2), makes up only about 1%; and radioactive carbon-14, which makes up a minuscule amount of overall carbon (10^{-12} of all carbon atoms) but is very important isotope in dating organic objects.

In writing the electron configuration for carbon the first two electrons will fill the inner shell 1s orbital. Since 1s can only hold two electrons the next 2 electrons for C goes in the 2s orbital, because the 2p ($2p_x$, $2p_y$, $2p_z$) orbital is of 4 eV higher than the 2s orbital, it is energetically favorable for electrons to fill the 2s before and thus, the remaining two electrons will go in the 2p orbital. Therefore, the C electron configuration will be $1s^2\ 2s^2\ 2p^2$ (Figure 1.15d). In the presence of other atoms, a covalent bond can be formed providing higher energy than the 4 eV, resulting in the excitation of one electron from the 2s to third 2p orbital (Figure 1.15e). The excited state of carbon therefore results in four equivalent quantum-mechanical states, $|2s\rangle$, $|2p_x\rangle$, $|2p_y\rangle,\ and\ |2p_z\rangle$. A quantum-mechanical superposition of the 2s state with n 2p where (n=1, 2 or 3) states is referred by sp^n hybridization. Giving this carbon can thus have three hybridizations, the sp^1 hybridization, occurs when the $|2s\rangle$ state mixes with one of the 2p orbitals while the other two p orbitals will remain unaffected. A state with equal weight from both original states is obtained by the symmetric and anti-symmetric combinations.

$$|sp_+\rangle = \frac{1}{\sqrt{2}}\left(|2s\rangle + |2p_x\rangle\right), \qquad |sp_-\rangle = \frac{1}{\sqrt{2}}\left(|2s\rangle - |2p_x\rangle\right).$$

These sp hybridized orbitals are oriented with bond angle of 180 degrees (Figure 1.15a), in a linear geometry. The remaining two p orbitals are unchanged, and perpendicular to each other and the plane of the hybridized orbitals. An example of sp hybridization can be seen in the ethyne molecule.

In the case of a superposition of the $|2s\rangle$ state and two 2p orbitals (e.g., p_x and p_y), one obtains the planar sp^2 hybridization and the three quantum mechanical states are giving by:

$$|sp_1^2\rangle = \frac{1}{\sqrt{3}}\,|2s\rangle - \frac{2}{\sqrt{3}}|2p_x\rangle$$

$$|sp_2^2\rangle = \frac{1}{\sqrt{3}}\,|2s\rangle + \sqrt{\frac{2}{3}}\left(\frac{\sqrt{3}}{2}|2p_x\rangle + \frac{1}{2}|2p_y\rangle\right),$$

$$|sp_3^2\rangle = -\frac{1}{\sqrt{3}}\,|2s\rangle + \sqrt{\frac{2}{3}}\left(-\frac{\sqrt{3}}{2}|2p_x\rangle + \frac{1}{2}|2p_y\rangle\right),$$

These sp^2 hybridized orbitals are oriented with bond angle of 120 degrees, in a trigonal planar (triangular) geometry (Figure 1.15b). An example of sp^2 hybridization can be seen in the ethene molecule.

In the case of sp^3 hybridization, the 2s orbital is mixed with all the three 2p orbitals to form four

sp^3 hybridized orbitals, which consists of four club-like orbitals that mark a tetrahedron. The orbitals form angles of 109.5° degrees (Figure 1.15c). A chemical example for this sp^3 hybridization can be seen in the ethane (C_2H_6) or methane (CH_4) molecules, where the four hybridized orbitals are used to form covalent bonds with the 1s hydrogen atoms. In condensed matter physics, the sp^3 hybridization is at the origin of the formation of diamonds.

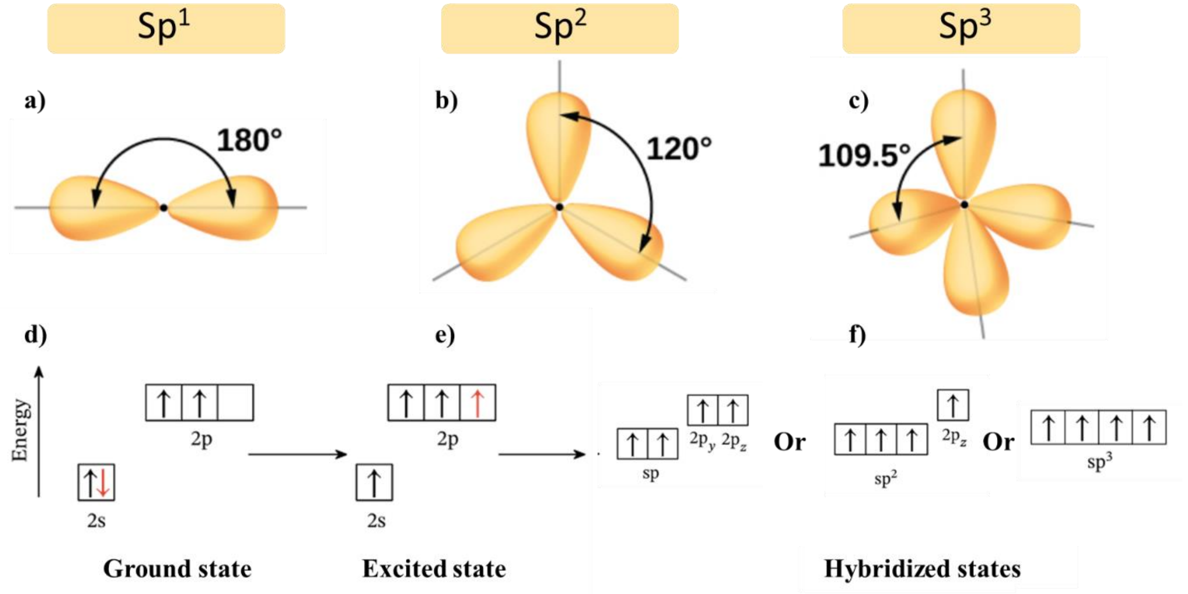

Figure 1.15: a-c) Orientation of the hybridized orbitals in respective geometries and d-f) the mixing of orbitals.

1.5.2.2 Crystal structure of Graphene

A single layer of carbon atoms isolated from the overall structure of graphite is called "graphene". Carbon atoms in a graphene layer form three strong in-plane bonds per atom, condense into a honeycomb atomic arrangement due to their sp^2 hybridization. It should be pointed out that the honeycomb lattice is not a Bravais lattice since the two neighboring sites A and B are not equivalent. However, the two sublattices A and B form a hexagonal Bravais lattice (Figure 1.16a). The distance between two carbons is $a_{c-c} = 1.418$ Å, calculated from the average of single (C-C) and double (C=C) covalent bonds.

The three vectors connecting the carbon atom in sublattice A to it nearest neighbor in the sublattice B (Figure 1.16a) are given by:

$$\vec{\delta}_1 = \frac{a_{c-c}}{2}(\sqrt{3}\,\vec{e}_x + \vec{e}_y) \quad ; \quad \vec{\delta}_2 = \frac{a_{c-c}}{2}(-\sqrt{3}\,\vec{e}_x + \vec{e}_y) \quad ; \quad \vec{\delta}_3 = -a_{c-c}\,\vec{e}_y$$

While the hexagonal Bravais lattice basis vectors are:

$$\vec{a}_1 = \sqrt{3}\,a_{c-c}\,\vec{e}_x \qquad \text{and} \qquad \vec{a}_2 = \frac{\sqrt{3}a_{c-c}}{2}(\,\vec{e}_x + \sqrt{3}\,\vec{e}_y)$$

The modulus of these basis vectors (a_1 and a_2) yields a = a_1 = a_2 = 2.456 Å, therefore the area of the unit cell (A_{uc}) and the density of carbon atoms of one single layer (n_c) can be calculated with:

$$A_{uc} = \sqrt{3}\,\frac{a^2}{2} = 5.22\ \text{Å}^2, \qquad \text{and} \qquad n_c = \frac{2}{A_{uc}} = 0.38\ \text{Å}^{-2}\,.$$

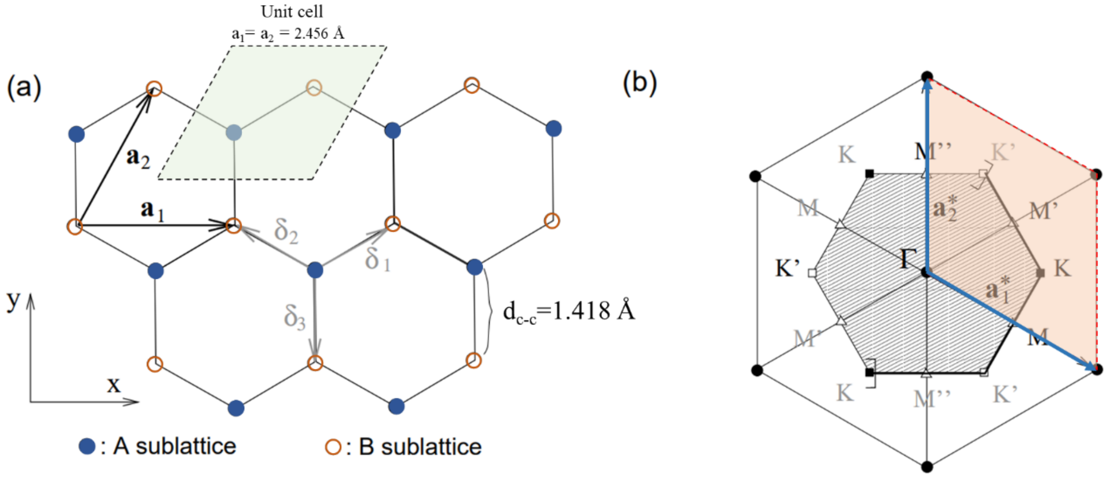

Figure 1.16: (a) Honeycomb lattice showing the graphene unit cell mapped in green, (b) the reciprocal lattice represented by the lattice vectors a_1* and a_2*. The shaded area displays the first Brillouin zone with its center Gamma

The reciprocal lattice, which is defined with respect to the hexagonal Bravais lattice, is depicted in Figure 1.16b and spanned by the vectors:

$$\vec{a}_1^* = \frac{2\pi}{\sqrt{3}a_{c-c}}\left(\vec{e}_x - \frac{\vec{e}_y}{\sqrt{3}}\right) \qquad \text{and} \qquad \vec{a}_2^* = \frac{4\pi}{3a_{c-c}}\,\vec{e}_y$$

All the sites of the reciprocal lattice represent equivalent wave vectors, giving that any wave propagating on the lattice with a wave vector differing by a reciprocal lattice vector has indeed the same phase up to a multiple of 2π, due to the relation between direct and reciprocal lattice vectors:

$$\vec{a}_i^*.\,\vec{a}_j = 2\pi\,\vec{\delta}_{ij}\ ;\ \text{with (i,j = 1,2)}$$

1.5.2.3 Proprieties and fabrication technique of Graphene

First described as an 'academic material', graphene was not expected to exist until 2004, when Novoselov and co-workers isolated a single-atom-thick layer of carbon. Since then, interest in graphene has continued to grow, driven by intense research efforts motivated by the many interesting properties of graphene compared to other structurally different forms of carbon. Some of these properties' comparison are listed in Table 1.5.

Interestingly, a wide range of graphene's experimentally measured features outperformed those of any other material, including the highest room-temperature electron mobility of 2.5×10^5 cm^2 V^{-1} s^{-1}; a Young's modulus of 1 TPa accompanied by an intrinsic strength of 130 GPa; a greater than

3000 W mK^{-1} ultra-high thermal conductivity; an optical absorption of $\pi\alpha \approx 2.3\%$ (in the infrared limit, where α is the fine structure constant); complete impermeability to all gases, and the ability to sustain extremely high electrical current densities (one million times higher than copper). A further property is that it can be easily chemically functionalized.

Table 1.5: The properties of graphene in comparison with other carbon-based materials. [59]

	Graphene	**Carbon nanotube**	**Fullerene**	**Graphite**
Dimensions	2	1	0	3
Hybridization	sp^2	Mostly sp^2	Mostly sp^2	sp^2
Hardness	Highest (For single layer)	High	High	High
Tenacity	Flexible, elastic	Flexible, elastic	Elastic	Flexible, non-elastic
Experimental SSA ($m^2\ g^{-1}$)	~1,500	~1,300	80–90	~10–20
Electrical conductivity ($S\ cm^{-1}$)	~2,000	Structure-dependent	10	Anisotropic: $2–3 \times 10^4$ (a direction), 6 (c direction)
Thermal conductivity ($W.m^{-1}.K^{-1}$)	4,840–5,300	3,500	0.4	Anisotropic: 1,500–2,000 (a direction), 5–10 (c direction)

The numerous outstanding properties of graphene have justified its reputation as being a "miracle material". However, some of these exceptional qualities have only been achieved in the highest quality samples. Given that the presence of defects can predominantly affects the quality of the final material, the methods adopted for the production of graphene play a crucial role in determining its properties. The most common methods are presented in and Table 1.6 and Figure 1.17.

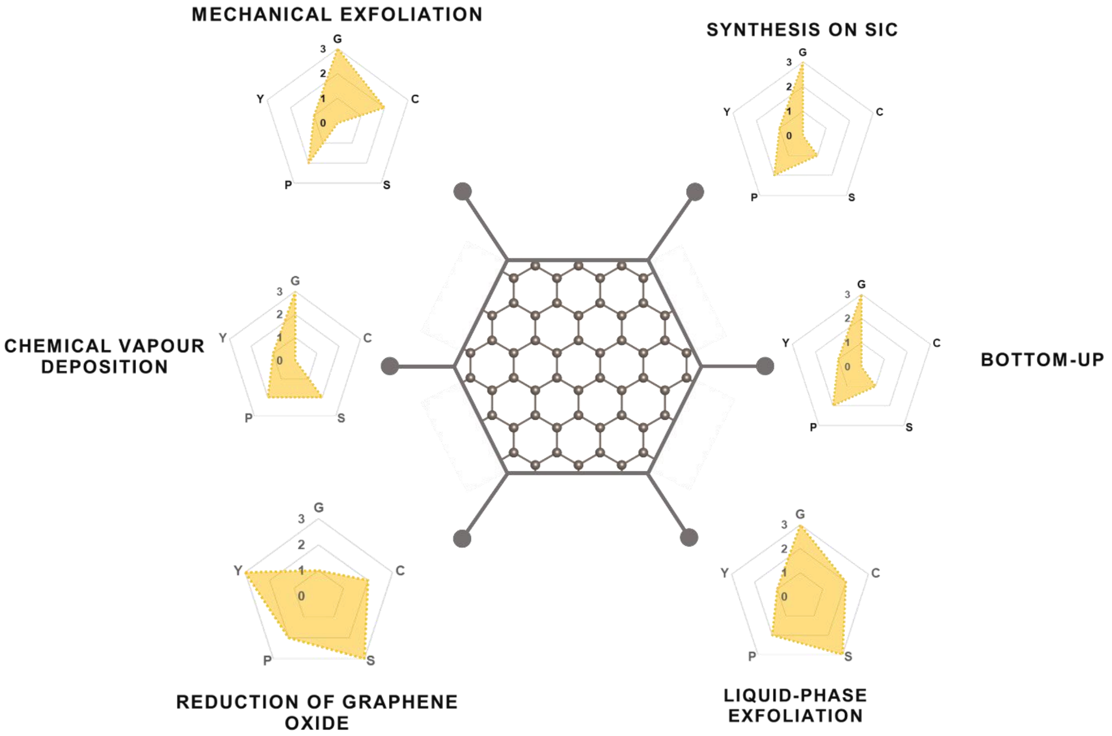

Figure 1.17: Schematic representation of the most common graphene production methods evaluated in terms of graphene quality (G), cost aspect (C; a low value corresponds to high cost of production), scalability (S), purity (P) and yield (Y) of the overall production process, the values are taken from [59]

- **Mechanical exfoliation**[60] was presented as the original method that involves the use of an adhesive tape to exfoliate the top layer of graphite material and press it against a substrate of choice. Once the adhesion of the lower graphene layer to the substrate is stronger than the interaction between the graphite layers, a layer of graphene can be transferred to the substrate.
- **Chemical Vapor Deposition**[61]: This process uses a transition metal substrate, typically copper or nickel, being exposed to a hydrocarbon gas (commonly methane) at high temperature. Graphene growth occurs on the substrate surface by thermal decomposition of the hydrocarbons on the surface, and once a single layer forms, graphene growth can be then interrupted by very low gas pressure.
- **Liquid phase exfoliation**[62] process typically involves three steps: 1) solvent dispersion, 2) exfoliation, and 3) purification. Once dispersed in a solution, exfoliation of the graphite can be achieved by ultrasonics, electric field, or shearing. A further purification step is necessary to separate the exfoliated graphene from the unexfoliated one, and usually requires ultracentrifugation.
- **Epitaxial Growth on SiC**[63] consists in exposing a Silicon carbide (SiC) crystal obtained by epitaxial growth to high temperatures above 1500 °C in vacuum, or preferably in an

inert gas atmosphere, in order to evaporate the least bonded Si atoms from the surface. The remaining carbon atoms will be mobilized due to the high temperatures involved and will be re-arranged in a stable configuration, forming a graphitic layer.

- **Reduction of graphene oxide**:[64] In this process, graphene is produced by strong oxidation of pristine graphite through liquid phase exfoliation to form graphene oxide (GO). The latter is then reduced in the presence of strong reducing agents (e.g., hydrazine, sodium borohydride, hydrogen gas, etc.) to form RGO (reduced graphene oxide).

Due to their limited scalability, high production costs, low yields, and the need of some of them to operate at high temperatures (1500 °C), methods like mechanical exfoliation, synthesis on SiC, and bottom-up techniques confine the use of graphene to fundamental research and a limited scope of niche applications, e.g., high frequency transistors. To a lesser extent, despite its high cost, high processing temperatures (~1000 °C), and rather low yield and moderate product purity (defects). Chemical vapor deposition of hydrocarbons has been reported as an effective method to produce vertically oriented graphene nanosheet electrodes. Of the techniques shown in Figure 1.17, liquid phase exfoliation and graphene oxide reduction are widely used for large-scale graphene production. For the first technique, the low yield of this process, however, leaves a considerable amount of unexfoliated graphite, which needs to be disposed of. Nevertheless, the high scalability and low cost of liquid-phase exfoliation make it a suitable process for producing graphene in large quantities (nanometer to micron sizes). In the second method, in spite of the low to medium material quality obtained from the presence of structural and extrinsic (heteroatoms) defects, these methods allow the production of bulk quantities with high yield and limited costs.

Table 1.6: Properties of graphene obtained by different methods.[65]

Method	Crystallite size (µm)	Sample size (mm)	Charge carrier mobility (At ambient temperature) ($cm^2\ V^{-1}\ s^{-1}$)
Mechanical exfoliation	> 1,000	>1	$> 2 \times 10^5$ $> 10^6$ (at low temperature)
Liquid phase exfoliation	≤ 0.1	Infinite as a layer of overlapping flakes	100 (For a layer of overlapping flakes)
Reduction of graphene oxide	~100	Infinite as a layer of overlapping flakes	1 (For a layer of overlapping flakes)
Chemical vapour deposition	1,000	~1,000	10,000
Epitaxial Growth on SiC	50	100	10,000

Although graphene is very sensitive, it is not selective towards several reducing gases. Therefore, functionalization, doping and defect creation processes are necessary for improving its selectivity. For doping, a small quantity of noble metals is added to the sensitive sensor layer. This modifies the layer morphology (grain size, roughness...) and improves the sensor sensitivity. Most used metals are palladium, platinum, indium, ruthenium, or metal oxides. Metals can be either sensitizers or activators, which improve the sensitivity and selectivity for some gases, or reduce the sensor operating temperature.

Considering functionalization, (i.e., modifying their chemical characteristics with specific functional groups, and by hybridization with other elements) it allows the possibility of creating high efficiency detection sites where gas desorption is difficult and allows improving selectivity and electrical response. Compared to graphene, functionalized materials are more versatile and tunable with greater flexibility and diversity in composition, structure, and functionality.

Additionally, the recent success in synthesis and functionalization via various protocols offers great opportunities to create more complex functional nanostructures and facilitates their application in sensing and critical areas. Specifically, promising 2D graphene-like nanomaterials, such as graphitic carbon nitride (gC_3N_4), transition metal dichalcogenides (TMDs), boron nitride (BN), and transition metal oxides, have been extensively studied in the recent years due to their unique physical, chemical, and electronic properties.

Detection mechanism of these carbon-based materials with respect to gases is based on a decrease in conductivity, which corresponds to a p-type doping. Under ambient conditions, holes play a predominant role in charge transfer. When exposed to reducing gases such as ammonia, an increase in resistance is linked to the depletion of holes in the sensing material.

1.5.3 Reported sensors for radioactive species detection

There is a considerable lack of focus and investigations regarding the use of iodine detectors. Unfortunately, even for existing studies, it should be noted that not all types of sensors are suitable for nuclear applications. Many of these sensors, have drawbacks like limited sensing range, short limit of detection, complicated process and/or the necessity of special detection equipment.

Considering optical application of iodine detectors some substituted pyrazines gained special attention due to their optical properties. Geng et al.[66] constructed microporous polymers CMPs (i.e., TDTPAPz and TTDPz) with pyrazine moieties to investigate the iodine adsorption capacity with fluorescence detection. CMPs showed good iodine adsorption capacity for iodine vapor with 441% and 312%, respectively together with a high sensitivity. It has been reported that the introduction of the pyrazine ring had no significant effect on iodine adsorption, but it could increase the fluorescence detection performance for iodine. Furthermore, Dong et al.[67] claimed that for a fluorescent and electrochemical iodine vapour response in the presence of humidity, a range of Ln-based stable MOFs with BTC linkers (Ln-BTCs) may provide a dual response. The resulting output signals showed a high sensitivity and a good capacity to reduce the false positives, which could be useful for a potentially integrated detection of radioactive iodine vapor. Similarly, the use of copper nanoclusters (CuNC) with poly(vinylpyrrolidone) as luminescent sensors was used in this work.[68] An exceptionally high enrichment factor of about 1100 was achieved under optimal conditions, yielding detection and quantification limits of 1.0 ng/mL and 3.4 ng/mL, respectively. The 9-ethyl-3-carbazylidene carbazole hydrazone (ECCH) has been employed[69] as the fluorescent support for preparing an iodine-sensitive optical chemical sensor. The sensor behavior was based on iodine quenching of the ECCH fluorescence. The sensor exhibited a linear iodine response throughout the range of 1 to 100 μmol L^{-1}, with a limit of detection of 0.8 μmol L^{-1} at a pH of 7.0. Common coexisting ions did not interfere with the measurement of iodine. It had adequate repeatability and accuracy, a two-month operational life, and a fast response time lower than 50 seconds.

Leaving optical sensors, Cho and coworkers[70] have developed a rapid and accurate electrochemical iodine sensor based on mechanically treated carbon nanofiber (MCNF) electrodes, which have a special microstructure and composition that allows them to be especially well suited for iodine detection. Their experiments have proven how effective they are at sensing iodide without requiring complicated sample preparation and post-processing. Additional analysis has revealed that MCNF electrodes exhibit wide dynamic ranges that allow the detection of excess iodine.

On the other hand, inspired by the promising results obtained with silver-exchanged zeolites for the capture of iodinated compounds, Nenoff et al.[71] have investigated silver mordenite zeolite (Ag-MOR) as an iodine sensor. Ag-MOR has revealed a noticeable response in impedance upon being exposed to I_2 gas at 70°C, with the magnitude and direction of the response depending on the redox state of Ag-MOR (Ag^+ or Ag^0) prior to I_2 exposure. The equivalent model has been developed describing the charge flow along the surface and across the pores of mordenite grains. Relative impedance changes along these conduction pathways are related to the chemical changes from Ag^+ or Ag^0 to the subsequent AgI polymorphic phase. These results together provide the basis for the design of a compact Ag-mordenite sensor for the direct electrical sensing of I_2 gas.

Since that, many other researchers have been interested in the detection of iodine species by porous materials, particularly by Metal Organic Frameworks (MOFs), offering a good basis for the design of the I_2 gas sensor. An early ZIF-8 based electrical impedance spectroscopy (IS) sensor for I_2 gas was suggested by Small et al.[72] The suspension of "ZIF-8" was initially dispersed using methanol and then placed on platinum interdigitated electrodes. At room temperature in air, I_2 gas was easily sensed for 720s of exposure time. In addition, ZIF-8 exhibited excellent selectivity for I_2 gas. Nevertheless, it was demonstrated that even with a significant change in impedance (>105), the sensor's signals were nearly irreversible. Two years later, the same authors overcame this drawback by obtaining a widely reversible electrical sensor for I_2 gas based on similar IS method with rational selection of MFM-300(X) (X=Al, Fe, In, and Sc) with various metal centers.[73] The findings revealed that MFM-300(Al) and MFM300(In) showed the greatest response magnitude (up to 106), but their recyclability was inadequate after 5 cycles of I_2 adsorption. In contrast, MFM-300(Fe) and MFM-300(Sc) kept a high adsorption capacity within the same conditions, despite their moderate responses.

In other studies, Zheng and co-workers[74] presented a sensing strategy for iodine by using metal-organic frameworks (MOFs) with aromatic functional groups. As revealed by X-ray crystallography, absorbed I_2 molecules directly contact the $\{Cu_4I_4\}_n$ chains, forming a virtual polarizable tetraiodide anion (I_4^{2-}) through a strong I^----I_2---I^- interaction. Thus, resulting in a $\{Cu_4I_5\}_n$ near-copper-iodide layer having semiconducting properties, leading to a significant ($\Delta\sigma = 10^7$ times) enhancement of the electrical conductivity compared to the free I_2. The drastic increase in electrical conductivity was used to suggest the possibility of detecting I_2 electrically.

1.6 Methods of radioactive iodine capture

As shown in section 4, isotopes ^{131}I and ^{129}I are the most dangerous iodine species in reactors and nuclear waste treatment facilities, respectively. One major challenge today is to trap these toxic and volatile species for reducing health and environmental risks.

Two types of processes can be used to remove radioactive iodine from gaseous effluents:

- Wet processes (alkaline purification, electrolytic purification, Mercurex and Iodox processes, etc.)
- Adsorption processes on inorganic porous materials (activated carbons, titanosilicates, porous oxide materials, as well as Zeolites and MOFs).

In general, the performance of these solid absorbent is evaluated by the following factors:

1) The ***Retention capacity*** or loading capacity which is the amount of iodine that can be captured by the sorbent.

2) The ***Penetration*** of the target species into the column, which is defined in Eq 1.1 as the iodine that is not captured.

$$Penetration = 1 - Efficiency \qquad \text{Eq 1.1}$$

3) The *Efficiency*, which is the fraction of iodine captured.

4) The *Decontamination Factor DF* which is defined in Eq 1.2 as the inverse of penetration.

$$DF = \frac{1}{1 - efficiency} \qquad \text{Eq 1.2}$$

All these parameters depend on the experimental setup where many variables can affect the results and sorbent ranking based on these parameters, including (but not limited to): sorbent bed thickness, packing density, flow rate, target species (e.g., sorbent selectivity for different iodine species), target species concentration, and temperature.

1.6.1 Wet processes

1.6.1.1 The Mercurex process

The Mercurex process involves a solution of mercuric nitrate and Hg {0.4 M $Hg(NO_3)$ and ~14 M HNO_3} flowing through a column with a 14M HNO_3 solution to form mercury iodate and other iodide complexes. The process removes inorganic iodide (reaction 1) and organic iodide (reaction 2 and 3), improving the extent of organic iodine removal, while producing $Hg(IO_3)_2$ and HgI_2.[75]
Elemental iodine:

$$6\,I_2 + 6\,Hg\,(NO_3)_2 + 6\,H_2O \leftrightarrow 5\,HgI_2 + Hg\,(IO_3)_2 + 12\,HNO_3 \qquad (1)$$

Methyl iodine:

$$2\,ICH_3 + Hg\,(NO_3)2 \leftrightarrow HgI_2 + 2\,CH_3NO_3 \qquad (2)$$

$$ICH_3 + Hg\,(NO_3)2 \leftrightarrow HgI + CH_3NO_3 + NO_3^- \qquad (3)$$

The use of nitric acid which are regulated as highly toxic metals may limit the application of this process.[76]

1.6.1.2 Iodox

The Iodox process involves an acid wash solution of $20 - 23$ M HNO_3 (hyperazeotropic) to dissolve and oxidize the elemental and organic iodine (Figure 1.18). Primary reactions associated with this process and shown in equations 4 to 6:[75]

$$2CH_3I + 4HNO_3 \leftrightarrow 2CH_3NO_3 + I_2 + N_2O_4 + 2H_2O \tag{4}$$

$$I_2 + 4HNO_3 \leftrightarrow 2I^+ + 2NO_3^- + N_2O_4 + 2H_2O \tag{5}$$

$$I^+ + 3HNO_3 + NO_3^- \leftrightarrow IO_3{}^- + H + + 2N_2O_4 + H_2O \tag{6}$$

In this way, the resulting washed species is the iodate ion, $(IO_3)^-$.

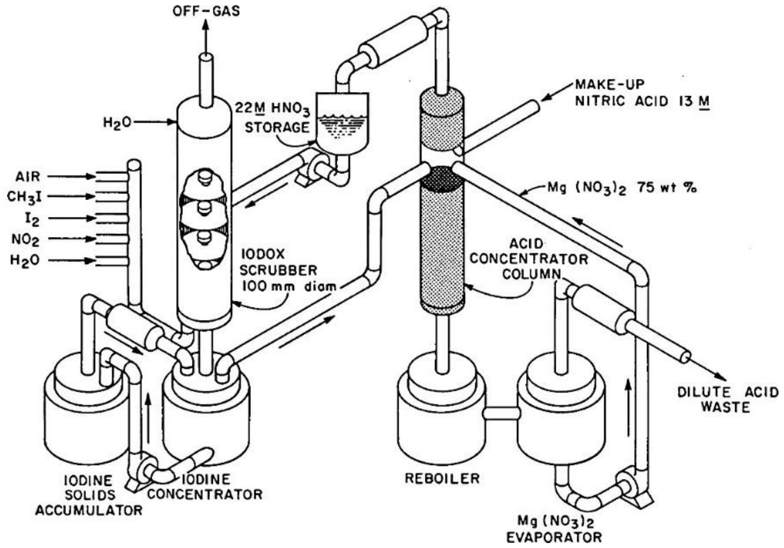

Figure 1.18: Iodox process diagram for iodine scavenging. [77]

The product iodine is formed by nitric acid evaporation from the liquid effluent at the bottom of the bubble column. In this way, a solid iodine product is obtained. Still, this solid iodine product is soluble in water and needs additional treatment before its final purification. The conversion step recommended converts soluble iodic acid into insoluble Ba $(IO_3)_2$ by a simple reaction with $(Ba(OH)_2)$. Excess $(Ba(OH)_2)$ should be used to ensure a complete conversion and does not adversely affect the stability of the cement. Up to 9% by weight of iodine can be included in a cement matrix in the form of barium iodate.[78]

In addition, the corrosiveness of hyperazeotropic nitric acid, as well as the potential of forming organic nitro compounds (CH_3NO_3) in the system are also a significant and potentially unattractive feature of the Iodox process.[76]

1.6.1.3 Electrolytic purification

The electrolytic washing process involves 1 M Co_3^+ in 8-12 M HNO_3. In this process, the continuously renewed oxidant Co_3^+ oxidizes iodine to a non-volatile form. After solution evaporation, a mixture of Co $(NO_3)_2$ and Co $(IO_4)_2$ is obtained.

The lab tests report DFs of about 600 for elemental iodine and 100 for methyl iodine.[76] The assays also showed, that NO_2 is found to compete with I_2 and ICH_3 for the available Co_3^+ oxidant, however, the presence of 1% NO_2 or more will reduce the DF of the iodine by a factor of 10.

1.6.1.4 Alkaline purification

This process of scrubbing is well recognized and in use at both *La Hague* reprocessing plant in France and *THORP* plant in UK.[76]

Alkaline or caustic scrubbing solutions are based on the disproportionation reaction represented in reaction (7).

$$3\,I_2(g) + 6\,OH^-(aq) \rightarrow\ 5\,I^-(aq) + \ IO_3{}^-\,(aq) + \ 3\,H_2O(l) \tag{7}$$

A report on the alkaline scrubbing process employing NaOH (1-2 M) as a solvent is given by McKay et al.[79] Here the solvent interacts with both organic and non-organic iodine compounds to generate sodium iodide (NaI).

Reported[76] decontamination factors (DFs) can vary, but are generally in the range of 10 to 100. This variation may, at least in part, be due to the form of iodine in the gas stream. While elementary form is effectively removed by caustic scrubbing, organic forms (e.g., methyl iodide) are not, and a process with a significant fraction of organic iodine will have a low removal efficiency.

1.6.2 Solid sorbents

Solid sorbents have been in the forefront of the removal of radioactive contaminants (Figure 1.19) and have the following advantages by comparison with liquid systems:

1. They allow a simpler design.
2. They are non-corrosive.
3. The waste is in a dry form that is easy to handle and contain.
4. The simpler design, with few moving parts, allows for greater reliability and quality control.

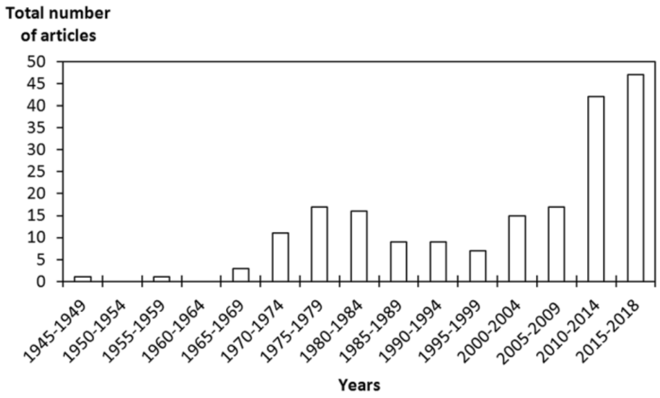

Figure 1.19: Evolution of the number of publications per year on the capture of radioactive iodine contaminants by solid porous sorbent materials. [80]

1.6.2.1 Activated Carbon

Among the available solid sorbents for iodine removal, activated carbon has been the most widely studied globally due to its high surface area and pore size. At present, Activated carbons (ACs) have been extensively employed within ventilation systems used in nuclear plants in order to eliminate volatile molecules being released into the environment.[81]

Activated carbons (AC) are carbon-based materials with a porous structure. Because of their low production cost, high specific surface area (300-4000 $m^2.g^{-1}$), flexible structure and porosity (pore size 4.5-60 Å) and high adsorption capacity, ACs are especially attractive for the capture of radioactive iodine compounds.

They are produced in two stages:

- Carbonization (or pyrolysis) of raw materials, which generates porosity within the raw carbonaceous material, removing organic matter and leaving carbon.
- An activation step, which increases the adsorption capacity of the material. Different types of activation procedures can be implemented, namely physical activation (in the presence of water vapor and air under pressure) or chemical activation (generally by phosphoric acid).

Considering that the present focus of this thesis will be on the capture of iodine gaseous forms, I_2 and ICH_3, the use of activated carbon to remove them will be considered as follows:

- I_2 removal

Elemental iodine can be bound to activated carbon either by chemisorption, which is the preferred method, or by physical adsorption. Physical adsorption is the primary method of adsorption on activated carbon, due to its large specific surface area (BET surface area = 800 to 1000 $m^2.g^{-1}$) and pore structure. Various functional groups, phenolics and other alcoholichydroxyl groups, can create chemical bonds that considerably increase the amount of iodine retained.[77]

- ICH_3 removal

The simultaneous adsorption of water vapor from the gas stream significantly impairs the adsorption of methyl iodide (ICH_3), making it somewhat more difficult to be removed compared with elemental iodine. At low relative humidity (<5%), water vapor has little effect. For relative humidity between 5% and 30%, capillary condensation occurs in the micropores, and some of the larger pores are also filled with water. For relative humidity above 30%, the adsorption of methyl iodide (ICH_3) becomes negligible. In this case, to improve ICH_3 adsorption, activated carbon is impregnated with many materials that generate chemisorption or iodine isotope exchange sites. The two most common impregnations reagents are potassium iodide ($K^{127}I$) and triethylenediamine (TEDA).[77] KI provides an isotope exchange site with other airborne iodine isotopes according to the following reaction:

$$K^{127}I(Activated\ Carbon) + CH_3{}^{131}I(Air) \leftrightarrow K^{131}I(Activated\ Carbon) + CH_3{}^{127}I(Air) \qquad (8)$$

On the other hand, it has been recognized[82] that the presence of TEDA in activated carbons increases their iodine capture capacity (especially for ICH_3). As regards this aspect, Chebbi et al.[81] support this concept by revealing that the progressive impregnation with KI and TEDA leads to a decrease of the global adsorption capacity in relation with partial porosity blocking phenomena, resulting from the presence of these molecules within the internal porosity. In contrast, the presence of TEDA seems to be fundamental to provide a stronger and more specific storage of the ICH_3 molecules through chemical reactions. Such contribution is essential to ensure an accepted retention behavior towards ICH_3 at higher temperatures and in the presence of high excess water vapor.

According to Gonzalez-Garcia et al.[83] and Joo-Hyung,[84] TEDA in activated carbons is converted to a quaternary amine by reaction with iodine compounds such as ICH_3 via SN_2 nucleophilic substitution.[80] The general mechanism developed by these authors is shown in Figure 1.20.

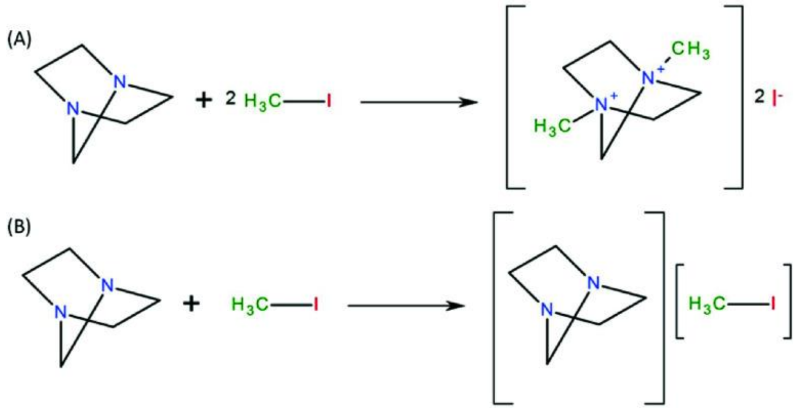

Figure 1.20: (A) Formation of a non-volatile quaternary ammonium salt by an SN_2 mechanism between TEDA and ICH_3. an SN_2 mechanism between TEDA and ICH_3. (B) Secondary neutral complex formed between TEDA and ICH_3.

Moreover, activated carbons also present several disadvantages in relation to the type of application envisaged and they were quickly eliminated. Indeed, activated carbons are characterized by a relatively low ignition temperature, especially in the presence of NO_x (NO_2 is a powerful oxidant). AC are sensitive to irradiation. In addition, NO_x compounds can also become unstable or explosive in the carbon bed. The trapping performances seem to be significantly altered at high temperature and in the presence of a strong excess of water vapor (the temperature can reach 150 °C). Finally, due to their heterogeneous nature, these materials do not have well-defined trapping sites, which makes it difficult to adjust certain characteristics such as porosity or surface chemistry.

1.6.2.2 Titanosilicates

The titanosilicates are a class of adsorbents similar to zeolite aluminosilicates, with Ti substituted for Al. Wu et al.[85] investigated silver substituted titanosilicates (ETS-10 and ETS-2) to trap iodine (I_2). ETS-10 has a stable chemical composition (isolated titanium octahedral chains in the top part of the adsorbent) with pores composed exclusively of silicon. This gives it hydrophobic properties and high chemical stability under acidic conditions. ETS-2, in contrast, includes sodium and titanium and has a reasonable specific surface area (260 $m^2.g^{-1}$), corresponding to its external surface, but without structural microporosity. As opposed to ETS-10, ETS-2 has a high capacity for cation exchange (with sodium) as zeolites. Higher iodine adsorption capacities around 220 g_{I_2}/kg of adsorbent and 243 g_{I_2}/kg of adsorbent in dry conditions were reported for ETS-10 (35 wt.% Ag) and ETS-2 (40 wt.% Ag), respectively.

According to the previous studies,[80] the porous structure of the ETS-10 adsorbent promotes the condensation of water inside the pores, limiting the accessibility of silver adsorption sites for iodine.

1.6.2.3 Porous oxide materials

Another class of adsorbents are oxide materials as follows:

- Silver-doped silica and alumina (Ag/SiO_2, Ag/Al_2O_3):

Oxide type materials like alumina (Al_2O_3) and silica (SiO_2) impregnated with silver, designated Ag/Al_2O_3 and Ag/SiO_2 respectively, constitute another class of adsorbents. These materials have been used for the capture of iodine (I_2) and iodomethane (ICH_3) at industrial scale (spent fuel reprocessing plant). They contain silver nitrate ($AgNO_3$) which reacts with elemental iodine and iodomethane (ICH_3) to produce stable silver iodide(AgI) or silver iodate ($AgIO_3$) by the following reactions (Wilhelm et al.[86]):

$$AgNO_3 + I_2 \rightarrow AgI + INO_3 \tag{9}$$

$$AgNO_3 + ICH_3 \rightarrow CH_3NO_3 + AgI \tag{10}$$

Silver-doped silica, commercialized as AC-6120, has been applied at the Karlsruhe Spent Fuel Reprocessing Plant (WAK) in Germany for iodine (I_2) capture.[80] DFs for iodine ranging from 100 (>99.0% efficiency) to 50 (98.0% efficiency) have been achieved in industrial scale use. At laboratory scale, this silver doped silica showed decontamination factors for I_2 greater than 104 (>99.99% efficiency) at a temperature of 150 °C. Efficiency decreased from 99.9944% to 27% at 70% and 100% relative humidity, respectively. Furthermore, Wilhelm and Schuttelkopf [80] stated that an increase in temperature up to 200 °C slightly improved the performance. However, an increase in temperature becomes less attractive in terms of the balance between cost and efficiency.

- Silver-doped mesoporous silica.

A further category of materials, specifically structured mesoporous silica, has gained scientific attention for iodine trapping purposes. In fact, these materials have been studied for catalysis and adsorption. Mesoporous silica materials are characterized by amorphous silica walls that delimit well-ordered mesocavities, a regular arrangement of mesopores with large specific surface area (it can reach values of more than 1000 $m^2.g^{-1}$). These materials present the advantage of pore sizes close to 3-10 nm, which ultimately improves the accessibility of pores and active sites by substrates. In addition, silanol functions localized on the silica surface, can be replaced by functionalization with organic and/or organometallic functional groups to improve their properties and performances according to targeted applications.

Studies focused on iodine capture applications using these materials are the works of Mnasri et al.[87] on three types of silver doped mesoporous silica MCM-41, of Yang et al.[88] on bismuth doped SBA-1586, and of Chebbi et al.[89] on silver doped SBA-1581. Using these materials for iodine adsorption at 35°C in the gas phase, Mnasri et al.[87] indicated adsorption capacities of unimpregnated materials of 90-130 $\mathrm{g_{I_2}.kg_{adsorbent}}^{-1}$. Their adsorption capacity was significantly improved through silver impregnation, with values reaching 760 to 770 $\mathrm{g_{I_2}.kg_{adsorbent}}^{-1}$. This difference in performance was associated to differences in the pore size and specific surface area. Chebbi et al.[89] reported an adsorption capacity of 49 $\mathrm{g_{ICH_3}.kg_{adsorbent}}^{-1}$ for unimpregnated mesoporous silica SBA-15, while results were significantly improved by various loadings of Ag^0 nanoparticles on SBA-15.

The main drawback of these materials is the high cost of silver, prompting researchers to determine the effectiveness of some cheaper and more abundant metals in the hope of finding a viable alternative to silver-based adsorbents for iodine removal.

In addition, the lack of exchange sites in mesoporous silica and the large pore diameter allows for easy migration of silver to the surface, leading to silver aggregation in the form of metal nanoparticles, which eventually block access to the pores.

- Silver-based silica aerogels

Aerogels are porous materials with a high specific surface area (>1000 m^2 g^{-1}). Matyas et al.[90] have developed silver functionalized aerogels for the capturing iodine species. These studies indicated promising results with an iodine adsorption capacity of 310 $g_{I_2}.kg_{adsorbent}{}^{-1}$ and a decontamination factor (DF) greater than 105. More recently, Riley et al.[91] reported an iodine adsorption capacity greater than 500 $mg_{I_2}.g_{adsorbent}{}^{-1}$ using silver-functionalized d-aluminosilicate aerogels (Na-Al-Si-O) whereas only 190 $mg_{I_2}.g_{adsorbent}{}^{-1}$ was observed with silver-exchanged mordenite (Ag^0MOR). These studies proved that silver-functionalized aerogels may be potential candidates for iodine capture. Nevertheless, very few publications on the subject are available in the literature and no real tests have been carried out under conditions similar to those of real use.

- Aerogels based on chalcogen (chalcogels)

Groups of chalcogens ($Ge_4S_{10}{}^{4-}$, $Sn_2S_6{}^{4-}$, $Sn_4S_4{}^{4-}$, $MoS_4{}^{4-}$) interconnected by a secondary metal species (such as Pt^{2+}, Co^{2+}, Sn^{2+}, Sb^{3+}, Bi^{3+}, Ni^{2+} and Zn^{2+}). Chalcogens included in chalcogels are classified as weak Lewis bases according to the HSAB (Hard and Soft Acids and Bases) concept.[92] Therefore, they have a strong affinity for iodine (I_2), which is known to be a weak Lewis acid. This high affinity for iodine has been demonstrated for a wide range of chalcogels, including $PtGe_2S_5$, Sn_2S_3, $CoMoS_4$, $NiMoS_4$, CoS_5, $Sb_4(SnS_4)_3$ and $ZnSn_2S_6$. Riley et al[93]. developed SnS (Sn_2S_3) structured chalcogels with iodine uptake of 32.7 and 68.3 wt.%. In addition, using X-ray diffraction analysis they showed that iodine interacts with SnS-type chalcogels through chemical reactions (chemisorption) to produce SnI_4 and $SnI_4(S_8)_2$ crystalline species. This reaction is particularly favorable, with a high iodine absorption rate.

TGA analysis showed that $Zn_2Sn_2S_6$ and $Sb_4Sn_3S_{12}$ chalcogels with stored iodine are stable up to 150 °C, but over this temperature, iodine is gradually released (40 wt.% in 30 days)[80]. In conclusion, the thermal stability of the iodine (or iodides formed) capture is quite limited.

1.6.2.4 Covalently bonded porous organic polymers (POP)

Porous organic polymers (POPs) have recently attracted attention due to their highly tunable molecular design and porosity, large surface area, low backbone density (light elements), strong covalent bonds and high physicochemical stability. Although POPs are generally amorphous solids, they suit real applications because of their excellent physicochemical stability. They have an enormous potential for the capture of volatile radioactive iodine. Moreover, introduction of active sites such as metal species, N, S and C into the POPs pore network greatly improves their affinity for iodine molecules, significantly increasing iodine uptake. To date, several POPs have been employed for this purpose, such as nano porous organic polymers (NOPs), conjugated microporous polymers (CMPs) and crystalline covalent organicframeworks (COFs).

Using gravimetric measurements at 75 °C, Chen et al.[94] investigated the iodine uptake (I_2) of a series of hierarchically porous tetraphenyl adamantane-based organic polymers (named NOP-53, NOP-54, and NOP55), introduced into a sealed container with iodine pellets. Iodine uptake increased gradually over a 4-hour period until saturation. NOP-54 showed the highest iodine uptake up to 2.02 $g_{I_2}.kg_{adsorbent}{}^{-1}$, followed by NOP-53 (1.77 $g_{I_2}.kg_{adsorbent}{}^{-1}$) and NOP-55 (1.39 $g_{I_2}.kg_{adsorbent}{}^{-1}$). According to the authors, NOP-53, and NOP-54 adsorbed iodine at a faster rate than NOP-55 because of hierarchical porous structures, which facilitate the transport of iodine in the networks.

Unfortunately, POP's preparation requires expensive monomers and a complex preparation process and are still a new laboratory material, so they are produced in very small quantities. The data obtained confirmed that, for volatile iodine, these devices do not allow an efficient capture

1.6.2.5 Zeolites

Zeolites are very promising candidates for iodine capture thanks to their high tunable proprieties and adsorption capacities. According to literature, a number of zeolites of different structural types have been investigated for the trapping of iodine species, for instance, mordenite (structural type MOR), NaX and NaY zeolites (FAU type), ZSM-5 (MFI type), ferrierite (FER type), zeolite beta (*BEA type) and others. Riley et al.[95] have tested the trapping of gaseous I_2 at room temperature and at 150 °C over five different types of zeolites, (two faujasites (FAU), one ZSM-5 (MFI), one meso MFI, one ZSM-22 (TON), and two mesoporous material). Three of them (i.e., Ag-FAU, Ag-MFI, Ag-TON) were subjected to ion exchange with Ag^+. Energy dispersive X-ray spectroscopy data suggest that the Ag-FAU structures were the materials with the highest capacity for I_2(g), ~three times more than Ag-mordenite (Ag-MOR), but analysis of X-ray diffraction showed that unlike the MFI and TON zeolites, the faujasite-type zeolite structure broke down during the iodine-loading experiment at 150°C. Therefore, in field applications, the authors suggested Ag-MFI zeolites as a suitable sorbent, offering good sorption properties and greater consistency.

Unfortunately, a major drawback of silver exchange zeolites is the high cost of the silver metal employed. With a view to possibly replacing the high-cost silver-containing zeolites other elements were investigated to obtain low-cost metal-exchanged zeolites for iodine adsorption. Porous copper-doped silica, (microporous silicalite-1 (Cu-S-1) and mesoporous SBA-15 (Cu-SBA-15) zeolites), were evaluated.[96] The effect of their pore diameter on the adsorption behavior was intensively discussed. Because of the nanoscale pore structure, Cu-S-1 and Cu-SBA-15 demonstrated significant iodine adsorption capacities of 501 $mg.g^{-1}$ and 59 $mg.g^{-1}$, respectively. In comparison to other silver-containing materials already reported, the iodine adsorption capacity of Cu-S-1 was significantly higher. Accordingly, alternative copper-loaded porous zeolites, including CuCl-loaded NaY reduced by H_2 (H_2CuY) and CO (COCuY), have been explored.[97] The current study also deals with the impact of copper valence on iodine adsorption. Because of the copper sites and the nanometric pore structure, H_2CuY and COCuY exhibited high iodine adsorption capacities of 450 and 219 mg/g, respectively. Iodine adsorption efficiency of H_2CuY exceeded that of the silver-filled zeolites. Moreover, H_2CuY and COCuY adsorbed volatile iodine by a different chemical mechanism using copper sites of different valences, and Cu^0 showed a higher adsorption capacity than Cu^+. Such copper-loaded zeolites having a strong chemical interaction with iodine as well as high iodine adsorption capacities have the potential to be applied in nuclear industry. Nevertheless, the adsorption selectivity of these porous materials has not been explored.

Additionally,[98] a research group has validated the previous results for methyl iodide using M-exchanged faujasite of type X and Y (FAU) (M= H^+, Na^+, Cu^+/Cu^{2+}, Ag^+, Pb^{2+}). It has been found that the iodine trapping efficiency follows the order: $Cu^+/Cu^{2+} > Ag^+ \gg Pb^{2+} > Na^+ > H^+$. This efficiency order approximately follows the trend of different cations to form stable MI_x precipitates from ICH_3. Regardless, for nuclear application the authors states that Ag/Y is preferred over Cu/Y, due to the undesirable copper site-catalyzed oxidation of ICH_3 to I_2. Furthermore, the effect of the Si/Al ratio was reported for Ag/Y zeolites with similar silver content (23 wt.%). It is shown that this parameter has a significant influence on the oxidation state and dispersion of silver as well as on the adsorption/desorption behavior of ICH_3. In another study,[99] up to 13 different silver zeolite sorbents were prepared by repeated ion exchange from their parent structures (FAU X and Y, MOR, *BEA, MFI, FER). The Ag/Y zeolites exhibited the highest fractions of trapped AgI precipitates as a result of the presence of large amounts of silver species that were dispersed at affordable locations in the bulk supercages, as well as their reduced sodium content. A long-standing benchmark for iodine capture is silver-containing mordenite (MOR). Chapman et al.[100] have demonstrated multiple AgI species in the same AgMOR/I_2 system. However, two phases of AgI after I_2 adsorption have been found. The iodine is dispersed between nanoparticles of γ-AgI on the zeolite surface and clusters of subnanometer α-AgI in the pores for reduced-silver MOR, in the case of unreduced-silver-exchanged MOR, the iodine is confined to the pores exclusively as subnanometer α-AgI. Consequently, zeolites containing unreduced silver may afford a safer pathway for the capture of radioactive iodine, with the opportunity to trap iodine more effectively for long-term storage. For the same kind of zeolite MOR exchanged with silver (Ag^0MOR) Nenoff et al.[101] suggested a mechanism for the trapping of ICH_3. It was explained that ICH_3 was decomposed on the Brönsted acidic sites (Si-OH-Al) of the zeolite forming adsorbed methoxy species (CH_3O^-) resulting in reaction with water to form methanol and therefore releasing the acidic sites of the zeolite. Released iodine interacts with Ag in the MOR pores to create sub nanometer-sized clusters of AgI, which are smaller than the MOR pores, thus making it possible to assume that iodine is both physically and chemically confined in the zeolite. A crucial factor which can strongly affect the adsorption capacities is temperature. Vance et al.[102] studied the thermal stability in iodine uptake of silver-exchanged zeolites AgY (28 wt.%), AgX (37 wt.%), and AgMOR (20 wt.%). However, a significant decrease in the iodine content captured in the zeolites was seen upon increasing the temperature. The iodine content in AgY zeolite (28 wt.%) decreased from 210 $\mathrm{mg_{I_2}.g_{adsorbent}}^{-1}$ to 50 $\mathrm{mg_{I_2}.g_{adsorbent}}^{-1}$ at temperatures of 130 °C and 1300 °C, respectively. However, it can be observed that at temperatures above 700 °C, the zeolite structure generally tends to lose its crystallinity. Later, the influence of temperature on AgX zeolite loaded with 10, 20, and 30 wt.% silver has been studied by Choi et al.[103] Increasing the temperature led to a decline in the adsorption capacities of the zeolite for iodine compounds. For AgX zeolite (10 wt.%), the adsorption capacity decreased from 180 $\mathrm{mg_{I_2}.g_{adsorbent}}^{-1}$ to 130 $\mathrm{mg_{I_2}.g_{adsorbent}}^{-1}$ at temperatures of 100 °C and 400 °C, respectively. Nan et al.[104] noted an increasing adsorption capacity of silver-reduced Ag^0MOR (12 wt.%) upon an increase in temperature from 100 °C to 150 °C. Still, the adsorption capacity decreased further at temperatures above 150 °C.

1.6.2.6 Metal Organic frameworks

In the development of organometallic structures, the acquired knowledge on zeolites has been used unquestionably as an essential background. Zeolite discovery, and particularly their controlled synthesis and applications have led chemists to imagine well-defined porous structures, and to develop new materials for targeted applications. The area of porous materials has evolved with the development of metal-organic frameworks (MOFs). The latter, also referred as coordination polymers (CPs), are a type of hybrid crystalline porous materials with a framework consisting of inorganic building units (an extended network of metal ions (or clusters)) coordinated to multidentate organic molecules. Similarly to zeolites, the metal-organic components produce extended 3D frameworks by the combination of secondary building units (SBUs). Whereas zeolites only contain an inorganic part (i.e., SiO_4 and AlO_4 tetrahedra), a MOF consists of organic linkers covalently connected to a metal center Figure 1.21, resulting in an opened structure with outstanding characteristics of permanent porosity, stable structure, huge surface area and pore volume. [105–108]

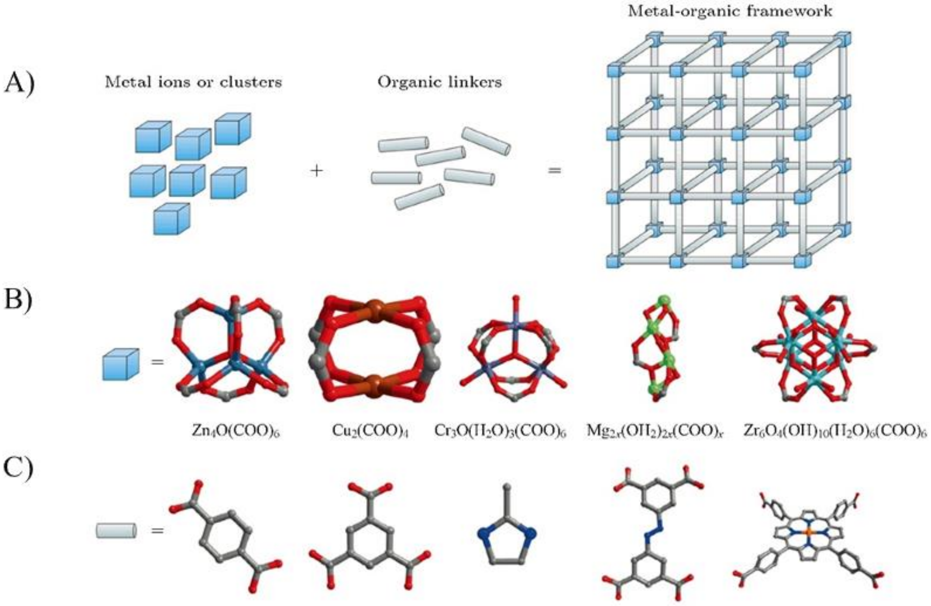

Figure 1.21: A) Structural model of MOF and the representative of B) the secondary building units (SBUs), and C) ligands (organic linkers)[109].

In general, MOFs exhibit a much lower framework density than zeolites, down to 0.13 g.cm $^{-3}$. Consequently, some MOF materials exhibit 90 % free volume and specific surface areas up to 7000 $m^2.g^{-1}$. Which allows them to take up voluminous amounts of gas such as hydrogen, methane, and carbon dioxide.[110] In addition, the MOF structure can be controlled and tuned by varying both inorganic (SBUs) and organic units (bridging ligand). Inorganic units can be mono (Ag, Cu), bi (Cu, Ni, Mn, Co, Fe), tri (Fe, Cr, Al) and tetravalent (Zr) metal ions or more complex clusters such as $Zn_4O(COO)_6$, $Cu_2(COO)_4$ or $Zr_6O_4(OH)_{10}(H_2O)_6(COO)_6$. Meanwhile, linkers can be ditopic, tritopic, tetratopic or multitopic ligands (Figure 1.22). The presence of diverse inorganic and organic components in MOFs leads to successful synthesis of over 90 000 different structures with various properties.[111]

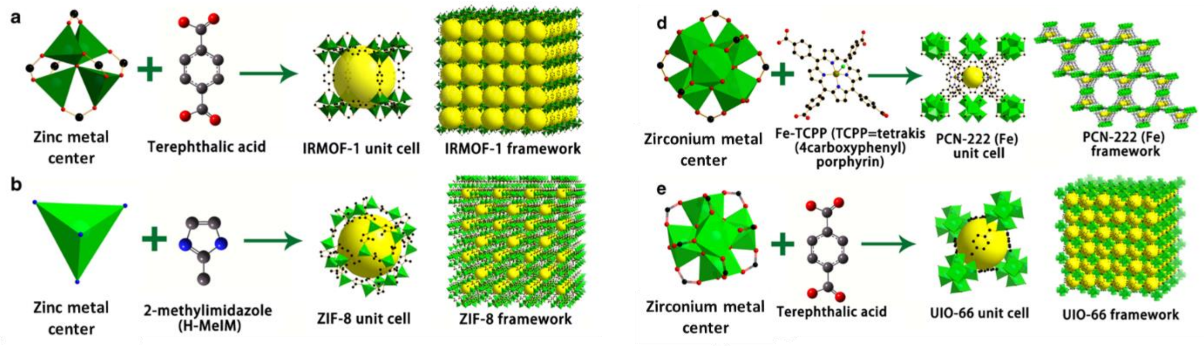

Figure 1.22: Schematic illustrations of some examples of MOF structures, combination of metal centers (SBUs) and organic linkers to form the IRMOF-1 (a), ZIF-8 (b), PCN-222(Fe) (c), and UiO-66 (e) frameworks[112].

1.6.2.6.a MOFs Classification

Metal–organic frameworks (MOFs) have been classified on the basis of four main categories as follows: the crystal structure arrangement, the stage of synthesis, the structural framework, and stimuli[113–116] (Figure 1.23).

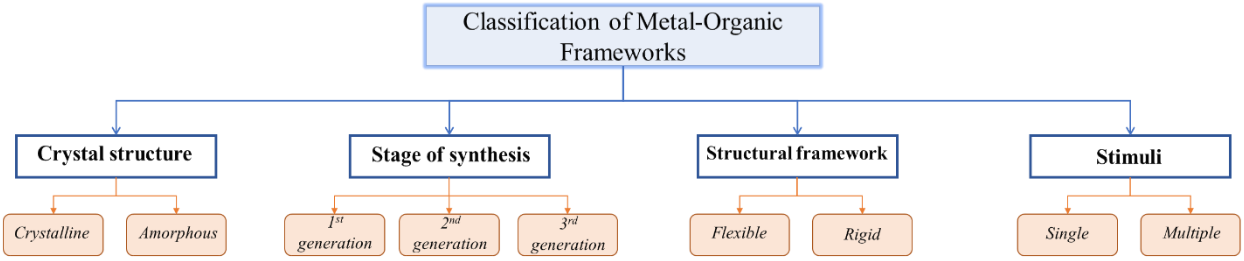

Figure 1.23: Classification of Metal-Organic Frameworks.

Based on the stage of synthesis, metal-organic structures have been classified into three generations:

(i) *First-generation metal–organic frameworks (Normal MOFs):* These MOFs have the basic structure consisting of an organic, and inorganic moiety.

(ii) *Second-generation metal–organic frameworks (Functionalized MOFs):* These are the MOFs that undergo post-synthesis surface modification through chemical functionalities.

(iii) *Third generation metal–organic frameworks (Smart MOFs):* These MOFs contain biomolecules (i.e., drugs, bioactive, toxins, ...) within their framework.

According to **the arrangement of the crystal structure**, metal-organic frameworks have been classified into two groups:

(i) *Crystalline metal–organic frameworks:* These MOFs have infinite arrangements of a very regular solid porous framework, beneficial for physicochemical sorption.

(ii) *Amorphous metal–organic frameworks*[113]*:* These MOFs consist of a highly disordered structure.

Generally, metal–organic frameworks are triggered by an external stimulus such as pH, temperature, pressure, etc. and their performance improves upon activation by this stimulus. Hence, based on **the stimuli** response,[116] MOFs have been classified into two groups:

(i) *Single-stimulus responsive* (triggered by a single stimulus).

(ii) *Multi-stimuli responsive* (triggered by multiple stimuli).

Based on **the structural framework,**[115] metal–organic frameworks are classified into:

(i) *Flexible metal–organic frameworks:* These MOFs can have a reversible change of their structural conformation in the presence of an external stimulus (i.e., temperature, pressure, etc.)

(ii) *Rigid metal–organic frameworks:* The structural conformation of these MOFs is maintained even in the presence of an external stimulus.

1.6.2.6.b MOF-74

MOF-74, also known as CPO-27 (coordination polymer of Oslo), M_2(dhtp) or M_2(dobdc) is constructed from metal (II) oxide chains connected by the organic ligand dobdc^{4-} (2,5-dioxido-1,4-benzenedicarboxylate) or dhtp^{4-}(2,5-dihydroxyterephthalate), and the remaining unsaturated metal are coordinated using DMF (DMF = N,N-dimethylformamide) resulting in Lewis acidic open metal sites (OMs) after the removal of DMF[117] (Figure 1.24). Since its discovery in 2005, MOF-74 has become one of the most promising MOFs because it features a high porosity, high surface area, and high density of open metal sites in the one-dimensional (1D) hexagonal channel of ~1.1 nm diameter along the c-axis.[117,118]

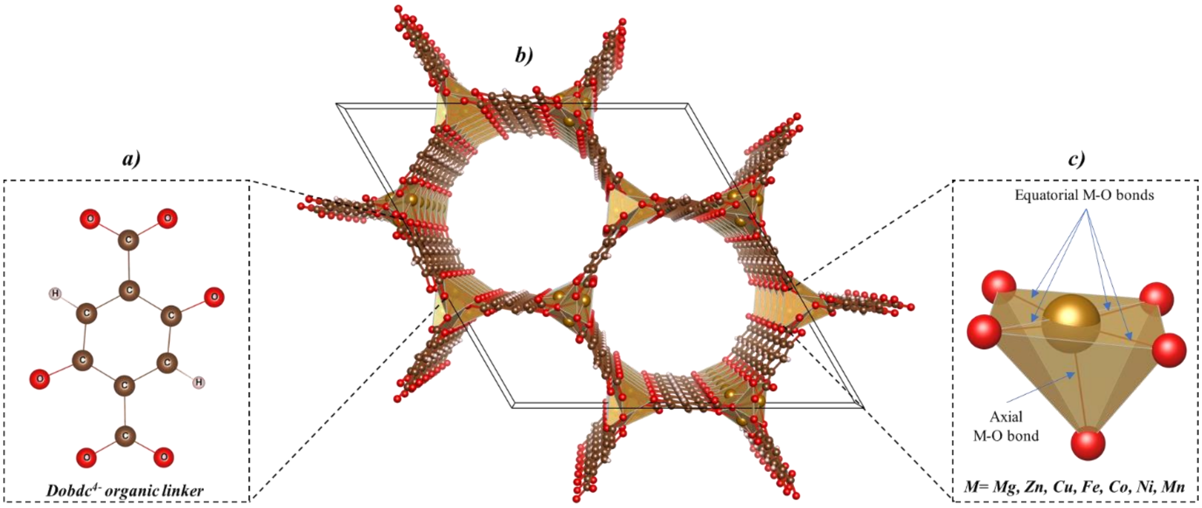

Figure 1.24: a) Schematic illustrations of the MOF-74 frameworks a) organic linkers, c) metal centers.

- *Tuning MOF-74 pore environment by metal and ligand modifications.*

In the attempt to create strong Lewis acidic sites, different porosity, and surfaces areas, significant efforts have been devoted toward the MOF-74 metal and ligand synthesis modifications with enhanced and unique properties. MOF-74s have been synthesized using various metal ions, including Zn, Cu, Ni, Co, Mn, Fe and Mg.[118] In addition, M. Yaghi and coworkers[119] reported the synthesis and characterization of five mixed metal MOF-74 structures having a combination of Lewis acidic sites of 2 (Mg and Co), 4 (Mg, Co, Ni, and Zn), 6 (Mg, Sr, Mn, Co, Ni, and Zn), 8 (Mg, Ca, Sr, Mn, Fe, Co, Ni, and Zn), and 10 (Mg, Ca, Sr, Ba, Mn, Fe, Co, Ni, Zn, and Cd) divalent metals. Each of these MOF-74, depending on the type of metal ions, exhibits intrinsic properties with respect to the catalytic active site, binding affinity of guest molecules, and chemical stability according to the strength of the open metal sites in the framework.[118,120]

Considering the ligand side, the MOF-74 structure can be expanded using elongated organic linkers giving the rise to a variation of pore sizes and surface areas without changing the topology of this open metal site MOF. Using a microwave-assisted solvothermal reaction Hong et al,[121] successfully prepared three Co(II) based MOF-74 structures, where metallic sites are connected by three different organic linker lengths [1_benzene: dobdc^{4-}= *2,5-dihydroxybenzene-1,4-dicarboxylic acid* , 2_biphenyl: dobpdc^{4-}=*4,4'-dihydroxy-[1,1'-biphenyl]-3,3'-dicarboxylic acid*, and 3_p-terphenyl: dotpdc^{4-}=*4,4"-dihydroxy-[1,1':4',1"-terphenyl]-3,3"-dicarboxylic acid*]. As confirmed by PXRD, the Co-Co distances vary from 8.1 Å for Co_2(dobdc) to 10.9 Å for Co_2 (dobpdc) and 14.7 Å for Co_2 (dotpdc). They further showed that the Co (II) in the chains 1 and 2 interact antiferromagnetically, resulting in field-induced metamagnetic transitions, whereas no magnetic interactions were observed when exceeding ~14.7 Å. Similarly, Yaghi and coworkers,[122] reported a systematic expansion of the MOF-74 pore aperture through ligand extension from its original link of 1 phenylene ring (I) to 2, 3, 4, 5, 6, 7, 9, and 11 phenylene rings (II to XI, respectively) resulting in eight isoreticular structures of MOF-74 with high thermal stability (up to 300 °C) (called IRMOF-74-I to XI) and pore apertures ranging from 14 to 98 Å. Resulted pore apertures of IRMOF-74-VII and IRMOF-74-IX are large enough for natural proteins to enter the pores.

A notable strategy to further enhance the unique features and properties of MOF-74 is the functionalization of the above-mentioned MOF structures. Due to the larger pore size of these extended variants of MOF-74, additional functional groups or diverse phenylene units can be easily incorporated to the organic ligand. Yaghi et al. in 2014,[123] reported the functionalization of the early well synthesized IRMOF-74-III with a variety of functional groups (IRMOF-74-III-CH_3, -NH_2, -CH_2NHBoc, -$CH_2NMeBoc$, -CH_2NH_2, and -CH_2NHMe) to selectively capture CO_2 in the presence of water. This study demonstrated how the presence of functional groups within the interior of IRMOF-74-III enhanced the selective CO_2 capture under humid conditions. In another attempt, Long et al.[124] investigated the catalytic performance Fe_2(dobdc) along with its two expanded organic linkers Fe_2(dobpdc) and Fe_2(dotpdc). Among them, the expanded Fe_2(dotpdc) to three benzene moieties were larger to accommodate various organic substituents (tetrafluoro-, tetramethy^{l-}, or 1,4 di-*tert*-butylaryl groups) on the central rings without interfering with MOF synthesis, abbreviated as $Fe_2(dotpdc^R)$ where (R = F, CH_3, and t-Bu), respectively. The resulting BET surface area and pore size of these functionalized MOF-74 series were 1880, 1860, and 1820 $m^2.g^{-1}$ and 27, 26, and 24 Å, respectively from the smallest to the largest substituents (F, CH_3, and t-Bu). In addition, the t-Bu group spread out into the pore surface with a hydrophobic nature and provided additional van der Waals forces with cyclohexane affinity without influencing the iron-oxo reactivity.

It has been shown that MOF-74 structures are a promising material, considering their structural diversity and adjustable properties through various modification methods. In particular, it is worth noting that open metal sites with high densities can serve as Lewis's acid sites and interact strongly with guest molecules within the framework. Given that MOF-74-type frameworks have significant potential and advantages for various applications over some other MOFs, MOF-74 has aroused great enthusiasm for research in many aspects, such as gas adsorption, separation, and catalysis and so on.[125,126]

1.6.2.6.c Application of MOFs for the capture of radioactive species

Many excellent explorations on iodine adsorption have been carried out using MOFs. Iodine was introduced into MOFs by guest exchange in iodine solution or by diffusion of high concentration iodine vapor, such experiments have shown that porous MOFs are good candidates for iodine capture.

For example, the ZIF-8 (zeolitic imidazolate framework) class of MOFs,[127] was selected for its important structural feature of relatively large pores (11.60 Å) connected by small apertures of (3.4 Å) close to the I_2 kinetic diameter of (∼3.35 Å), as well as its high specific surface area (1810 $m^2.g^{-1}$), high thermal (up to 550 ºC) and chemical stability (under the extreme operating parameters of industrial chemical processes).[127] Nenoff and coworkers,[128] presented a comprehensive structural evidence for I_2 uptake into ZIF-8. Results revealed a high sorption capacity for I_2, up to 125 wt.%, where only 25 wt.% of I_2 interacts with the MeIM linker of the framework, while ~100 wt.% of I_2 was effectively confined within ZIF-8 sodalite cages. This confined I_2 was found to be secured in ZIF-8 pores until the framework decayed at ~300 °C. Furthermore, ZIF-8 binds iodine 4 times more strongly than activated carbon.[129] This thermodynamic analysis of iodine binding on ZIF-8 raises awareness of the use of MOFs for the capture of volatile radio isotopes and provides clues for the design of effective functional MOFs for specific guest-host interactions. Assaad et al.[130] reported the adsorption of iodine by MIL-101. Typical results of sorption kinetics and absorption isotherms showed that MIL-101 has the same efficiency for the capture of radioactive iodine ^{123}I (96.61%) than activated carbon (98%) but with much faster kinetics with 97.9% removal of the iodine after 24 hours. More recently, Lobanov and coworkers[131] reported the iodine adsorption capacity by two microporous MOFs (SBMOF-1 and SBMOF-2) under dry and humid conditions (33% and 43% RH). Results showed that the MOF structures adsorbed iodine preferentially at room temperature over water in a humid environment due to the specific interactions between I_2 and the phenyl ring in their channels. These results are driving further interest into moisture-stable metal-organic porous structures that can selectively adsorb iodine in mixed gas streams from nuclear power processes.

As previously outlined, radioactive species (organic iodides-ICH_3) must also be selectively captured to provide safe use of nuclear energy. Indeed, a variety of MOF structures have been reported for ICH_3 adsorption. Li and coworkers[82] reported an efficient capture of radioactive organic iodides (ICH_3) from nuclear waste by post-functionalization of MIL-101-Cr MOF with tertiary amine binding sites. The synthesized molecular trap MIL-101-Cr-TED exhibits a high saturation uptake capacity for ICH_3 of 71 wt.% at 150 °C, being more than 340% higher than the industrial adsorbent Ag^0@MOR in identical conditions. In addition, the resulting MOF can be recycled multiple times without loss of capacity. These properties combined with chemical and thermal stability and low cost of MIL-101-Cr-TED suggested this MOF a promising material for the industrial capture of radioactive organic iodides from nuclear waste. Besides, in a detailed review,[132] Jiang and co-workers listed all different MOF structures used for the capture of iodine molecules (I_2 and ICH_3), including Cu-BTC, UiO-66, MFM-300(M) (M=Al, Sc, Fe, and In) and others.

Table 1.7: Summary of the advantages and drawbacks of the wet processes and solid sorbents described previously.

Methods	Advantages	Drawbacks
Mercurex	● High DF, up to 106 and 104 for Mercurex and Iodox	● Nitric acid, highly toxic and corrosive, will make the equipment susceptible to

	respectively. ● Trapping of inorganic and organic iodine. ● Low sensitivity to H_2O. ● The HI_3O_8 product (Iodox method) provides flexibility for various waste forms.	corrosion fractures. ● Very expensive.
Iodox		● The eliminated iodine is in a solid form (water soluble), which requires additional processing to complete the immobilization.
Electrolytic scrubbing	● Allows precise control of iodine conditions and specifications. ● DFs of about 600 for elemental iodine and 100 for methyl iodine.	● Not easily incorporated into any form of radioactive waste. ● The presence of NO_2 reduces the DF of iodine by a factor of 10.
Activated carbons	● Improved adsorption performance when impregnated with KI and/or TEDA. ● Less expensive.	● Decreased of the iodine adsorption efficiency at high T° and in presence of humidity. ● The formation of explosive compounds is probable.
Silver-doped silica	● Less expensive. ● Good adsorption performance.	● Efficiency decreases at temperatures of < 200°C. ● Reduction in efficiency in the presence of high excess of organic contaminants. ● Changes in adsorption performance with humidity (>70%).
Aerogels/chalcogels	● High porosity, and ability to sorb iodine gas. ● Excellent adsorption performance.	● Limited research on the influence of humidity and/or inhibitors. ● Expensive. ● The thermal stability of the iodine capture is poor.
Titanosilicates	● Better adsorption performance when doped with silver.	● Poor adsorption capacity. ● Limited research on the influence of humidity and/or inhibitors.
Porous organic polymers	● High surface area, adjustable pore structure. ● reversible and good physico-chemical stability for iodine adsorption.	● No data on ICH_3 capture. ● The influence of humidity and/or inhibitors is missing. ● Expensive.
	● Silver-loaded zeolites can be regenerated. ● AgZ – silver exchanged mordenite: Thermally stable	● ICH_3 uptake is reduced by high concentrations of NO_2 (>2%). ● AgX – silver exchanged

Zeolites	to 500°C and can be regenerated. ● Silver has the ability to form thermodynamically and chemically stable compounds with iodine.	faujasite: Presence of hydrocarbons and NOx adversely affects performance, and they are not acid resistant. ● High cost.
MOFs	● High adsorption capacities. ● Promising alternative for the capture of iodine. ● Tested in the real conditions of a severe nuclear incident.	● Not produced on a large scale. ● Expensive.

1.7 The interest of simulation methods

Theory and experiments each have different strengths and limitations, but they are complementary to a large extent and there is much to be gained by building research that combines the two. Since the late 1970s, atomistic theories and simulation methods based on statistical and quantum mechanics have played an increasing role in studying confinement effects on a wide variety of equilibrium phenomena and thermodynamic properties such as adsorption, free energies, chemical reactions, etc. Theory and simulation can provide fundamental understanding of observed phenomena, detailed information at the atomic level that is often difficult to obtain by experimental methods, and are often used to predict systems that are difficult to study experimentally (e.g., adsorption of highly toxic gases, or behavior at very high/low temperatures or pressures). All of these factors along with money and time cost, suggest that it may be advantageous to study highly idealized adsorbent models containing realistic adsorbate molecules to better understand the underlying nature of the physical phenomena.

Ab initio ("from the beginning") methods, as their name implies, do not require any experimental data apart from the knowledge of the atomic species implied. Such methods are essential where there is a significant motion or rearrangement of electrons, as in chemical reactions in porous materials (MOFs and Zeolites), in electrical conduction in electrodes and electronic devices (sensors), etc. These methods are the most rigorous in principle, but the most computationally demanding, so that their application remains limited to rather small systems and short times.

Among the various ab initio methods, the density functional theory (DFT) currently offers the best compromise between rigor and computational cost. The accuracy obtained with DFT varies depending on the application but is often in the range of 0.1 to 1 kcal mol^{-1} in energy.[133] The use of DFT provides a deep understanding of the nature of chemical reactions at the molecular level, a better understanding of trapping and sensing reaction mechanisms in terms of structures, electronic properties, activation energies, charge transfer, and finally, the discovery of key points that affect the reaction rate. Furthermore, DFT can be combined with a classical atomistic simulation (Monte Carlo and classical molecular dynamics) where the results will be extended to (T, P) of interest with the objective to deduce macroscopic properties.

In the present work, DFT calculations have been used to predict promising materials for the capture and detection of radioactive iodine gas species using porous materials and sensors, respectively. Adsorption energies, binding distances, charge transfers, electronic band structures and conductance modulations are calculated to understand in depth the interaction of these gaseous molecules with adsorbent materials. Thus, before illustrating our achievements in detail in Chapters III-VII, an overview of the previous DFT studies performed to address this challenging application will be outlined. Later in Chapter II a brief presentation of the theoretical background and methods, as well as the applied computational protocols used to address the posed challenges and achieve the respective objectives will be discussed.

1.7.1 *ab initio* screening for trapping of radioactive iodine species

1.7.1.1 Screening for Zeolites

In a recent study, Ayadi et al.[134], using ab initio calculations, investigated in detail the performance of silver-exchanged zeolites (i.e., faujasite, mordenite, chabazite, and clinoptilolite) with various Si/Al ratios on the selective adsorption of iodine species (I_2 and ICH_3) in the presence of potential inhibitory species (CO, H_2O, $ClCH_3$ and Cl_2). Results revealed that CO exhibits an inhibitory effect on the capture of iodine compounds in zeolites having a high Si/Al ratio, while spontaneous dissociation of Cl_2 was observed for a low Si/Al ratio, which significantly increases its inhibitory effect. However, a combination of sodium and silver cations in the zeolite structure significantly enhanced the performance of mordenite for the selective trapping of iodine compounds, since the presence of Na cations in faujasite and mordenite prevents the spontaneous dissociation of Cl_2, thus limiting its strong inhibitory effect. Summarizing their work with a comprehensive comparison, Ag-chabazite with a Si/Al of 5 and AgNa-mordenite with a Si/Al of 11 were suggested as the best candidates for a selective trapping of iodine species. In a similar work, the impact of various inhibitory substances (H_2O, NO, CO, CH_3Cl and Cl_2) on the adsorption of I_2 and ICH_3 was explored by chebbi et al.[135] through periodic dispersion corrected DFT calculations on several faujasites interchanged by monovalent cations (H, Li, Na, K, Rb, Cs, Cu and Ag). Results provided the following conclusions: (i) CO and H_2O were the most significant inhibitory species; (ii) H^+ or Li^+ hard cations were highly sensitive to water whereas soft cations (Cu^+ and Ag^+) may strongly adsorb I_2 and ICH_3. Consequently, Ag-FAU is apparently the most promising adsorbent in the presence of all contaminants, excepted for CO.

Similarly, Chibani et al.[136] also investigated various cation-exchanged mordenites (H^+, Na^+, Cu^+, and Ag^+). DFT calculations revealed that interaction energies of ICH_3 and I_2 on Ag- and Cu-MOR were higher than those of water, while computed interaction energies of water on H-MOR and Na-MOR were 20%–50% respectively higher than those of iodine species. In addition, they observed that iodine compounds are preferably adsorbed in the large mordenite channel, while the water prefers the small channel or lateral cavity where it forms stronger hydrogen bonds. Considering other inhibitors, the capacity of Ag-exchanged mordenite (Ag-MOR) for iodine trapping could be severely limited by the presence of volatile organic compounds (VOCs). In this context DFT calculations performed by Jabraoui et al.[137] showed that the adsorption process of iodine species is improved when the Si/Al ratio decreases. In fact, at higher Si/Al ratio, some VOCs such as benzene, 1,3-dimethylbenzene and propan-2-ol present high inhibiting effects, whereas at lower Si/Al ratio, only the adsorption of ICH_3 is limited by the presence of aromatic hydrocarbons.

1.7.1.2 Screening for MOFs

In a recent work, Leloire et al,[138] used a combination of theoretical and experimental investigations, for assessing a series of UiO-n MOF materials (n=66, 67, 68) as well as UiO-n compounds, with organic functionalities (-H, $-CH_3$, -Cl, -Br, $-(OH)_2$, $-NO_2$, $-NH_2$, $(-NH_2)_2$, $-CH_2NH_2$) for iodine capture. Calculated interaction energies of I_2 obtained with the unmodified UiO series (UiO-66, UiO-67, and UiO-68), were low and did not exceed -57 kJ/mol following the order in absolute value of UiO-66 > UiO-67 > UiO-68. In agreement with the increase in the length of organic linkers, this implies larger pore openings that reduce the interaction between I_2 and the UiO-n structures. Furthermore, this interaction of I_2 with the UiO-n series was found to be dominated by dispersion interactions (>60% of the total interaction energy). Following kinetic results, functionalization of organic linkers in UiO-66, UiO-67, and UiO-68 with $-NH_2$ groups, appears to be an effective adsorbent for trapping iodine. The interaction of the I atom (I_2) and the lone pair $-NH_2$ of the group attached to the organic ligand leads to a good adsorption energy with a small range of (from -43 to -68 kJ/mol) for the three MOFs structures. Further enhanced results for I_2 capture were observed by replacing the $-NH_2$ group with $-CH_2NH_2$ on UiO-67, where the lone nitrogen pair is not conjugated with the aromatic group and is more available to interact with iodine. Indeed, the adsorption energy was significantly high by -128.5 kJ/mol accompanied by a significant electron transfer between the -CH_2NH_2 group and iodine. Theoretical calculations and experimental values resulting from thermogravimetric analyses have shown a good correlation and have both suggested that UiO-67-CH_2NH_2 is one of the most efficient adsorbents for iodine immobilization. In a similar work[139], a comparative study of the adsorption of gaseous I_2 molecule on a series of five thiophene-based MOFs (DUT-67, DUT-68, MIL-53-TDC(In), In-TDC and Ho-TDC) was reported. Raman analysis, XPS and DFT calculations have revealed a good charge transfer effect between thiophene groups and trapped iodine. The optimized adsorption energy of -44.5 kJ/mol for the first iodine molecule interacting with the thiophene groups bound to the Zr node (DUT-67 and DUT-68) has suggested a strong interaction between the linkers and the iodine molecules. The different configurations of the metal (In) nodes have not influenced the affinity towards I_2 molecules, as for MIL-53-TDC(In), In-TDC, the adsorption energy and charge transfer of the attracted iodine molecule are similar for the two indium node configurations (of -25 kJ/mol and -27 kJ/mol, respectively). This work predicts that MOFs with cage-like pores are likely to have better iodine adsorption capacity, and the consideration of thiophene groups with different metal nodes may further boost the significant anisotropy with respect to iodine capture.

Taking into consideration the capture of organic iodides-ICH_3. Chibani et al.[140], reported a periodic DFT study of the adsorption properties of I_2 and ICH_3 in MIL-53(Al), MIL-120(Al), and HKUST-1(Cu) MOFs. Calculated results revealed a weak interaction of iodine molecules with MIL-120(Al) and HKUST-1(Cu) MOFs. On the other hand, MIL-53(Al) was found to be a promising material for the capture of I_2 and ICH_3 with an interaction energy of -111.2 kJ/mol (I_2) and -94.3 kJ/mol (ICH_3). However, long-range interaction (dispersion) was the key factor in the nature of interactions between iodine and MOF structures. Further analyses were reported on MIL-53(Al) by functionalizing it with (-Br, -Cl, -OH, -NH_2, -CH_3, -NO_2, -COOH), but these substitutions did not demonstrate any significant effect. Moreover, using molecular dynamics calculations at 373K, they reported the infrared spectrum of I_2 and ICH_3 in MIL-53(Al). Results showed the formation of a hydrogen bond located at 3630 cm^{-1} between the two iodine molecules and the hydroxyl group of the MOF framework.

1.7.2 *ab initio* screening for sensing of radioactive iodine species

In a recent study, Ibarra et al.[141] discussed the change in fluorescent properties of MIL-53(Al)-TDC that are drastically affected by the presence of iodine, even present in small trace amounts. Density function theory calculations have demonstrated that, within the most stable MIL-53(Al)-TDC$\cdots I_2$ configuration, I_2 is primarily hydrogen-bonded by O-H$\cdots$I. However, QTAIM analysis indicated that additional non-covalent interactions provide additional stability to MIL-53(Al)-

TDC···I_2. Electrostatic potential analysis suggested that I_2 molecule adsorption takes place by a combination of both specific interactions with a high electrostatic contribution, and weak interactions. Such results hypothesized that fluorescent MIL-53(Al)-TDC could be an efficient I_2 sensor. Similarly, by using density functional theory (DFT) calculations, the geometries, stabilities and electronic properties of iodine adsorbed on fullerenes (SFs) with both parallel and perpendicular configurations have been explored.[142] Computational results have revealed an adsorption process where the iodine molecule can be adsorbed on the surface of SFs for free energies ranging from 6.33 to 26.70 kcal/mol. NBO analyses demonstrated the powerful interaction between doped sulfur and iodine. DOS plot of SFs differed from that of undoped fullerene; the HOMO/LUMO energy gap of SFs was between 0.061 and 0.071 eV whereas in single fullerene it was of 0.106 eV. Furthermore, the Eg decrease has been found to be in the complexes with iodine and results were in the range of 0.004-0.053 eV. Thus, the electrical conductivity of SFs was increased upon iodine adsorption and SFs might be suitable for use as iodine sensing devices. With the same group, Tavakol et al.[143] using DFT calculations being implemented up here for various sulfur-doped carbon nanotubes (SCNTs) as iodine sensors.

Interaction energies proved that interactions at stable configurations were exothermic, particularly in solvents. Additionally, AIM analyses supported the potency of this interaction, and the 2ρ values reflected that this interaction was noncovalent in nature. NBO computations also indicated a correct interaction between SCNTs and iodine. Population-based analyses have demonstrated an increase in the reactivity of SCNT-Is compared to SCNTs. Besides, electrical conductivity of SCNTs was increased upon iodine adsorption and they have the potential to be used in iodine detection.

According to this bibliography concerning zeolites, MOFs, and sensors, three concrete conclusions can be drawn from these investigations:

(1) Zeolites have been the most studied and evaluated materials in the literature compared to MOFs and sensors. Almost all types of structures have been studied and the influence of different parameters on the capture performance has been considered, i.e., influence of silver content, zeolite type, Si/Al ratio, operating temperature, inhibitors, water, organic compounds, and halogens...etc.

(2) Concerning MOFs, they have not been very well described, differently from the case of zeolites. In fact, among the available investigations, very few of them have investigated iodine compounds in the form of I_2 and ICH_3 together and no investigation in the presence of different inhibitors as in the nuclear context.

(3) Sensors have been described with a predominance of the optical aspect and very few studies have been performed on carbon-based sensors to detect radioactive iodine. Moreover, very rare are the directions investigated by DFT.

These enlightenments provide the real motivation with the focus of our efforts to fill the gaps in the literature and provide a meaningful study addressing all of these circumstances. To this end, with the intention of offering superior detection/capture of iodinated species (I_2, ICH_3) in the presence of (H_2O, CO), we have specifically targeted carbon-based 2D materials to serve as sensors and MOF materials as trapping materials. Chapter 3 to 5 will be devoted to present our theoretical investigations concerning these materials.

Chapter 2 : Theory and Methods

> "Theory provides the maps that turn an uncoordinated set of experiments or computer simulations into a cumulative exploration. " – **David E. Goldberg**

2.1 Introduction

The goal of materials science is to study the properties of materials and to develop innovative materials for the benefit of society. Computer modeling of materials with theories and algorithms based on mathematics, physics, chemistry, material and computer science allows us to achieve this goal. For example, an experiment that can be studied in the laboratory using an equipment, can also be performed by computer using an atomic scale method.

As discussed in section 1.7.1 computational approach may also in many cases become the only way to manipulate materials under extreme and harsh conditions that can never be achieved in the laboratory (e.g., under high pressures, at high temperatures and in the presence of toxic substances). For that, materials used in nuclear fusion environments are of today’s great concern. The various damages caused radioactive iodine species can be avoided with simulation without having to worry about expensive equipment or the danger of radiation.

This chapter presents a brief description of simulation methods, after that we give a short survey over quantum chemistry particularly density functional theory method, while a more detailed description could be found elsewhere[133,144–147].

2.2 Atomic Scale Methods

In the environment, matter is subject to four types of interactions: electromagnetic, weak nuclear, strong nuclear and gravitational. Fortunately, when it comes to materials science, only the electromagnetic interaction is concerned; we rarely find cases with the other three. Thus, what happens in any material, under any conditions, is due to electromagnetic interactions between nuclei, and electrons. Based on this simple fact, the successive steps in the study of a material in computational science are to:

- Define what needs to be calculated.
- Build a system model that correctly represents the real system.
- Select the appropriate rules (classical and quantum mechanics, etc.).

- Look for a program, a code to do the simulation.
- Analyze the results and generate information and review it with other relevant studies and experiences.

Different methods are employed for these studies. All of them have advantages and limitations in terms of system size and simulation time, as shown in Figure 2.1. One can note that as the time or size scale increases, the discipline shifts from physics to chemistry to materials science to engineering.

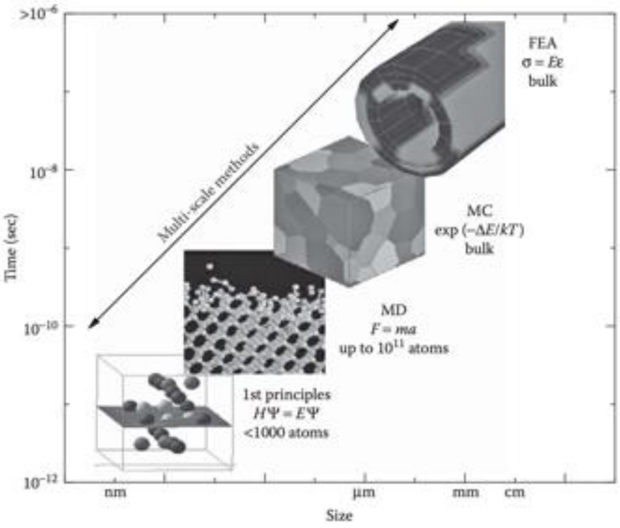

Figure 2.1: Computational material science methods in terms of size and time.

2.2.1 Monte Carlo method

The Monte Carlo (MC) approach[148] is a statistical technique that uses random walks for sampling and the Boltzmann factor $e^{\frac{-U}{k_B T}}$ (where U is the energy of a state, k_B is the Boltzmann constant, and T is the temperature) to solve material and systemic problems such as finance, engineering, supply chain and science. The method is conceptually very easy and simple to use, as it allows the system to jump randomly from one configuration in the phase space to another looking for the state with the lowest energy. It can balance any degree of freedom, and since it is based on statistical mechanics, no dynamics are required. The scale of the MC method is in microns and can therefore handle microstructures of materials being appliable for different applications namely in random walk, magnetic phase transition, structural transformation of materials.

2.2.2 Molecular dynamics

Molecular dynamics (MD) simulation[149] is a computational tool used to describe the change over time of atomic positions, velocities, and orientations. It is based on a set of models that describe the interactions at the molecular level. These models relate the energy/force of a system to its configuration. In the 1960's, MD was able to simulate only a few hundred atoms; this number has now evolved to more than 100 billion. MD requires to insert empirically the interaction potential between atoms because this method excludes the origins of potentials (nuclei and electrons), as well as the electronic and magnetic characteristics of molecules. Once the potential has been defined, the initial positions, velocities, and temporal evolutions of the atoms can be revealed very simply. Therefore, thermodynamic properties can be calculated from positions and velocities for each configuration in the phase space as in statistical physics.

2.2.3 Quantum Chemistry

Quantum chemistry applies quantum mechanics to address numerous aspects and phenomena associated with the behavior of electrons and thus of chemistry. It aims, in principle, to solve the Schrödinger equation, postulated by the Nobel Laureate Erwin Schrödinger in 1925, later published in 1926.[150] It represents the most significant landmark in the given field. However, its complexity for all but the simplest of atoms or molecules requires simplifying assumptions and approximations, establishing a balance between accuracy and computational effort. The time-independent method is sufficient in the cases studied and the eigenvalue problem to solve is given by:

$$\widehat{H}\ \psi\,(\{ri\},\{Ri\}) \;=\; E\,\psi(\{ri\},\{Ri\}) \qquad \text{Eq 2.1}$$

Where:

- ✓ $\widehat{H}$ is the Hamiltonian operator of the system.
- ✓ $\psi(\{ri\}, \{Ri\})$ is the wave function describing the system under study.
- ✓ $\{ri\}$ and $\{Ri\}$ represents the electronic and nuclear coordinates respectively.

The Hamiltonian of the system is written : $H = T_e + T_N + V_{e-e} + V_{e-N} + V_{N-N}$ which can be summed in terms of two operators : $\widehat{H} = \widehat{H}_{ele} + \widehat{H}_{Nuclei}$, with the nuclei Hamiltonian is $\widehat{\mathrm{H}}_{\mathrm{ele}} = \widehat{T}_e + \widehat{T}_N + \widehat{V}_{e-e}$ and $\widehat{\mathrm{H}}_{\mathrm{nuclei}} = \widehat{V}_{e-N} + \widehat{V}_{N-N}$

Using atomic unit i.e., $\frac{1}{4\pi\varepsilon} = m_e = \hbar = 1$, the different terms of the Hamiltonian function can be expressed as:

- ✓ $\widehat{T}_e = -\frac{1}{2}\sum_{i=1}^{N}\nabla^2$; the kinetic energy of electrons. Eq 2.2

- ✓ $\hat{T}_N = -\frac{1}{2}\sum_{i=1}^{M}\frac{\nabla^2}{M_i}$; the kinetic energy of nuclei. Eq 2.3

- ✓ $\hat{V}_{e-e} = \sum_{i=1}^{N}\sum_{j>i}^{N}\frac{1}{|r_i - r_j|}$; the repulsive electron-electron coulombic interaction. Eq 2.4

- ✓ $\hat{V}_{e-N} = -\sum_{i=1}^{N}\sum_{j=1}^{M}\frac{Z_j}{|r_i - R_j|}$; the attractive electron-nucleus coulombic interaction. Eq 2.5

- ✓ $\hat{V}_{N-N} = \sum_{i=1}^{M}\sum_{j>i}^{M}\frac{Z_i Z_j}{|R_i - R_j|}$; the repulsive nucleus-nucleus coulombic interaction. Eq 2.6

Z_i and Z_j Are the charges of nuclei i and nuclei j.

The Schrödinger equation becomes under these conditions:

$$\left[-\frac{1}{2}\sum_{i=1}^{N}\nabla^2 + \sum_{i=1}^{N}\sum_{j>i}^{N}\frac{1}{|r_i - r_j|} - \sum_{i=1}^{N}\sum_{j=1}^{M}\frac{Z_j}{|r_i - R_j|} + \sum_{i=1}^{M}\sum_{j>i}^{M}\frac{Z_i Z_j}{|R_i - R_j|} - \frac{1}{2}\sum_{i=1}^{M}\frac{\nabla^2}{M_i}\right]\psi(r_1, \dots, r_N, R_1, \dots, R_M)$$

$$= E\,\psi(r_1, \dots, r_N, R_1, \dots, R_M) \qquad \text{Eq 2.7}$$

Due to the high complexity of the system, this equation cannot be solved exactly. Therefore, some approximations have been introduced.

2.2.3.1 Born Oppenheimer approximation

This is one of the first approximations that can be performed to solve the Schrödinger equation of a complex system[151]. It is based on the fact that the mass of the nuclei is much heavier than that of the electrons (1800-time greater). For that, the kinetic energy of the nuclei can be neglected when compared to that of the electrons ($T_N = -\frac{1}{2}\sum_{i=1}^{M}\frac{\nabla^2}{M_i} = 0$). This is equivalent to assume that electrons move in a fixed field of nuclei. Thus, the repulsion between the nuclei is considered constant ($V_{N-N} = \sum_{i=1}^{M}\sum_{j>i}^{M}\frac{Z_i Z_j}{|R_i - R_j|} = constant$).

This approximation, called the adiabatic approximation, is the first step towards the solution of the Schrödinger equation, because it separates the motion of the electrons from that of the nuclei. In this context, the wave function can be written as a product of two wave functions: one is electronic and the other is nuclear.

$$\psi(\{r_i\},\{R_i\}) = \psi(R_i)\psi_{R_i}(r_i) \qquad \text{Eq 2.8}$$

The problem of solving the Schrödinger equation is hence reduced since it depends now only on the behavior of the electrons. Nevertheless, the Born-Oppenheimer approximation is not fully sufficient to solve the Schrödinger equation because of bi-electronic integrals. Hence further approximations are required. In this context, Hartree, Hartree-Fock[152], Post Hartree-Fock[153], and

Density functional theory (DFT) method are extremely useful. Herein we will be focusing only on DFT that has been adopted for the following work.

2.2.4 Density Functional Theory

The density functional theory is based on the postulate proposed by Thomas and Fermi in 1927 [154] who attempted to express the total energy of a system as a functional of its electron density by representing its kinetic energy according to a functional of this quantity. Thomas and Fermi used their theory for the description of atoms, but the lack of precision, as well as the impossibility to treat molecular systems made it too simplistic model when it was proposed. In 1964, Hohenberg and Kohn (HK) showed that there is an energy functional E $[\rho(\mathrm{r})]$ (with $\rho(\mathrm{r})$ being the electronic density) associated with variational principle, which allowed to determine all the properties of the ground state. A year later Kohn and Sham proposed a set of monoelectronic equations analogous to the Hartree-Fock equations from which it became possible to obtain the electron density of a system and thus its total energy.

2.2.4.1 The Hohenberg and Kohn theorem

In the HK theorem[155], Hohenberg and Kohn have showed that there is a one-to-one correspondence between the density of the ground state and the energy of the system. Consequently, the total energy of the ground state can be expressed as a functional of this electron density $E = E[\rho] = F_{HK}[\rho] + \int \rho\,(r).V_{ext}(r)\,dr.$ Where $\int \rho\,(r).V_{ext}(r)\,dr$ is the external potential acting on these particles and $F_{HK}[\rho] = T[\rho] + V_{e-e}[\rho]$ is the universal HK functional. As a result, by the use of electron density functionals HK's theorem establishes the basis of reducing the many-body problem of n electrons with 3n space coordinates to three space coordinates. Having the functional $F_{HK}[\rho]$ would be sufficient to determine the total energy of the system as well as its properties in the ground (fundamental) state. Unfortunately, the explicit forms of the two terms that compose the functional $F_{HK}[\rho]$ are unknown, and therefore, further improvement of the theory is needed.

2.2.4.2 The Kohn and Sham equation

The vagueness of the $F_{HK}[\rho]$ functional of KH, led Kohn and Sham in 1965 to transform the real interactive system into a fictitious non-interactive system[156,157]. This approach realizes an exact correspondence between the electron density of the system ground state consisting of non-interacting fermions placed in an effective potential, and the real system with several interacting electrons subjected to the real potential, i.e., the electron density is conserved when switching from an interacting to a non-interacting system (Figure 2.2).

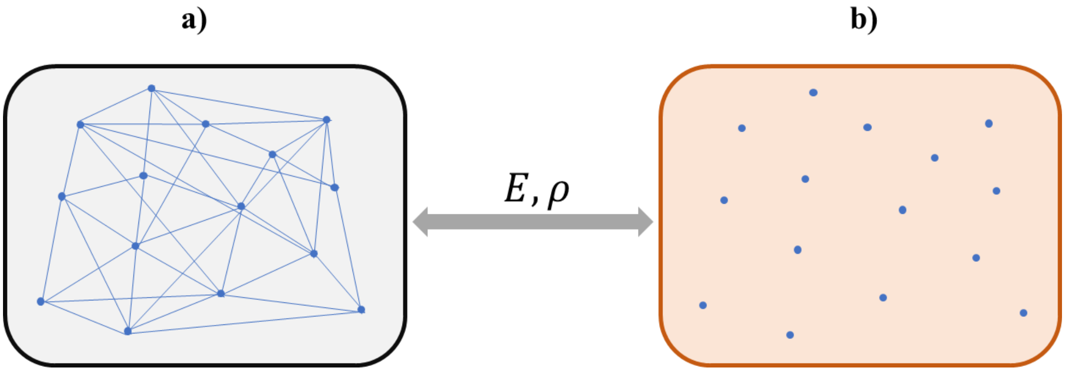

Figure 2.2: Schematic representation of a) real system of interacting electrons and b) fictitious system of non-interacting electrons.

According to the KS-DFT scheme, the total energy functional can then be calculated as follows:

$$E_{KS-DFT} = T_{KS} + E_{Coul} + E_{xc} + E_{ext} = T_{KS} + V_{eff} \qquad \text{Eq 2.9}$$

Here, T_{KS} is the kinetic energy of the non-interacting system of electrons $\mathrm{T_{KS}}[\rho(r)] = \sum_{i=1}^{N} n_i \left\langle \phi_i \middle| -\frac{\nabla^2}{2} \middle| \phi_i \right\rangle$, E_{Coul} is the classical coulomb term representing the electronic interaction, E_{xc} is the unknown exchange-correlation interaction that count all missing non-classical many-body effects between electrons, and E_{ext} is the energy from the external field due to the positively charged nuclei. Following this, one can rewrite the KS equation in a wave function form as follows: $\left(-\frac{\nabla^2}{2} + V_{eff}(r)\right) \phi_i(r) = \mathcal{E}_i \phi_i(r)$. Eq 2.10

The resulting equation corresponds to the Kohn-Sham equation which has to be solved in a self-consistent way [156] see Figure 2.3. Starting from a given initial density, a potential is obtained for which the equation is solved, and a new electron density is then determined. From this new density, a new "improved" effective potential can be calculated. This process is repeated in a self-consistent way until meeting the convergence criteria, i.e., until the new electron density is equal or very close to the previous one.

The two researchers have thus enabled DFT to become an effective tool for the study of complex systems. Nowadays, the vast majority of DFT calculations are performed in the scope of this equation. In spite of this great effort of Kohn-Sham, this equation presents a major drawback, due to the unknown exchange-correlation functional. Therefore, in order to solve the Kohn-Sham equations, different exchange-correlation functions have been considered.

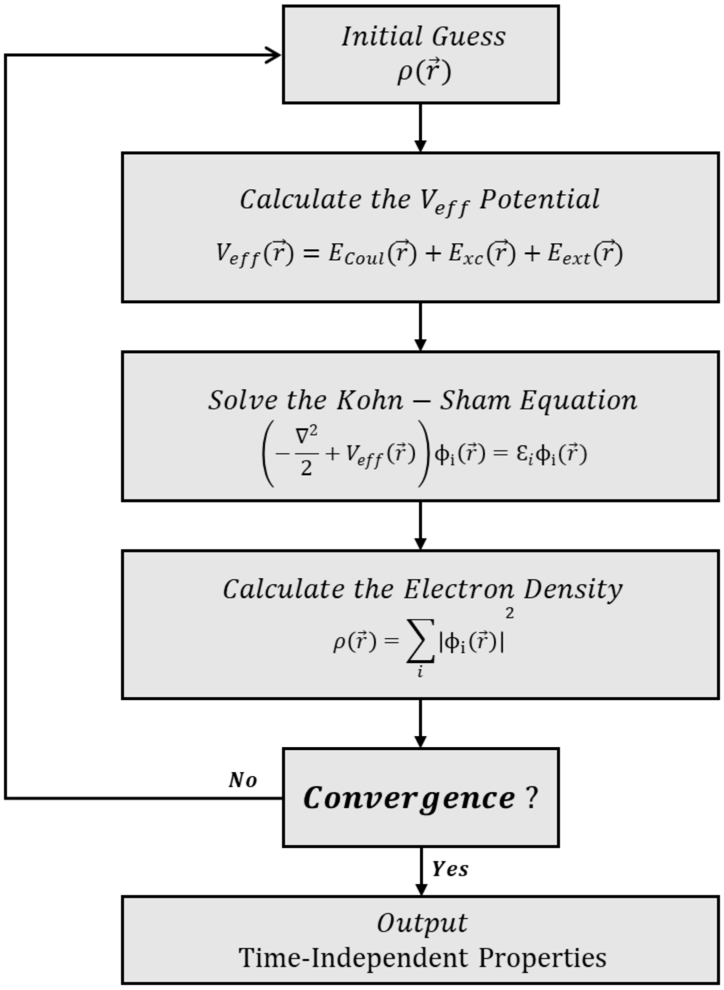

Figure 2.3: A typical time independent KS-DFT calculation cycle.

2.2.4.3 The exchange-correlation functional

The density functional theory applied in the framework of the orbital approach of Kohn and Sham remains accurate in its formalism. Progressively, the unknown part in the energy $[\rho(r)]$ has been reduced from the universal functional of Hohenberg and Kohn $F_{HK}[\rho(r)]$ to an exchange and correlation energy $F_{XC}[\rho(r)]$. At this stage, it is necessary to approximate the expression of this exchange and correlation functional, so that it provides the most accurate description possible.

In 2001, Perdew[158] introduced the organizing principle that he called "Jacob's ladder". Its description is illustrated in Figure 2.4, as well as the description of two functional ones (LDA and GGA) afterwards.

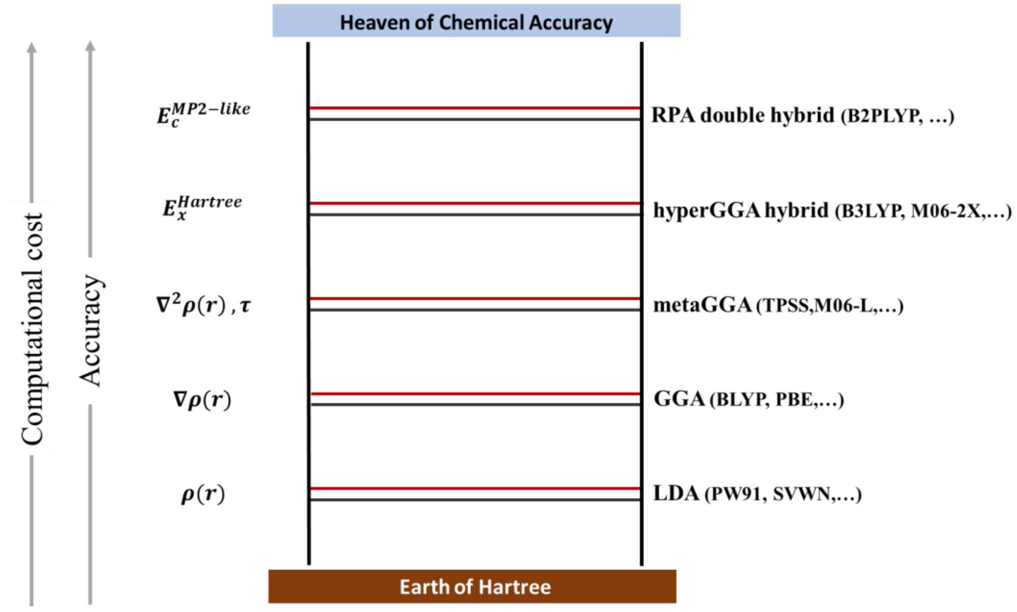

Figure 2.4: The "Jacob's ladder" diagram of exchange-correlation functions proposed by J. P. Perdew.[158]

✓ The local density approximation LDA

The local density approximation is developed in 1995 by Kohn and Sham in order to estimate the exchange and correlation energy. Its main idea is to assume that the electron density can be treated locally at a point r which varies slowly around this same point, in a homogeneous electron gas. The exchange-correlation energy in the LDA approximation can be written as : $E_{XC}[\rho(r)] = \int \rho(r)\, \varepsilon_{XC}{}^{LDA}[\rho(r)]dv$, where $\varepsilon_{XC}{}^{LDA}[\rho(r)]$ is the energy for a homogeneous gas of electrons of density $\rho(r)$. The functional $\varepsilon_{XC}{}^{LDA}[\rho(r)]$ can be split into an exchange contribution $\varepsilon_{X}{}^{LDA}[\rho(r)]$ and correlation $\varepsilon_{C}{}^{LDA}[\rho(r)]$ such as : $\varepsilon_{XC}{}^{LDA}[\rho(r)] = \varepsilon_{X}{}^{LDA}[\rho(r)] + \varepsilon_{C}{}^{LDA}[\rho(r)]$. Eq 2.11

Overall, the LDA results are in very good agreement with the experiment regarding structural and vibrational properties, dipole moments and elastic moduli. This is mainly true for systems when the density is highly uniform as in the case of transition metals, but it failed in the opposite case, namely where the variation of the electron density is significant around the starting position r.

✓ The generalized gradient approximation (GGA) function

The generalized gradient approximation (GGA) comes to follow the improved treatment of exchange and correlation energy.[159] It takes into consideration the properties of the inhomogeneity of the electron density and its significant variation in space (when going from one electronic layer to another in an atom, or when going from one atom to another in a molecule) of a real gas. GGA makes the functional $E_{XC}[\rho(r)]$ dependent on the electron density and its gradient $|\nabla\rho(r)|$, to account for the non-uniform character of the real gas. The exchange-correlation expression can be rewritten in a similar form to LDA:

$$E_{XC}{}^{GGA}[\rho(r), |\nabla\rho(r)|] = \int \rho(r)\, \mathcal{E}_{XC}{}^{GGA}[\rho(r), |\nabla\rho(r)|]dv \qquad \text{Eq 2.12}$$

Where $\mathcal{E}_{XC}{}^{GGA}[\rho(r), |\nabla\rho(r)|]$ is the exchange-correlation energy density of an inhomogeneous gas. Often the contributions for exchange and correlation are developed separately:

$$E_{XC}{}^{GGA}[\rho(r), |\nabla\rho(r)|] = E_X{}^{GGA}[\rho(r), |\nabla\rho(r)|] + E_C{}^{GGA}[\rho(r), |\nabla\rho(r)|] \qquad \text{Eq 2.13}$$

The use of GGA functionals significantly increases the accuracy of the calculations compared to the description provided by the LDA.

Several functionals have been developed to estimate the exchange and correlation energy. Among the best known and most used are the exchange functionals of Becke (B88) and Perdew and Wang (PW91) and (P86). For the correlation term, the corrections relating to this term are much more complex to formulate than those relating to the exchange term, we have, among others, the functionals of Perdew (P86), of Lee, Yang and Parr (LYP) and of Perdew and Wang (PW91). GGA-like functionals also provide a better description of the optimizations of geometries, elastic moduli and magnetic properties of compounds compared to LDA calculations. Unfortunately, GGA fails to properly treat the molecular long-range interactions, like dispersion forces.

2.2.4.4 Dispersion correction methods

The most common approaches LDA and GGA depend on the local and semi-local density, respectively. However, non-local interactions such as van der Waals (vdW) are not taken into account. The correct description of these interactions is critical in the determination of physical, chemical, and even biological properties. There are empirical and semi-empirical approaches based on the asymptotic forms r^{-4} and r^{-6} describing the vdW interactions or more precisely the London dispersion forces. Some known are: D2 by Grimme [160]; D3 by Grimme [161,162]; TS of Tkatchenko-Scheffler[163,164]; TS/HI of Tkatchenko-Scheffler with iterative partitioning of Hirshfeld [165]; many-body dispersion (MBD) [166] and the fractional ion method FI/MBD [167]. In this case, the total energy is expressed as follows:

$$E_{Total} = E_{KS-DFT} + E_{disp} \qquad \text{Eq 2.14}$$

Each scheme represents a different level of complexity in the formulation of the correction.

- ***D2 scheme***

This method was proposed by Grimme and co-authors[160] and includes adjustable parameters calculated using high-level wave function methods. In this case, the dispersion energy is expressed as follows:

$$E_{disp} = -S_6 \sum_{i=1}^{N} \sum_{j=1}^{Nat} \frac{C_{6ij}}{r_{ij,L}^6} f_{damp}(r_{ij}) \qquad \text{Eq 2.15}$$

Where N is the total number of atoms in the system, C_{6ij} is the dispersion coefficient for a pair of atoms ij, r_{ij} is the distance between two atoms and the term f_{damp} is a Fermi-type damping function whose role is to avoid the divergence of the corrective term for $r_{ij} = 0$. Here, the factor C_6 is equal to 0.75 for the PBE functional.

- ***TS scheme***

This scheme was proposed by Tkatchenko and Scheffler in 2009[164] and is based on the calculation of the dispersion coefficients C_{6ij} and the effective polarizabilities α_i as a function of the environment of each atom of the molecule contrary to the D2 method of Grimme. In this method, the C_{6ij} term is expressed as: $C_{6ij} = (\frac{V_i^{eff}}{V_i^{free}})^2 C_{6ij}^{free}$ Eq 2.16

Where V_{eff} and V_{free} are respectively the volume occupied by the atom in its environment and the reference volume for the non-interacting atom.

- ***TS/HI scheme***

In the Tkatchenko-Scheffler scheme with iterative Hirshfeld partitioning (TS/HI) the coefficients C6 depend on the electron density as in the original Tkatchenko- Scheffler method[165]. However, in this method, Bucko and co-authors proposed a partition based on the iterative Hirshfeld scheme, in which the partially charged atomic reference state is determined consistently. This method shows good accuracy for the treatment of ionic systems and adsorption phenomena on surfaces with ionic character such as zeolites.

- ***FI/MBD scheme***

The MBD method of Tkatchenko et al. goes beyond simple pairwise correction to take into account multibody interactions[167], which are modeled in this case by a set of coupled harmonic oscillators. In this case, the multibody correction is written:

$$E_{disp,MBD} = -\frac{1}{2\pi} \int_0^{\infty} d\omega Tr[\ln (1 - A_{LR}(\omega) T_{LR}] \qquad \text{Eq 2.17}$$

where $A_{LR}(\omega)$ is the short-range dipole polarizability and T_{LR} is the long-range interaction dipole tensor that describes the interaction of screened polarizabilities. This method was then improved in 2016 to take into account the ionic character of atoms, using polarizabilities for atoms with fractional charge.

2.2.4.5 The Hubbard "DFT+U" model: Approaches

As discussed earlier, the accuracy of a DFT calculation depends heavily on its ability to describe the exchange and correlation function (xc). It is generally challenging to model the dependence of the xc function on the electron charge density and, thereby, it may inappropriately describe the multibody characteristics of the N-electron ground state. Therefore, systems whose physical properties are controlled by electronic many-body interactions (i.e., correlated systems) are poorly described by DFT as they pose difficulties in accurately predicting their formation energies, intermolecular interactions, and transition states. To describe the behavior of these systems, one must consider the multi-determinant nature of the N-electron wave function and the multiple terms of the electronic interactions.

- ***DFT+U***

The DFT+U [168,169] method has been developed to improve the description of the ground state of correlated systems with a slightly higher computational cost than that of classical DFT calculations. The term "U" refers to the correction that can be added to the local and semi-local density functions (i.e., LDA+U, GGA+U...). The fundamental role of the U-correction is to treat the strong Coulombic interaction on the localized electron sites (d and f orbitals) with an additional Hubbard term while treating the rest of the valence electrons by the classical DFT approximations. Therefore, the total energy of the system (E_{GGA+U}) is the sum of the classical GGA energy for all states $E_{GGA}[\rho(r)]$ and the energy correction of the Hubbard function that describes the correlated states $E_{Hub}[\{n_{mm}^{I\sigma}\}]$. However, with the additive Hubbard term, there will be a double counting error for the correlated states; therefore, this term E_{dc} must be deduced from the total GGA energy to accurately describe the electronic interactions.

$$E_{GGA} + U[\rho(r)] = E_{GGA}[\rho(r)] + E_{Hub}[\{n_{mm}^{I\sigma}\}] - E_{dc}[n^{I\sigma}] \qquad \text{Eq 2.18}$$

Where $n_{mm}^{I\sigma}$ are the localized orbital occupancy numbers identified by the atomic site index I, the state index m, and by the spin σ.

2.2.4.5.a Use of DFT for periodic systems

- ✓ **Bloch's theorem**

The atoms in a perfect crystal are placed regularly to create a three-dimensional periodicity of space. Thus, the periodicity of the potential can be presented as follows[170]: $V(r + R) = V(r)$ where R is a linear combination of the vectors defining the periodic mesh. Due to this property, the wave function Ψ can be expressed as:

$$\Psi_K(r) = exp(ikr)u_k(r) \text{ with } u_k(r) = u_k(r+R) \quad \text{Eq 2.19}$$

Where k is a vector of the reciprocal space. This constitutes Bloch's theorem.

- ✓ **Plan waves**

In order to solve the Kohn and Sham equations in a practical way, it is necessary to develop the monoelectronic wave functions on a given basis. In the case of a periodic system, a plane wave basis set proves to be particularly well suited because the plane waves are themselves periodic. In this case, the wave function is written as:

$$\Psi_k(r) = \sum_{G<G_{max}} C_G \exp(i(k+G)r) \quad \text{Eq 2.20}$$

Where k and G are respectively a wave vector and a reciprocal grating vector. Systematic convergence can be achieved by increasing the number of plane waves, i.e., by increasing the value of G_{max}. This scheme is particularly effective when the plane wave description is combined with the use of pseudopotentials.

- ✓ **Pseudopotentials**

The electrons involved in chemical bonds are the valence electrons, while the so-called core electrons are relatively inert. The idea of pseudopotential methods is precisely to replace the interactions coming from the atomic nucleus and the core electrons by an effective potential, which allows to simplify the calculation and also to reduce considerably the calculation time. In our work, we have chosen to use the PAW (Projector Augmented Wave)[171,172] method which generalizes the pseudo potential method by allowing to completely reconstruct the density and the wave function.

2.2.4.5.b VASP code and main calculation parameters

- ✓ **VASP Code**

The VASP code is a periodic plane wave code[173,174]. It allows an extremely fast (80 jobs/h for 16 cores) and accurate resolution of the Schrödinger equation for systems with a large number of atoms, thanks to the use of specific pseudo-potentials such as "Projector Augmented Wave" PAW. This technique is adapted to the study of adsorption and reactivity of molecules in porous solids.

- ✓ **Geometry relaxation**

As we have seen previously, the DFT approach and its application through the Kohn-Sham equations allow to evaluate the total energy of a system for given atomic positions (fixed nuclei according to the Born-Oppenheimer approximation). In our calculations, a Gaussian smoothing function ($\sigma = 0.1$ eV)[175] was applied to ensure continuity of the electron density as it passes from the last occupied level (BV) to the first unoccupied level (BC). The Kohn-Sham equations were solved in a self-consistent field (SCF) process using the RMM-DIIS (Residual minimization scheme, direct inversion in the iterative subspace) electron minimization algorithm. The forces acting on the different atoms can be calculated according to the following equation:

$$F_i = -\frac{\partial E(R_1,\dots,R_N)}{\partial R_i} \qquad \text{Eq 2.21}$$

The Hellman-Feynman theorem states that the electron density can be kept constant when evaluating the forces acting on the different nuclei [176]. This property makes it possible to calculate the forces acting on the ions. Once these forces are determined, the atoms are then relaxed to obtain a new geometry and the Kohn-Sham equations are solved again. This scheme is repeated until the geometry corresponding to a minimum energy is obtained. In practice, the different studied configurations have been optimized until the forces exerted on each atom are lower than a certain threshold. The parameters responsible for the ab initio convergence (k-point mesh and cutoff energy) will be presented for each chapter.

2.3 Conclusion

Computing is a continuous balance between speed and accuracy since there is no complete calculation tool. Before any study, it is necessary to answer the following questions:

- What method should be used to meet the identified objectives?
- What is the best software to perform the simulation?
- The availability of a potential (FF) or a pseudo potential?
- Is there enough computer power to do the job?
- What size system will be affordable if computing resources are limited?

Indeed, there is no right or wrong method because each approach represents a different balance between computer efficiency, size of the tractable system, accuracy, and predictive power.

Chapter 3

Graphene based materials for fission gas detection (I_2 and ICH_3) in presence of contaminants (H_2O, CO and O_2): A Density Functional Theory approach.

"Every creation must be like graphene-strong, pristine and valuable. "

– Ira Periyavallur

This chapter is a draft of a work that has not yet been published.

3.1 Abstract

The development of rapid and efficient sensors for volatile radionuclides (I_2, ICH_3) detection after nuclear accidents or nuclear fuel reprocessing appears a necessity and current challenge for public safety. To this end, sensing performances of pristine and defected graphene, as well as Ag- and Cu-doped graphene monolayers have been investigated using periodic density functional theory calculations along with Grimme dispersion correction scheme D3(BJ), with respect to four important sensing criteria (selectivity, sensitivity, stability, and recovery time). Our results have revealed that pristine graphene, Cu-decorated pristine graphene and to a lesser extent Ag-doped monovacancy defected graphene are the best candidates for effective sensing of I_2 and ICH_3 in the presence of competing common air gases (H_2O, CO, O_2). Although copper-decorated pristine (Cu_PG) and silver-doped graphene (Ag_PG) showed a high recovery time (about 10^{14}s), we believe they are still of interest as disposable sensors and promising materials for iodine capture applications, due to their high selectivity and sensitivity.

3.2 Introduction

Efficient and prompt detection of volatile radionuclides during nuclear accidents and nuclear fuel reprocessing is a current challenge for public safety [14,177]. Among radioactive gas wastes, iodine compounds require special attention because they lead to serious health consequences and long-term environmental impacts. Two iodine radioisotopes are particularly dangerous, ^{131}I and ^{129}I.

The volatile and short-life isotope ^{131}I (half-life of ∼8.02 days) is a specific substrate of thyroid receptors and responsible for the long-term development of thyroid cancers. The highly volatile long-life isotope ^{129}I (half-life of ∼15 million years) can damage human cells and cause genetic mutations.[178,179] Additionally, in the environment, radioactive iodine I_2 interacts with hydrocarbons (methane CH_4) and other volatile organic compounds with producing methyl iodide ICH_3.[180] Hence, detection of volatile iodine I_2 and ICH_3 among air and volatile radionuclides in nuclear power stations requires highly selective and fast-response sensors.

Considering sensing devices, Metal Oxide Semiconductors (MOS) have been widely used for successfully sensing various gases due to their high sensitivity. However, their high operating temperature (>200 ºC) and poor selectivity limit their industrial applications for ambient air gas sensing [181]. Discovery of graphene (a monolayer of 2D carbon atoms) by mechanical exfoliation [182] introduced a sharp twist in the applicability of 2D nanomaterials. Since then, graphene has been extensively studied as an ideal solid-state chemical sensor because of its unique two-dimensional structure owing abundant adsorption sites, high surface area, excellent carrier mobility, high electrical conductivity, chemical stability, and tunable surface chemistry.[183,184] Schedin and co-workers[184] have been the first to explore exfoliated graphene as a gas sensor, and have claimed that its detection limit is down to the ppb level, which is comparable to the most sensitive sensors reported in 2007. Subsequently, various other groups have investigated pristine graphene for gas detection.[183,185]

Moreover, defects in graphene have gained significant attention because of their considerable effects on graphene fundamental properties, including chemical, electronic, mechanical, and magnetic properties.[186–189] These defects inevitably occur during production and transfer processes. In their experimental and theoretical study, Lee et al. [187] have reported that the presence of vacancies improves graphene sensitivity towards NH_3 and NO_2 gases by about 614% and 33%, respectively. Moreover, Ghaderi et al.[188] have revealed that hydroxyl adsorption on defected graphene is much stronger than for pristine graphene, and its dissociation occurs with a low energy barrier of about 0.2 eV, leading to the formation of stable ether groups with a strong magnetic character.

Various approaches allow the improvement of semiconducting properties of graphene by engineering its band gap.[190,191] Graphene doping with various atoms (e.g., Cu and Ag) is an efficient approach which affects sp^2 hybridization of carbon atoms and hence, tunes electronic properties of graphene.[192,193] So far, zeolites and metal organic frameworks (MOFs) have been widely used for the selective capture of the I_2 and ICH_3 gas molecules.[54,194,195] Chebbi et al.[196] have revealed that under extreme irradiation and humidity conditions, silver exchanged Y-type zeolite displays superior I_2 and ICH_3 adsorption properties, both in terms of working adsorption capacities and thermal stability of trapped iodine species. In a recent study, del Rio and co-workers[197] have indicated that silver-functionalization of UiO-66 metal-organic framework significantly enhances ^{131}I extraction capacity (~1 MBq/g) by comparison with standard UiO-66. Moreover, with a view to possibly replacing the high-cost silver-containing zeolites. Zhou and his coworkers [198] have shown that copper doping of zeolites accelerates iodine adsorption rate through strong copper-iodine interactions, especially with metallic copper Cu(0) rather than ionic copper Cu(I).

In the present work, density functional theory (DFT) calculations have been performed to predict the sensing ability of 9 graphene layers (i.e., pristine graphene layer, monovacancy and divacancy defected graphene as well as their corresponding Ag and Cu doped graphene layers) towards iodine species (I_2, ICH_3) in the presence of CO, H_2O and O_2 as competitive inhibitors. The present paper first investigates the interaction of I_2 and ICH_3 with the selected graphene monolayers and proceeds to unveil the most promising iodine gas sensors in respect to various key characteristics such as stability, thermodynamic and electronic selectivity, and short recovery time.

3.3 Computational and structure details

3.3.1 Computational settings

Our spin polarized DFT calculations[155,157] for the study of the interaction of iodine species (I_2, ICH_3) with the graphene monolayers were conducted with the Vienna *ab initio* simulation package (VASP).[173,174] We used the Perdew-Burke-Ernzerhof (PBE) functional within GGA approximation to describe the exchange–correlation interaction.[159] To effectively account for van der Waals (vdW) forces, different correction schemes were thoroughly examined and listed in detail in Table SI. The Grimme dispersion correction scheme (DFT-D3(BJ)) [161,162] resulted in the most reliable lattice parameters, and was therefore employed for the present study. All the studied structures were relaxed using the conjugate gradient method. The plane wave cut-off energy was set at 700 eV, the Kohn-sham self-consistent energy,[156] and the forces convergence criterion were set at 10^{-8} eV and 0.02 eV/Å per atom respectively.

The Brillouin zone sampling with Gamma centered mesh was set to 3 × 3 × 1 grid for geometry optimizations, a 12 × 12 × 1 for the density of state (DOS) calculations, and a K-path G-M-K-G for the band structure calculations. Besides, a number of grid points (NEDOS) was set to a very high value of 16,000 to get an appropriate fine DOS. These convergence criteria were justified by comparing our resulted band gap energy and density of states (DOS) of pristine graphene with previous studies,[199,200] at which the energy gap and density of states at Fermi level were almost zero.

To understand the interaction between the gas molecules and the graphene monolayer, the adsorption energy was calculated at 0K using the following equation:

$$\Delta E_{ads} = E_{(Graphene+guest)} - (E_{graphene} + E_{guest}) \qquad \text{Eq 3.1}$$

where $E_{(Graphen+guest)}$ is the total energy of the graphene monolayers with a single adsorbed gas molecule, $E_{graphene}$ and E_{guest} are the total energies of the graphene monolayers and the isolated gas molecule, respectively.

Similarly, the dispersion forces contribution ΔE_{disp} to the adsorption energy formula is defined as:

$$\Delta E_{disp} = E_{disp(Graphene+guest)} - (E_{disp(graphene)} + E_{disp(guest)}) \qquad \text{Eq 3.2}$$

To better understand the interaction of adsorbed gas molecules with graphene monolayers, the charge density difference ($\Delta\rho$) and charge transfer (ΔQ) were determined. The charge transfer upon adsorption of the gas molecules is examined using the Bader charge analysis [201–203] from the differences in the charge concentrations before and after adsorption with :

$$\Delta Q = Q_{Graphene+guest} - (Q_{graphene} + Q_{guest}) \qquad \text{Eq 3.3}$$

And the charge density difference (CDD) was visualized by the VESTA code [204] with :

$$\Delta\rho = \rho_{Graphene+guest} - (\rho_{graphene} + \rho_{guest}) \qquad \text{Eq 3.4}$$

Where $\rho_{Graphene+guest}$, $\rho_{graphene}$ and ρ_{guest} are the charge density of a gas adsorbed on the graphene monolayer, that of the graphene monolayer, and that of an isolated gas molecule, respectively.

Ab initio molecular dynamics (AIMD) simulations including the Grimme D3(BJ) correction[161,162] were performed to study the thermal stability of graphene monolayers. These simulations were performed using a Nose-Hoover thermostat[205,206] during 20 ps at 300 K with a time step of 1 fs. Regarding the computational cost of the AIMD simulations, the plane wave kinetic energy cutoff and the convergence energy difference criterion between cycles were reduced to 400 eV and 10^{-5} eV, respectively.

3.3.2 Structures investigated

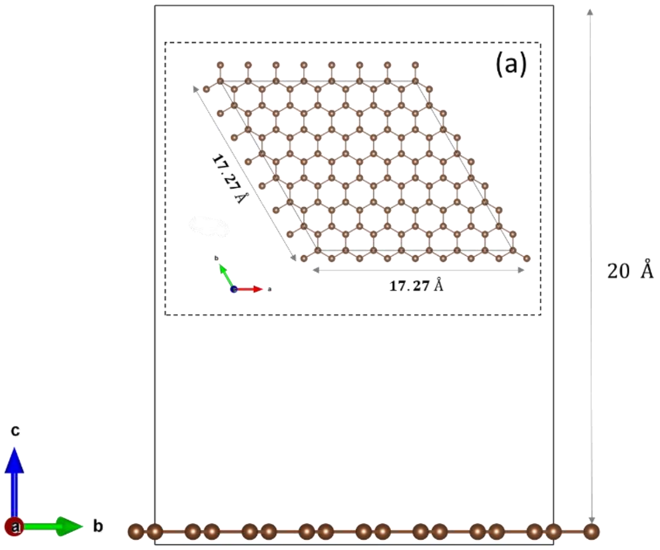

Figure 3.1: Illustrations of the optimized graphene 7x7 supercells, a) top view.

The optimized structure of the pristine graphene monolayer (PG) is shown in Figure 3.1. A 7x7 supercell of pristine graphene with 98 carbon atoms and 20 Å between the graphene layer and its image along the c axis was considered. The calculated bond length (C-C) and bong angle (C-C-C) are 1.42 Å and 120º respectively, in agreement with previously reported values.[207,208] The optimized atomic structures of vacancy-defected graphene are shown in Figure 3.2, with monovacancy graphene (MG) obtained by removing one carbon atom from PG, while for divacancy graphene (DG) a neighboring atoms pairs were removed.

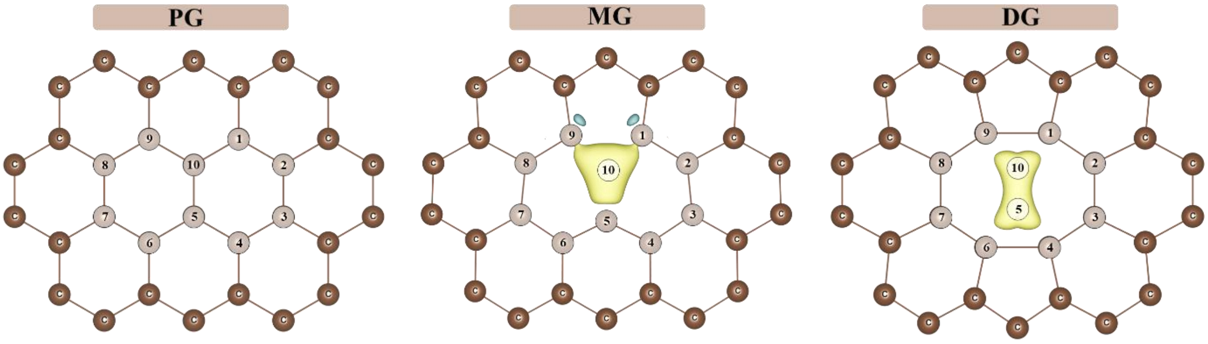

Figure 3.2: Optimized structures of the PG (left column), MG (middle column) and DG (right column).

The calculated (C-C) bond lengths around the defected sites are listed in Table 3.1. Carbon 1 and carbon 9 tend to from an extended C-C bond and found to be shortened from 2.47 Å in PG to 2.01 Å and 1.70 Å for MG and DG, respectively. This is in agreement with reported studies indicating the value of 2.02 Å and 1.80 Å for MG and DG, respectively.[209,210] The Bader charges values are shown in Table 3.1, the calculation revealed a homogenous charge distribution on all carbon atoms of the PG, while an increase in density is observed between atoms 1-9 for MG and 1-9; 4-6 for DG, indicating a weak covalent bond formation (Figure 3.2)

Table 3.1: Calculated carbon-carbon distance and carbon atomic charge in the three graphene layers.

	PG	***MG***	***DG***
(Carbone - Carbone) Distance (Å)			
C1−C2	1.42	1.47	1.45
C1−C9	2.47	2.01	1.70
C1−C4	2.85	3.00	3.11
C1−C5	2.47	2.59	-
Bader Charge |e|			
C1	0.04	-0.08	-0.02
C5	0.04	-0.11	-
C9	0.04	-0.02	-0.01

The optimized structures of (Ag and Cu) doped graphene monolayers are illustrated in Figure 3.3. On the pristine graphene, three different sites were considered for the adsorption of the metals, Top site (top of carbon atom), Hollow (center of the carbon hexagon) and bridge (center of C-C bond). After relaxation, our results revealed that the hollow site was more favorable for Ag adsorption, while for Cu, the top position was energetically preferable. The metal atoms adsorb at 2.94 and 2.15 Å from the PG plan for Ag and Cu, respectively. These results are in agreement with previous finding, where the Ag metal atom found to adsorb on the hollow site of the graphene monolayer at 2.90 Å, while the Cu metal atom settled on the upper site at 2.11 Å.[211]

On the monovacancy graphene (MG), because of the difference in atomic radii of these two metal atoms (Ag: 165 pm; Cu: 145 pm) compared to that of the C atom (67 pm). The adsorption of these metals on the monovacancy graphene (MG) induced a lattice distortion near the defected site, both atoms protrude out of the plane by 2.20 and 1.64 Å for Ag and Cu, respectively. As shown in Figure 3.3, upon adsorption both metal atoms interact with three neighboring carbon atoms at an average distance of 1.98 and 1.87 Å for Ag and Cu, respectively, in agreement with the values reported by D. Düzenli ($Ag - C = 2.18$ Å and $Cu - C = 1.91$Å).[212] As for the case of adsorption of metals on the divacancy graphene (DG), the removal of two carbon atoms creates a sufficiently large vacant site for the metal atoms, making possible Ag and Cu to retain the planar form of the graphene layer. The optimized bond lengths of C-Ag and C-Cu are calculated to be 2.27 and 1.90 Å, respectively.

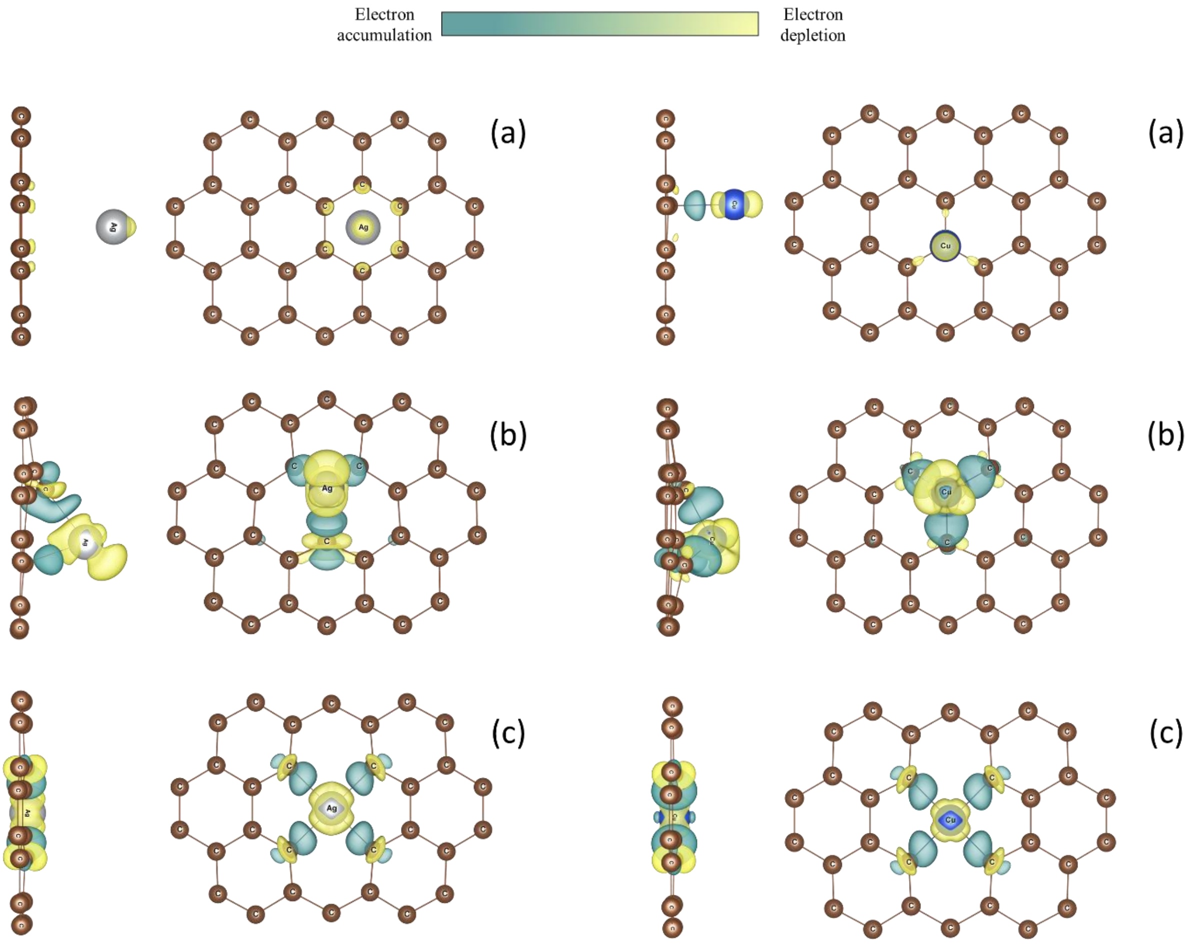

Figure 3.3: Optimized structures of the Ag (left column) Cu (right column) doped a) PG b) MG and c) DG graphene monolayers. The brown, gray, and blue spheres represent Carbon (C), Silver (Ag) and Copper (C) atoms respectively.

3.4 Results and discussion

3.4.1 Adsorption of iodine species on pristine graphene and vacancy-defected graphene layers

Adsorption of I_2 and ICH_3 gas molecules on pristine graphene and vacancy-defected graphene layers has been investigated through theoretical determination of adsorption energies (E_{ads}), minimum adsorption distances (d_{min}) and Bader charge transfer (Δq) (Table 3.2). Various molecule orientations (in-plane and perpendicular to plane) have been assessed onto hollow, bridge, and top sites of graphene layer. The most stable configurations have been identified and later discussed.

Table 3.2: Calculated adsorption energies (Eads), minimum adsorption distances (dmin) and charge transfer (Δq) between gas molecules and graphene layers. PG, MG, and DG are for pristine graphene, monovacancy graphene and divacancy graphene, respectively.

		d_{min} (Interacted molecule atom) (Å)	**E_{ads} (E_{disp})** (kJ/mol)	**Bader Charge Difference** Molecule $\lvert e^- \rvert$
I_2	PG	3.88 (I)	−30.3 (−35.5)	-0.018
	MG	2.30 (I)	−91.9 (−31.3)	0.189
	DG	3.80 (I)	−32.6 (−36.1)	0.035
ICH_3	PG	2.87 (H)	−26.7 (−29.4)	0.006
	MG	3.14 (I)	−31.0 (−24.0)	0.022
	DG	3.81 (I)	−25.6 (−27.1)	0.017

Our investigation revealed that the influence of the adsorbed molecules on the pristine graphene (PG) structure is negligeable, the calculated bond lengths (C-C) and bong angles (C-C-C) were not significantly varied. Gas molecules adsorb weakly on PG, with adsorption energies of -30.3, and -26.7 kJ/mol for I_2 and ICH_3 respectively, including -35.5 and -29.4 kJ/mol of vdW contributions showing that adsorption is mainly directed by long-range dispersion contributions (Table 3.2). This weak adsorption is in line with calculated molecule-PG monolayer distances of 3.88 and 3.00 Å, respectively. Rudenko et al [213] reported similar results for I_2 adsorption on pristine graphene, indicating that iodine molecule adsorbs on a planar mode at a distance of 3.83 Å, as shown with our results in Figure 3.4.

The results from the molecular interaction on the monovacancy graphene (MG) were significantly stronger over that of pristine graphene (PG). It appears that the unsaturated dangling bonds of graphene are highly reactive and interact strongly with the gas molecules. The adsorption of I_2 and ICH_3 has led to a small geometry deformation at the defected site with the carbon atom being slightly lifted and bent towards the iodine species, resulting in a strong interaction. Gas molecules adsorb on the defected site at a short distance of 2.30 and 3.14 for I_2 and ICH_3 with corresponding adsorption energies of -91.9 and -31.3 kJ/mol respectively, including -31.3 and -24.0 kJ/mol of dispersion contribution. For divacancy defected graphene (DG), adsorption of I_2 and ICH_3 gas occurs without any geometric distortion around the defective site. The gas molecules adsorb weakly with an interaction energy of -32.6 and -25.6 kJ/mol at a distance of 3.54 and 3.81 Å, respectively (Table 3.2).

To evaluate charge transfers between the graphene monolayers and adsorbed gas molecules, the Bader charge difference (Δq) has been calculated and reported in Table 3.2 and the charge density difference (CDD) has been computed using Eq. 3.4 and plotted in Figure 3.4. A negative (Δq) means a charge transfer from the graphene monolayers to the adsorbed gas molecules, and a positive (Δq) implies the charge transfer in the opposite direction.

Bader charge analysis reveals a weak charge transfer of 0.018 and 0.006 |e| respectively between PG and adsorbed molecules of I_2 and ICH_3. Similarly, the CDD maps predict no electron orbital overlap between gas molecules and PG. These results together with the low adsorption energies and the long adsorption distances confirm the weak physisorption of I_2 and ICH_3 on PG monolayer. Introduction of C defect into the GM remarkably enhances the charge transfer. Iodine species (I_2, ICH_3) forward, respectively 0.189 and 0.022 |e| to the sensing material. This strong chemical adsorption is confirmed by the significant overlap in charge density difference map in Figure 3.4. With divacancy defected graphene, iodine species (I_2, ICH_3) act as donors with a small electron transfer towards DG material of 0.035 and 0.017 |e|, respectively.

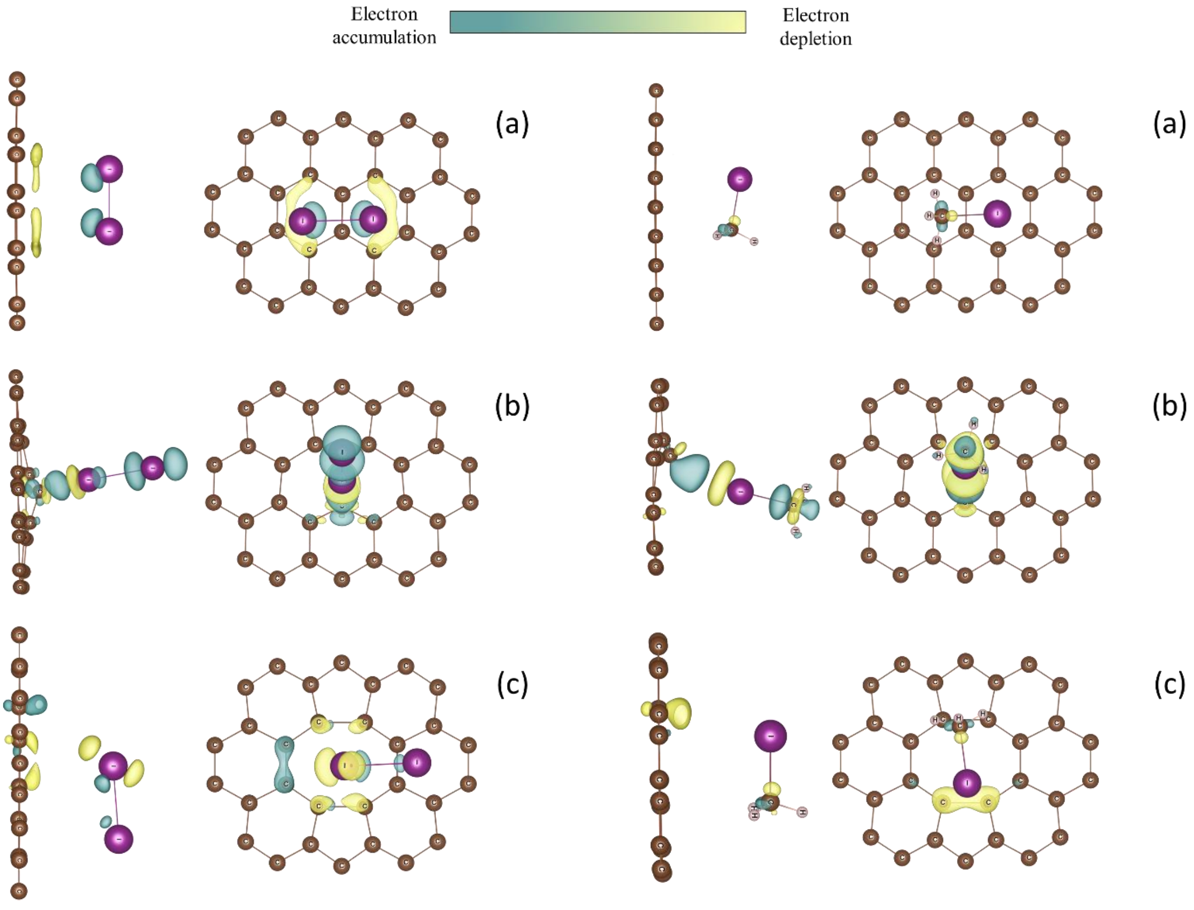

Figure 3.4: Optimized structures with charge density difference for I_2 (left column) and ICH_3 (right column) adsorption on a) PG b) MG and c) DG. Brown, purple, and gray spheres represent Carbon (C), Iodine (I) and Hydrogen (H) atoms respectively. The iso-surface of CDD maps is set as 0.05 e/Å^3.

3.4.2 Ag and Cu doped graphene layers

As has been indicated so far, the high structural stability of graphene confers the adsorbent a low sensitivity towards gas molecules. In addition to vacancy defect sites, adding adatoms is one of the main promising methods to increase graphene sensitivity towards gas molecules. The present part of the work shows the stability of Cu and Ag deposited in pristine graphene (PG), monovacancy graphene (GM) and divacancy graphene (GD) respectively. Adsorption of gas molecules has been examined after optimization of all surfaces. Molecules have been tested in various orientations and the most stable adsorption configurations have been determined.

3.4.2.1 Adsorption of iodine species on Ag doped graphene

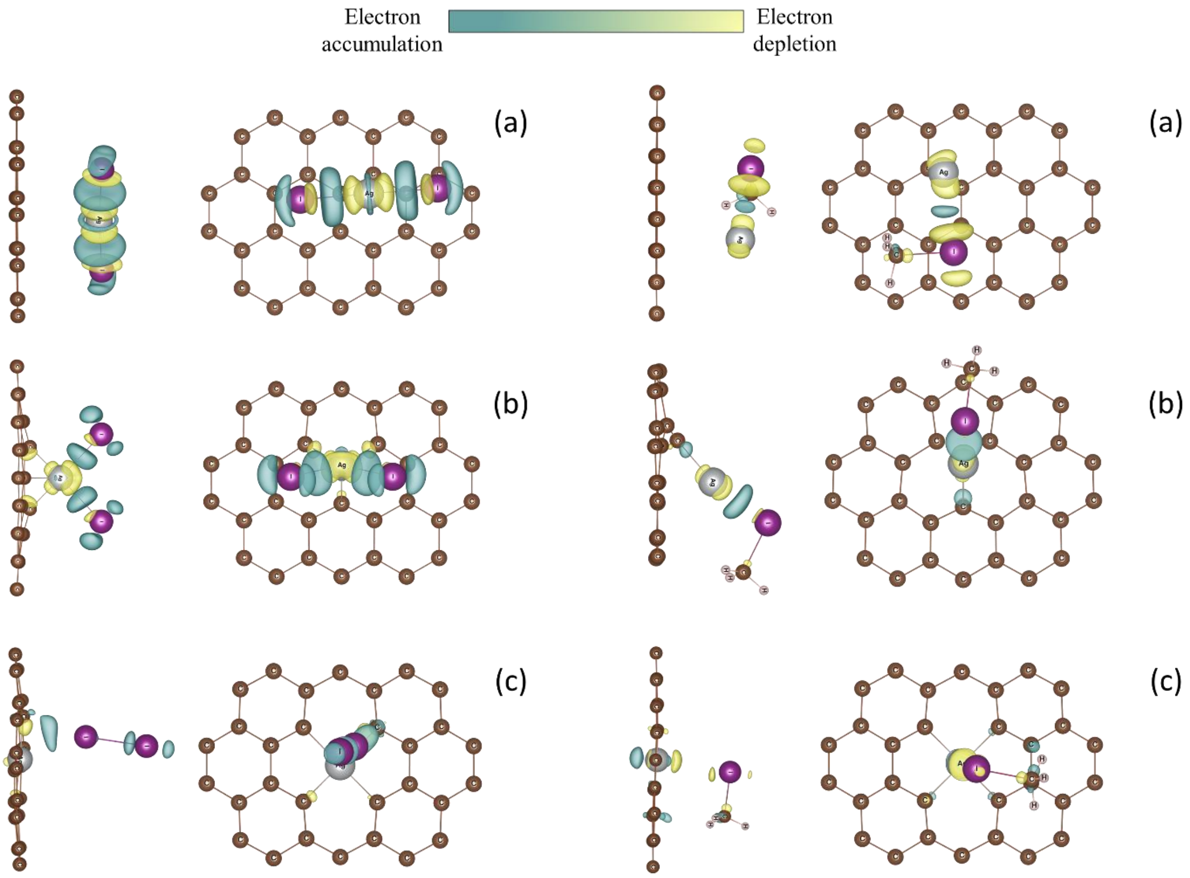

Figure 3.5: Optimized structures with charge density difference for I_2 (left column) and ICH_3 (right column) adsorption on a) Ag_PG b) Ag_MG and c) Ag_DG. Brown, purple, silver, and gray spheres represent Carbon (C), Iodine (I), Silver (Ag) and Hydrogen (H) atoms respectively. The iso-surface of CDD maps is set as 0.04 e/$Å^3$.

Our results show that the presence of the Ag atom upon the graphene monolayer significantly strengthens the interaction of the gas molecules by comparison with pristine graphene. Iodine molecule I_2 strongly interacts with the Ag_PG and Ag_MG monolayers, with an adsorption energy of -249.5 and -216.0 respectively (Table 3.3). This high E_{ads} results from I_2 dissociation into two I atoms interacting with the silver metal atom at 2.58 and 2.69 Å, respectively (Figure 3.5). The formation of silver iodide (AgI) upon the interaction of Ag with I_2 has been observed and reported previously.[214] However, on the GD monolayer where the Ag metal atom is unexposed, Ag adsorbs I_2 in the molecular form, with a weak adsorption energy of -48.2 kJ/mol at 3.15 Å (Table 3.3). These results of adsorption energies and minimum adsorption distances are well correlated with charge transfer calculations. Indeed, I_2 dissociation and AgI formation of the Ag_PG and Ag_MG graphene monolayers generate a significant amount of charge transfer of about -0.48 and -0.68|e| respectively, while a lower charge transfer of -0.11 |e| was gained by I_2 when adsorbed on Ag_DG.

For ICH_3 molecule, adsorption occurs without molecular dissociation, and the strongest interaction is observed between Ag_MG monolayer and the iodine atom of ICH_3 with an adsorption energy of -109 kJ/mol and a minimum adsorption distance of 2.67 Å (Figure 3.5). Ag_PG and Ag_DG showed low sensitivity towards ICH_3 gas molecule, with low adsorption energies of -42 and -31 kJ/mol, and long adsorption distances of 3.03 and 3.50 Å respectively (Table 3.3), indicating the physisorption of ICH_3 on these surfaces. Moreover, charge transfer analysis confirms these results. Interaction of ICH_3 with Ag_MG leads to the highest charge transfer of about 0.19 |e| while a weak charge transfer is observed for its interaction with Ag_PG and Ag_DG (Table 3.3).

Table 3.3: Calculated adsorption energies (Eads), minimum adsorption distances (dmin), placement distances of Ag deposited on the substrates (Ag-C) and charge transfer (Δq) between the gas molecules and graphene layers.

		d_{min} (molecule atom) (Å)	Ag-C (Å)	**E_{ads} (E_{disp})** (kJ/mol)	**Bader Charge Difference** Molecule $\|e^-\|$
I_2	Ag_PG	2.58 (I1) / 2.58 (I2)	3.61	−249.5 (−31.9)	-0.488
	Ag_MG	2.69 (I1) / 2.69 (I2)	2.11	−216.0 (−42.2)	-0.684
	Ag_DG	3.15 (I1) / 3.15 (I2)	2.00	−48.2 (−28.2)	-0.012
ICH_3	Ag_PG	3.03 (I) / 3.47 (C)	3.34	−42.0 (−26.5)	-0.094
	Ag_MG	2.67 (I) / 3.65 (C)	3.31	−109.3 (−30.3)	-0.198
	Ag_DG	3.50 (I) / 3.95 (C)	1.98	−31.7 (−32.6)	-0.047

3.4.2.2 Adsorption of iodine species on Cu doped graphene

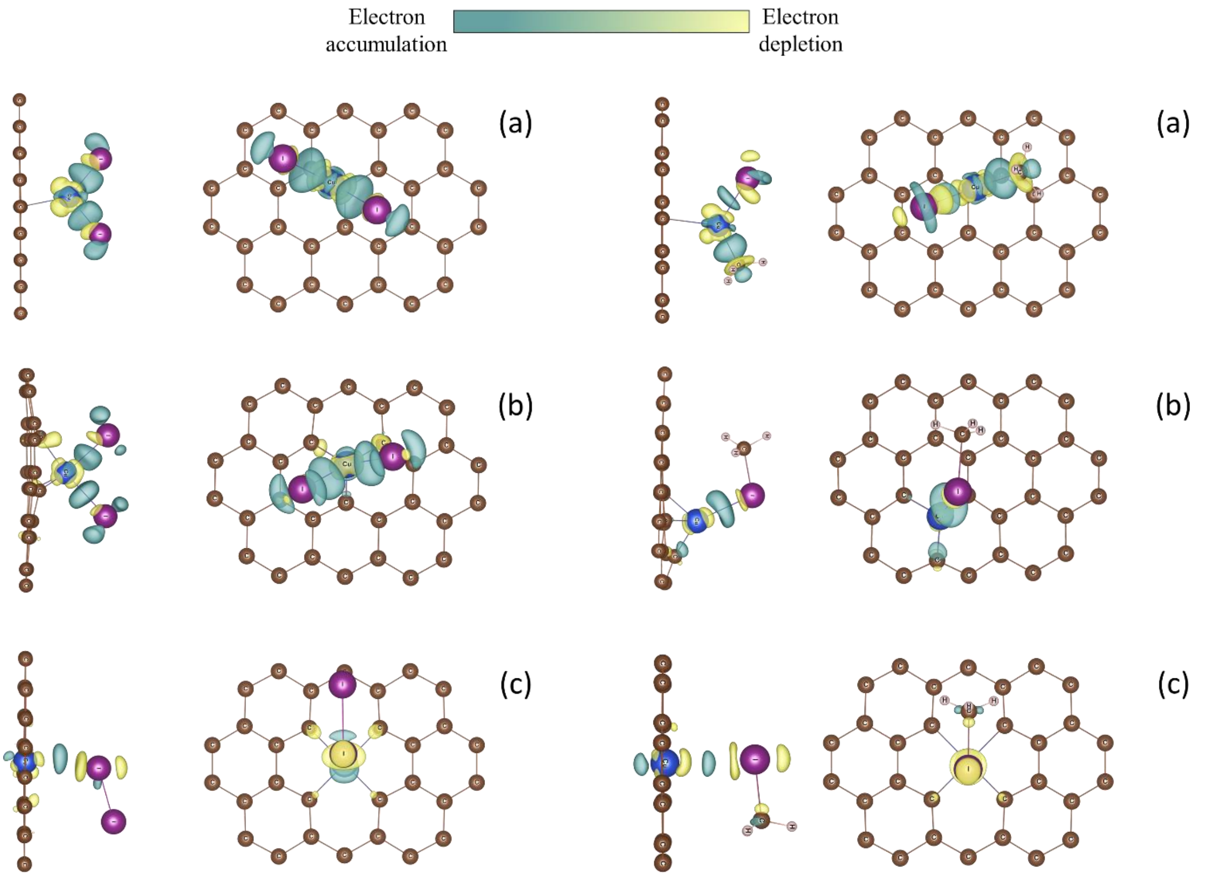

Figure 3.6: Optimized structures with charge density difference for I2 (left column) and ICH3 (right column) adsorption on a) Cu_PG b) Cu_MG and c) Cu_DG. Brown, purple, blue, and gray spheres represent Carbon (C), Iodine (I), Copper (Cu) and Hydrogen (H) atoms respectively. The iso-surface of CDD maps is set as 0.04 e/Å^3.

The presence of Cu on graphene monolayers further strengthens the interaction of iodine species on those surfaces. Copper-decorated pristine graphene is highly reactive and interacts strongly with the I_2 and ICH_3, leading to a spontaneous dissociation of the two iodine molecules and the the formation of CuI species.[215] Gas molecules interact with Cu atom at a small distance of 2.44/2.44 Å for $(\mathrm{I}-\mathrm{Cu}-\mathrm{I})$ and 2.43/1.94 Å for $(\mathrm{I}-\mathrm{Cu}-\mathrm{CH_3})$ respectively. Adsorption energies (together with charge transfer) were significantly high of about -316.7 kJ/mol (-0.59|e|) and -201.5 kJ/mol (-0.53|e|) for I_2 and ICH_3, respectively (Table 3.4). On Cu_MG, I_2 unlike ICH_3, dissociates spontaneously. The two molecules interact with the copper at a distance of 2.55 Å leading to high adsorption energies of -196.2 and -88.8 kJ/mol for I_2 and ICH_3, respectively. Bader charge calculations show a significant charge transfer from graphene monolayer to I_2 and ICH_3 of 0.62|e| and 0.12|e| respectively (Table 3.4). On the other hand, Cu_DG shows no structure deformation, and Cu remains fully attached to the defected site carbons (Figure 3.6). This results in the absence of molecular dissociation along with low adsorption energies of about -42 and -37 kJ/mol at a distance of 3.10 and 3.11 Å for I_2 and ICH_3, respectively. These findings together with the resulted weak charge transfer of 0.02|e| and 0.07|e| respectively, provide insight into the physisorption of these iodine molecules on the Cu_DG monolayer.

Table 3.4: Calculated adsorption energies (Eads), minimum adsorption distances (dmin), placement distance of the Cu on doped substrates (Cu-C) and charge transfer (Δq) between gas molecules and graphene layers.

		d_{min} (molecule atom) (Å)	Cu-C (Å)	**E_{ads} (E_{disp})** (kJ/mol)	**Bader Charge Difference** Molecule $\|e^-\|$
I_2	Cu_PG	2.44 (I1) / 2.44 (I2)	2.99	−316.7 (−39.0)	-0.590
	Cu_MG	2.55 (I1) / 2.55 (I2)	1.99	−196.2 (−46.1)	-0.619
	Cu_DG	3.10 (I1) / 3.10 (I2)	1.90	−42.2 (−40.9)	-0.026
ICH_3	Cu_PG	2.43 (I) / 1.94 (C)	2.46	−201.5 (−33.0)	-0.537
	Cu_MG	2.55 (I) / 3.73 (C)	1.95	−88.8 (−34.1)	-0.122
	Cu_DG	3.11 (I) / 3.85 (C)	1.90	−37.9 (−34.5)	-0.074

3.5 Selection of the most promising sensing material

A good gas sensor must satisfy several key requirements, namely stability, sensitivity, selectivity, and good recovery time. Therefore, these parameters have been determined for all previously studied graphene layers to identify the optimal sensor for I_2 and ICH_3 gases in the presence of H_2O, CO and O_2 gases.

3.5.1 Thermodynamic selectivity

Thermodynamic selectivity depends on the affinity of a sensor for a substrate. The higher the interaction energy, the stronger the affinity and thermodynamic selectivity of a sensor for the substrate. Interaction energies have been reported for all studied systems in Figure 3.7. Knowing that in nuclear fuel reprocessing plants, iodine species concentrations are much lower than those of contaminants, the sensor needs therefore to have a much higher affinity for I_2 and ICH_3 than for CO, H_2O and O_2.

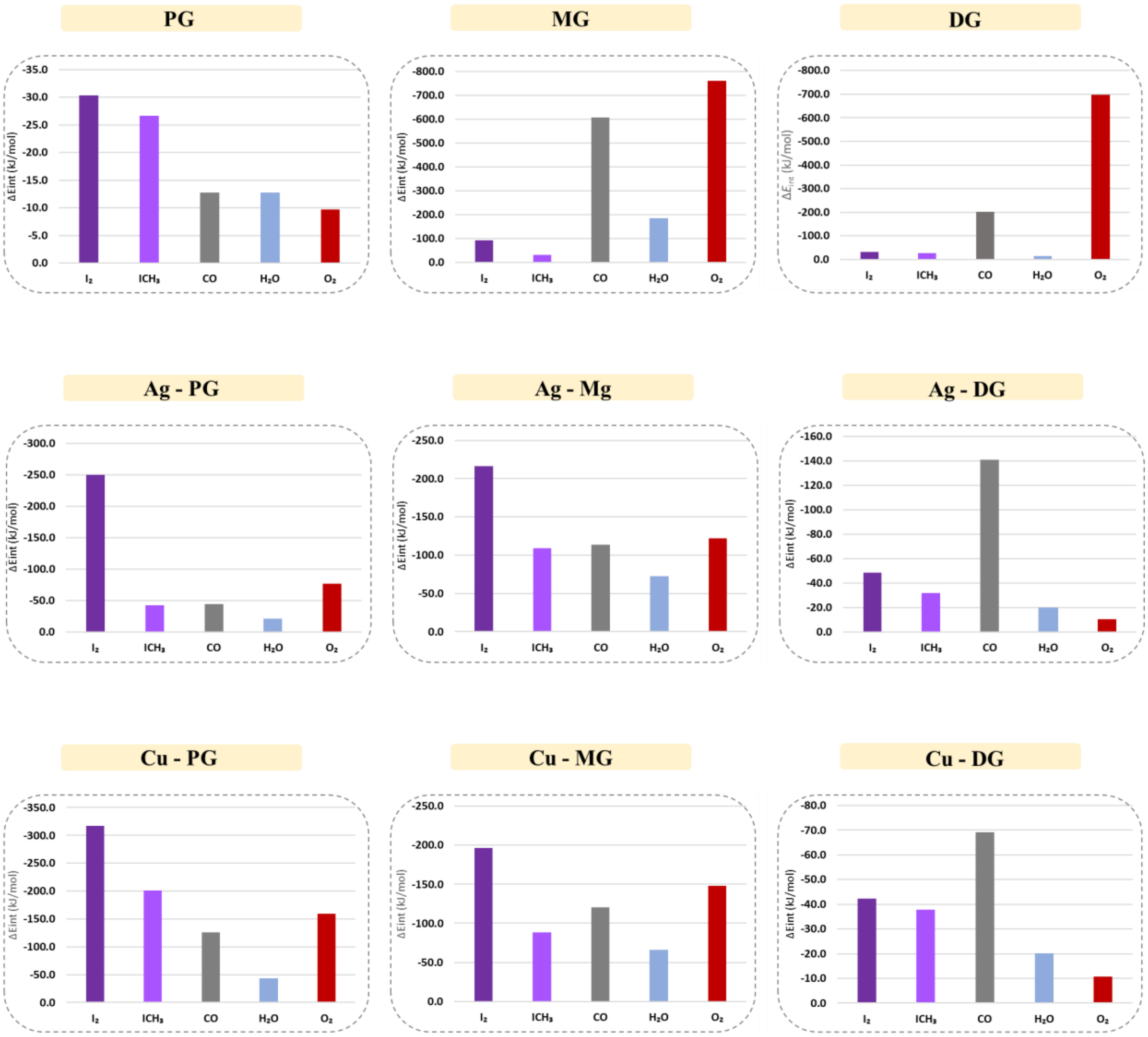

Figure 3.7: The total interaction energies of graphene monolayers with I2, ICH3, CO, H2O and O2, calculated using the PBE + D3(BJ) level of theory.

Pristine graphene (PG) monolayer exhibits a higher affinity for I_2 and ICH_3 than for CO, H_2O and O_2 (Figure 3.7), indicating that this material is suitable for a selective adsorption of iodine species. Defects on graphene (MG and DG) have shown a favorable interaction with CO and O_2, with a dissociation of the two atoms during adsorption followed by a merging near the vacancy to occupy the empty defected site. Therefore, MG and DG graphene monolayers are poor sorbents for I_2 and ICH_3, and unsuitable for the intended sensing application.

Considering silver-doped graphene monolayers, Ag_PG and Ag_MG monolayer exhibit a higher or equivalent affinity for O_2 and H_2O than for ICH_3 respectively, but much higher affinity for I_2 than for other gas molecules. This means that water and oxygen are expected to play a detrimental role on the ICH_3 adsorption. Therefore, Ag-doped PG and MG monolayers could be appropriate only for selectively adsorb I_2 in the presence of other contaminants. On the other hand, Ag_DG exhibits a higher affinity for CO than for I_2 and ICH_3, which negates its ability to correctly detect the iodinated species.

Cu_PG is the only monolayer showing a higher affinity for I_2 and ICH_3 than for all other contaminants. Therefore, CO, H_2O and O_2 are not expected to play a negative role on the adsorption of these two iodine species. Cu_MG interacts strongly with CO and O_2 than with ICH_3 and only exhibits a higher affinity for I_2 than other gas molecules. Cu_DG exhibis a higher affinity for CO than for I_2 and ICH_3. These results reveal that in terms of thermodynamic selectivity (Figure 3.7), PG, Cu_PG and to a lesser extend Ag_MG are clearly the most interesting graphene monolayers for the selective capture of I_2, ICH_3 in presence of CO, H_2O and O_2. Therefore, their performances regarding electronic sensitivity, recovery time and stability will be further discussed.

3.5.2 Thermal stability

AIMD simulation has been performed for determining the thermal stability of the selected systems (i.e., PG, Ag_MG and Cu_PG) at room temperature (300K). Figure 3.8 shows the time evolution of the total potential energy fluctuation during 20 ps with a time step of 1 fs, with geometric structures at the end of AIMD simulations (after 20 ps) for I_2 and ICH_3 adsorbed on the three graphene monolayers. Meanwhile, Table 3.5 present a bond length analysis of the final configurations for I_2, ICH_3 adsorption on Ag_MG and Cu_PG. The results show that there is no broken bonds or significant structural distortion. The planar structure of graphene is well maintained and no atomic shift in the z-direction was observed.

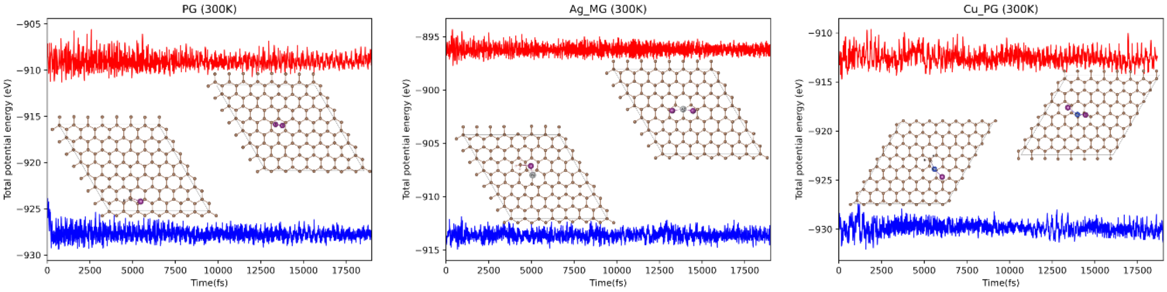

Figure 3.8: Fluctuations of total potential energy of I_2 (red) and ICH_3 (blue) adsorbed on PG, Ag_MG and Cu_PG during AIMD simulations of 20ps at 300 K. Insets represent the snapshots of I_2 (up) and ICH_3 (down) adsorption at the end of simulations.

In addition, all our previous final configurations revealed by the DFT calculations at 0K were preserved at 300K, With Ag-MG, AgI formation was only possible upon I_2 adsorption while ICH_3 adsorbs in its molecular form. In contrast, with Cu_PG, both I_2 and ICH_3 adsorption led to the CuI formation. After full relaxation, measured bond lengths were similar to our previous determination at 0K, with the exception of the copper that drifts away by 5Å from graphene surface upon I_2 adsorption, by comparison with a drift distance of 3 Å at 0K. This indicates that the three graphene monolayers are thermally stable at room temperature.

Table 3.5: Measured bond lengths (Å) after I_2, ICH_3 adsorption on Ag_MG and Cu_PG at 300K.

	$Ag-C$(Graphene)	$Cu-C$(Graphene)	I(molecule)$-Ag$	I(molecule)$-Cu$
I_2@Ag_MG	2.11	-	2.64	-
ICH_3@Ag_MG	2.14	-	2.67	-
I_2@Cu_MG	-	5.04	-	2.33
ICH_3@Cu_MG	-	2.24	-	2.29

3.5.3 Recovery time of graphene monolayers

The recovery time (τ) being the time required to desorb gas molecules from the surface of nanoplatelets, allows the prediction of the performance of a sensor. τ is exponentially related to the adsorption energy through the conventional transition state theory as follows.

$$\tau = \frac{1}{\vartheta_0} \exp\left(\frac{-E^*}{K_B T}\right) \qquad \text{Eq 3.5}$$

where T is the temperature in K, ϑ_0 is the attempt frequency, K_B is the Boltzmann's constant and E^* is the desorption energy barrier which is equivalent to the adsorption energy[216]. The above equation implies that the higher adsorption energy suffers from a longer recovery time. Experimentally, Schedin et al.[184] revealed that graphene sensors can be recovered from gas molecule adsorption (NH_3, CO, H_2O and NO_2) through vacuum annealing at 150 °C. Furthermore, they pointed that a short-time ultraviolet (UV) irradiation offers a good alternative to thermal annealing. Additionally, Peng et al.[217] applied an attempt frequency of ($\vartheta_0 = 10^{12} s^{-1}$) for studying carbon nanotubes as NO_2 gas sensors. In order to assess a suitable recovery time, different attempt frequencies (10^{12}, $8.10^{14} s^{-1}$(UV)) and temperatures (300, 400, 500 K) have been applied in the present work. Obtained results are listed in Table 3.6. Our results predict that because of the weak interaction between I_2, ICH_3 and pristine graphene monolayer, PG recovers from the iodine molecules adsorption in a very short time, in the range of micro to nanoseconds for both molecules at room temperature. For Ag_MG, the calculated recovery time for ICH_3

adsorption was set to several days under vacuum at a room temperature. With UV irradiation at the same temperature (T=300K), the predicted recovery time was reduced to 2 hours. Whereas, increasing the temperature to 500K in vacuum resulted in a suitable recovery time of 0.1 sec. For I_2@Ag_MG, I_2 and ICH_3@Cu_PG since spontaneous molecule dissociation and strong binding energies were observed, the predicted recovery time was found to be in the order of ($>10^{14}$ s) and remains high of the order of ($>10^{9}$ s), even at higher temperature (500K). This recovery time is unsuitable for practical applications. However, despite such a high recovery time, Ag_MG and Cu_PG are still of interest as single use (disposable) sensors. In fact, as these sensors, are cost-effective and easy to use, they are a practical alternative to the reusable ones. To date, disposable graphene-based sensors have been widely used in many industrial applications[218–220], and will be extremely useful in the areas of hazardous materials handling by offering an additional protection. Y. Ting et al [220] reported Ag-doped graphene as a novel disposable sensor for detection polar antibiotics using Electrophoretic Preconcentration and Surface-Enhanced Raman Spectroscopy (EP-SERS) technique.

Table 3.6: Calculated recovery time (in second) of adsorbed gas iodine molecules on the selected graphene monolayers at different frequencies (in s−1) and temperatures (in K).

Frequency (ϑ_0)	$\mathbf{10^{12}}(s^{-1})$			$\mathbf{8.10^{14}}(s^{-1})$
Temperature (T)	**300 K**	**400 K**	**500 K**	**300 K**
I_2@PG	$3.7.10^{-7}$	$1.5.10^{-8}$	$2.2.10^{-9}$	$4.6.10^{-10}$
ICH_3@PG	$7.3.10^{-8}$	$4.4.\ 10^{-9}$	$8.3.10^{-10}$	$9.1.10^{-11}$
I_2@Ag_MG	$1.5.10^{25}$	$7.6.10^{15}$	$2.0.10^{10}$	$1.9.10^{22}$
ICH_3@Ag_MG	$7.1.10^{6}$	$1.4.10^{3}$	0.10	$8.9.10^{3}$
I_2@Cu_PG	$2.8.10^{43}$	$3.8.10^{29}$	$1.9.10^{21}$	$3.5.10^{40}$
ICH_3@Cu_PG	$3.1.10^{23}$	$4.2.10^{14}$	$2.0.10^{9}$	$3.9.10^{20}$

3.6 Conclusions

In summary, the adsorption of I_2, ICH_3 gas molecules on PG, MG, and DG as well as on these monolayers doped with Ag and Cu was investigated by DFT calculations. A detailed geometrical analysis of the adsorption of iodine gas species revealed that except for DG and DG doped with Ag and Cu that displayed a moderate adsorptions energy, all of the other systems exhibited a strong tendency to adsorb iodine molecules with significant charge transfer. However, upon examination of the thermodynamic selectivity of these monolayers to adsorb I_2 and ICH_3 in the presence of H_2O, CO and O_2, only the PG, Cu_PG and, to a lesser extent, Ag_MG monolayers achieved an advantageous selectivity.

Chapter 4

Potential of nanostructured carbon materials for iodine detection in realistic environments unraveled by first−principles calculations

"Life exists in the universe only because the carbon atom possesses certain exceptional properties. " **– James Jeans**

This chapter is a draft of a work that has not yet been published.

4.1 Abstract

An effective detection of iodine species (I_2, ICH_3) mainly formed in nuclear power plants and nuclear fuel reprocessing facilities is vital for the development of the nuclear industry and for human safety. We perform a comparative study of potential sensing performance of four expectedly promising 2D materials (*8−Pmmn* borophene, BC_3, C_3N, and BC_6N towards the above-mentioned iodine-containing gases and, in view of checking selectivity, towards common inhibiting gases in the containment atmosphere (H_2O and CO), applying dispersion-corrected density functional theory.

A covalent is formed between the CO molecule and the boron in BC_3 or in *8−Pmmn* borophene materials, compromising the anticipated applicability of these materials for iodine sensing. The presence of nitrogen atoms in BC_6N-2 prevents the formation of a covalent bond with CO; however, the closeness of adsorption energies for all the four gases studied does not distinguish this material as specifically sensitive to iodine species. Finally, the energies of adsorption on C_3N yield a significant and promising discrimination between the adsorption energies of (I_2, ICH_3) vs. (CO, H_2O), opening perspectives for this material's use as iodine sensor. The conclusions are supported by simulations at finite temperatures; underlying electronic structures are also discussed.

4.2 Introduction

The release of volatile iodine fission products such as I_2 and ICH_3 from nuclear power plants or fuel reprocessing facilities [221–223] is dangerous for human health due to these products' relatively easy assimilation by thyroid.[224] Many efforts are made to confine these species and limit their spread in the environment. In this context, the development of sensors for an accurate detection of iodine species is of utmost importance for safety of the population. The suitability for iodine detection of various materials such as metal−organic frameworks,[225,226] polymers,[227] or metal−oxide sensors[54] for iodine detection has been explored. Even if these sensors demonstrate good sensitivity, fact that their operating temperatures need to be quite high makes them expensive to employ and to maintain.[54] In addition, the sensor operation at elevated temperatures may degrade the long−term stability, reduce the sensitivity, and even modify the morphology of the sensor.[55] Therefore, new alternatives, i.e., carbon nanomaterials, have been explored as gas sensors to overcome these limitations.[228,229] During the past decades, the research on carbon−based two−dimensional nanomaterials, e.g., graphene and graphene−like materials, have attracted tremendous attention due to their exceptional physical and chemical properties.[230] Notably, their huge surface−to−area ratio, high chemical, and mechanical stability along with the tunability of band gap make these materials promising as sensors to detect different gases. In fact, carbon nanofibers have been already tested for iodine detection.[231,232] The adsorption of diatomic halogen molecules, including iodine, on graphene and graphite have been investigated by dispersion−corrected density functional theory (DFT) – see, e.g., Refs.[233] and[234] for recent reviews of corresponding methods and applications. Rudenko et al.[213] confirmed that the van der Waals (vdW) interactions contribute significantly to the interaction between the iodine molecules and graphene.

In addition, the analysis of the electronic structure showed the presence of an ionic interaction due to a charge transfer from graphene to the iodine molecules. Similarly, Arabieh et al.[235] revealed that the interaction between iodine and 2D pristine boron nitride (BN) is mainly driven by vdW forces. This work also demonstrated that the presence of defects significantly increases the reactivity of the iodine molecule.

Following the same path, we opted to study the *8−Pmmn* borophene in a preliminary screening, in anticipation that a substitution of graphene with boron (resulting in BC_3), nitrogen (resulting in C_3N) or both (resulting in BC_6N) would enhance the sensing properties of graphene towards iodine gas. Since the valences of boron and nitrogen are "symmetric" with respect to that of carbon and the atom sizes are close, in combined doping they easily accommodate into carbon structures.

In fact, Beniwal et al.[236] reported a successful synthesis of 2D hexagonal graphenic BCN monolayers. BC_6N has two different structures referred to as BC_6N-1 and BC_6N-2, whereby a theoretical study reveals that the band gap of the latter is smaller than that of the former.[237] The properties of graphene−like BC_3, C_3N and BC_6N-2 monolayers have been studied [238–240], and their potential for use as gas sensors has been discussed.[241–244] For Example, Ma et al. [244] reported that pristine C_3N monolayer is a good room−temperature NO_2 sensor with high selectivity, sensitivity, and good reversibility. Moreover, they revealed that boron doping replacing nitrogen atoms in C_3N monolayer significantly enhances the adsorption strength and the charge transfer. This further improves the sensing selectivity of C_3N towards NO_2 molecules.

Despite all these promising manifestations of graphene−like materials, they have not yet been tried for iodine detection, whereas we believe they are worth an investigation. An additional consideration for shaping the current work is the fact that most of the reported studies for iodine detection have only focused on the I_2 molecule and not on other iodine−containing species, e.g., ICH_3. It is noteworthy that the nuclear containment atmosphere is mainly composed of water steam.[245] Moreover, other gaseous compounds such as CO can be formed during a severe accident.[246,247] These two gases (CO and H_2O) are known to be able to compete with the adsorption of iodine species[248–251] which is likely to perturb or to bias the performance of the sensor. To the best of our knowledge, no systematic experimental nor theoretical works have been devoted to the evaluation of nanostructured carbon−based materials to selectively detect iodine species in presence of other gases.[252]

The accuracy of DFT calculations is sufficient to discriminate adsorption enthalpies of competing molecules on surfaces.[253–256] Therefore, we used this approach to compare the adsorption of I_2, ICH_3, H_2O and CO over *8−Pmmn* borophene, BC_3, C_3N and BC_6N 2D materials. The article is organized as follows: first, we detail our computational methods, after which the results obtained with the DFT tools are presented and discussed, while focusing on the sensing performances of the listed materials towards the iodine molecule. Finally, we present the main conclusions of our study.

4.3 Simulation details

In order to reliably compare the adsorption energies of different molecules on an, in principle, infinite sheet, we needed to take care of the following issues:

(i) When applying a simulation method with periodic boundary conditions (which is not absolutely necessary but convenient and largely acceptable, in order to not get biased by ambiguities related to the sheet termination, be the latter chosen as a limited fragment), large enough lateral supercell has to be chosen, in order to minimize the interference between periodically placed molecules. In principle, the results need to be tested for convergence against an increase of the supercell size.

(ii) Dispersion interactions are expected to play an important role in adsorption processes, affecting equilibrium geometries and electron energies; they ought to be – at least –included into the analysis with the help of one of "reliable" (practically recognized) methods, although a careful inspection of performance of different possible schemes would be even better.

(iii) A priori, preferential adsorption site or the ground−state configuration of adsorbed molecule might be far from evident; hence a big number of trial initial configurations may need to be inspected.

Our first−principles calculations have been done using the Vienna Ab initio Simulation Package (VASP)[174,257], which is based on plane wave pseudopotential approach and uses ultrasoft pseudopotentials or projected augmented wave (PAW) technique to cope with the core states [258,259]. The specific form of the exchange−correlation (XC) functional used was the generalized gradient approximation (GGA) with the Perdew–Burke–Ernzerhof (PBE) parametrization.[159] For the DFT calculations, the planewave cutoff has been set to 800 eV. The integration over the Brillouin zone was sampled by 12×12×1 Γ−centered k−point Monkhorst−Pack grid using a Gaussian integration method with a width of 0.2 eV for 2x2 supercell size in the cases of BC_3, BC_6N−2 and C_3N, and 2x3 supercell in the case of *8−Pmmn* borophene. These cutoff values were justified by convergence tests staged in order to check that total energy differences between distinct positions of molecules remain stable to the accuracy relevant for the present work. Unit cells of all the structures considered was fully relaxed, yielding the lattice constants of 5.17 Å, 4.97 Å, 4.86 Å and 4.51 Å x 3.25 Å for BC_3, C_3N ,BC_6N−2 and *8−Pmmn*, respectively, the values are in good agreement with the previously published results.[237,260,261] In order to reliably resolve the energy difference relevant to the present work, it was essential to use the "Accurate" calculation mode within VASP, which sets the 10^{-7} eV threshold for self-consistency criterion in solving the Kohn−Sham equations; the relaxation loop is stopped when the forces on all atoms get smaller than 0.02 eV/ Å. Dispersion interactions in most cases have been taken into account following the Grimme−D2 scheme;[262] however, other correction schemes (DFT−D3 method of Grimme with Becke–Jonson damping, Many−body dispersion energy method, and Tkatchenko–Scheffler method with iterative Hirshfeld partitioning) have also been applied, in cases of adsorption on C_3N, for comparison. For the calculation of the densities of states (DOSs) and partial densities of states (PDOSs), a 20x20x1 k−points mesh has been applied. The adsorption energy

(E_{ad}) of a molecule considered (m) on each 2D sheet (s) at different positions has been calculated according to the equation:

$$E_{ad} = E_{m/s} - E_s - E_m, \qquad \text{Eq 4.1}$$

where $E_{m/s}$ is the energy of the 2D sheet with the adsorbed molecule, E_s is the energy of the pristine 2D sheet and E_m is the energy of the isolated molecule calculated in a box with the same size of the system.

In each of these parts, dispersion contribution to the energy is straightforwardly identified, on top of the "conventional" DFT result, of the type $E = E^{DFT} + E^{disp}$. Since the energy is additive within each term, one can identify the dispersion contribution within the full adsorption energy:

$$E_{ad}^{disp} = E_{m/s}^{disp} - (E_s^{disp} + E_m^{disp}) \qquad \text{Eq 4.2}$$

Beyond the values of adsorption energy, the redistribution of charge in the course of adsorption might be revealing in the discussion of trends. In order to minimize the dependence on a particular calculation code, the "absolute" charge transfer will be expressed according to the Bader analysis [263], in the spirit of the above expressions for energy:

$$\Delta Q = Q_{m/s} - (Q_s + E_m) \qquad \text{Eq 4.3}$$

Along with this, the difference charge density as continuous spatial function will be communicated:

$$\Delta\rho(r) = \rho_{m/s}(r) - [\,\rho_s(r) + \rho_m(r)\,] \qquad \text{Eq 4.4}$$

There is a subtlety in the definition of differential energies and charges. If the latter are compared between two separately relaxed and hence not identical structures (molecule on the substrate vs free substrate plus free molecule), the charge distributions are compared for the same placement of atoms, i.e., $\rho_s(r)$ corresponds to self−consistent charge density in the adsorption geometry, with the molecule removed, and $\rho_m(r)$ stands for the charge density of a free molecule, brought into its equilibrium adsorbed position.

As a complement to static (T = 0) DFT calculations, dynamical simulations have been done using Born−Oppenheimer *ab initio* molecular dynamics (AIMD) within the *NVT* ensemble during a simulation time of 200 ps with a time step of 1 fs. The temperature was set to 305 K and controlled using the Nose−Hoover thermostat.[205,206] The planewave cutoff and the k−grid for the Brillouin zone were reduced to 500 eV and 6x6x1, respectively, in order to reduce the computational cost, while keeping the same threshold for self−consistency in solving the Kohn−Sham equations.

From these dynamical simulations, the internal energies of adsorption were extracted by averaging the internal energy of each system and its components separately (2D sheets and molecules) over the last 100 ps of the simulation. The internal energy of adsorption is expressed as follows:

$$E_{ad}^{AIMD} = \langle E_{m/s}^{AIMD} \rangle - (\langle E_{s}^{AIMD} \rangle + \langle E_{m}^{AIMD} \rangle) \qquad \text{Eq 4.5}$$

where $\langle E_{m/s}^{AIMD} \rangle$ is the average of the internal energy of the 2D sheet with the adsorbed molecule, $\langle E_{s}^{AIMD} \rangle$ −the average of the internal energy of the pristine 2D sheet, and $\langle E_{m}^{AIMD} \rangle$ −the average of the internal energy of the isolated molecule.

4.4 Results and discussion

The main idea of the present work was to probe several layer materials with respect to their aptitude to adsorb the iodine−containing molecules, I_2 and ICH_3, likely to emerge in case of severe nuclear accident, in presence of so−called contaminant molecules in the confinement building, e.g., CO and H_2O, in view of identifying a substrate which will clearly discriminate the former two from the latter two by their corresponding adsorption energies.

In the following, the results are outlined substrate by substrate. The full data are available in Supporting Information. In the main text we cover the results selectively – not only those which served our ultimate goal, but also “negative” ones which were nevertheless instructive, in one context or the other. Every substrate offered a number of adsorption positions – hollow site, atop an atom, etc. – subject to symmetry constraints of the lattice in question. In combination with possible initial orientations of the gas molecule, this yields a multitude of initial trial configurations. They are numbered in an arbitrary way and specified in the figures and tables. For adsorption of all the trial molecules, 54 configurations in total have been tried on BC_3 and 53 configurations on C_3N. As a rule, scenarios of conjugate−gradient structure relaxation starting from these trial configurations ended up in just few final configurations (adsorption site / orientation of a molecule / possible deformation of the substrate), for which the adsorption energy and electronic properties are reported.

Out of the four 2D materials probed, three were hexagonal monolayers with 8 atoms per unit cell; the fourth one (borophene) represented a “thick” structured layer of rectangular symmetry, with 8 atoms per unit cell as well. In order to minimize spurious interaction between (translated, by force of periodic boundary conditions) adsorbed molecules, sufficiently large lateral supercells must be chosen. In our simulations, the unit cells being already relatively large, we used 2x2 supercells for all hexagonal systems and 2x3 supercells for borophene.

The relevant adsorption energies of the considered molecules on all studied 2D materials are investigated. For each combination substrate/molecule, the relaxed structure of the most preferable position, i.e., that with strongest adsorption energy, is shown in Figs. 4.1, 4.3, 4.4, 4.5, and the corresponding adsorption energies and interaction distances are specified in Table 4.1.

Table 4.1: Calculated adsorption energies and minimal interaction distances for molecules over substrates, in the configurations shown in Figs. 4.1,4.3, 4.4, 4.5.

	Adsorption energy (eV)				Interaction distance*(Å)			
Substrate	I_2	ICH_3	CO	H_2O	I_2	ICH_3	CO	H_2O
BC_3	−0.491	−0.437	−0.746	−0.207	3.20	2.54	1.53	2.33
8−Pmmn borophene	−0.663	−0.351	−0.651	−0.236	2.51	1.79	1.40	2.41
BC_6N−2	−0.400	−0.265	−0.122	−0.172	3.08	3.29	3.06	2.41
C_3N	−0.801	−0.335	−0.152	−0.194	3.38	2.53	2.95	2.41

*minimum height separating the atoms of the molecule from the atoms of the substrate.

The overview of adsorption energies helps to understand the expectations of the present study, with respect to selectivity of different substrates towards the molecules tested, and our logic behind the quest for a “good” substrate material. The trial of BC3 was motivated by several recent works [243,264,265]. It revealed a noticeable selectivity towards iodine−containing molecules as compared to water; however, the adsorption of carbon monoxide turned out to be much stronger than that of all other molecules, with a danger to contaminate, or to bias, the prospective sensor. Guided by an idea of importance to have boron in the substrate, we tried the ultimate case of borophene, which revealed an enhanced sensitivity towards pure iodine, albeit not for ICH_3, whereas a strong sensitivity to CO persisted. Saturation of the BC3 substrate with nitrogen, in the form of balanced co−doping towards BC6N, gave first promises of clear positive discrimination of (I_2, ICH_3) against (CO, H_2O). Finally, an idea to get rid of boron whatsoever, turning to C3N substrate, produced a reasonable combination of outstanding selectivity towards I_2 molecules and a fair selectivity towards ICH_3, as compared to both CO and H_2O. In the following, we discuss some interesting results from simulations on the first three substrate systems, even if they did not fully respond to expectations, and address in more detail the performance of C_3N.

4.4.1 Adsorption on BC_3

The I_2 molecule, tentatively placed over the BC_3 sheet in 15 different trial configurations, stabilizes in several end configurations. The strongest adsorption energy (−0.49 eV) is found in “flat” configuration, the iodine atoms being situated over opposite boron atoms of a C_4B_2 hexagon, see Figure 4.1. Very close energies (−0.44 to −0.42 eV) correspond to nearly upright yet tilted placement of I_2 above a C–B bond. Further on, there is a group of "flat" configurations with adsorption energies −0.38 to −0.33 eV, the iodine atoms being stabilized over centers of adjacent C_4B_2 hexagons, or over a boron atom and the center of its "next−neighboring" C6 hexagon. Finally, "weak" adsorption energies (−0.29 to −0.27 eV) correspond to "flat" configurations over a C6 or C_4B_2 hexagon, anchored over the opposite C–C bonds and avoiding the boron atoms in the latter case. About the same adsorption energy, −0.27 / −0.26 eV, corresponds to the cases of upright placement of I_2 over the center of a C6 hexagon, or atop a B atom.

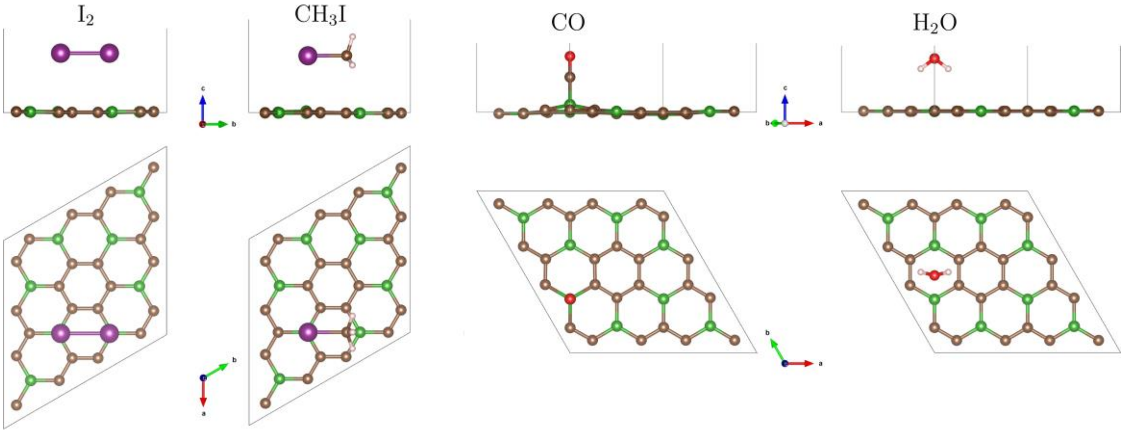

Figure 4.1: Top and side views of the relaxed conformations (corresponding to the largest adsorption energy, among the trial structures studied) of I_2, CH_3, CO and H_2O molecules adsorbed on BC_3 monolayer. Brown spheres: carbon, green: boron, large purple: iodine, red: oxygen. See text for detail.

The ICH_3 molecule, for which 19 trial initial configurations have been tested, prefers to be adsorbed (with the energy −0.41 eV) in a "flat" position (the I–C bond parallel to the substrate), with iodine atom atop boron, see Figure 4.1. The "next−choice" configurations (adsorption energies −0.35 to −0.31 eV) is equally "flat", with I "head" over the C_4B_2 hexagon. Placing the iodine atom over a C6 hexagon results in a slightly weaker adsorption energy (−0.28 eV). Of comparable adsorption energies (−0.28 to −0.26 eV) are also positions with upright orientation of the molecule, iodine downwards, over different competing sites: carbon atom, C–C or C–B bond, C_4B_2 hexagon, or (−0.21 eV) over a boron atom. Finally, the least favorable (−0.19 to −0.18 eV) are upright iodine−up positions, the carbon of the methyl group being placed over C or B atoms or C–C or C–B bonds. Summarizing, an ICH_3 molecule can "glide" on its methyl tail but gets trapped if its iodine head approaches boron, and gets fixed in a flat position, anchored to two boron atoms in the substrate. In the adsorption of carbon monoxide, dominating configuration is the upright one, with the carbon end of the molecule being atop a boron atom at a distance of 1.53−1.58 Å, yielding an adsorption energy of −0.75 eV. Other final configurations, flat or tilted or oxygen downwards, are almost indiscriminately characterized by much larger distance from the substrate (about 3 Å) and much smaller adsorption energies (−0.11 to −0.06 eV). The abovementioned strongest−bound (oxygen−up) configuration brings about a substantial distortion in the substrate, the underlying boron atom being pulled upwards by ≃ 0.53Å, so that the C(molecule)−B−C(substrate) angle makes 101°, as it can be seen in Figure 4.1. DFT calculations for CO (among other molecules) adsorption on BC_3 have been recently reported by Mehdi Aghaei et al. [243] (who used PBE with D2 Grimme correction) and by Zhang et al. [266] (who used VASP with PBE, not mentioning any inclusion of dispersion interactions). Agreement between our present calculation and the two cited ones is excellent in what regards the orientation of the molecule, interatomic distances, and angles. Namely, the "anchor" boron atom raises above the substrate layer by 0.5 Å and bounds the carbon atom on top of it at 1.53−1.54 Å. Our adsorption energies are however almost two times smaller than those reported in Refs. [243] and [266] (1.34 and 1.30 eV, correspondingly). In the latter of these works, the buckling of the BC_3 layer is much stronger than in our case, consistently with a larger adsorption energy.

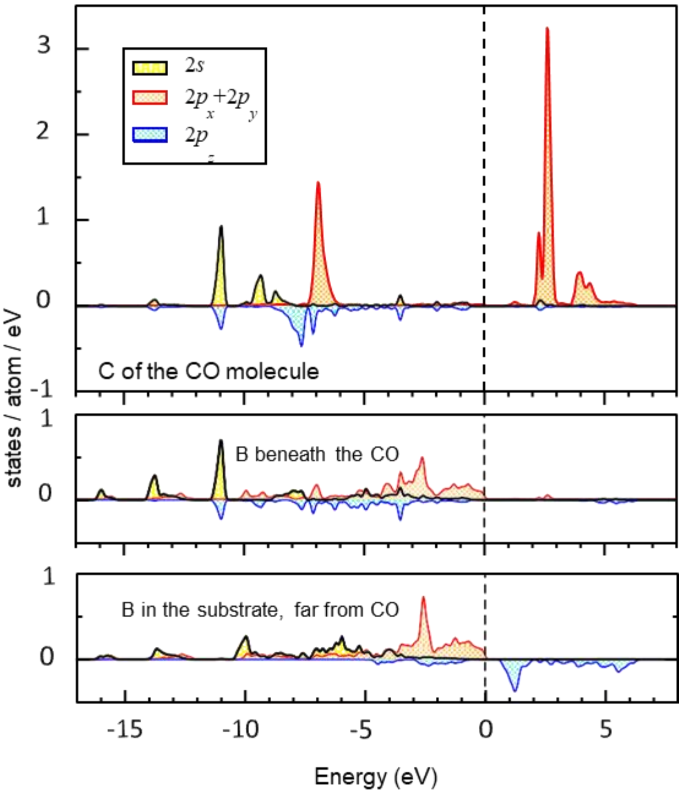

Figure 4.2: PDOS of carbon (upper panel) and boron atoms (lower panels) in the case of adsorption of CO on BC_3. See text for detail.

The remarkable adsorption of CO on BC_3 deserves some more detailed discussion, so we briefly mention the calculated PDOS shown in Figure 4.2. There is clear evidence of chemical bonding between the (downwards directed) carbon atom of the CO molecule and the underlying boron atom in the substrate. This bonding involves 2s and $2p_z$ states of the atoms concerned, that could have been a priori anticipated and is indeed evidenced by a similar pattern of peaks in the corresponding PDOS. It is noteworthy that the patterns of 2s and $2p_z$ PDOS at boron atoms distant from the adsorbed molecule (cf the bottom panel of Figure 4.2) is completely different; the marked peaks are situated at different energies. However, the spectrum of $2p_x$, p_y states is very similar for the boron atom beneath the adsorbed molecule and that far away; obviously the in−plane hybridizations are not strongly affected by the adsorbed molecule.

We note in this relation that the perturbations in the substrate layer caused by the adsorption of other molecules (I_2, ICH_3 and H_2O) is negligible, which hints at an absence of a noteworthy hybridization between the orbitals of the molecules and those of the substrate atoms.

In the case of water molecule, the largest adsorption energy (−0.21 eV) corresponds to a symmetric hydrogen−down/oxygen−up placement over the center of a C_4B_2 hexagon. A slightly weaker adsorption (−0.15 eV) occurs over the C6 hexagon. In both cases, turning the molecule upside down (hydrogens−up/oxygen−down) results in a metastable configuration, with adsorption energy reduced by 0.09 eV (−0.12 eV over C_4B_2, −0.06 eV over C_6). All the start configurations tested end up in one of these four possibilities. We note that the turnover of the molecule does not cost much energy, and the discrimination of different adsorption sites is not much pronounced. In fact, the same span of adsorption energies, −0.21 to −0.06 eV, will cover the cases of water molecule adsorption over other substrates to be considered in the following subsections.

Summarizing the situation with BC_3, the adsorption energies of I_2 and ICH_3 on this substrate seem interestingly large, exceeding (in configurations which correspond to the largest adsorption energies) that of water by a factor of two. (The adsorption of iodine−containing molecules tends to happen on top of boron atom in the substrate. Both I_2 and ICH_3 molecules, in their respective configurations with the strongest adsorption energy, place themselves flat over the substrate, roughly spanning the distance between two closest boron atoms in the substrate – cf. Figure 4.1). The problem is that the carbon monoxide, in its optimal adsorption configuration, bonds, in its turn, two times more strongly than the iodine−containing molecules, therefore the latter cannot be discriminated over the background of CO. Moreover, the ICH_3 molecule may happen to be adsorbed, at several metastable sites, with about the same energy as the water molecule, hence even the discrimination against water looks problematic. For this reason, we conclude that BC_3, a rising star in a number of interesting applications [237,238,264–266] is hardly promising for the detection of iodine−containing molecules. In the hope that this would be different for other substrates, we turned to the study of Pmmn8−borophen and BC_6N-2 in the following subsections.

4.4.2 Adsorption on borophene

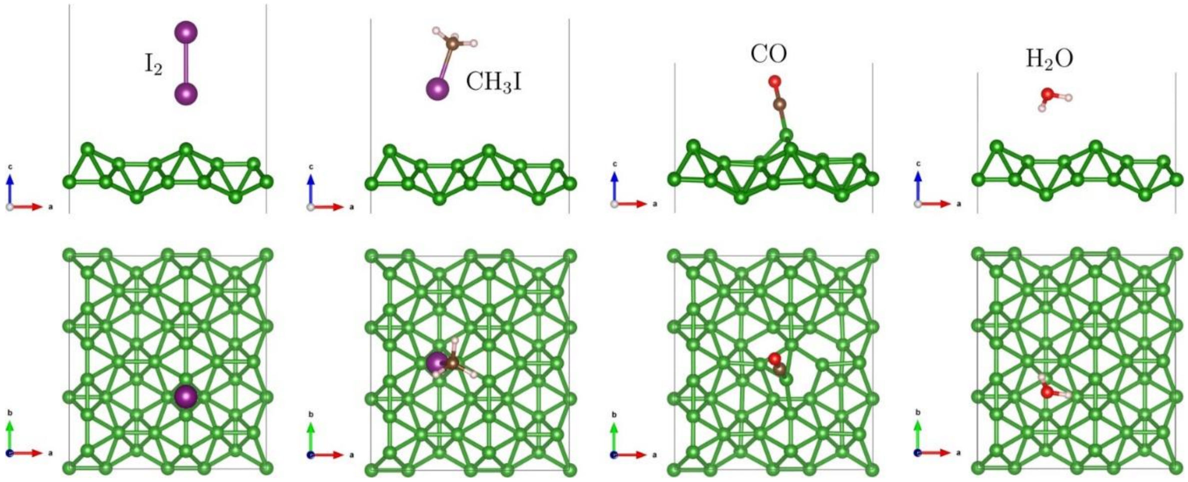

Figure 4.3: Top and side views of the relaxed conformations (corresponding to the largest adsorption energy, among the trial structures studied) of I_2, CH_3, CO and H_2O molecules adsorbed on BC_3N monolayer. Brown spheres: carbon, green spheres: boron atoms. See text for detail.

8−Pmmn borophene is singled out among other substrates explored in our work in that its structure is neither hexagonal nor flat, and thicker than one atomic layer. In fact, its surface consists of parallel ridges, separated by valleys, see Figure 4.3. We won't discuss the adsorption in large detail, because borophene failed to offer a satisfactory solution for iodine selectivity problem, yet we overview the results briefly, for completeness. The configuration of I_2 molecule with the strongest adsorption energy (−0.66 eV) is upright, anchored at the ridge (over a B–B bond along the ridge). The distance between the iodine atom and the closest boron atom underneath is 2.7 Å. The position parallel to the first one, upright over a valley (atop a B–B bond bridging the opposite slopes across the valley) yields the adsorption energy of 0.48 eV; the distance between iodine and the closest underlying boron atom is 3.3Å. Two "flat" positions are along (atop) the ridge, with adsorption energy −0.38 eV, the closest I–B distance being 3.51Å, and along the valley between the two ridges, with adsorption energy −0.54 eV and the closest I–B distance of 3.86Å. Carbon monoxide molecule adsorbs preferentially (adsorption energy of −0.65 eV) in oxygen−up (tilted) configuration, atop a boron atom in the ridge. This atom protrudes upwards, by about as much as the "contact" boron atom in BC_3. The B–C distance is 1.51 Å, again like in the case of adsorption on BC_3. The strongest−energy (−0.24 eV) adsorption position of water molecule is above the valley, in hydrogens−down orientation. A number of metastable configurations have been found, with adsorption energies −0.17 to −0.12 eV. Similarly, to the case of BC_3, the adsorption energy of H_2O is (in major part of adsorption configurations) weaker than that of I_2 and ICH_3, which satisfies the target condition of our study. However, again in similarity with the case of BC_3, the CO molecule tends to make a stronger bond with the borophene sheet than the iodine−containing molecules do, in the case when it is adsorbed, with its carbon side, on top of a boron atom. Even if the difference between the adsorption energies (on borophene) of, from the one hand, CO and, from the other hand, I_2 and ICH_3 is smaller than in the case of adsorption on BC_3, this does not yet make of borophene a good sensor for I_2 and ICH_3. It is interesting to mention that the adsorption of CO on borophene leads also to a significant distortion in the borophene sheet (Figure 4.3), which can be considered as a sign of the formation of a covalent bond between the molecule and the substrate.

4.4.3 Adsorption on BC_6N-2

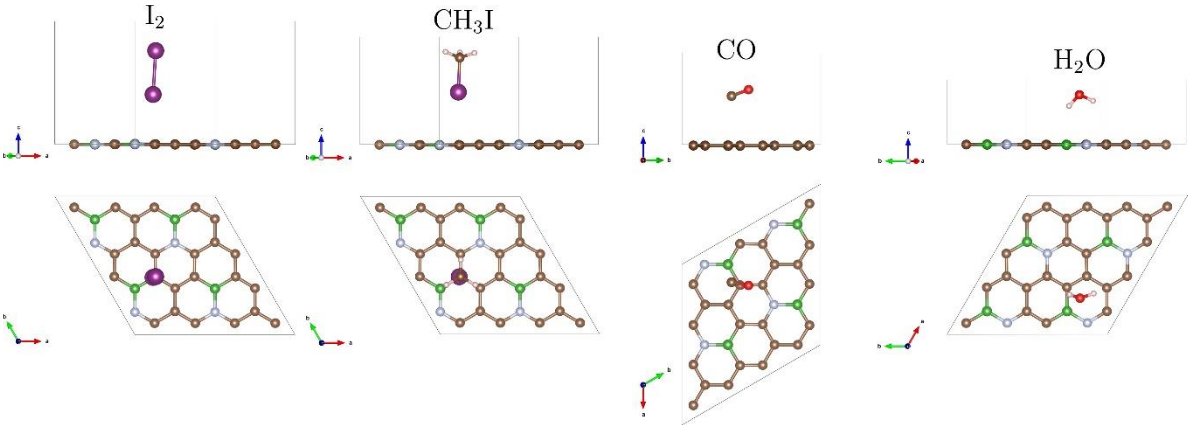

Figure 4.4: Top and side views of the relaxed conformations (corresponding to the largest adsorption energy, among the trial structures studied) of I_2, CH_3, CO and H_2O molecules adsorbed on BC6N-2 monolayer. Brown spheres: carbon, green spheres: boron, silver spheres: nitrogen atoms. See text for detail.

We have seen that boron has a good affinity for iodine−containing species in contrast to that for water. However, when confronted with carbon monoxide, the boron atom in BC_3 and in borophene materials exhibits an enhanced tendency to share electrons with a fourth carbon atom whenever it comes into its vicinity, and to covalently bond with it, changing its (boron's) hybridization scenario. We hoped to cope with this problem in the next system tested, that contained some amount of nitrogen, an element with an extra electron in its valence band over that of carbon, which may fill the need of the boron atom in the sheet. Specifically, we considered BC_6N-2 in which the nitrogen atom is directly bonded to the boron atom. As we anticipated, the DFT calculations confirmed that the formation of covalent bond with CO is prevented by the presence of nitrogen in the sheet (Figure 4.4). However, let us discuss the adsorption preferences of different molecules in the same order as before. The preferential position of adsorbed I_2 (with energy −0.40 eV) is upright (as shown in Figure 4.4), atop a carbon atom bonded with boron. Another competitive configuration (−0.39 eV) is upright atop the boron atom. On the contrary, the I_2 molecule initially placed atop a nitrogen atom escapes from this position. “Flat” configurations come about as “second choice” for adsorption, with slightly weaker energies (−0.35 to −0.33 eV). The I_2 molecule with about the same probability may lay over opposing carbon atoms in C5B hexagon, or over opposing either (C and B) or (C and N) atoms in a C4BN hexagon.

The ICH_3 molecule, similarly to I_2 as is seen in Figure 4.4, also preferentially adsorbs in upright position, iodine atom down, over a carbon atom bonded with boron (with the adsorption energy −0.27 eV), or otherwise atop B or N atoms (with adsorption energies −0.26 and −0.23 eV, correspondingly). The inverted configurations, with methyl group turned to the substrate, are metastable with slightly weaker adsorption energies (−0.21 to −0.19 eV).

The carbon monoxide molecule stabilizes in tilted carbon−down configuration, over a substrate C atom bonded to B (at a distance of 3.14 Å, with adsorption energy 0.12 eV), or immediately over boron atom. Several not clearly discriminated end configurations with slightly different positions and tilting’s come up with about the same adsorption energies, −0.12 to −0.11 eV. Upturned tilted position, with oxygen towards the substrate, are equally possible with adsorption energy −0.08 eV; in these cases, the oxygen is anchored at the N atom in the substrate. This makes sense because the nitrogen is more electronegative than boron, and the oxygen end of the CO molecule is slightly positively charged. “Good news” in the context of our study is that in no configuration does the CO molecule bond to the substrate as strongly as it was the case with previously discussed substrates, and moreover the “adsorption energy landscape” of carbon monoxide is quite smooth and not much depending on the position and orientation. Stable adsorption configurations of the water molecule, which span the range of adsorption energies −0.17 to −0.15 eV, are characterized by “hydrogen−down” orientation atop of boron atom, or over C5B, or over C4BN hexagon. In the “absence” of boron, when the molecule is docked over the C5N hexagon, the absorption energy is only slightly weaker, −0.14 eV. The “oxygen−down” orientation is also possible over a C atom close to B, with the energy −0.07 eV.

As a result, the adsorption energies of CO and H_2O for all the considered sites are systematically smaller than those of I_2 and ICH_3. Consequently, the BC_6N-2 can be considered as good candidate for sensing I_2 and ICH_3 molecules. These results encourage us to push the investigation one step further by checking the adsorption on a 2D material where boron atoms are totally substituted by nitrogen atoms. This ls as to consider the C_3N sheet in the next section.

4.4.4 Adsorption on C_3N

4.4.4.1 General considerations and adsorption configurations

The adsorption of I_2, ICH_3, CO and H_2O on C_3N gives very promising results, as our DFT calculation reveals that the (absolute) adsorption energies for both iodine−containing molecules are in almost all cases larger than for the two iodine−free ones, over a wide range of possible initial positions. The structures identified as those with the largest (the most negative) adsorption energy for each adsorbing molecule are shown in Figure 4.5.

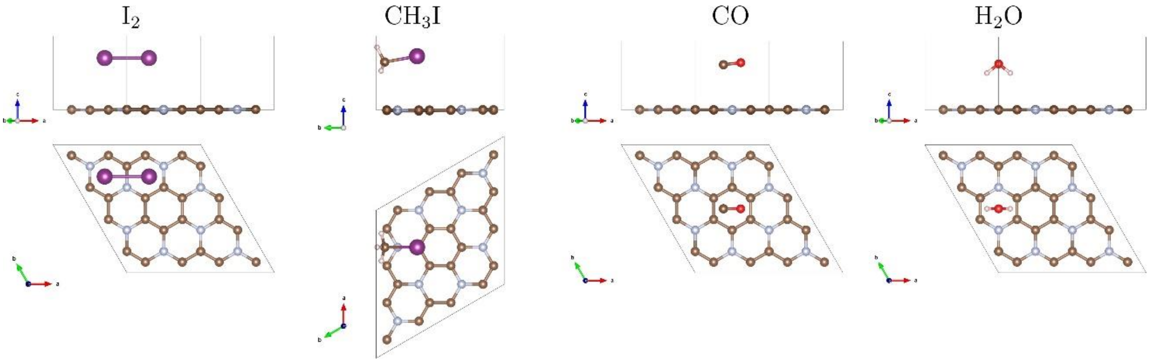

Figure 4.5: Top and side views of the relaxed conformations (corresponding to the largest adsorption energy, among the trial structures studied) of I_2, CH_3, CO and H_2O molecules adsorbed on C_3N monolayer. Brown spheres: carbon, silver spheres: nitrogen atoms. See text for detail.

In more detail, the trial configurations of the I_2 molecule, initially placed over different sites of the substrate, end up either in “flat” or in “upright” (probably slightly tilted) geometry. The former span the range of adsorption energies from −0.80 to −0.73 eV; the latter from −0.60 to −0.51 eV; hence the two “families” of solutions are clearly separated. Among the “flat” solutions, those with the lowest energy correspond to the iodine atoms placing themselves either approximately over the centers of adjacent C_4N_2 hexagons, or roughly over opposite nitrogen atoms in the same hexagon. The placement of iodine atoms atop of opposite C–C bonds in a hexagon, or over carbon atoms, are in certain disadvantage in what concerns the adsorption energy (measuring in these cases −0.78 to −0.73 eV); nevertheless, one can conclude that the “Adsorption relief” for the flat I_2 molecule stuck to (or, moving over) the C_3N layer is relatively even.

Among the “upright” positions of I_2, the strongest adsorption energy (−0.60 eV) is attributed to placements at a carbon atom or at a C−C bond, whereas the weakest energy (−0.51 eV) corresponds to anchoring at an N atom. Somehow simplifying, one can conclude that I_2 dimer sought to share its coupling over two nitrogen atoms in the substrate, whereas a terminal iodine atom in the upright molecule, on the contrary, avoids nitrogen in the substrate.

The ICH_3 molecule may be adsorbed in a number of sites and configurations, which can be sorted out into three groups, according to the molecule's orientation. The strongest adsorption energies (−0.31 to −0.34 eV) correspond to "flat" geometry (the I–C bond being roughly parallel to the C_3N plane), whereby the position of the iodine "head"–over C, N, or hollow site – is relatively unimportant (with a slight preference nevertheless towards docking the iodine atom atop of carbon).

Adsorption of ICH_3 in an upright configuration (I atom towards the surface) is equally possible, with slightly weaker adsorption energy (−0.28 to −0.24 eV). The strongest energies (−0.28 eV) correspond to the cases of the molecule's iodine "head" being docked over a carbon atom, a C–C bond, or a C_6 hexagon. The weakest adsorption energies are over a C4N2 hexagon (−0.25 eV) or atop a nitrogen atom (−0.24 eV).

Finally, an adsorption in upright iodine−up configurations is also possible, with yet lower energy (−0.22 to −0.18 eV). Of these possibilities, the weakest adsorption (−0.18 eV) occurs over a center of C_6 hexagon; all other possibilities are very close in energy (−0.21 to −0.22 eV). It is remarkable that, having three distinct groups of possible ICH_3 dockings, the adsorption energies in all of them remain (even if just slightly) larger than in "best" configurations for the "competing" molecules, CO, and H_2O.

For carbon monoxide, part of trial initial configurations ends up in relaxed positions with adsorption energies −0.15 through −0.07 eV, hence markedly weaker than for iodine−containing molecules. The strongest coupling occurs in almost "flat" configuration (the oxygen end slightly higher, the carbon end hangs over the hollow C_6 site, off−centered towards the C–C bond). Otherwise, upright (or slightly tilted) oxygen− up configurations are possible over different sites, with adsorption energies −0.13 to −0.10 eV, and upright carbon−up configurations, also over different sites, with adsorption energies −0.09 to −0.07 eV.

Finally, the water molecule would preferably stabilize itself in symmetric "hydrogens−down" configuration over hollow C_6 or C4N2 site or atop a carbon atom, with adsorption energies −0.19 to −0.17 eV. Another dense set of favourable configurations (with adsorption energies −0.12 to −0.07 eV) is "oxygen−down", again either over hollow sites, or – here – atop a nitrogen atom. Hydrogens−down position over a nitrogen atom in the substrate is kind of intermediate one between the abovementioned two groups, with adsorption energy of −0.13 eV.

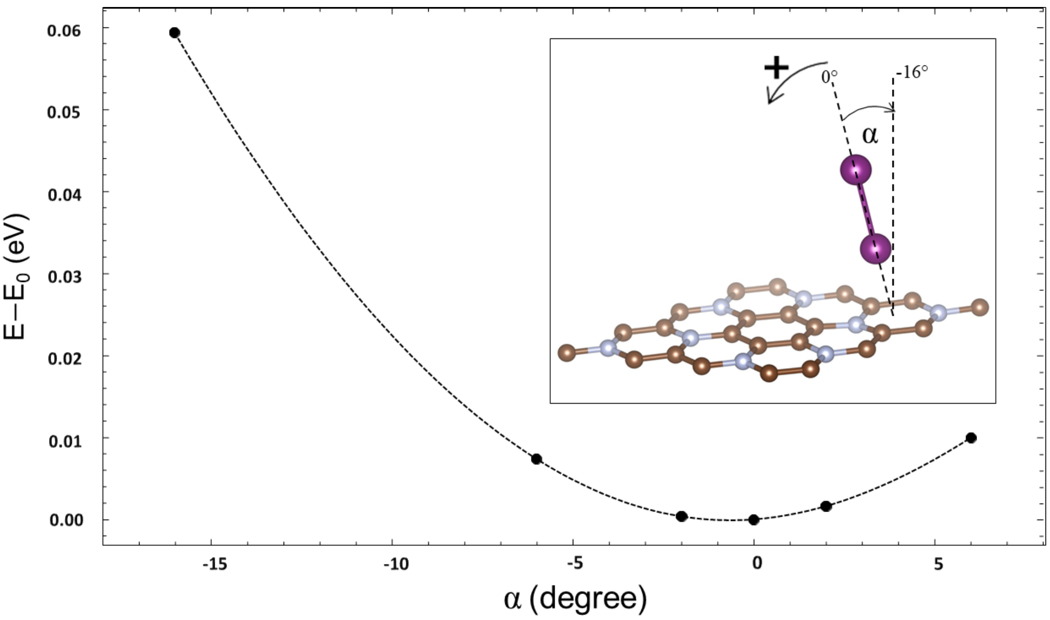

Figure 4.6: Effect of deviating the inclination of the I_2 on C_3N with respect to its relaxed position given by the DFT calculation. E_0 is the energy of the relaxed system. The inset shows the system at its relaxed position and specifies the inclination angle of I_2.

It is noteworthy that some molecules, when adsorbed, stabilize themselves in a low−symmetry inclined position. In order to verify that this indeed corresponds to the genuine energy minimum, and to estimate its “flatness”, we scanned in one of such cases, that of the I_2 molecule adsorbed on C_3N, its total energy as function of deviation from the nominal equilibrium angle; see Figure 4.6. The total energy profile turned out to be well “centered” and symmetric with respect to this inclined configuration.

One can expect from these results that CO and H_2O molecules do not show any marked preference for a particular adsorption geometry, and the adsorption energies are “uniform” over different sizes and not large in their magnitude. One can anticipate certain volatility of adsorption configurations for these gases and, in principle, their mobility over the substrate. This reduces the risk of CO and H_2O getting stuck at some positions, degrading sensing capability of substrate for iodine−containing molecules. These latter show clear preference for particular adsorption configurations, which are characterized by considerable adsorption energies. The adsorption energies of I_2, at different sites and in different configurations, are larger than those of CO or H_2O by 0.36−0.73 eV, while for the case of ICH_3, this difference ranges between 0 and 0.27 eV. The relaxed structures of the positions with the strongest adsorption energy for each molecule are shown in Fig. 5. We noticed that, like the case of BC_6N-2, no covalent bond has been formed between the CO and the C_3N. On the other hand, no significant distortion in the C_3N was observed after the adsorption of the molecules.

4.4.4.2 Role of dispersion interactions

It could have been anticipated that dispersion interactions will be important in shaping the adsorption energies in different configurations. Consequently, the existing diversity of practical methods to implement these interactions in a DFT calculation may contribute to confusion and biasing the results. All the energies reported so far have been obtained with the DFT−D2 method of Grimme [262], as indicated in Sec. 2. In the present section, dealing with our potentially interesting results for adsorption on the most promising (for the purposes of iodine sensitivity) substrate, we provide a more detailed analysis, based also on the use of the DFT−D3 method of Grimme with Becke–Jonson damping [161], Many−Body Dispersion energy method [267], and Tkatchenko–Scheffler [164] method with iterative Hirshfeld partitioning [268]. The obtained results are presented in Figure 4.7.

One can note a reasonable consistency of results for the molecules and dispersion−energy schemes considered. It seems important that the order of the adsorption energies throughout the row of the molecules considered remains the same, irrespectively of the scheme applied. We cannot judge about the true accuracy of the methods without comparing them to experimental results. However, we refer to this comparison as an argument in favour of credibility of our results concerning equilibrium energies and conformations.

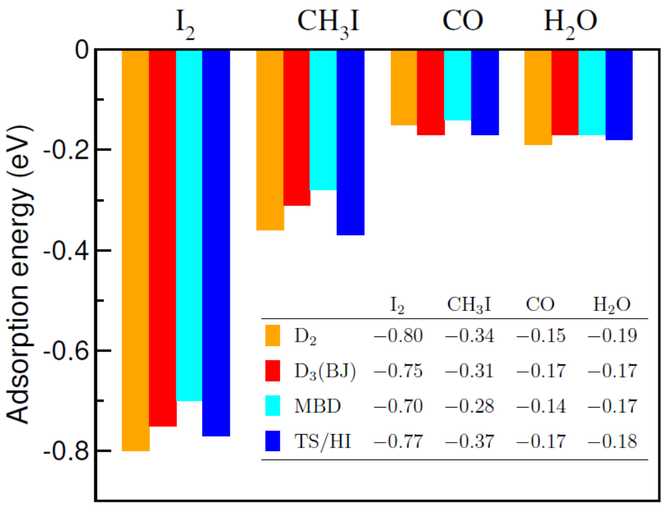

		I_2	CH_3I	CO	H_2O
🟧	D_2	−0.80	−0.34	−0.15	−0.19
🟥	D_3(BJ)	−0.75	−0.31	−0.17	−0.17
🟦	MBD	−0.70	−0.28	−0.14	−0.17
🟦	TS/HI	−0.77	−0.37	−0.17	−0.18

Figure 4.7: Adsorption energies in (eV) in the most preferable positions of I2, ICH$_3$, CO, and H2O molecules on C3N sheet. D2, D3(BJ), MBD and TS/HI are DFT+D2 method of Grimme, DFT+D3 method of Grimme with Becke-Jonson damping, Many-Body Dispersion energy method, and Tkatchenko – Scheffler method with iterative Hirshfeld partitioning, respectively.

The relevant question is how large the net contribution of dispersion interactions is, expressed according to Eq. (2), in the total adsorption energy of the molecules. Figure 4.8 shows these contributions (calculated with the DFT−D2 method of Grimme) for the four molecules adsorbed on C_3N. For the two iodine–containing molecules, for comparison, the estimations of the adsorption energy from MD calculations, according to Eq. (5), and the corresponding dispersion contributions in them are also given.

A remarkable observation is that the dispersion part makes all the adsorption energy in case of CO and H_2O adsorption and exceeds the resulting adsorption energy for ICH_3. In other words, according to a “conventional” DFT calculation, the ICH_3 molecule would “flow away” from the C_3N substrate, whereas carbon monoxide and water molecules won’t show any adsorbing tendency at this surface. In the case of the I_2 molecule, the situation is different, and the dispersion part makes just slightly more than the half of the resulting adsorption energy. This means that “chemistry” is important in this case and will be discussed further on.

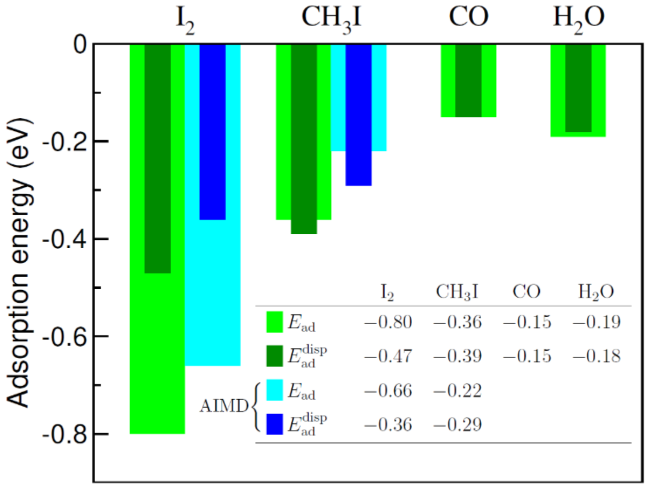

		I_2	CH_3I	CO	H_2O
	🟩 E_{ad}	−0.80	−0.36	−0.15	−0.19
	■ E_{ad}^{disp}	−0.47	−0.39	−0.15	−0.18
AIMD	🟦 E_{ad}	−0.66	−0.22		
	■ E_{ad}^{disp}	−0.36	−0.29		

Figure 4.8: Contribution of the dispersion energy correction (E_{disp}) in the total adsorption energy (E_{ad}) for four molecules, computed at the PBE+D2 level of theory. The corresponding estimates from AIMD calculations are added for I_2 and ICH_3.

4.4.4.3 Effect of adsorption on electronic properties of C_3N

The previously discussed trends in the adsorption energies (at least, in what regards the DFT parts) are manifestations of underlying changes in the electronic structure in the course of adsorption. Figure 4.9 depicts the summary of partial densities of states (PDOS) and total density of states (DOS) for a supercell cut out of C_3N monolayer, with the four different molecules adsorbed on it (in their respective lowest–energy configurations, shown in Figure 4.5). The DOS within the substrate are not visibly affected by interaction with adsorbed molecules; however, in principle, these tiny modifications in the band structure of the substrate, resulting from superposition with molecules’ electronic states (also slightly modified) bring about tiny preferences in the total energy for one or other structure conformation.

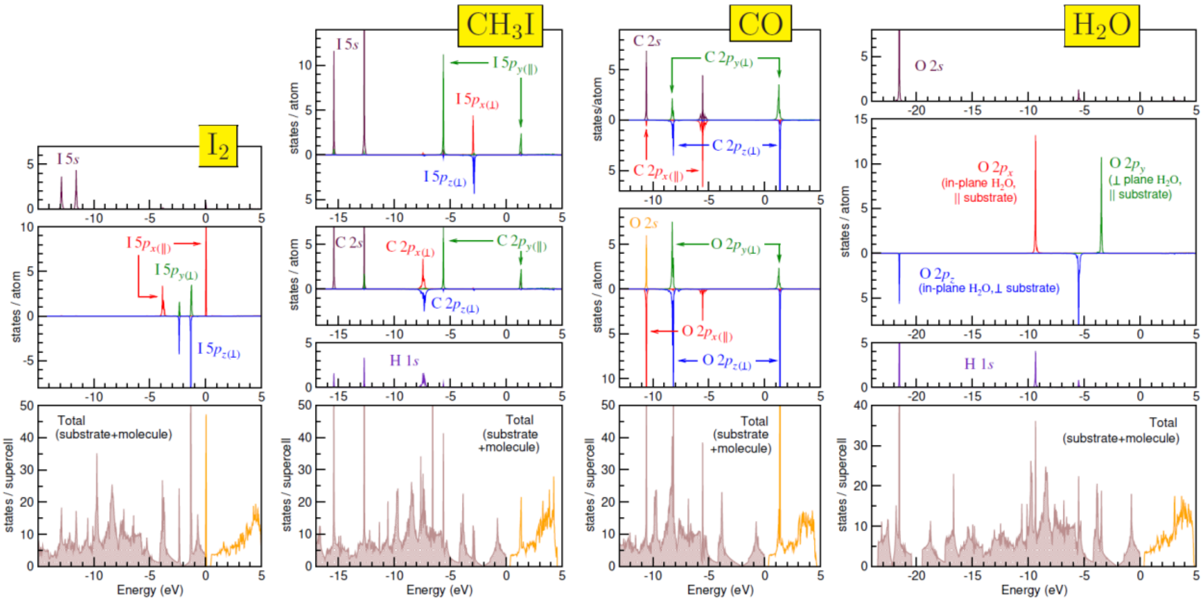

Figure 4.9: Total density of states for the four molecules (indicated at the top of each column) adsorbed on C3N substrate (bottom panel in each column) and partial densities of states in adsorbed molecules (in the panels above it). Zero energy delimits the occupied states (shown shaded in the bottom panel).

In a brief overview, we cannot do more than to make notes on how exactly the molecules' energy levels split and superpose with the substrate DOS. These results, obviously, correspond to pure DFT (GGA) calculations (since the dispersion interactions are included via a correction to total energy and do not yield and specific electronic structure), with all usual shortcomings related to addressing the electronic structures of molecules. Different DOS are aligned by the corresponding Fermi levels, set to zero in the common energy scale. The attribution of p_x, p_y, p_z projections in the PDOS relates to the global Cartesian system as chosen in Fig. 5, i.e., x along the "a" lattice vector, y perpendicular to it in the layer, and z at normal to the layer. (Additional markers, refer to the axis of the molecule in question). The resulting (near) degeneracies of p levels, highlighted by choosing to mirror up/down directions of corresponding PDOS axes in some panels of Figure 4.9, may therefore vary, due to different orientations of molecules in Figure 4.5.

According to our calculation, the band gap of the C_3N sheet is 0.35 eV which is in agreement with a recent computational result based on the same method of calculation [269]. This is (expectedly) underestimated with respect to hybrid functional (HSE06) calculation [270] (1.042 eV) and to reported experimental value [271] (2.67 eV). We already mentioned that the "chemical" part in the adsorption energy, which can be grasped in a "pure" DFT calculation, is negligible in case of ICH_3, CO and H_2O molecules. Consequently, no appreciable traces in the electronic structure can be anticipated upon adsorption. One can otherwise express this as physisorption being the principal mechanism.

For the case of I_2, the situation is a bit different. The system of energy levels of the I_2 molecule includes (occupied) 5s states, split into bonding / antibonding combinations and situated at $\simeq -13/-11.5$ eV, respectively, in Figure 4.9 [I_2]. The 5p states directed along the molecule axis undergo a relatively strong σ hybridization, yielding energy levels at $\simeq -4$ and $\simeq -0$ eV in Fig. 9[I_2], which are marked $p_x(\parallel)$, according to the choice of the coordinate system. Moreover, a weaker $\pi-$bonding splits the (doubly degenerate) 5p states extended in the perpendicular directions to the I−I axis, labelled $p_y(\perp)$ and $p_z(\perp)$. The corresponding peaks at $\simeq -2.3$ and $\simeq -1.2$ eV bracket the Dirac cone (at -2 eV) in the electronic structure of the substrate. Therefore, prominent peaks of molecular origin superpose with "sensitive" places of the substrate DOS: just at the top of the valence band and flanking the Dirac cone.

The counting of electrons to be placed onto a system of 5s + 5p hybridized states in a I_2 molecule would leave the highest (5pσ−antibonding) state empty, and so it stays also on adsorption. In fact, the sharp peak in the DOS at (just above) 0 eV is empty (indicated by color in Figure 4.9 [I_2]) and plays a role of acceptor level in a semiconductor. Somewhat counter−intuitively, during adsorption, this level is not populated with electrons, but, on the contrary, the I_2 molecule loses its charge to the benefit of the substrate. This can be evidenced by the Bader analysis, [201–203,263,272] according to which 0.43 electrons flaw away from the basins associated with the I_2 molecule, comparing the cases of the latter being free and adsorbed on C_3N.

The attribution of Bader charges is an unambiguously defined (hence comparable throughout calculation methods) yet not necessarily a physically (chemically) enlightening procedure. A different representation of charge flow can be given by a map of differential charge density, comparing the cases of adsorbed molecule on a substrate and a superposition of these two entities calculated in their separation. These charge density differences (CDD) are shown in Figure 4.10 by conveniently chosen isosurfaces. We note that for the figure depicting the I_2 molecule, the isolevel (chosen arbitrarily but so as to emphasize non−trivial features) is set much higher than it would be good for other molecules, in accordance with generally higher amount of charge transfer. One can see from Figure 4.10 [I_2] that the charge flow mostly depopulates 5p states of iodine (to a slight profit of 5s states) and more or less uniformly enriches the substrate atoms below the adsorbed molecule, the main recipients, also at some distance, being the nitrogen atoms. In simple terms, this can be considered as a manifestation of relative electronegativities, that of nitrogen (3.04, in the Pauling scale) being larger than for iodine (2.66) and carbon (2.55). As a result, the adsorption energy includes an important chemical (DFT) part (cf. previous discussion around Figure 4.7), of partially ionic origin. This observation won't hold anymore for other adsorbed molecules.

For the ICH_3 molecule, the hybridization of I5s and C2s levels produces two peaks split by $\simeq 2.5$ eV − cf. Figure 4.9 [ICH_3]. A much larger splitting ($\simeq$ 7 eV) occurs due to σ bonding between I5p_y and C2p_y (along the molecule axis) states, followed by smaller ($\simeq$ 4.5 eV) splitting induced by π hybridization between I5$p_\perp$ and C2$p_\perp$ states. PDOS are almost identical within each pair of (p_x, p_z) states (perpendicular to the molecule's axis but either parallel or normal to the substrate layer); this reveals indifference of the molecule's electronic states to the presence of the substrate. Except in the case of I_2, all the molecular states place themselves relatively far from the band gap, either below or above (the closest being the empty σ level a 1.5 eV). The net charge transfer, according to the difference of Bader charges, is 0.00.

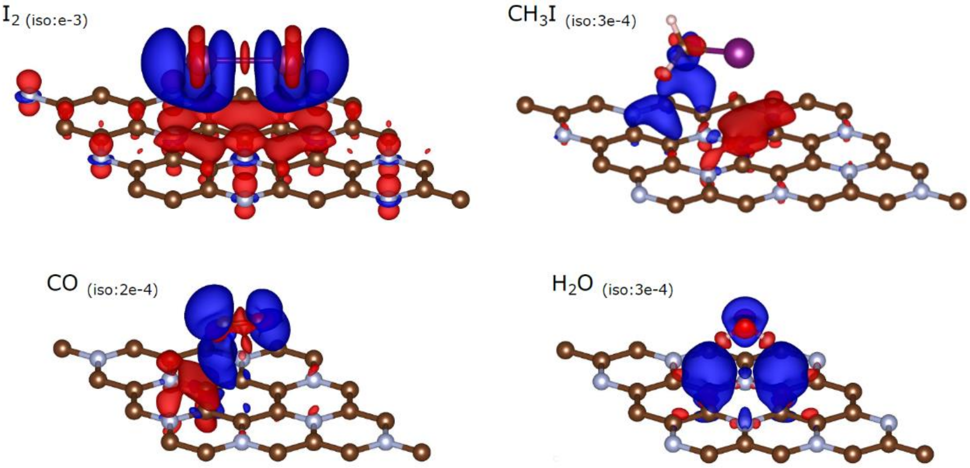

Figure 4.10: Charge density difference (CDD) due to the adsorption of molecules on C_3N sheet. Isosurfaces corresponding to an inflow of electron density (negative charge) are shown in red, those to an outflow (loss of electrons; extra positive charge) are shown in blue. The absolute value of the (+/−) differential charge density (in units of e/Å^3) are indicated in each panel.

The CDD isosurfaces shown in Figure 4.10[ICH_3] (note a very low isolevel value chosen) reveal a disappearingly small relocation of electron density from In5p states perpendicular to the C–I axis (the highest occupied among the molecular states, cf. upper panel of Fig. 9[ICH_3]) onto the substrate underneath. From "chemical" considerations, this interaction does not result in any bonding. As shown in Figure 4.8, the dispersion energy correction dominates in the resulting adsorption energy, compensating for a slightly "underbonding" character of DFT prediction. From Figure 4.8, the net "chemical" contribution in the adsorption energy is also absent for the two remaining molecules, CO, and H_2O; correspondingly the CDD isosurfaces shown for them in Figure 4.10 can only be chosen almost at a level of numerical noise, without a chance to draw any enlightening conclusions from their shape.

The net values of the Bader charge transfer are −0.04 e for CO and −0.02 e for H_2O, hence formally from the molecule to the substrate but on the brink of disappearance. Some words can be however said about the superposition of the molecular levels with the substrate DOS for these two systems.

The peaks of the other molecules are relatively far from the Fermi energy which explains the vdW nature of interaction between these molecules and the sheet, therefore we cannot except a great impact on the electronic properties of the sheet in these cases.

4.5 Conclusions

Summarizing, we simulated from first principles the adsorption of I_2, ICH_3, CO, and H_2O molecules on BC_3, borophene, BC_6N-2, and C_3N 2D materials in a search for a sensor or detector which would readily adsorb iodine−containing molecules and so help to discriminate them from other atmospheric ones. BC_3 and borophene, even if suggested by some considerations, did not prove themselves promising in this context. The major problem consisted in that a strong covalent bond was formed between the CO molecule, oriented upright with carbon end downwards, and the underlying boron atom, thus resulting in a "contamination" of the prospective sensor. In BC_6N-2, the presence of nitrogen atoms prevents the formation of the covalent bond with CO; however, the energy difference between the adsorption energies of I_2 and ICH_3, from one side, and those of CO and H_2O, from the other side, is not convincingly large; therefore, even if this system can, in principle, be used for sensing I_2 and ICH_3 gases, its selectivity might be in a need of improvement. Finally, the results from the adsorption on C_3N seem very promising in that the difference between the adsorption energies of (I_2, ICH_3) vs (CO, H_2O) is significant. Our calculations reveal that the "pure DFT" part of adsorption energy (e.g., due to chemical bonding) is appreciable, out of the systems considered, only in case of adsorption of I_2 molecule, which was accompanied by a redistribution of charge (of about half an electron, estimated from calculations of Bader charges) from the molecule towards the substrate. About 60% of the resulting adsorption energy (in the case of I_2 adsorption on C_3N) and nearly the whole energy in case of ICH_3, CO and H2 adsorption are due to dispersion interaction, which can be included in calculation on top of the "conventional" interactions grasped by the DFT. A variety of practical methods (at different levels of accuracy) suggested to grasp the effect of dispersion interactions have been applied within the present work; they did not result in big scattering of estimations for the adsorption energy in each given system. For a detailed discussion of the trends (energies in different adsorption geometries etc.), the results obtained with semi−empirical Grimme D2 method have been therefore considered.

Understanding the complexity of a read adsorption process, we took care of including possibly many (in principle, “all” in view of symmetry of perfect surfaces) initial configurations as starting conditions of conjugate−gradient search towards a few metastable adsorption configurations, which could have been thus identified. Aware of limitations of this “static” (zero−temperature) approach, we attempted molecular dynamics simulations for two systems, I_2 and ICH_3 on C_3N, which reinforced the conclusion on stability of molecules “dancing” in adsorbed state. The order−of−magnitude consistence of adsorption energy estimates from these (exploratory / trial) dynamic and from (systematic / controllable) static simulations is encouraging; yet these are only far approximations from different sides to the physics of process. As obvious improvements of the present approach, one should consider vibrations and zero−point energy corrections. Moreover, a model of monolayer substrate is likely to be in a need of adjustment to the conditions of practical realisation. However, already on the basis of results so far obtained one can suggest verification of our findings in experiments, in view of practical use of C_3N for iodine sensing.

Chapter 5

Iodine Selective adsorption of M-MOF-74 (M=Zn, Mg, Cu, Fe, Co, Ni, Mn) from first-principles calculations.

> "Cesium, iodine from the Chernobyl reactor accident went around the world many times and everyone on the Earth has a piece of Chernobyl in their bodies, but it's very tiny - too small to cause much damage." ~ ***Michio Kaku***

This chapter is a draft of a work that has not yet been published.

5.1 Abstract

Open metal-sites metal organic frameworks (OMS-MOFs) have attracted great interest for the selective capture of gas molecules from a gas stream. In this paper, using density functional theory (DFT) calculations, we performed a systematic evaluation of the adsorption performance of M-MOF-74 where M = Mg, Zn, Cu, Fe, Co, Ni and Mn. The adsorption modes and energetics of iodine species (I_2, ICH_3) and contaminants (H_2O, CO) on the M-MOF-74 series were systematically examined using periodic DFT calculations to determine the optimal metal (II) for the selective capture of I_2 and ICH_3. The best Cu-, Mn-, and Fe-MOF-74 series were further tuned by replacing their linker ("dobdc") with a smaller molecule ("dhfuma") aiming at enhanced affinity of the metal site for adsorbed iodine compounds.

The structural description of the M_2(dhfuma) series have revealed a dissociation of iodine into two I atoms bound to two distinct metal sites of Mn-MOF and Fe-MOF, while on Cu-MOF, a molecular adsorption has been observed. These adsorption modes resulted in ~13 kJ/mol higher interaction energies for I_2 and ICH_3 than in the DOBDC series, along with a large $\Delta E_{ads,I_2} - \Delta E_{ads,H_2O}(\Delta E_{ads,CO})$, reaching a maximum of 62.8(89.3) kJ/mol for Mn_2(dhfuma). These results predict that Cu-, Mn- and Fe-MOF are promising materials for the selective capture of I_2, ICH_3,

in presence of water and carbon monoxide and the strong chemi-adsorption displayed by Fe and Mn will be extremely useful in the fields of hazardous material handling (i.e., nuclear power plants) by providing additional protection, while the long-range dispersion controlling Cu-MOF interaction gives the possibility for a regenerable iodine capture material which can be of great interest as an iodine gas preconcentrator for chemical sensing.

5.2 Introduction

Nuclear power plants allow a constant production of electricity through disintegration of radioactive uranium. However, although nuclear energy advantages allow to compensate for the intermittence of renewable energies, it presents several risks for the health of humans and ecosystems. After a severe nuclear accident, highly radioactive and volatile by-products are released in the environment, representing major risks for the surrounding population. In particular, ^{131}I, a volatile short-lived isotope with a half-life of ~8.02 days responsible for the long-term development of thyroid cancer, and ^{129}I, with half-life of 15.7 million years damage human cells and cause genetic mutations [178,179]. In addition, radioactive iodine can reacts with hydrocarbons (methane CH_4) and other volatile organic compounds present in the gas stream to form methyl iodide ICH_3 [180].

For reducing the risks associated to the presence of radioactive iodine compounds in the atmosphere, the current challenge is to trap these toxic and volatile species in a very efficient way on an industrial scale. Existing iodine trapping techniques are mainly based on several porous adsorbent materials, namely activated carbon and silver-exchanged zeolites (especially Ag-MOR).[194] However, these materials were quickly discarded. Activated carbon materials, have been found to be flammable and too sensitive to humidity and high temperatures (>150°C), thus not adaptable to the severe nuclear accident conditions. In addition, due to their heterogeneous nature, these materials do not have well-defined trapping sites, which makes it difficult to adjust certain characteristics such as porosity or surface chemical composition. Meanwhile, Ag-MOR, being very stable to temperature and oxidation, has proven to be one of the most interesting sorbent for trapping iodinated compounds.[214] Unfortunately, the high cost of silver has forced scientists to turn to alternative materials. Other cheaper metal-exchanged zeolites (with lead, cadmium, thallium, palladium, manganese, mercury, and copper) have been evaluated as a feasible alternative to silver-based zeolite for the capture of iodine species. However, although some have shown promising results for iodine (I_2) removal, all of them have exhibited unsatisfactory removal efficiency and/or low methyl iodide adsorption capacity. It was therefore needed to explore the potential of another class of porous materials. Compared to zeolites, metal-organic frameworks (MOFs) exhibit unique characteristics. The tunability of their pores[105–108] and their considerably high porosities (> 6000 $m^2.g^{-1}$ surface area)[273–275] have prompted these materials to be widely examined for their applications in gas separation.[276,277]

Recently, many excellent explorations of iodine adsorption have been carried out using Metal Organic Frameworks (MOFs). Namely, the ZIF-8 (zeolitic imidazolate framework) class of MOFs[127] was selected for its relevant structural feature comprising relatively large pores (11.60 Å) connected by small apertures of (3.4 Å) close to the kinetic diameter of I_2(∼3.35 Å), as well as its high specific surface area (1810 $m^2.g^{-1}$), thermal and chemical stability (under the extreme operating conditions of industrial nuclear processes).[127] Nenoff and coworkers,[128] presented a comprehensive structural evidence for I_2 uptake into ZIF-8. The results revealed a high sorption capacity for I_2, up to 125 wt.%, which was reported to be safely confined in the pores of ZIF-8 until the framework decayed at ∼300 ºC. Interestingly, they revealed that ZIF-8 binds the iodine 4 times more strongly than activated carbon (− 41.5 kJ/mol vs −10.1 kJ/mol) [129]. On the other hand, Li and coworkers [82] reported an efficient capture of radioactive organic iodides (ICH_3) from nuclear waste by post-functionalization of MIL-101-Cr MOF with tertiary amine binding sites. Synthesized MIL-101-Cr-TED molecular trap exhibited a high saturation uptake capacity for ICH_3 of 71 wt.% at 150 °C, being more than 340% higher than the industrial adsorbent Ag^0@MOR at identical conditions.

We must emphasize that these studies have dealt only with iodine, whereas under real conditions other molecules are present in large proportions in the gas stream, namely steam (40-90%) and CO (1-20%).[251] The structure of MOF must therefore be selective towards the iodine compounds. MOFs with open metal sites (OMS) are an excellent choice in this regard, as they provide a greater level of control over selectivity, producing an enhanced interaction with different sorbate molecules, compared to MOFs with fully occupied metal sites.[278,279] Several previous studies have evidenced the efficiency of these OMS-MOFs in many applications, such as catalysis,[280,281] sensing [282,283] and gas separation.[284–286] Among these we investigated MOF-74 family materials, also known as CPO-27 (coordination polymer of Oslo) or M_2(dobdc). They are constructed from metal (II) oxide chains connected by the organic ligand dobdc^{4-} (2,5-dioxido-1,4-benzenedicarboxylate) while the remaining unsaturated metals are coordinated using DMF (DMF = N,N-dimethylformamide), resulting in Lewis acidic coordinatively unsaturated sites (CUS) after DMF removal (i.e., activation).[117] Since its discovery in 2005, MOF-74 became one of the most promising MOFs because it features a high density of open metal sites in the one-dimensional (1D) hexagonal channel of ~1.1 nm diameter (along the c-axis), as well as high porosity and surface area.[117,118] Several MOF-74 structures have been synthesized using a variety of metal ions, including Zn, Cu, Ni, Co, Mn, Fe, and Mg.[118] Depending on the type of metal ions and the strength of the Lewis acidity, each of these MOF-74 exhibits intrinsic properties regarding chemical stability and binding affinity to guest molecules.[118,120] In addition, the MOF-74 pore environment can be tuned by ligand modification giving rise to variable pore sizes and surface areas without changing the topology of this open metal site MOF. Berend Smit et al.[287] obtained a new framework with twice larger open metal sites volumetric density over the original M_2(dobdc) (0.0084 Mg/$Å^3$ vs 0.0044 Mg/$Å^3$), by replacing the regular linker of MOF-74 with a smaller, cheaper and commercially available aliphatic ligand (i.e., DHFUMA). The use of this smaller ligand (6.17Å vs 8.22Å) shortened the metal-metal distance, and CO_2 was able to bind to two open metal sites while small molecules like H_2O only bind to one metal site. This results in ~10 kJ/mol higher $\Delta E_{bind,H_2O} - \Delta E_{bind,CO_2}$ than in the DOBDC series and thus higher CO_2/H_2O selectivity compared to the regular MOF-74.

Density functional theory (DFT) has become the method of choice for modeling with sufficient accuracy to treat MOFs capture of iodine molecules, with reasonable energy accuracy.[138] Using this approach, the present work is dedicated to the study of the volatile radionuclides gas molecules (I_2, ICH_3) capture in the presence of CO and H_2O using M_2(X) series where (M= Zn, Cu, Ni, Co, Mn, Fe, and Mg) and (X=dobdc and dhfuma). This paper is organized as follows: first, we detail our computational methods and the MOF structural models used, after which our DFT results are presented and discussed leading to a selection of the most promising materials of the listed MOF series for the selective iodine species capture in presence of carbon monoxide and water, followed by a real condition model study of these best materials at 413 K with competition of iodine species together with contaminants. Finally, we provide the main conclusions of our work.

We believe our work is conducive to gain insight into the interaction on MOF-74 series at the atomic-level, to understand the trapping mechanism of the iodine compounds, and to provide theoretical guidance for the experimental design of more efficient iodine capturing MOFs.

5.3 Computational and structural details

5.3.1 Methods

Computational simulations to investigate the iodine species selective capture with MOFs were performed through spin polarized Density Functional Theory (DFT)[155,157] implemented in the

Vienna *ab initio* simulation package (VASP).[173,174] We used the Perdew-Burke-Ernzerhof (PBE) exchange-correlation functional within GGA approximation.[159] The plane wave kinetic energy cut-off was set at 1000 eV and the convergence criteria for the Kohn-sham self-consistent energy,[156] and the forces were set at 10^{-8} eV and 0.02 eV/Å per atom respectively, ensuring accurate calculation of the adsorption energies. Owing to the large size of the MOF structures the Brillouin-zone integration was restricted to the Gamma point.

The Grimme dispersion correction D2 scheme was included in the calculations to effectively correct the van der Waals (vdW) forces, and Hubbard-like U parameter[168] was employed to better treat the localized d-states of the transition metal cations. The U values (4.0, 4.0, 3.3, 6.4, and 4.0 eV for Mn, Fe, Co, Ni, and Cu, respectively) were derived based on Wang et al. study,[288] where they were determined to reproduce the experimental oxidation energy of metal monoxide to M_2O_3. Considering the metal spin state, our results revealed a high-spin ground state for all metals, and we assumed a ferromagnetic order along the M-O chain direction and an antiferromagnetic ordering between the chains as observed previously.[289]

To understand the interaction between the gas molecules and the MOF framework, the adsorption energy was calculated at 0K using the following equation:

$$\Delta E_{\text{ads}} = E_{(\text{MOF+guest})} - (E_{\text{MOF}} + E_{\text{guest}}) \qquad \text{Eq 5.1}$$

where $E_{(\text{MOF+guest})}$ is the total energy of the system comprising the single gas molecule and the MOF structure, while E_{MOF} and E_{guest} are the total energies of the bare MOF structure and the isolated gas molecule, respectively.

Similarly, the dispersion force contribution ΔE_{disp} to the adsorption energy formula is defined as:

$$\Delta E_{\text{disp}} = E_{\text{disp(MOF+guest)}} - (E_{\text{disp(MOF)}} + E_{\text{disp(guest)}}) \qquad \text{Eq 5.2}$$

To reveal the charge transfer between the MOF metal sites and gas molecules, charge density difference (CDD) and charge difference (ΔQ) were determined. The charge transfer upon adsorption of the gas molecules is examined using the Bader charge analysis [201–203] from the differences in the charge concentrations before and after adsorption with :

$$\Delta Q = Q_{\text{MOF+guest}} - (Q_{\text{MOF}} + Q_{\text{guest}}) \qquad \text{Eq 5.3}$$

And the charge density difference (CDD) was visualized by VESTA code with:

$$\Delta\rho = \rho_{\text{MOF+guest}} - (\rho_{\text{MOF}} + \rho_{\text{guest}}) \qquad \text{Eq 5.4}$$

Where $\rho_{\text{MOF+guest}}$, ρ_{MOF} , ρ_{guest} and are the charge density of the system comprising the gas molecules adsorbed on the MOF structure, the bare MOF structure, and the isolated gas molecules respectively.

5.3.2 Structural Models

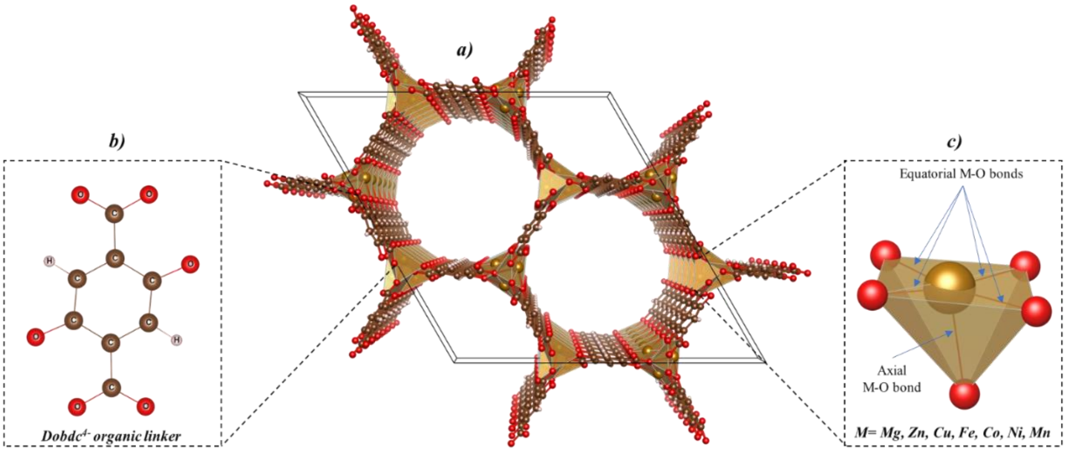

Figure 5.1: Honeycomblike pore structure of M-MOF-74 (M = Mg, Zn, Cu, Fe, Co, Ni and Mn) with a polyhedral representation. (inset) b) MOF-74 organic linker, and c) The equatorial and axial M−O bonds of the metal site.

The crystal structure of the primitive rhombohedral unit cell containing 162 atoms (18Mg, 54O, 72C, and 18H) of Mg-MOF-74 was obtained from Jeffrey R. Longet al.[290] while the rest of the M-MOF-74 (M=Zn, Cu, Fe, Co, Ni, Mn) series have been derived by substituting the Mg element by the M-metal series, respectively. The structure of MOF-74 presents a honeycomb topology (Figure 5.1), where the metal sites (M) are located in the center of the square plane, coordinated to five oxygen atoms in a square pyramid environment. This makes the metal site M open and accessible to adsorb guest molecules. As shown in Figure 5.1, each of these metal nodes in MOF-74 is characterized by two chemically distinct M-O bond lengths. equatorial and axial. Equatorial M-O bonds are defined as bonds located in the plane of the MOF-74 open metal site; axial M-O bonds are bonds located on the opposite side of the "removed" coordinated quasi-octahedral metal cation after activation.

By employing the parameters described in section 2.1, a geometric optimization was carried out where all the atomic positions and lattice parameters of the M-MOF-74 series were allowed to be completely relaxed. The calculated lattice constants and M-O bond lengths are listed in Table 1 in comparison with previous experiments and theoretical work.

$$Absolute\ errors\ =\ |((Calculated\ value\ -\ Exp\ value)/Exp\ value)\ x\ 100| \qquad \text{Eq 5.6}$$

The calculated lattice constants of the M-MOF-74 series (M = Mg, Mn, Fe, Co, Ni, Cu, and Zn) are in excellent agreement with the experimental values (Table 5.1). The absolute errors calculated using Eq 5, and listed in parentheses in Table 5.1, reach a maximum of 0.7% (Fe), 1.3% (Fe), 2.7% (Fe), 2.0% (Ni), and 2.0% (Cu) for the a=b axis, the c axis, the cell volume, the equatorial

M-O bond, and the axial M-O bond, respectively. This slight drift in the lattice constants and M-O bond lengths is an indicator of the accuracy of the DFT level used for our relaxations.

Table 5.1: A summary of calculated lattice constants and Bond Lengths (equatorial[a] and axial) of M-MOF-74 (M=Mg, Zn, Cu, Fe, Co, Ni and Mn) in comparison with previously reported experimental (underlined in italic) and theoretical data. In parentheses, the average absolute error relative to the experimental data calculated using Equation 5, are presented.

	$a = b$ (Å)	c (Å)	V ($Å^3$)	**Bond lengths**		**Ref**
				d(M-Oeq)/Å	**d(M-Oax)/Å**	
Mg-MOF-74	26.00 (0.5%)	6.88 (0.1%)	4029.9 (1.2%)	2.03	2.02	This work
	26.03	6.86	-	2.03	2.02	Oliveira et al.[291]
	25.87	*6.87*	*3982.7*	-	-	Queen et al.[118]
Zn-MOF-74	25.97 (0.2%)	6.77 (0.6%)	3957.6	2.07 (0.5%)	2.17 (0.5%)	This work
	25.93	*6.83*	-	*2.06*	*2.18*	Yaghi et al.[117]
	25.93	*6.79*	*3957.1*	-	-	Queen et al.[118]
Cu-MOF-74	25.96 (0.2%)	6.34 (1.4%)	3702.6 (2.1%)	1.97 (0.3%)	2.49 (0.8%)	This work
	25.99	*6.25*	-	*1.97*	*2.50*	Sanz et al.[292]
	25.87	*6.26*	*3627.8*	*1.96*	*2.44*	Queen et al.[118]
Fe-MOF-74	26.28 (0.7%)	6.94 (1.3%)	4149.2 (2.7%)	2.07	2.13	This work
	26.47	6.97	-	2.08	2.13	Lee et al. [293]
	26.10	*6.85*	*4041.3*	-	-	Queen et al.[118]
Co-MOF-74	26.05 (0.6%)	6.88 (0.7%)	4041.5 (1.4%)	2.03 (1.5%)	2.05	This work
	25.98	6.78	-	2.01	2.04	Oliveira et al.[291]
	25.91	*6.85*	*3984.3*	-	-	Queen et al.[118]
	25.90	*6.82*	-	*2.06*	-	Dietzel et al.[294]
Ni-MOF-74	25.90 (0.5%)	6.80 (0.4%)	3945.8	1.99 (2.0%)	2.01 (1.4%)	This work
	25.97	6.84	-	2.02	2.06	Lee et al. [293]
	25.78	*6.77*	-	*2.03*	*2.11*	Dietzel et al.[295]
Mn-MOF-74	26.32 (0.04%)	7.13 (1.1%)	4278.7 (1.1%)	2.13	2.16	This work
	26.30	7.09	-	2.10	2.13	Oliveira et al.[291]
	26.33	*7.05*	*4232.3*	-	-	Queen et al.[118]

[a] The equatorial M-O bond lengths reported for this study are the average of the four equatorial M-O bond lengths.

Interestingly, with the exception of Mn, which exhibits a larger unit cell, all M-MOF-74 structures display very similar lattice parameters a, b, c, and volume V. This lattice parameter fluctuation can be rationalized with the different ionic radii of these metal sites. According to R. D. Shannon [296], the ionic radii (as a function of high spin state for Fe, Co, Mn, and Ni and 5-coordinate of Mg, Zn, Cu, Co, and Ni) are reasonably close to each other with values of 0.66, 0.68, 0.65, 0.67, 0.63 Å, respectively, whereas Mn possesses the largest atomic radii of 0.75 Å.

Regarding the bond lengths, Table 5.1 shows that among all the metals studied, the axial Cu-O is significantly elongated, giving a value of 2.49 Å with an average of 0.40 Å higher than the other M-O_{ax}, this may be associated with the Jahn-Teller distortion of the coordination environment of Cu^{2+} ions. Sanz et al.[292] have observed a Jahn-Teller distortion of the coordination environment of the Cu metal site in their synthesis of the Cu-based MOF-74 material, , where one of the Cu-O bonds is elongated. Such distortion results in a low partial positive charge of the Cu metal site [297], and could lead to a weak interaction with guest molecules compared to those of other transition metal homologues due to the long interaction distance between the Cu^{2+} metal sites and the adsorbed gas molecules.[297,298]

By replacing the "dobdc" linker of the regular MOF-74 with a short "dhfuma" linker, we obtain the M_2(dhfuma) MOF framework with the same topology as M_2(dobdc).[287] Similarly, this new MOF structure offers the advantage of being an isostructural series of frameworks that can be formed with a variety of metals, providing an additional level of control to tune the framework for specific interactions. The crystal structure of the primitive rhombohedral unit cell containing 108 atoms (18 Mg, 54 O, and 36 C) was obtained from, [287] and the rest of the M-MOF-74 (M=Cu, Fe, Co, Ni and Mn) series have been derived by substituting the Mg element by the M-metal series, respectively.

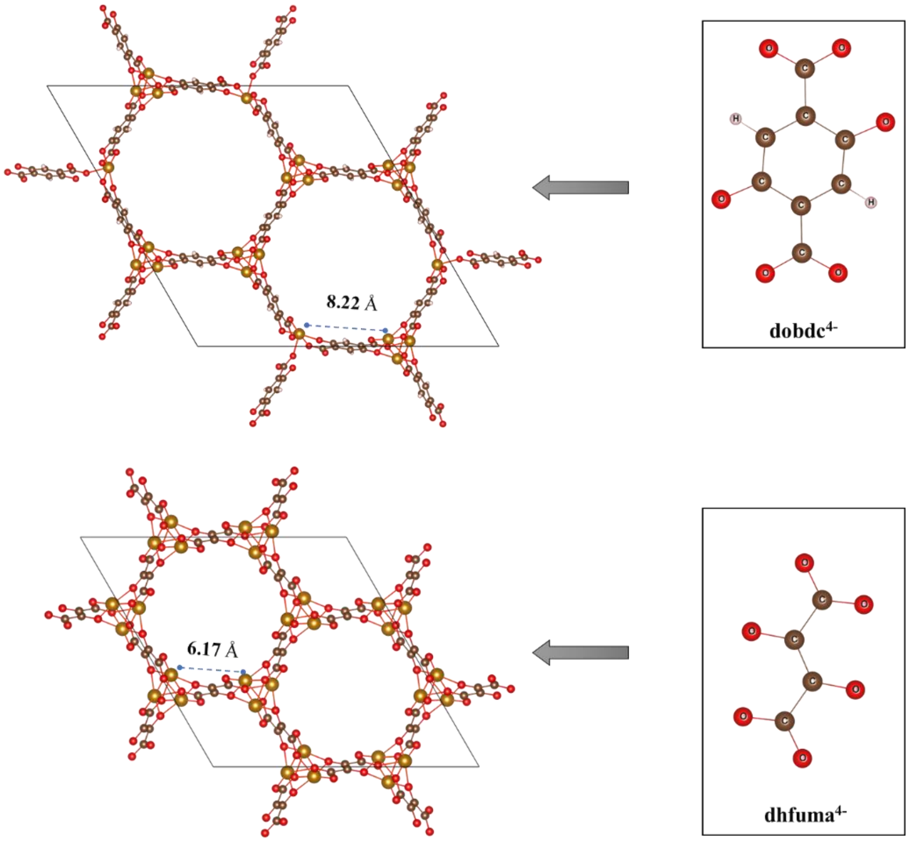

Figure 5.2: “dobdc” organic ligand is visually compared to the “dhfuma” ligand, along with their corresponding MOF-74 frameworks up) M_2(dhfuma) and down) M_2(dobdc).

Using the same approach, a complete relaxation of the atoms and lattice parameters of M-MOF-74 has been carried out and the resulting parameters are listed in Table 5.2. The a=b lattice parameters of M_2(dhfuma) were comparatively 26-28% smaller than those of M_2(dobdc), whereas the c lattice parameters were maintained at almost the same values as those of the M_2(DOBDC) series. Indeed, as a direct result of this smaller a- and b-axis, the unit cell volume of M_2(dhfuma) was 50% smaller than that of M_2(dobdc). Consequently, the metal-to-metal distance has been shortened to 6.17 Å compared to 8.22 Å for M_2(dobdc) (Figure 5.2). We therefore hypothesized that greater selectivity for iodine compounds could be achieved in M-MOF-74 materials by altering the affinity of metal sites. Thus, the two organic linkers (dobdc and dhfuma) were incorporated into the M-MOF-74 series structures (where M=Mg, Zn, Cu, Fe, Co, Ni and Mn) and their performance for selective iodine capture is thoroughly discussed.

Considering the large kinetic diameter of I_2 (~5 Å) and ICH_3 (~5-6 Å), a 1x1x2 supercell was realized for the adsorption of these iodine gas molecules to avoid the interaction with their periodic image along the c axis.

Table 5.2: A comparison of the calculated lattice constants for M_2(dobdc) and M_2(dhfuma) frameworks.

	M_2(dobdc)			M_2(dhfuma)		
	$a = b$ (Å)	c (Å)	V (Å^3)	$a = b$ (Å)	c (Å)	V (Å^3)
Cu	25.96	6.34	3702.6	18.98	6.23	1944.1
Fe	26.28	6.94	4149.3	19.06	6.94	2181.8
Co	26.05	6.88	4041.5	18.81	6.85	2097.9
Ni	25.90	6.80	3945.8	18.72	6.74	2043.9
Mn	26.32	7.13	4278.8	18.84	7.27	2235.6

5.4 Results and discussion

As mentioned above, DMF removal on M-MOF-74 (M=Fe, Co, Mn, Ni, Cu, Mg, and Zn) results in highly reactive open metal sites (OMS) that are effective and used as an adsorption site for a wide range of applications. The organic linker in MOF-74 has been reported to provide low electrostatic and dispersive forces. On the basis of the above, the present work mainly focuses on the adsorption of gas molecules on the unsaturated of M-MOF-74 while excluding the absorption on the organic linkers. In addition, Lee et al [293], in their theoretical study of the adsorption of 14 small molecules on the MOF-74 series, reported that the zero-point energy (ZPE) and thermal correction via phonon calculations are expected to be equal to (3-6 kJ mol^{-1}) and would not significantly alter the qualitative results. Therefore, these corrections are not applied to the following adsorption energy results.

To achieve the most stable configurations of I_2, ICH_3, CO and H_2O adsorption on M-MOF-74, a geometry optimization was performed on several initial orientations of the gas molecules in combination with different positions at different distances and directions over the metal sites. It appears that all studied molecules were pulled close to the metal site, confirming the strong affinity of the CUS site of MOF-74 against the organic linker. Furthermore, the optimized structures for all the same gas trial configurations yield the same final configurations where CO always interacts through its C, ICH_3 through its iodine and H_2O through its oxygen. The adsorption energies (E_{ads}), the minimum interaction distance (d_{min}) and the Bader charge transfer (Δq) are summarized in Table 5.2 and 5.3. The CDD maps of the most stable configurations are shown in Figure 5.2 and 5.3.

5.4.1 Adsorption of guest molecules on the M_2(dobdc) MOF

5.4.1.1 Structure description and adsorption energies of the volatile iodine compounds I_2 and ICH_3

According to the adsorption energy calculations, all of the seven selected metal sites of MOF-74 can adsorb gas molecules of iodine compounds to some extent. Among all adsorbates, Zn and Mg showed the weakest affinity for the I_2. The latter gets preferentially adsorbed in a 'flat' configuration i.e., I—I being parallel to the metal site with its iodine atom being situated over Mg and Zn metal sites at 3.25 and 3.19 Å, respectively. The calculated interaction energies were -69.4 and -68.4 kJ/mol, including -49.1 and -64.5 kJ/mol of dispersion contributions. Higher interaction energies of -85.7, -97.5, -104.2 kJ/mol have been calculated on Cu, Co, and Ni, respectively, including an average of 63 kJ/mol dispersion contribution. In addition, I_2 got dissociated during adsorption on Mn and Fe metal sites into two I atoms bound to two pairs of MOF-74 metal sites (Figure 1). The bond distance between the two iodine atoms was elongated by $I \cdots I = 4.56\ and\ 4.92$ Å, respectively, and each atom was shown to interact at distances $Mn \cdots I = 2.67$ Å and $Fe \cdots I = 2.58$ Å resulting in a strong adsorption energy of -94.9 and -116.4 kJ/mol for Mn and Fe, respectively (Table 5.3). The ICH_3 gas molecule was less strongly adsorbed than I_2 and preferentially adsorbs in a 'flat' configuration i.e., I-C being parallel to the metal site, with the atom head of iodine over the MOF-74 metal site. The computed adsorption energies differed in a slight magnitude by 19 kJ/mol and followed the order of Ni > Fe > Co > Mn > Zn > Mg > Cu. The bond length between the gases and the metal site supported this order, with a minimum of 2.87 Å for Ni and a maximum of 3.19 Å for Cu.

Table 5.3: Calculated adsorption energy (E_{ads}), minimum adsorption distance (d_{min}) and charge transfer (Δq) between I_2 or ICH_3 gas molecules and MOF-74 metal site.

	I_2				ICH_3			
	d_{min} (Å)	E_{ads} (E_{disp}) (kJ/mol)	Bader Charge difference		d_{min} (Å)	E_{ads} (E_{disp}) (kJ/mol)	Bader Charge difference	
			I(molecule)	M (metal site)			I(molecule)	M (metal site)
MOF-Mg	3.25	-69.4 (-49.1)	-0.02	0.00	3.14	-64.1 (-47.8)	0.02	0.00
MOF-Zn	3.19	-68.4 (-64.5)	-0.01	0.00	2.92	-65.9 (-49.1)	0.02	0.00
MOF-Cu	3.39	-85.7 (-60.5)	-0.04	0.01	3.19	-60.8 (-42.2)	-0.03	0.01
MOF-Fe	2.58	-116.4 (-67.3)	0.40	-0.20	2.94	-76.0 (-45.2)	-0.05	0.03
MOF-Co	2.92	-97.5 (-64.0)	-0.04	0.03	2.89	-75.8 (-48.9)	-0.06	0.04
MOF-Ni	2.98	-104.2 (-65.8)	-0.05	0.06	2.87	-80.7 (-50.1)	-0.07	0.05

MOF-Mn	2.67	-94.9 (-60.6)	0.49	-0.07	3.05	-69.7 (-40.8)	-0.02	0.02

5.4.1.2 Carbon monoxide and water contaminant's structure description and adsorption energies

In the case of carbon monoxide adsorption, the dominating configuration was the upright one, with the carbon end of the gas molecule being attached to the metal site and the oxygen end pointing toward the center of the pore cage. The total interaction energy (Table 5.3) reached a maximum of −71.5 kJ/mol with CO strongly interacting with Co-MOF-74 at 1.94 Å, followed by Ni with -57.7 kJ/mol at 2.07 Å. The weakest interaction energy was observed for Cu and Zn with an adsorption energy of -23 and -35.4 kJ/mol, respectively. These results agree with previous reported studies. Investigation of J.R. Long and co-workers [299] on CO/H_2 and CO/N_2 separations in metal-organic structures showed that the isosteric heats of adsorption of CO at 298 K follow the order Ni > Fe > Mg > Mn > Zn, consistent with our findings (Table 5.4). They further observed that the isosteric heat decrease at higher temperatures. For example, their predicted isosteric heat for CO adsorption on Ni provided a result of -52.7 kJ/mol and -40.4 kJ/mol at 289 K and 398 K respectively, ~5 and ~ 17 kJ/mol lower than our computed DFT 0K adsorption energies. Similar finding were also reported by S. Bordiga et al [300]. Using DFT, they predicted that CO interacts with Mg-MOF-74 at a distance of 2.48 Å with an adsorption energy of -34.3 kJ/mol. The slight difference of ~8 kJ/mol with our results stems first, from their consideration of the full-load adsorption of 6 CO molecules on a 6-site CUS structure and second, from the employment of a different level of theory (hybrid B3LYP and exclusion of Hubbard 'U' corrections). For copper, S.Sholl et al.[301] investigated the interaction of CO with CuBTC (a MOF structure with open metal site characterized by Cu dimers), and reported an interaction energy of 27.9 Å, being closer to our finding on the open metal site of Cu-MOF-74 (Table 5.4).

In the case of the water molecule, the most stable configurations corresponded to a symmetrical arrangement of hydrogens oriented towards the pore cage, with oxygen placed on top of the metal site. As predicted by the HSAB theory [92,302], Mg being the hardest acidic site in the above selected list of divalent metal cations, exhibited the highest affinity towards the water molecule with an O-Mg distance of 2.14 Å and an interaction energy of -83.0 kJ/mol, the dispersion corrections staying at only -19.8 kJ/mol. Interaction energy with water for the borderline acids as classified by the HSAB varied between -77.1 kJ/mol for Ni and -39.21 kJ/mol for Cu (Table 5.4). An excellent agreement between our findings and the works of H. Baoling [303] and Berend Smit [304] in what regards the orientation of the molecule, interatomic distances, and interaction energy is obtained. In particular, the former study revealed that the oxygen end of the water molecule bounds at the top of the zinc metal site at 2.23 Å with an adsorption energy of -67.5 kJ/mol, identical to our listed results in Table 5.4. The latter work reported adsorption energies of water along with their interaction distances with the metal site as follows: Ni (-78.1 kJ/mol and 2.13 Å), Fe (-63.5 kJ/mol and 2.28 Å), Cu (-36.4 kJ/mol and 2.39 Å), Co (-65.7 kJ/mol and 2.21 Å), Mg (-81.6 kJ/mol and 2.13 Å) and Zn (-64.8 kJ/mol and 2.22 Å), similar to our computed results (Table 5.4).

Table 5.4: The Adsorption energy (E_{ads}), minimum adsorption distance (d_{min}) and charge transfer (Δq) between the gas molecules and MOF-74 metal site.

	CO				**H_2O**			
	d_{min} (Å)	E_{ads} (E_{disp}) (kJ/mol)	Bader Charge difference		d_{min} (Å)	E_{ads} (E_{disp}) (kJ/mol)	Bader Charge difference	
			C(molecule)	M (metal site)			O(molecule)	M (metal site)
MOF-Mg	2.44	-42.6 (-16.5)	0.06	0.00	2.14	-83.0 (-19.8)	0.10	0.01
MOF-Zn	2.30	-35.4 (-26.6)	-0.02	0.00	2.23	-67.8 (-22.3)	0.02	-0.02
MOF-Cu	2.28	-23.0 (-17.1)	0.01	0.00	2.41	-39.2 (-16.4)	0.01	-0.03
MOF-Fe	2.13	-53.3 (-17.2)	0.05	-0.06	2.27	-63.2 (-16.8)	0.02	0.07
MOF-Co	1.94	-71.5 (-20.7)	0.06	-0.05	2.21	-65.8 (-20.8)	0.01	-0.03
MOF-Ni	2.07	-57.7 (-20.6)	-0.03	0.01	2.13	-77.1 (-20.9)	0.03	-0.01
MOF-Mn	2.40	-39.1 (-16.7)	0.03	-0.02	2.27	-69.7 (-24.2)	0.06	-0.04

5.4.1.3 Bader charge analysis and iso-surface electron density

Bader charge analysis was carried out to examine the net charge transfer between M-MOF-74 and adsorbed gas molecules. The charge difference (Δq) and charge density difference (Δρ) were calculated using Equations 3 and 4, respectively. Corresponding results are listed in Table 5.3 and 5.4 and plotted in Figure 5.3 and 5.4, respectively. A negative value of (Δq) means that the atom lost electrons, while a positive value implies that the atom gained electrons. For the sake of simplicity, the CDD maps are displayed only for the most strongly and weakly interacted molecule-MOF, while the rest are kept in the supplementary information document.

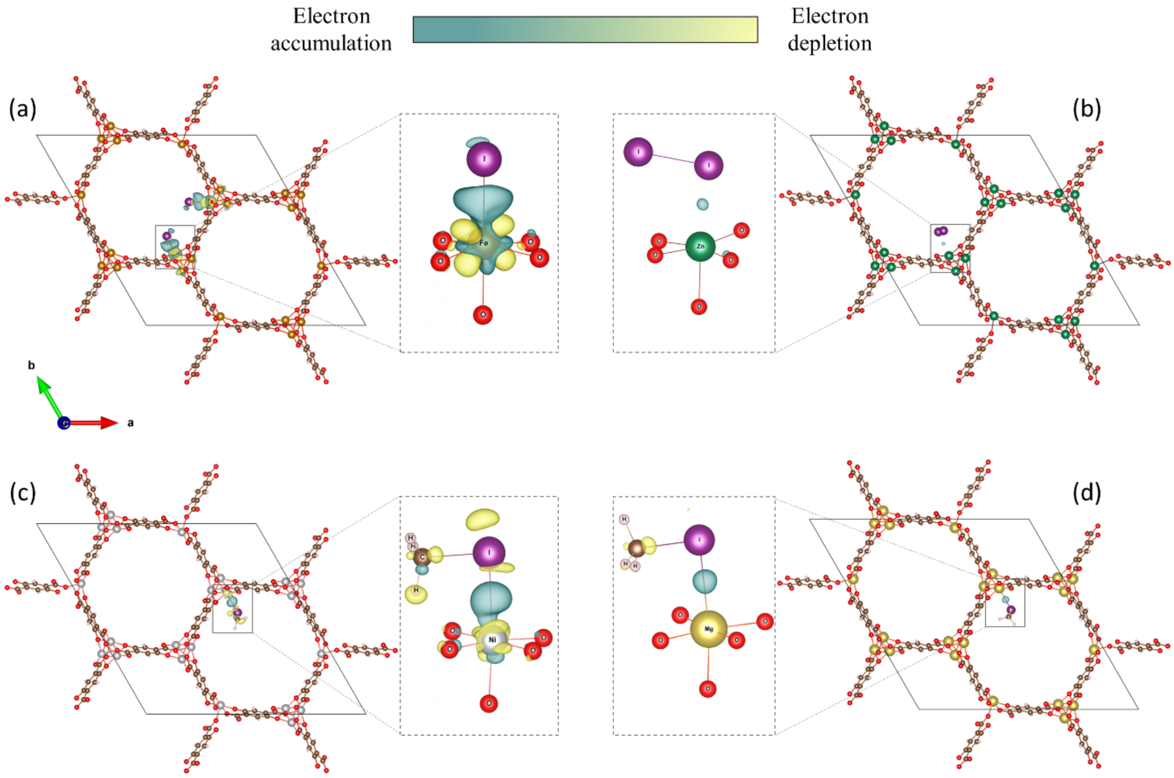

Figure 5.3: Iso-surface electron density for the most stable configuration of I_2 adsorption on a) Fe-MOF-74, b) Zn-MOF-74, and ICH_3 adsorption on c) Ni-MOF-74, d) Mg-MOF-74.

Upon dissociation of I_2 on Fe-MOF-74. Bader charge analysis reveals a significant positive charge excess on the bound iodine atoms of 0.40 e, while a significant negative charge excess was observed on the MOF metal site atoms of -0.20 e. This indicates that charges are transferred from the Fe metal site to the iodine atom. Indeed, from the CDD plots in Figure 5.3, a strong charge accumulation is observed at the iodine atom, which supports the Bader charge difference findings, that the Fe metal sites donate electrons to the dissociated I. Consequently, the magnetic moment of the Fe-MOF-74 structure has been elevated from 72 μ_B for the bare structure to 74 μ_B after I_2 adsorption. Such high adsorption energies, small adsorption distances, and significant charge transfer predict chemical bond formation between Fe and I atoms. A similar pattern was observed for the dissociation of I_2 on Mn-MOF-74. However, the distance between the two separated iodine atoms was 0.4 Å shorter than in the case of Fe. This results in a smaller charge transfer from Mn to I (-0.07 e) supported by the slight charge depletion around the Mn metal site and thus a lower adsorption energy. An opposite charge transfer pathway was observed for the non-dissociated I_2 adsorption. Figure 5.3 shows a negative charge excess found in the M-MOF-74 (M=Cu, Co, and Ni) metal sites, while positive charge was observed on the iodine atom. This indicates that charges are transferred from the iodine molecules to the CUS site. Furthermore, Bader charge analysis and CDD maps revealed no charge transfer between Zn and I_2, in agreement with the lowest adsorption energy already reported.

For ICH_3, excepted for Mg- and Zn-MOF-74 where no charge transfer occurred. a modest charge transfer reaching a maximum of 0.05 e was observed between the iodine atom of ICH_3 and the Ni metal site of MOF-74 (Table 5.3). The CDD map in Figure 5.3 supports these results with a strong charge accumulation around the Ni metal site. In addition, a slight charge depletion is observed on the hydrogen atom of the molecule, indicating the formation of a hydrogen bond with the oxygen of the MOF-74 ligand. This further clarifies the strong adsorption energy reported for Ni-MOF-74 in Table 5.3.

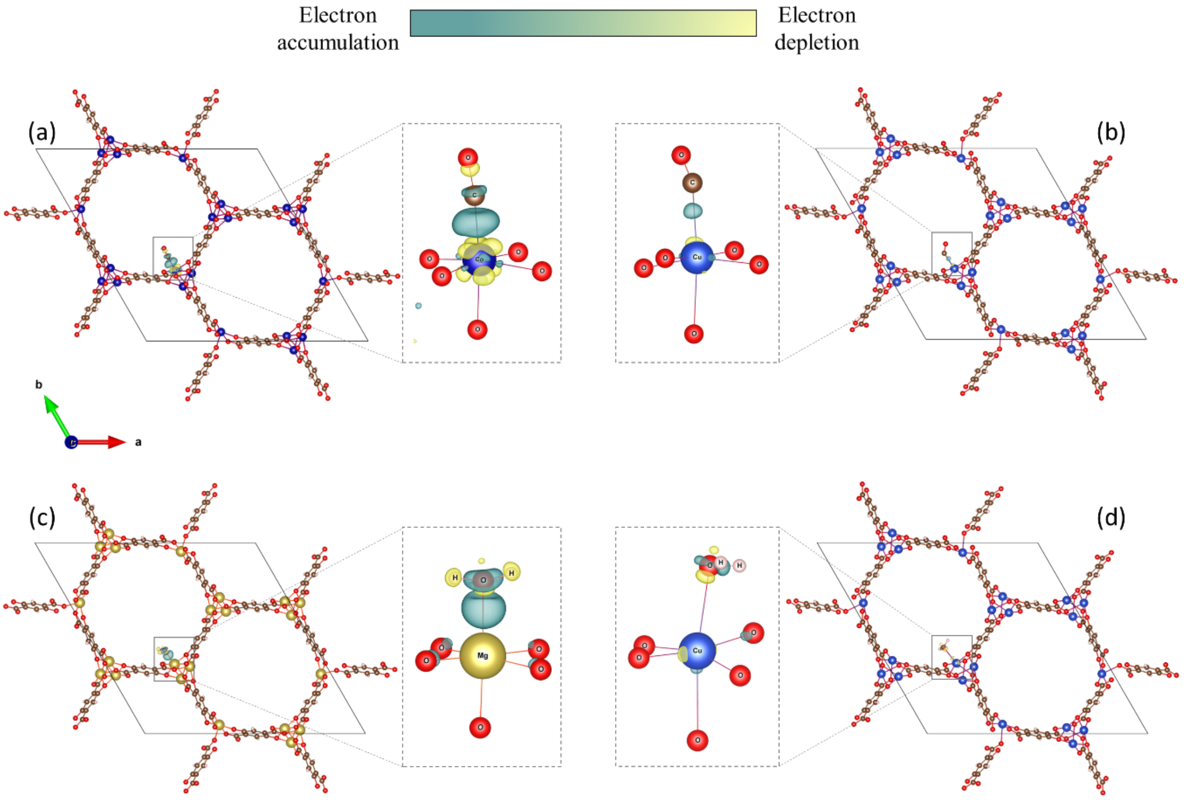

Figure 5.4: Iso-surface electron density for the most stable configuration of CO adsorption on a) Co-MOF-74, b) Cu-MOF-74, and H2O adsorption on c) Mg-MOF-74, d) Cu-MOF-74.

As illustrated in Figure 5.4, the adsorption of CO on Co-MOF-74 is accompanied by a significant re-ordering of the electronic density. The majority of the charge is depleted from the vicinity of MOF metal site as revealed by an excess of positive charge of 0.05 e assigned to it by Bader charge analysis. This indicates that the charge-flow is directed toward CO. In the case of H_2O, a high negative charge of 0.1 e was assigned to the oxygen atom of water when adsorbed on Mg-MOF-74, this possibly owing to the sp^3 hybridization nature of the molecular orbitals of water's O. The slightly tilted metastable configuration of H_2O (Figure 5.4), causes the H-O-H bond angle to decrease from the ideal 109º to 105º upon adsorption on Mg, leaving the two lone pairs of the water molecules degenerate, which is further evidenced by the difference in charge density in the

Figure 5.4 where the strong charge accumulation between the oxygen lone pairs and Mg-MOF-74 is clearly shown.

5.4.1.4 Thermodynamic selectivity

The interaction energies of water or CO have been subtracted from those of iodine compounds, aiming to identify the most promising M-MOF-74 structure capable of capturing I_2 and ICH_3 in the presence of contaminants (H_2O and CO). Figure 5.3 shows values obtained for the various M-MOF-74 structures. The higher the value, the stronger the interaction between iodine compounds and M-MOF-74 structure. Moreover, since CO and H_2O concentrations in nuclear plants are higher than those of I_2 and ICH_3, the highest binding energy difference is desirable.

Mg and Zn, although presenting a higher binding energy of I_2 and ICH_3 than that of CO, they both display a much higher affinity for water over the rest, providing no interesting results for our intended nuclear compound capture application. On the other hand, Ni and Mn show good affinity for I_2 in the presence of CO and water, but concurrently exhibit similar affinity for H_2O and ICH_3, indicating a strong chance of competitive adsorption between the two molecules. As shown in Figure 5.3, owing to the earlier reported strong interaction of cobalt with CO molecule, it was expected that CO would play a detrimental role in the adsorption of iodine compounds, in particular for ICH_3. Copper (Cu) and Iron (Fe) are the only MOF-74 metal sites showing a higher affinity for I_2 and ICH_3 than for H_2O and CO. The highest I_2-H_2O and I_2-CO difference was reported for iron with values of 53 and 63 kJ/mol respectively, while for ICH_3-H_2O and ICH_3-CO, copper was on the lead by 17.6 and 33.8 respectively. Thermodynamically, these results reveal that Fe-MOF-74 and Cu-MOF-74 are clearly the most interesting MOF-74 structures for the selective capture of Iodine compounds from carbon monoxide and water.

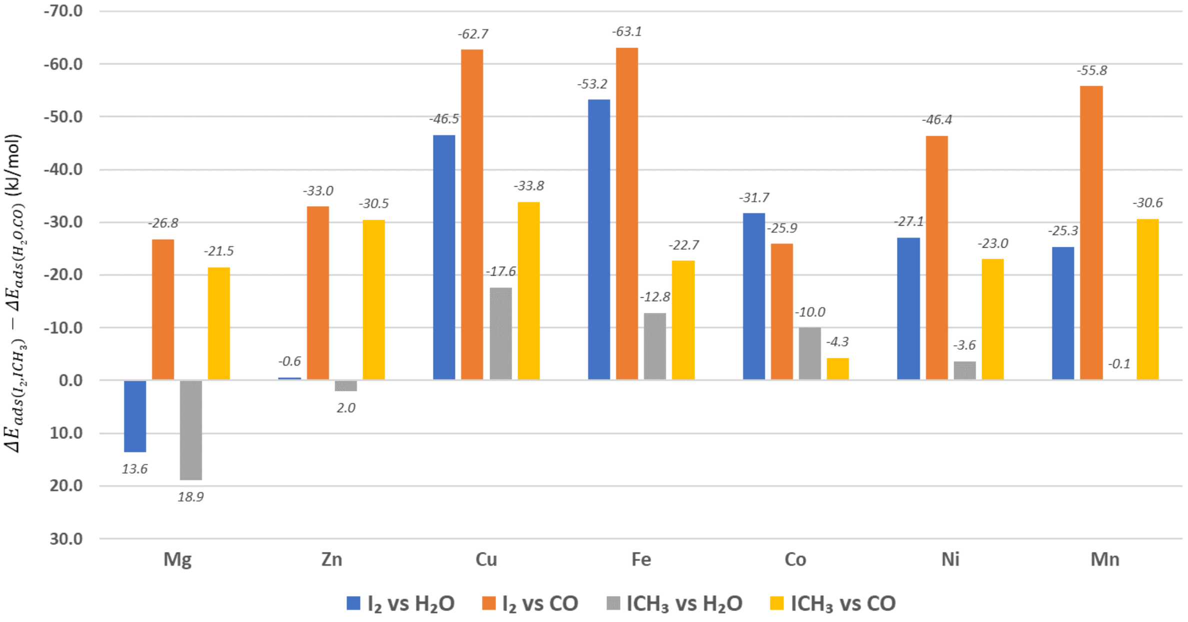

Figure 5.5: The difference in total interaction energies between ($I2$, and $ICH3$) and ($H2O$, and CO) in M-MOF-74 series (M=Mg, Zn, Cu, Fe, Co, Ni, and Mn,) calculated using the PBE + D2 level of theory.

To proceed with our exploration of more relevant MOFs materials to selectively capture iodine compounds in the presence of water and CO, we hypothesized that higher selectivity could be achieved in these promising M-MOF-74 materials by changing the affinity of the metal site for the adsorbed iodine compounds, to this end altering the MOF ligand is a promising choice.

5.4.2 Adsorption of guest molecules on the M_2(dhfuma) MOF

The computed interaction energies of I_2, ICH_3, H_2O and CO on M_2(dhfuma) were on average 18.2, 6.0, 3.0 and 2.9 kJ/mol stronger than on M_2(dobdc) (Table 5.5). Interestingly, the replacing of dobdc ligand with dhfuma linker shortened the metal-metal distance making the cross adsorption (i.e., interaction with two metal sites at the same time) of larger molecules like I_2 and ICH_3 with MOF metal sites possible, thus enhancing their affinity for the iodine compounds.

Table 5.5: Adsorption energy (E_{ads}), minimum adsorption distance (d_{min}) and charge transfer (Δq) between the interacted atom of gas molecules (Iodine atom for I_2 and ICH_3, Carbon atom for CO and oxygen atom for H_2O) and MOF-74 metal site.

	d_{min} (Å)	E_{ads} (E_{disp}) (kJ/mol)	Bader Charge difference		d_{min} (Å)	E_{ads} (E_{disp}) (kJ/mol)	Bader Charge difference	
			Y(molecule)*	M (metal site)			In(molecule)*	M (metal site)
		I_2				ICH_3		
MOF-Cu	3.35	-103.7 (-67.2)	-0.05	0.01	3.25	-72.9 (-55.2)	-0.03	0.01
MOF-Fe	2.72	-125.4 (-76.7)	0.38	-0.07	3.02	-72.9 (-59.3)	-0.03	0.03

MOF-Co	2.96	-109.9 (-72.6)	-0.08	0.03	2.92	-85.1 (-58.4)	-0.06	0.04
MOF-Ni	2.93	-120.4 (-78.2)	-0.05	0.06	2.91	-79.3 (-63.4)	-0.06	0.04
MOF-Mn	2.77	-130.1 (-72.1)	0.50	-0.04	3.11	-73.7 (-56.9)	-0.03	0.02
		CO				**H_2O**		
MOF-Cu	2.21	-32.2 (-19.1)	0.02	0.00	2.40	-51.6 (-15.8)	0.01	-0.03
MOF-Fe	2.14	-47.9 (-16.7)	0.06	-0.06	2.25	-63.3 (-18.7)	0.02	-0.03
MOF-Co	1.94	-73.3 (-21.1)	0.06	-0.05	2.20	-67.0 (-21.4)	0.02	-0.04
MOF-Ni	2.06	-59.1 (-22.4)	-0.03	0.01	2.13	-80.5 (-22.9)	0.03	-0.01
MOF-Mn	2.37	-40.8 (-20.5)	0.06	-0.03	2.30	-67.4 (-17.6)	0.07	-0.03

*is the molecule atom interacting with the MOF metal site iodine for I_2, iodine for ICH_3, carbon for CO and Oxygen atom for H_2O

Similar to M_2(dobdc), Ni2(dhfuma) and to a lesser extent Co2(dhfuma) exhibit poor affinity for ICH_3 in the presence of water and carbon monoxide, respectively, and continue to be of no interest for our challenging application. In contrast, copper's affinity has further improved as a result of using this alternative linker and highlighted Cu2(dhfuma) MOF structure as a promising material. The total interaction energy of Cu2(dhfuma) reaches a maximum of -103.7 kJ/mol for the strongly interacting I_2 molecule, followed by ICH_3 with -72.9 kJ/mol while H_2O and CO gas molecules weakly interacted with Cu-MOF, with an adsorption energy of -51 and -32 kJ/mol, respectively (Table 5.5). However, the significantly large contributions of long-range dispersion forces of -67.2 and -55.2 kJ/mol for I_2 and ICH_3, respectively, were in line with the long metal-radionuclide molecules interaction distances of 3.35 and 3.25 Å, respectively. Bader charge analysis and CDD maps further supported these results revealing a weak charge transfer between the copper metal site and radionuclides molecules (Figure 5.7).

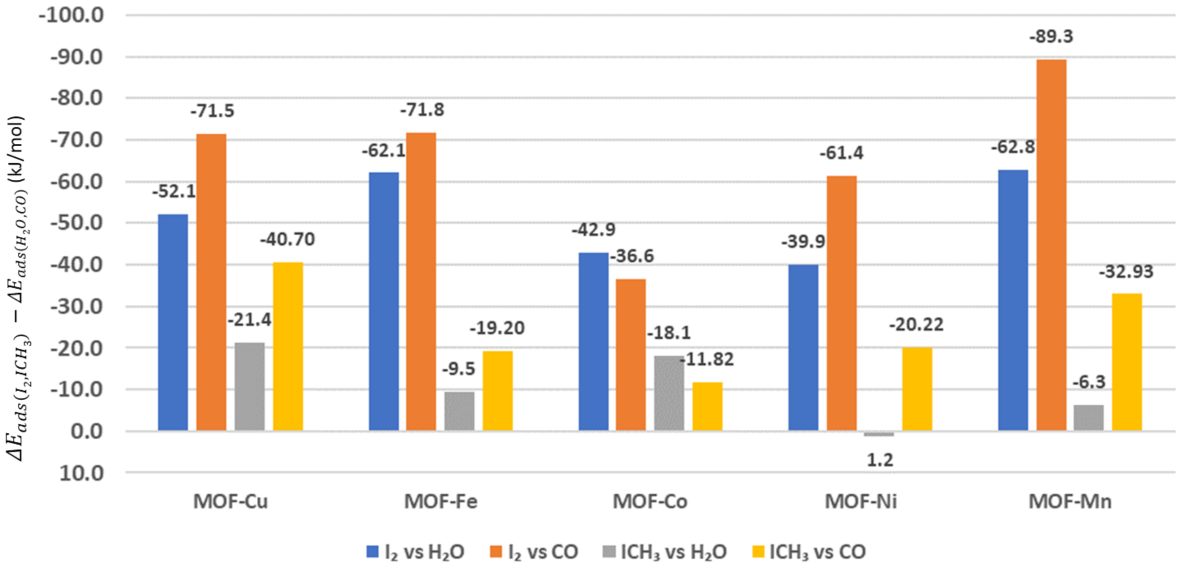

Figure 5.6: The difference in total interaction energies of I2, ICH3, H2O, and CO in M_2(dhfuma) series (M=Mg, Zn, Cu, Fe, Co, Ni, and Mn,) calculated using the PBE + D2 level of theory.

Upon adsorption on Mn-MOF and Fe-MOF, the iodine molecule seems to retain the same tendencies as in M2 (dobdc) with I_2 dissociating into two I atoms bound to two distinct MOF metal sites at distance equal to $Mn \cdots I = 2.79$ Å and $Fe \cdots I = 2.67$ Å (Figure 5.7). Owing to the shorter metal-to-metal distance in M_2(dhfuma) compared to that in M_2(dobdc), the bond distance between the two iodine atoms was less elongated with $I \cdots I = 3.59$ and 3.89 Å, for Fe and Mn respectively. The highest computed adsorption energies for I_2 are observed for Mn and Fe among all the studied metals of -130.1 and -125.4 kJ/mol, respectively. Bader charge analysis (Table 5.5) along with CDD plots indicated that Fe and Mn MOF metal sites donates electrons to the dissociated iodine atoms. Consequently, the magnetic moment of the Mn- and Fe-MOF-74 structures changed upon I_2 adsorption from 90 μB to 88 μB, and from 72 μB to 74 μB, respectively. The interaction of contaminants (H_2O and CO) on Mn and Fe-MOF was significantly weaker than that of the iodine gas molecule. Figure 5.6 indicates that the interaction of I_2 on Mn- and Fe-MOF is in average 62 and 83 kJ/mol stronger than that of H_2O and CO, interestingly higher than the already reported on M_2(dobdc). Water and carbon monoxide are not expected, therefore, to play a detrimental role on the volatile radionuclides gas molecules (I_2, ICH_3) adsorption in these M_2(dhfuma) MOF structures. In contrast to I_2, the radionuclide gas molecule ICH_3 show no dissociation and gets adsorbed with the iodine atom interacting with Fe and Mn metal sites at distances 3.02 and 3.11 Å and corresponding interaction energies of about -72.9 and -73.7 kJ/mol, respectively. These computed energies were more than 20 kJ/mol stronger than that of CO, while only 6.3 and 9.5 kJ/mol favorable than of H_2O (Figure 5.6). Therefore, Cu2, Mn2, and

Fe_2(dhfuma) are thermodynamically the most interesting MOF materials for the selective capture of I_2, ICH_3 in the presence of H_2O and CO.

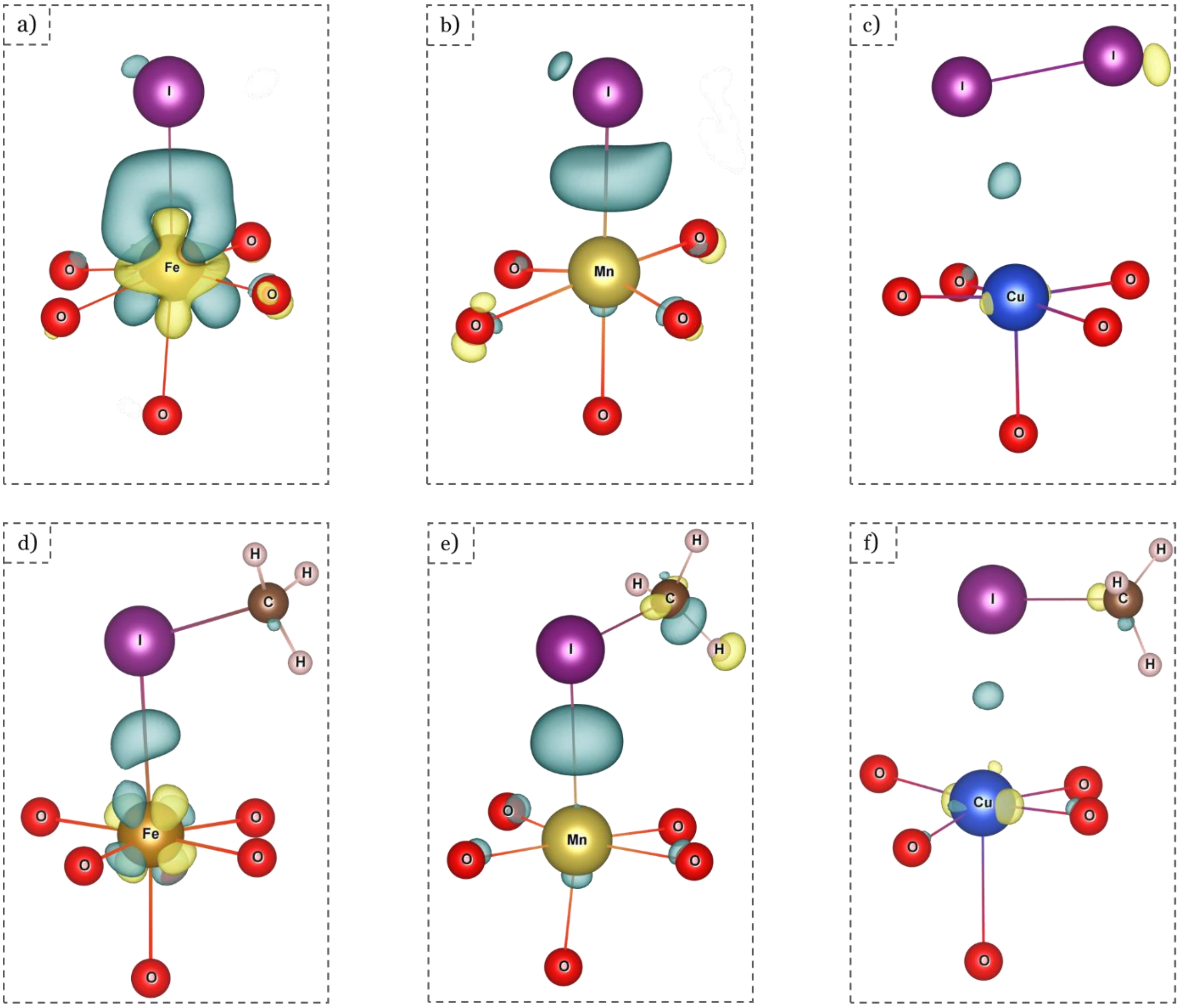

Figure 5.7: charge density difference of the adsorption of I_2 and ICH_3 a,d) Fe_2(dhfuma), b,e) Mn_2(dhfuma), and c,f) Cu_2(dhfuma), respectively. The iso-surface of CDD maps is set as 0.05 e/Å3 where green color denotes electron accumulation and yellow color denotes electron depletion.

5.5 Conclusions.

In summary, we computed from DFT calculations the adsorption of I_2, ICH_3, CO and H_2O molecules on MOF-74 series aiming to find a MOF structure that can readily adsorb iodine species gas molecules (I_2 and ICH_3) and separate them from the rest of the gases. Among all the MOF-74 metal ions (Mg, Zn, Cu, Fe, Co, Ni, Mn), Fe-MOF-74 and Cu-MOF-74 display the most interesting results for the selective capture of iodine compounds in the presence of carbon monoxide and water.

Upon replacing the “dobdc” ligand with the smaller “dhfuma”, the metal-to-metal distance was shortened, making it possible for larger molecules such as I_2 and ICH_3 to be cross-adsorbed (i.e., to interact with two metal sites at the same time). This resulted in ~13 kJ/mol higher interaction energies for I_2 and ICH_3 than in the DOBDC series, revealing that Cu_2, Mn_2, and Fe_2(dhfuma) are the most attractive MOF materials for the selective capture of I_2, ICH_3 in the presence of H_2O and CO. Interestingly, the strong adsorption on Mn-MOF and Fe-MOF drives I_2 to dissociate into two I atoms bound to two distinct MOF metal sites at equal distances, resulting in a significant $\Delta E_{ads,I_2} - \Delta E_{ads,H_2O}(\Delta E_{ads,CO})$ of 62.1(71.8) and 62.8(89.3) kJ/mol for Fe_2 and Mn_2(dhfuma), respectively. Regarding Cu_2(dhfuma), I_2 got adsorbed with an interaction energy of 52.1 and 71.5 kJ/mol more strongly than H_2O and CO respectively. From a practical point of view, the strong chemi-sorption displayed by Fe and Mn will be extremely useful in the field of hazardous material handling (i.e., nuclear power plants) by providing additional protection, but it may prevent the reuse of the material, since the molecule is completely integrated into the MOF structure and its chemical identity cannot be recovered. On the other hand, the interaction of Cu was found to mainly controlled by long-range dispersion which provides the potential for a regenerable iodine capture material that can be highly attractive as an iodine gas preconcentrator for chemical sensing. However, referring to the interaction energies of Cu_2(dhfuma) strongly altered by the long-range dispersion and to the closeness of adsorption energies between ICH_3 and H_2O on the Mn- and Fe-MOF frameworks. Water is expected to play a detrimental role on the separation of gaseous radionuclide molecules (I_2 and ICH_3). To further verify this, ab initio molecular dynamics simulations at realistic conditions will be performed to investigate the co-adsorption of these iodine molecules versus water and carbon monoxide at higher temperature (413 K).

Chapter 6

NO_x diesel vehicle pollutants and technologies developed to limit their emissions

> "I see a future where driving to work or school doesn't have to cause pollution."
>
> - ***Bernie Sanders***

6.1 Introduction

Harmful gases emitted by industrial plants, power plants, automobiles, and other transport vehicles, threaten human health by entering the respiratory tract, lungs, and bloodstream. Nitrogen oxides (NO_x) emissions predominantly in the form of nitric oxide (NO) and nitrogen dioxide (NO_2) considered among the most dangerous pollutants.[305] NO being a colorless and odorless gas and NO_2 a highly reactive gas with a reddish-brown color, and a suffocating odor.[306] Diesel vehicles have the important share in NO_x formation. In fact, the UK department for transport estimates that 80% of NO_x emissions in areas where the country is exceeding NO_2 limits are due to transport, with diesel vehicles being the main culprit.[307] Consequently, this chapter focuses on NO_x emissions from diesel vehicles, their damage to human health and current technologies for controlling them.

6.2 NO_x emissions: impact on human health

Road transport air pollution, of which NO_x emissions are the major component, is responsible for adverse effects on public health and on the environment. According to the World Health Organization (WHO), 9 out of 10 people worldwide are exposed to air pollution and seven million people lost their lives due to these emission.[308] At present, pollutant emissions and especially NO_x emissions are causing serious respiratory diseases. The 2017 European Environment Agency (EEA) report reveals the level of NO_x air pollution, its threat to global warming, and states that in 2014, About 80,000 premature deaths in Europe are related to NO_x emissions.[305] According to WHO, about 80% of lung diseases and cancers are induced by air pollution, primarily by NO_x.[309] The effects of NO_x on human health are directly proportional to their atmospheric concentration and to the duration of inhalation. Low levels or short-term exposure cause eyes, nose and throat inflammation, headaches, chest tightness and nausea (Figure 6.1). Prolonged or severe exposure to NO_x gases causes severe cardiovascular diseases, breathing difficulties, cyanosis, asthma, and sometimes cancer.[310]

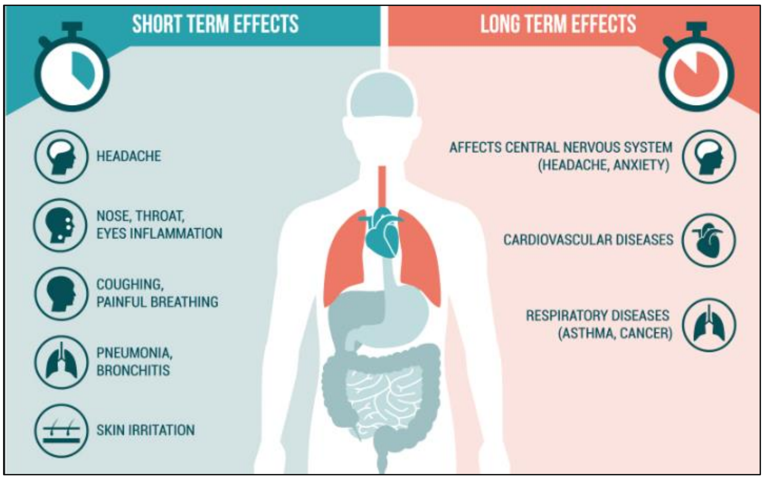

Figure 6.1: Health Effects of Air Pollution. [311]

For example, 14% of the overall premature deaths in 2019 were linked to nitrogen dioxide (NO_2) emissions in the EU.[312] Older people, as well as children and those with pre-existing health problems, are more susceptible to the health effects of these emissions.

6.3 NO_x emissions from diesel engines

Road transport is the largest contributor to NO_x emissions. Owing to their high-performance and low consumption of fuel, diesel engines operating in a wide range of applications in the transport sector emit a high rate of NO_x.

Generally, there are three mechanisms of the NO_x formation in diesel engines:

- **The fast mechanism**, linked to the rapid reactions taking place between nitrogen, oxygen, and hydrocarbon radicals.
- **The NO_x formation mechanism in fuel**, resulting from the reaction of nitrogen in the fuel, with oxygen.
- **The thermal mechanism**, resulting from the reaction of nitrogen with oxygen at high temperatures.[313] The latter mechanism considered as the main source of NO_x formation being described by Zeldovich mechanism reactions:

$$O + N_2 \leftrightarrow NO + N \qquad (1)$$

$$N + O_2 \leftrightarrow NO + O \qquad (2)$$

$$N + OH \leftrightarrow NO + H \quad (3)$$

The resulting NO emissions of reaction 1 and 3 can be converted to NO_2 or returned after to NO with the following mechanism reactions.

$$NO + HO_2 \leftrightarrow NO_2 + HO \ (4)$$

$$NO_2 + O \leftrightarrow NO + O_2 \ (5)$$

The thermal mechanism of NO_x is controlled by two key parameters: temperature and oxygen concentration. On one side, diesel engines operate on lean mixture (air>fuel) involving more oxygen than necessary. On the other side, the high compression ratios of diesel engines (14:1 to as high as 25:1) create high combustion temperatures. Both these factors provide the diesel engine a very efficient infrastructure for the NO_x emissions formation, considerably higher than those of gasoline engines.

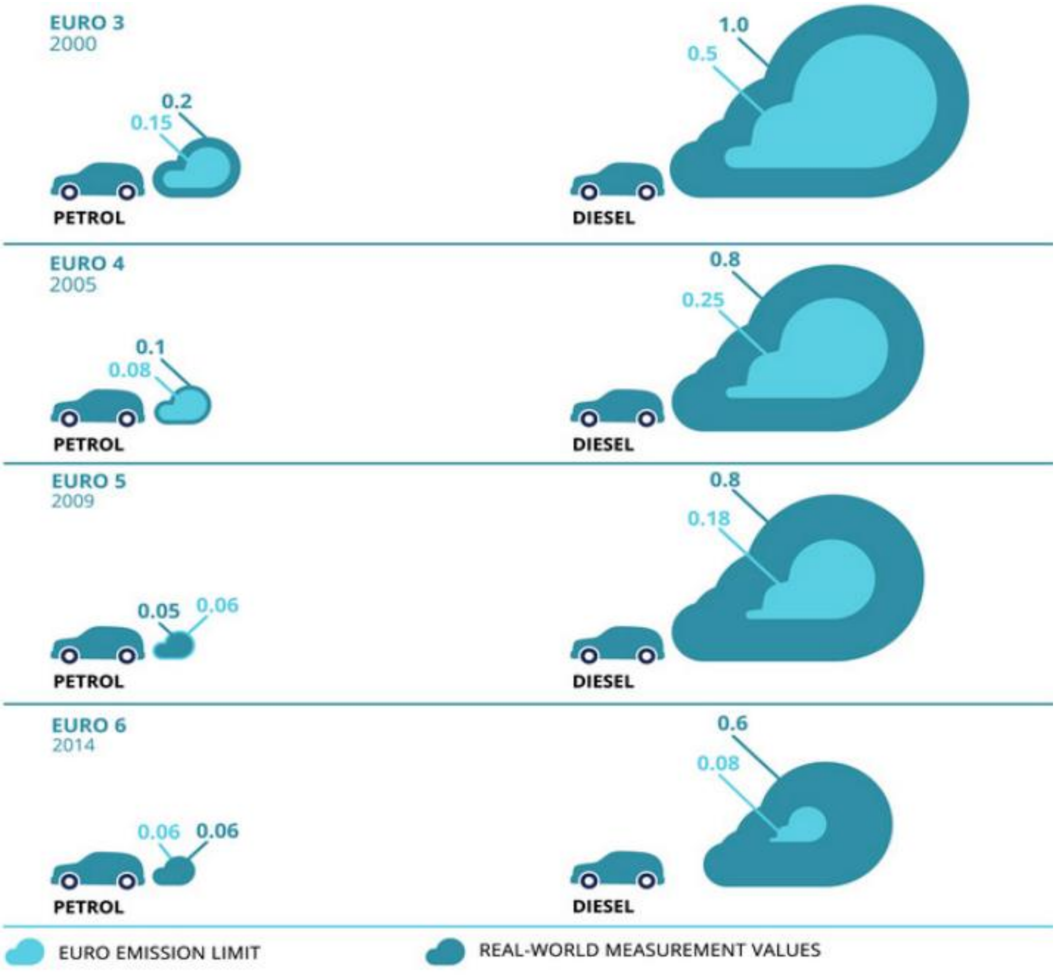

Figure 6.2: Comparison of NO_x emission standards for different Euro and classes.[314]

Since the introduction of the Euro 6 standard in the European Union in September 2014 (Figure 6.2-light blue), all new diesel passenger cars must comply with a NO_x emission limit equal to 0.08 g/km, significantly lower than the 0.18 g/km limit set in 2009 (Euro 5 standard). Nevertheless, in real driving conditions, automotive NO_x emissions can be significantly higher than the values certified by the manufacturers (Figure 6.20-dark blue). Concerning occupational exposure, the European Directive EU Directive (2017/164) imposes eight-hour occupational exposure limits for concentrations equal to no more than 2 and 0.5 ppm of NO and NO_2, respectively.

6.4 Current NO_x Reduction Technologies

Several strategies to limit NOx emissions have been evaluated and classified into two broad categories: pre-treatment and post-treatment methods, respectively, methods that reduce NOx emissions before and after they reach the engine exhaust port. A widely used pre-treatment method is exhaust gas recirculation (EGR), where part of the exhaust gas is re-injected into the fresh charge air of the combustion chambers, in order to reduce the NO_x concentration and the operating temperature. This process leads to a reduction in NO_x emissions of around 50%, but the downside is an exponential increase in particulate matter (PM) emissions. Additional post-treatment technologies exist to reduce the NO_x emissions. The most effective of these are NO_x storage reduction (NSR) and selective catalytic reduction (SCR).

6.4.1 Exhaust Gas Recirculation (EGR)

The EGR process reduces the oxygen level in the cylinder to prevent NOx formation, resulting in lower end combustion pressure and temperature. Exhaust gases reinjected into the cylinder release large amounts of CO_2 and H_2O, which increase the specific heat capacity of the intake charge (Figure 6.3), thereby lowering the temperature in the compression and combustion processes.[315] Displacement of some of the oxygen in the intake charge by the exhaust gases reduces the excess air ratio and increases the ignition delay. This in turn slows the mixing of oxygen with the fuel and thus the rate of combustion.

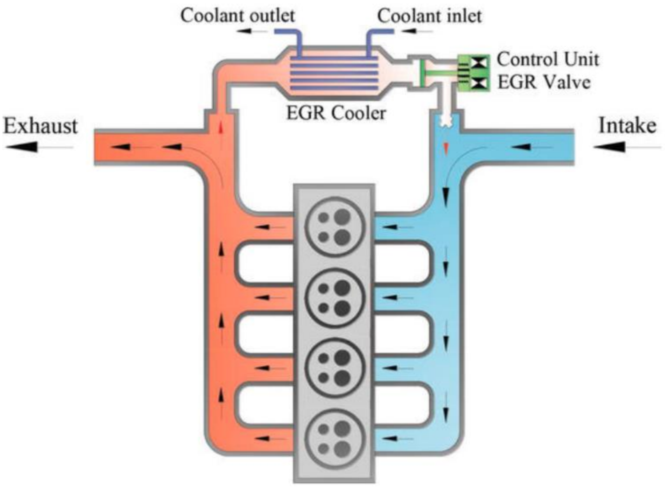

Figure 6.3: Schematic representation of the process (EGR).

Using the EGR process, Diesel engine NOx emissions can be reduced by about 50%. However, this process generates new pollutants, such as particulate matter (PM). Simultaneously, EGR causes a fuel consumption rise of ~2%.[316] As a result of the exhaust gas flow, the EGR system can negatively affect the quality of the lubricating oil, the durability of the engine, and the erosion of piston rings and cylinder liners.[317] These drawbacks and the development of new after-treatment technologies have led to the abandonment of the EGR process in the automotive industry.[318]

6.4.2 NO_x storage reduction (NSR)

NO_x storage reduction (NSR), also called Lean NO_x trap (LNT), was developed by Toyota Motor Corporation in the early 1990s.[319] This process works by alternating two phases:

- The first phase, which lasts one minute on average, corresponds to the storage of NO_x in a lean regime (in reducing agent), in the form of nitrate on a storage material.
- The second rich phase allows the reduction of nitrates to N_2 by catalyst surface of HC, CO and H_2, obtained by fuel over-injection.[320,321]

An NSR catalyst[322] consists of several components (Figure 6.4), in order to meet the desired functions:

- A metallic phase based on noble metals (Pt, Pd, Rh) which participates in two important steps of the mechanism: the oxidation of NO to NO_2 in a lean cycle before the storage step, and the reduction of NO_x in a rich phase.
- An alkaline storage material (Ba, K, Li) which allows the adsorption of NO_2 and its storage in the form of nitrates during the first phases (e.g., formation of $Ba(NO_3)_2$).
- A support with a large specific surface area, usually Al_2O_3, for the dispersion of the elements on its surface.

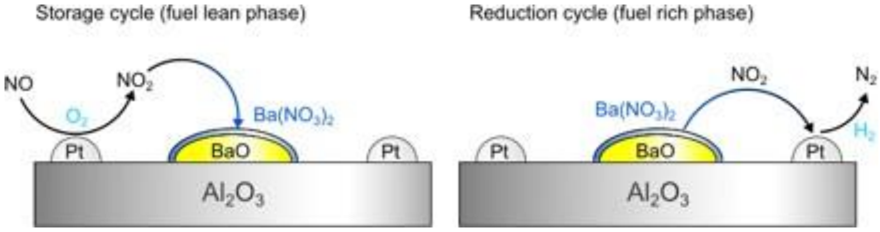

Figure 6.4: Schematic representation of the NO_x storage reduction process (NSR). Figure adapted from ref [323].

Currently, the most widely used catalyst in the NSR process is the $Pt/Ba/Al_2O_3$. However, its high sensitivity to sulfides results in very low resistance,[323] which can be improved by replacing Ba with K or Li.[324]

6.4.3 NO_x selective catalyst by ammonia (NH_3-SCR)

Another widely used technology to limit NO_x is selective catalytic reduction (SCR), which can reduce NO_x emissions from diesel engines by 80-100%. In the NH_3-SCR device, an aqueous urea solution called “Adblue” is commonly used to obtain ammonia and reduces NO_x to N_2 and H_2O (Figure 6.5), by the following scheme:

- Ammonia is first adsorbed on the catalytic active sites.
- Then reacts with NO to form a surface reaction intermediate.
- This intermediate decomposes to N_2 and H_2, also reducing the vanadium oxide sites, which are then re-oxidized by O_2, leading to recycling of the catalyst.

The most widely used catalyst in this device is V_2O_5-WO_3/TiO_2, due to its excellent activity, its selectivity, and its long lifetime. However, it operates efficiently in a narrow temperature range (250-400 °C) and is environmentally toxic due to its contains to vanadium.[325] The SCR can also have a diesel particulate filter (DPF). However, its regeneration exposes the catalyst to high temperatures (>700°C), leading to the formation of methyl and dimethyl substituted polycyclic aromatic hydrocarbons (PAHs), which are extremely toxic.[326,327] To reduce the toxicity of the catalyst, considerable efforts have been made by decreasing its vanadium loading or replacing this element with other metal components, such as Fe, Mn, Ce or Cu.[318]

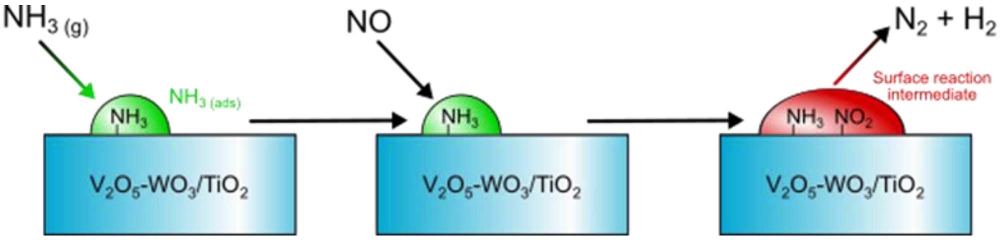

Figure 6.5: Schematic representation of the catalytic NOx reduction process NH3-SCR system on V2O5-WO3/TiO2. Figure adapted from ref [328].

The properties of commercial V_2O_5/TiO_2 catalysts can be significantly improved by undergoing aging treatment in an atmosphere of oxygen, water, and carbon dioxide. The improved catalyst exhibits greater resistance to sulfur and hydrocarbon poisoning as well as greater thermal stability.[329]

6.4.4 Limitations of the SCR system

There are major limitations associated with currently used SCR devices[318]:

- Their limited operation at high temperatures (250-400°C), which prevents the transformation of NO_x during the engine start-up and warm-up period. This period is accompanied by the release of NO_x and unburned hydrocarbons. Therefore, this device is not well suited for cold starting, and for non-road mobile machinery, running intermittently. However, it is well suited to light vehicles where the engine temperature rises rapidly due to continuous operation.

- The robustness and reliability of the catalytic materials not being guaranteed, the SCR device presents a risk of NH_3 release (reducing agent of the catalyst) into the environment.
- The risk of formation of toxic compounds such as HNO_3 or N_2O which need to be further treated. These compounds could represent a health problem for operators working in poorly ventilated confined spaces.

6.4.4.1 New proposals for NO_x emissions limitations.

The inefficiency of the SCR device at low temperature and cold start, has led the automotive industry to search for alternatives. Recently, Millo and Vezza (2012) [330] developed a passive NO_x adsorbent (PNA) in combination with an urea SCR catalyst, capable of adsorbing NO_x emitted by the engine during cold start, and then releasing it at higher temperatures (>200°C) compatible with the operation of the catalyst.[330]

Also, for the purpose of adsorbing NO_x, Ce-Zr mixed oxides have been evaluated in conjunction with Pt or Pd promoters. The incorporation of Ce cations and the use of Pt as a promoter significantly improves the NO_x storage efficiency at short storage times.[331]

Finally, one of the most promising technologies to adsorb NO_x is based on inorganic adsorbents such as zeolites, which will be presented in detail in the next section. These materials are used in gas-solid adsorption (physisorption) and catalytic processes (chemisorption) because of their unique properties: ion exchange capacity, high specific surface area, as well as low cost. In addition, good thermal stability and shape selectivity are additional factors that make zeolites widely used for this purpose.[332]

6.5 Zeolites

Zeolites are crystalline aluminosilicates materials, built from SiO_4 and AlO_4 tetrahedra as primary building units (PBUs) linked together by their oxygen ions, to form regular cavities and channels of molecular dimensions (i.e., secondary building units (SBUs)). They are also often called molecular sieves. A significant number of them occurs naturally as minerals and is widely exploited for industrial and medical applications. However, most zeolites are produced synthetically for commercial utilizations or for studies on their chemical composition. Currently, 191 unique zeolitic structures have been identified, and more than 40 natural zeolitic structures are known.[333]

The history of zeolite began with Crönstedt, a Swedish mineralogist, in 1756 and the heating of the mineral "stilbite," resulting in the appearance of moisture on its surface. Consequently, this mineral was named, "boiling stone" (ζέω (zéō) meaning "boiling" and λίθος (líthos) meaning "stone").[334]

A representative empirical formula for a zeolite is as follows.

$$M^{n+}_{x/n}\,.\,[(\,AlO_2)_x.\,(SiO_2)_y].^{n-}\,zH_2O$$

Where the negative zeolite charge caused by the presence of 'x' Aluminum, is compensated by exchangeable cations 'M', where it can be one of a large variety of cations, including monovalent (Na^+, Li^+, H^+, Cu^+, etc.), divalent (Mg^{2+}, Ca^{2+}, Mn^{2+}, Zn^{2+}, etc.), or trivalent cations (Gd^{3+}, Ce^{3+}, etc.). The variable 'n' represents the valence of this metal cation, and z stands for number of water molecule that can be reversibly desorbed upon mild thermal treatment. Interestingly, the physical and chemical properties of zeolites differ as a function of the proportion of SiO_2/AlO_2 ratio.[334,335] According to the Lowenstein's rule,[336] at least one silicon atom will be found in a zeolite framework for each aluminum atom, hence the Si/Al ratio is always ≥1.

6.5.1 Classification

The well-known and industrially important zeolites were discovered in the 1950s-1970s. They can be classified into four groups according to their Si/Al ratio as follows: [337]

- **"Low-silica or aluminum-rich" zeolites**

Zeolites A and X (the most common commercial adsorbents) discovered by R. M. Milton at Union Carbide Corporation Laboratories represent an optimum in composition, pore volume and channel structure. Both zeolites are nearly "saturated" with aluminum with a Si/Al ratio ≈ 1, which is considered as the highest aluminum content possible in tetrahedral aluminosilicate structures. As a result, they contain the highest number of cation exchange sites, and thus the highest cation content. Consequently, they have the most heterogeneous surface among known porous materials, due to exposed cationic charges embedded in an aluminosilicate framework. Their surface is highly selective for polar and polarizable water molecules, which is the basis for many applications, especially in drying and purification. Their pore volumes of nearly 0.5 cm^3/cm^3 are the best known for zeolites and give them a clear economic advantage in the field of product separation and purification. Their three-dimensional channel structures allow for maximum diffusion characteristics.

Table 6.1: Zeolite classification According to their Si/Al ratio.

Pore size	Si/Al	Type of zeolite
Low silica	1-1.5	A, X, LSX
Intermediate silica	2-5	A) Natural Zeolites: ▪ erionite, chabazite, clinoptilolite. B) Synthetic zeolites: ▪ Y, L, mordenite, chabazite, Erionite
High silica	5-500	A) By thermochemical modification of the reinforcement: ▪ Siliceous variants of Y, mordenite, erionite B) By direct synthesis: ▪ ZSM-5, IRON, BEA
All silica	∞	Silicate, Si-MFI, Si-ZSM-48

"Intermediate silica" zeolites

In the early 1950s, scientists at Union Carbide Laboratories showed that zeolites are vulnerable to acid attack and water vapor due to the instability provided by tetrahedral site of aluminum in the zeolite frameworks. Therefore, the subsequent evolution has consisted in the synthesis of more siliceous zeolites (increasing the silicon content of zeolites), with the goal of improving their thermal and chemical stability features. The Y-type molecular sieve zeolite, the third most important commercially, with a Si/Al ratio of 1.5 to 3.0, and a topology similar to that of X-zeolites. Its higher stability compared to zeolite X have had a significant impact on the properties of zeolite-based catalysts.

Other zeolites of "intermediate" Si/Al composition ratio ranging from 2 to 5, displaying unique topologies and commercial status, are mordenite, erionite, chabazite, clinoptilolite and synthetic omega zeolite. Their common characteristic is an improved stability compared to "low-silica" zeolites. In addition, their capabilities as adsorbents, catalysts, and ion exchangers are also recognized, reflecting their unique structural characteristics. The heterogeneous surface of these zeolites shows a high affinity for water and other polar molecules.

High silica zeolites

The development of silica-rich molecular sieves (Si/Al ratio higher than 5) such as zeolite Beta and ZSM-5 having a Si/Al ratio ranging from 10 to 100 or more started around the 1970s in Mobil R&D laboratories.[337]

In contrast to "weak" and "intermediate" siliceous zeolites with heterogeneous hydrophilic surfaces, high silica zeolites display more homogeneous surfaces with organophilic-hydrophobic selectivity. They have a strong affinity for low polarity organic molecules and weakly interact with water and polar molecules. In addition to this surface specificity, high-silica zeolites contain a low aluminum content and thus few cations exchange sites.

- **Silica molecular sieves**

The ultimate in siliceous molecular sieves is silicate, the first pure silica molecular sieve, developed in 1970; it contains no aluminum nor cationic sites. For this reason, it is completely devoid of field gradients and hydrophilic sites and has a hydrophobic character allowing adsorption of organic molecules present in water.

Table 6.2: Zeolite classification according to the number of T atoms in the member ring.

Pore Size	Number of T-atoms in the ring	Pore Diameter (Å)	Example
Small	8	4	LTA - SSZ13
Medium	10	5.5	ZSM-5 (MFI)
Large	12	7.5	FAU (Y, X) - Mordenite
Extra-large	> 12	> 7.5	CIT-5

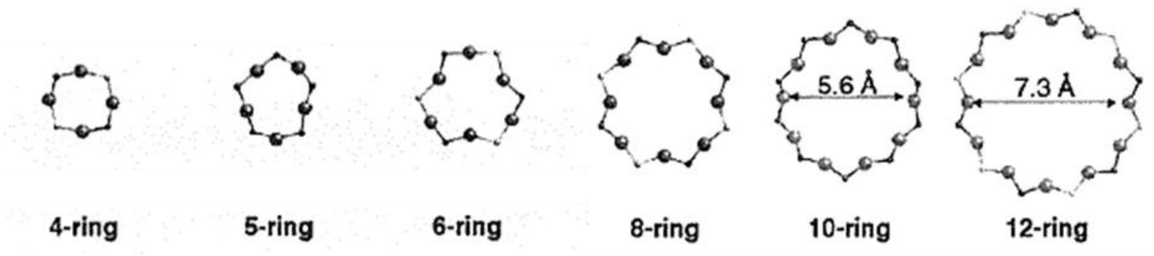

The number of T-atoms (namely Si or Al) that form a zeolitic channel, significantly determines the size of the pore opening, which is an important characteristic of microporous molecular sieves. Accordingly, zeolites can be also classified according to the number of T atoms in the member ring as shown in Table 6.2.

6.5.2 Faujasite-type Zeolite

Faujasite is the subject of the present work. This zeolite has been extensively studied from experimental, and modeling points of view, because of its numerous applications in nuclear, petroleum treatment processes, in catalysis, and separation-purification of molecules.[338]

6.5.2.1 Characteristics and structure

Faujasites (international code FAU) were synthesized and improved in the 1950s and 1960s by Mobil researchers. At present, this material is a reference in the field of gas separation thanks to its chemical and thermal stability. In FAU, after direct synthesis without organic structuring agent, the Si/Al ratio varies between 1 to 1.5, and from 1.5 to 2.6, for zeolite X and Y, respectively. No technique ensures the synthesis of purely silicate faujasite. However, some post-synthetic processing methods such as steam or acid treatment combined with dealumination allow the production of ultra-stabilized zeolites (USY) with high Si/Al ratios (>3). The name USY ("Ultra-Stable Y") account for its exacerbated hydrothermal stability and enhanced catalytic properties.

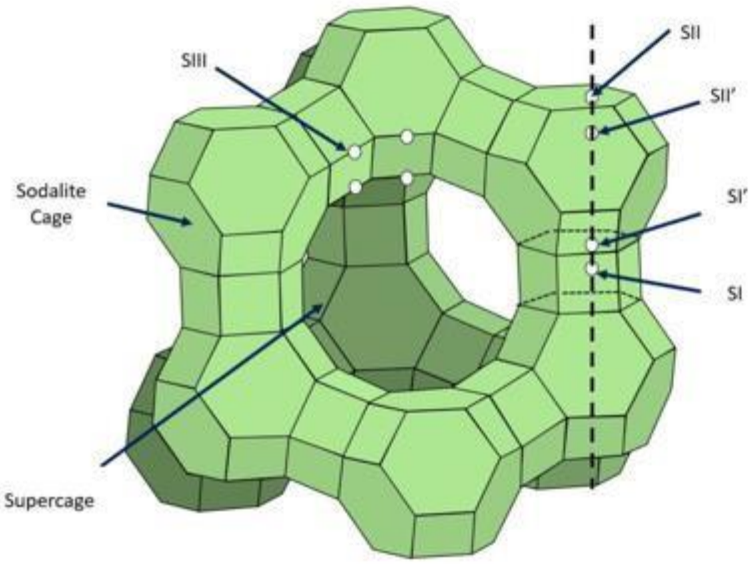

Figure 6.6: Structure of the (FAU) with the different types of cavities and cationic sites.

The FAU structure presents two types of pores called cages: sodalite cages and supercages. Additional secondary structural units are defined as follows:

- The tetragonal windows, comprising 4 T-atoms (i.e., Si or Al) at the top of the tetrahedron and 4 oxygens in the middle of each side of the edges.
- The hexagonal windows located between a sodalite cage and a supercage. They consist of 6 T atoms and 6 oxygens. Their diameter is about 2.2 Å. Molecules must cross them for

penetrating the sodalite cages.

- The hexagonal prism connecting two sodalite cages. It consists of two hexagons(6 T atoms and 6 oxygens each time) connected between them by bridges formed by an oxygen linked to a T atom of each hexagon.
- The supercages or cages α with a diameter of 12.5 Å. Each supercage is connected to four other supercages *via* a dodecagonal window (of diameter 7.5 Å), forming a tetrahedron. It is also connected to four sodalite cages via a hexagonal window.
- The sodalite cages or *β-cages* with a diameter of about 6.5 Å. Sodalite cages are connected to four other sodalite cages *via* a hexagonal prism. These cages are accessible to molecules from the supercages through a hexagonal window. This window blocks hydrocarbon molecules, but also relatively small molecules like methanol. On the other hand, they are accessible to water molecules.

6.5.2.2 Crystallographic sites

FAU belongs to the Fd-3 symmetry group. The elementary mesh is cubic and contains 16 hexagonal prisms, 8 sodalite cages and 8 supercages. Frising and Leflaive proposed a classification of cationic sites as described in Table 6.3.

Table 6.3: Characteristics of the different cationic sites of faujasite. The classification was proposed by Frising and Leflaive.

Cationic site	Multiplicity	Location	Description
I	16	Hexagonal prism	In the center of the hexagonal prism, octahedral coordination with the neighboring oxygen atoms.
I'	32	Sodalite cage	In the sodalite cage, near the hexagonal window of the hexagonal prism. Three oxygen atoms as nearest neighbors.
II'	32	*β cage*	In the sodalite cage, near the hexagonal window of the supercage.
U	8		Center of the sodalite cage.
II	32	Supercage	On the [III] axis, in the center of a hexagonal window between the sodalite cage and the supercage. Coordinated at 3 oxygens. Often grouped with site II*.
II'	32		On the [111] axis in the supercage, near the hexagonal window of the sodalite cage. Often considered as a site II. Coordinated at 3 oxygens.
III	48		In the supercage, near a square window between two other square windows. At the intersection of two mirror planes
III'	96 or 192		In the supercage, according to some authors near a square window between two other square windows. According to others on the inner wall

			of the supercage.
IV	8		Center of the supercages.
V	16		Center of the 12-ring window.

The nature and location of cations affect the separation and catalytic properties of zeolites. The different cations present in zeolites can be obtained by a cationic exchange. The latter can be total or partial as in the case of Cs+ and Rb+ where a total exchange has never been reached experimentally, resulting in a bi-cationic zeolite (e.g., Cs-Na-FAU). Identifying the distribution of cations in zeolitic materials is a major challenge in the search for new molecular sieves. For example, the distribution of sodium in a faujasite-type zeolite is well known and presented in Figure 6.7. This cation is found to be stable in site II (32 sites per conventional cell) and consequently this site is the first to be occupied, followed by site I (16 sites). Moreover, the Si/Al ratio significantly influences the distribution of these cations. Concerning Na, a decrease in the Si/Al ratio leads to the migration of cations from site I to site I' (32 sites). Once sites II and I' are fully occupied, site III starts to fill up until a complete occupation on a Si/Al=1 X zeolite.

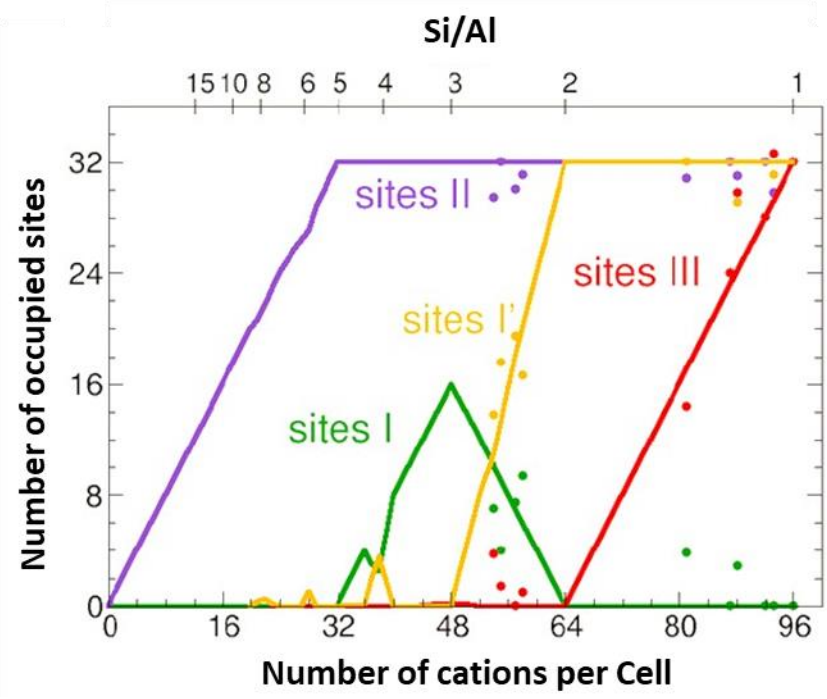

Figure 6.7: Sodium (Na) Cation distribution as a function of Si/Al ratio in a standard FAU-type zeolite (192 T atoms)

6.6 Conclusion

- Although the exhaust gas recirculation process can convert up to 50% of NO_x, it is not suitable to provide the desired emission values and is accompanied by additional pollutants

(PM), reduced engine performance and deterioration.

- In NSR (or LNT) and SCR post engine control systems, NO_x emissions can be reduced to the desired level without reducing engine performance by using catalysts. These are effective technologies for controlling NO_x emissions.
    - LNT technology is particularly suitable for light commercial vehicles. However, it does not have a high NO_x storage capacity. Highly susceptible to sulfide poisoning, it requires fuel-rich operating conditions for the regeneration process. These problems limit its efficiency.
    - Thanks to SCR technology, it is possible to achieve high conversion rates for NO_x emissions. Today, the SCR system is the most efficient system to limit NO_x emissions at temperatures above 200°C. It is ineffective at temperatures below 200°C, during engine start-up.
- A promising technique lies in the use of porous structures to trap these NO_x pollutants. Zeolites are one of the most widely used materials in many industrial processes, particularly for gas capture. These materials are therefore an excellent candidate for this challenging application.

Chapter 7

Adsorption of NO_x (NO, NO_2) in presence of water in divalent cation faujasite type zeolites

The studies summarized in this Chapter have been published as:

Adsorption of NO, NO_2 and H_2O in divalent cation faujasite type zeolites: A Density Functional Theory screening approach

Ayoub DAOULI, Etienne Paul HESSOU, Hubert MONNIER, Marie-Antoinette DZIURLA, Guillaume MAURIN,
Abdellatif HASNAOUI, Michael BADAWI

Phys. Chem. Chem. Phys., 2022,**24,** 15565-15578
DOI: 10.1039/D2CP00553K

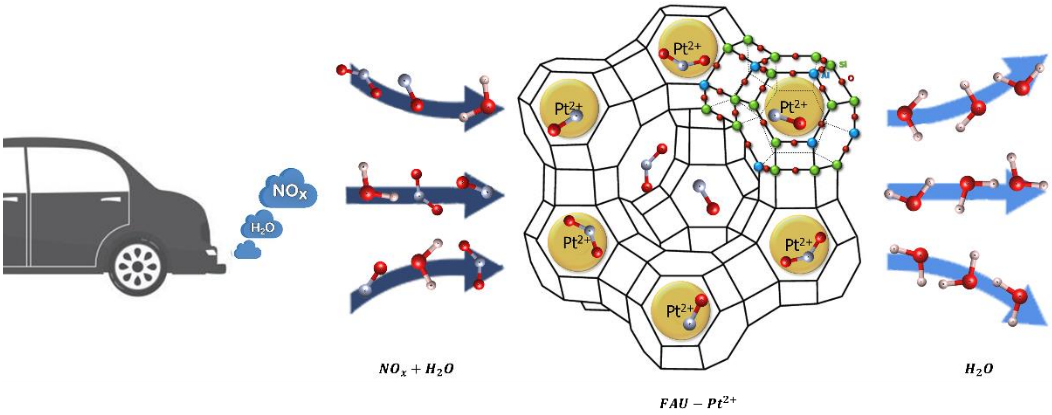

7.1 Abstract

Emissions of diesel exhaust gas in confined work environments are a major health and safety concern, because of exposition to nitrogen oxides (NO_x). Removal of these pollutants from exhaust gas calls for engineering of an optimum sorbent for the selective trapping of NO and NO_2 in the presence of water. To this end, periodic density functional theory calculations along with a recent dispersion correction scheme, namely Tkatchenko-Scheffler scheme coupled with iterative Hirshfeld partitioning TS/HI, were performed to investigate the interactions between NO, NO_2,

H_2O and a series of divalent cations (Be^{2+}, Mg^{2+}, Ca^{2+}, Sr^{2+}, Ba^{2+}, Fe^{2+}, Cu^{2+}, Zn^{2+}, Pd^{2+}, Pt^{2+}) faujasites. This enabled to identify the optimum zeolites to selectively capture NO_x in presence of H_2O, with respect to two important criteria, thermodynamic affinity, and regeneration. Our results revealed that Pt^{2+} and Pd^{2+} containing faujasites are the best candidates for an effective capture of both NO and NO_2 molecule that paves the way towards the use of these sorbents to address this challenging application.

7.2 Introduction

Air quality is currently a major environmental concern. The concentration of pollutants such as carbon oxides (CO, CO_2), ozone (O_3), volatile organic compounds (VOCs), nitrogen monoxide (NO) and nitrogen dioxide (NO_2), released by thermal motors needs to be reduced,[339,340] since these chemicals are known to be highly toxic, and responsible for serious health problems, e.g. chronic obstructive pulmonary disorder, respiratory infections and lung cancer among others.[340] According to the World Health Organization (WHO), 90% of the world population breathe polluted air, and seven million people die each year from diseases caused by air pollution.[341] Since humans spend more than 80% of their life indoors, including living and working places where pollutant levels are estimated to be typically 5 to 10 times higher than outdoor, they are particularly exposed to the typical indoor pollutants including NO, NO_2, CO and VOCs.[342]

Along with ozone (O_3), NO_x (both NO and NO_2) are amongst the most harmful indoor air pollutants.[343] NO gas is a colorless and odorless gas, while NO_2 is a reddish-brown gas with a strong smelly odor, and its toxicity is five times higher than NO.[344,345]

Moreover, NO_x released by engines (300-1000 ppm for both NO and NO_2) in a confined work environment lacking of ventilation and exhaust treatment, represents a major health and safety problem.[346,347] In France, almost 800 000 workers are exposed to such emissions. As a result, European Union regulatory requirements have attempted to address these concerns through EU Directive 2017/164, that set an occupational exposure level limit value for NO and NO_2 emitted from engines in a working environment of 2 and 0.5 ppm respectively.[348] Therefore reduction of NO_x emissions in exhaust gases of off-road vehicles is a current priority in occupational risk prevention. This calls for the development of efficient technologies to comply with these health standards, and for improving health and safety in confined work environments.

Several strategies such as NO_x storage-reduction (NSR) and selective catalytic reduction (SCR) have been proposed in the last decade, in order to limit NO_x release in lean-burn engines.[349–351] Being efficient at high temperatures, they have been already implemented on light vehicles where the engine temperature quickly increases thanks to their continuous run. However, these techniques face several problems.[352] In particular, their efficiency for NO_x reduction becomes limited on construction site machinery running discontinuously and therefore subjected to several cold starts, leading to low exhaust temperature.[353]

Therefore, effective sorbent for the selective capture of low concentrations of NO and NO_2 in the presence of water [354] needs to be engineered by paying attention that residual H_2O can react with NO_2 for producing NO and nitric acid.[354,355] In the context of ecological transition, adsorbent regeneration appears also crucial. Thus, a subtle balance between high selectivity and easy regeneration is required.

Recent studies revealed that inorganic sorbents such as zeolites can address the capture of NO_x.[355,356] Indeed, on a basis of 200 existing zeolites,[357–359] mordenite (MOR),[360,361] MFI (ZSM5),[362,363] and faujasite (FAU) architectures have been proposed as promising candidates for NO_x removal.[355] However, the identification of the most efficient zeolite in terms of topology, nature and concentration of extra-framework cations requires many experiments. To circumvent this limitation, molecular modeling is a powerful tool to narrow down the list of potential adsorbents.[364,365] Specifically, molecular simulations can assess accurately the adsorption energies and capacities for a large number of sorbents/sorbate pairs and therefore becomes a reliable screening tool for identifying the most efficient sorbents for the selective trapping of a target sorbate.

Herein, we present a screening approach based on Density Functional Theory (DFT) calculations to assess the efficiency and the selectivity of zeolite materials for the target applications.[59,366–368] Typically, faujasites are good candidates for NO_x trapping, thanks to the presence of the extra-framework cations that can act as strong adsorption sites combined with their large supercages that enable to optimize the amount adsorbed.[351,355,369,370] Furthermore, the structure composition (Si/Al ratio) can be fine-tuned from one up to infinite[371] by modifying the hydrothermal synthesis (ratio 1 to 3) or by applying post-synthetic modifications (ratio 3 onwards).

Among this family of faujasites, the Y version [372] was first synthesized with a Si/Al ratio of about 4.5, exhibiting a good chemical/thermal stability and high cation exchange capacity, and is it therefore became industrially widely used as molecular sieve and adsorbent.[373,374] In addition, the Si/Al ratio of Y zeolites, can be further increased and adjusted through stream and/or acid treatments,[371] yet still maintaining crystallinity. As a result, a zeolite featuring improved hydrothermal stability "Ultra Stable Y" (USY) was conceived and labeled for all structures with a Si/Al ratio of about 6 and above. The Y and USY zeolites have shown remarkable promise in many industrial applications.[375–377]

More specifically, the objectives of the present work are to investigate the preferential sittings of NO, NO_2 and H_2O in a series of divalent cation faujasite Y as well as to assess the associated interaction energies and the host/guest charge transfer. To that purpose our periodic DFT investigations focused on a series of ten divalent cation faujasite Y (Be^{2+}, Mg^{2+}, Ca^{2+}, Sr^{2+}, Ba^{2+}, Zn^{2+}, Cu^{2+}, Fe^{2+}, Pd^{2+} and Pt^{2+}) with a model Si/Al ratio equal to 23. The optimal divalent cation Pt^{2+} was further incorporated in the common zeolite Y (Si/Al = 2.4) and its adsorption behavior with respect to the 3 molecules mentioned above was predicted to confirm the potential of this zeolite for a selective capture of NO_x. The bond activation upon adsorption of the studied molecules were later analyzed to gain insight into the regeneration of these materials.

7.3 Computational and structural details

7.3.1 Structural Model

Faujasite is a three-dimensional network belonging to the wide-pored zeolites (Figure 7.1a). Its structure consists of 6.6 Å diameter sodalite cages (β cages) connected through hexagonal prisms (D6R) with an opening of 2.3 Å. By other windows, these β cages are connected to 12.4 Å diameter supercages (α cages) which are also linked together by a 7.4 Å diameter hexagonal window (12MR) leading to the formation of a porous network.[333]

The purely siliceous structure of Faujasite belongs to the Fd3m symmetry space group,[378] with the standard cubic lattice containing 576 atoms ($Si_{192}O_{384}$) and characterized by a lattice constant of 25.028 Å.[379,380] In the present study, to minimize computational efforts only a 144 atoms rhombohedral primitive cell was considered containing 8 hexagonal windows linking the two supercages to the sodalite cages and characterized by the following cell dimensions: a=b=c=17.3432 Å, α=β=γ=60° and V=3688.68 $Å^3$.

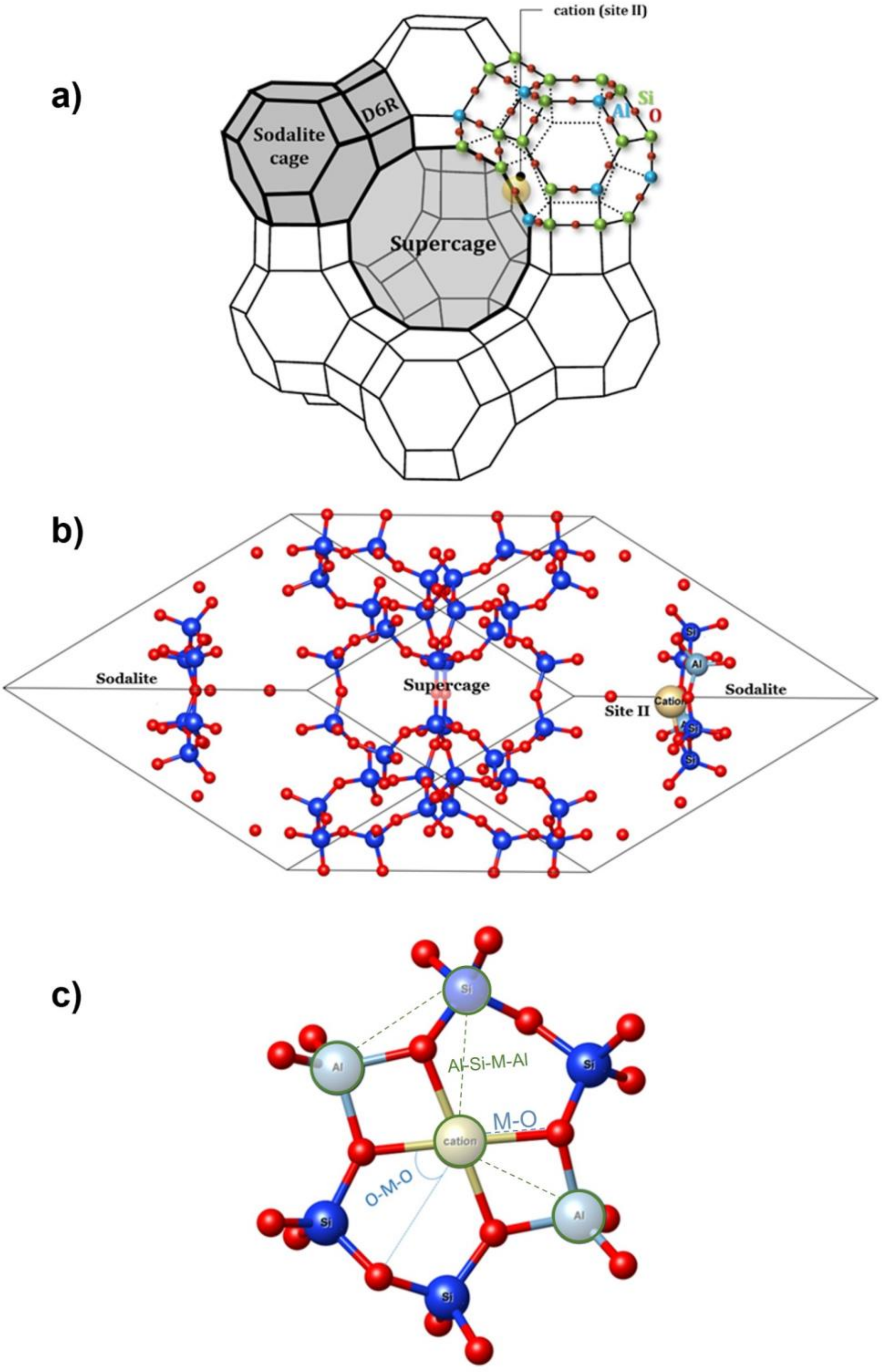

Figure 7.1: a) Scheme of the conventional cell of faujasite with three types of cavities. The hexagonal prism (D6R), the sodalite cage (β cage) and the supercage (α cage). b) The FAU zeolite primitive cell displayed in ball and stick, c) Representation of the Site II and its geometrical parameter considered during this study (i.e., the angle O-M-O).

To obtain a Si/Al ratio equal to 23, two Si atoms were exchanged by two Al atoms in the primitive cell (Figure 7.1c). Therefore, the molecular formula of the investigated cell is $M_1Al_2Si_{46}O_{96}$, with

M = Be^{2+}, Mg^{2+}, Ca^{2+}, Sr^{2+}, Ba^{2+}, Zn^{2+}, Sn^{2+}, Fe^{2+}, Pt^{2+} or Pd^{2+}. In zeolites, the Loewenstein rule which governs Al-O interactions excludes the sharing of one oxygen atom by two AlO_4 tetrahedra.[336] This means that Al-O-Al bond formation is excluded from the zeolite framework, and that the distance between two aluminum cations in a 6MR (SiO_2/Al_2O_3) ring needs to be as large as possible (Figure 7.1c).[379]

Several crystallographic investigations have shown that for a Si/Al ratio greater than five, site II (Figure 7.1) is the most favorable to be occupied by cations.[381,382] This site is situated within the supercage, more particularly upon the hexagonal window connecting the sodalite cage to the supercage. In addition, this site is known to be accessible to most of the adsorbates.[383,384] Therefore, in our study, only site II was considered for the location of the different envisaged divalent cations, consistent with previous works.[385,386]

7.3.2 DFT adsorption calculations

The adsorption modes and energies of NO_x and H_2O on site II of exchanged cationic zeolites were studied through periodic DFT calculations[155,156] using the code VASP (Vienna Ab Initio Simulation).[174] The functional of Perdew, Burke, Ernzerhof (PBE) of the Generalized Gradient Approximation was applied (GGA).[159] The electron-ion interactions were described using the Projector Augmented plane Wave (PAW) method developed by Blöchl[258] and adjusted later by Kresse and Joubert[259]. The plane wave cutoff energy was set to 450 eV and the Brillouin zone sampling at the Γ-point. The Kohn-Sham self-consistent total energy differences were converged within 10^{-6} eV.[156] A 0.1 eV Gaussian smearing was applied and the atomic positions were fully relaxed until all forces were below 0.02 eV/Å per atom.[387]

To describe the adsorption of the different guest molecules in the faujasite with a high accuracy, Van der Waals (vdW) interactions have to be accounted for.[163,268,388,389] For that, Tkatchenko-Scheffler scheme with iterative Hirshfeld partitioning (TS/HI) was considered. This vdW correction method was demonstrated to accurately describe the dispersion interactions for small molecules over exchange zeolites.[164]

Spin-polarized (collinear) calculations were performed for all the cations. Fe^{2+} with $3d^6$ orbital was found to be 1.74 eV more stable in the high spin state compared to the low spin state. To further treat the strong correlation effects of Fe, the GGA+U method of Hubbard[390] was applied with an effective Hubbard parameters U_{eff} of 4.0.

The interaction energies between the guest molecules and the cation containing faujasites were calculated at 0 K using the following equation:

$$\Delta E_{\mathrm{int}} = E_{(\mathrm{FAU+guest})} - (E_{\mathrm{FAU}} + E_{\mathrm{guest}}) \qquad \text{Eq 7.1}$$

where $E_{\mathrm{FAU-guest}}$ is the total energy of the zeolite with the adsorbate, E_{FAU} and E_{guest} are the total energies of the zeolite and the gaseous phase of the isolated molecule, respectively.

In a similar procedure, the dispersion forces contribution ΔE_{disp} to the interaction energy is given by :

$$\Delta E_{\mathrm{disp}} = E_{\mathrm{disp\,(FAU+guest)}} - E_{\mathrm{disp\,(FAU)}} - E_{\mathrm{disp\,(guest)}} \qquad \text{Eq 7.2}$$

In order to further improve our understanding and to look at the effect of adsorbed molecule's interaction with the zeolite, both charge density difference ($\Delta\rho$) and Bader charge difference (ΔQ) were determined.[201–203]

Charge density difference can be calculated taking the superposition (obtained from the initial condition of the self-consistency cycle) of non-interacting atoms (or isolated) as reference. The visualization of the charge density difference ($\Delta\rho$) upon adsorption of NO_x and H_2O into exchanged FAU, requires three calculations as shown in the equation below:

$$\Delta\rho = \rho_{\mathrm{FAU+guest}} - \rho_{\mathrm{FAU}} - \rho_{\mathrm{guest}} \qquad \text{Eq 7.3}$$

where $\rho_{\mathrm{FAU+guest}}$ stands for the charge density of the full system, ρ_{FAU} is the charge density of the empty faujasite and ρ_{guest} is the charge density of the isolated adsorbate in gas phase.

On the other side, the Bader approach consists of exploiting the topological properties of the charge density to partition the space in several regions, and the boundary of each Bader volume is defined as the surface through which the charge density gradient has a zero flux. Thus, the partial charge and polarization of single atoms are determined. To get the difference in electronic charge ΔQ, the following equation was used:

$$\Delta Q = Q_{FAU-guest} - (Q_{\mathrm{FAU}} + Q_{\mathrm{guest}}) \qquad \text{Eq 7.4}$$

where $Q_{\mathrm{FAU\text{-}guest}}$ is the Bader charge of all the atoms upon adsorption and Q_{FAU}, Q_{guest} are the Bader charges of the clean zeolite and the isolated molecule in the gaseous phase.

7.4 Results and discussion

7.4.1 Geometry of the cation exchanged FAU zeolites

The locations of all tested cations (M = Alkali metals and Transition metals) in the empty and guest-loaded Faujasites were determined by calculating different geometric parameters such as M-O distances (determined as the mean distance between M and the nearest 6MR oxygens), O−M−O angles (determined as the angle between the cation and two neighboring oxygens) and Al−Si−M−Al dihedral angle between M and the 6MR window plane (Figure 7.1c). All distances and angles values are listed in Table 7.1 and 2, respectively.

7.4.1.1 Bare empty faujasites.

The energy minimization of all bare empty faujasites revealed a significant increase of the dihedral angles between the cation and the 6MR windows, from 1.05° to 30.87° when going from the smallest to the biggest cation (i.e., from Be^{2+} to Ba^{2+}). This clearly indicates that the smallest cations are positioned within the plane of the 6MR windows whereas the biggest cations are rather out of the plane as shown in Figure 7.2.

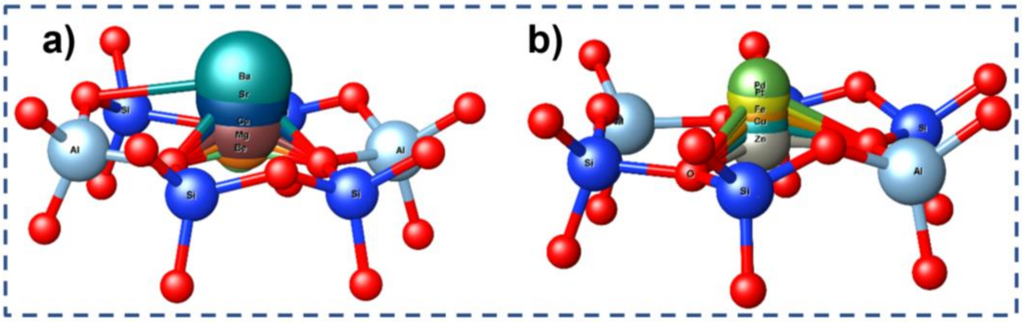

Figure 7.2: An illustration of how the cation size influences its initial position regarding the 6MR windows plane: (a) Alkaline earth family; (b) Transition metal series.

Furthermore, upon increasing the cation radius from Be^{2+} to Ba^{2+}, we noticed an increase in the M−O distance from 1.64 Å to 2.70 Å, respectively. Moreover, a decrease in the O−M−O angle from 74.0° to 59.7° can be observed when switching from magnesium to barium. This result is in agreement with a recent work which showed that more the cations are out of the zeolite windows plane, lower are the values of the O-M−O angle.[391] Variations of these three geometrical parameters, in line with the cation's ionic radius reported in Table 7.1 indicate that the cation position affects the interactions with the adsorbates.

Similarly, to alkaline earth metals, the relative positions of metal cations (Zn^{2+}, Cu^{2+}, Fe^{2+}, Pd^{2+} and Pt^{2+}) within the zeolite structure were also described through the determination of the M-O distances and O-M-O angles (Table 7.1 and 2). In addition, calculations of the dihedral angles revealed values ranging from 2.5° to 5.5° which are illustrated in Figure 7.2. These results clearly confirm that the most planar geometry between M and the 6MR window is obtained with Zn^{2+} and contradicts the fact that the cation position in the 6MR windows plane varies in the same way as its ionic radius. Similar trends were previously observed using ZSM-5 zeolite structure.[392]

Table 7.1 : The M–O distances (Å) of the alkaline earth and transition metals exchanged bare zeolites and loaded with NO, NO_2 and H_2O.

Cations	Be^{2+}	Mg^{2+}	Ca^{2+}	Sr^{2+}	Ba^{2+}	Zn^{2+}	Cu^{2+}	Fe^{2+}	Pd^{2+}	Pt^{2+}
Ionic Radii (pm)	45	72	100	118	135	74	73	78	86	80
Bare zeolite	1.66	2.06	2.35	2.53	2.70	1.97	2.03	2.19	2.07	2.06
NO	1.69	2.10	2.39	2.53	2.71	2.00	2.05	2.09	2.22	2.24
NO_2	1.70	2.10	2.40	2.54	2.71	1.99	2.05	2.23	2.07	2.07
H_2O	1.73	2.12	2.41	2.55	2.73	2.04	2.05	2.08	2.07	2.07

Table 7.2: The O–M–O angles (°) of the alkaline earth and transition metals exchanged bare zeolites and loaded with NO, NO_2 and H_2O.

Cations	Be^{2+}	Mg^{2+}	Ca^{2+}	Sr^{2+}	Ba^{2+}	Zn^{2+}	Cu^{2+}	Fe^{2+}	Pd^{2+}	Pt^{2+}
Ionic Radii (pm)	45	72	100	118	135	74	73	78	86	80
Bare zeolite	63.8	74.0	67.2	63.2	59.7	66.8	77.1	72.0	75.0	74.5
NO	65.0	72.9	67.0	63.1	59.3	67.4	67.3	69.1	71.0	70.4
NO_2	64.7	73.0	66.9	63.0	59.6	67.6	76.9	70.0	74.8	74.4
H_2O	67.4	72.3	66.5	62.8	59.5	65.5	76.8	71.4	75.1	74.6

7.4.1.2 NO, NO_2 and H_2O loaded faujasites

Adsorption of NO_x or H_2O on alkaline earth metal-exchanged zeolites induces no significant change in the cations position (Figure 7.3a). The cations remain mostly attached to the FAU zeolite through strong covalent bonds with the nearest oxygen atoms, except for water adsorption where a slight elongation of the O-M bond (with an average of 0.05 Å) was observed (Table 7.1). Determination of the O-M-O angles (

Table 7.2) for alkaline earths showed that Be^{2+} is the most adsorption-sensitive cation, as its corresponding angle increased from 3.6°, 1.2° and 1° after adsorption of H_2O, NO and NO_2, respectively.

Similar trends were also observed for transition metals exchanged zeolite. Zn^{2+} was found to be sensitive to water as the O-M bond slightly increased from 1.95 Å to 2.04 Å (Table 1). Pt and Pd cations were found to be affected by NO adsorption as their O-M bonds significantly increase by 0.18 and 0.15 Å, respectively. In contrast to alkaline earth metals, for transition metals the O-M-O angle decreases as the O-M bond increases, which could be due to the cation shift towards the side of the 6MR windows (near the Al atom) (Figure 7.3b), while with alkaline-earth metals, cations remain in the 6MR windows plane (Figure 7.3a).

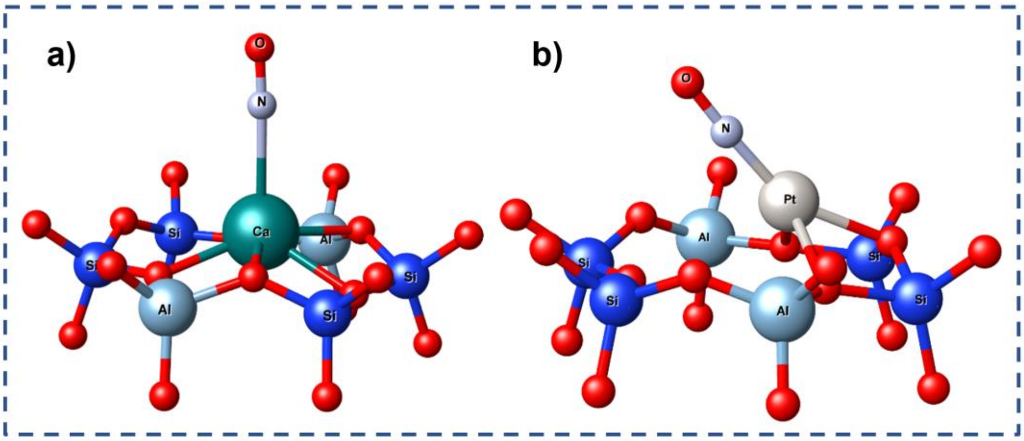

Figure 7.3: Illustration of the cation shift upon NO adsorption on the alkaline earth, Calcium (a) and transition metal Platine (b) zeolites.

These different geometric features of the two categories of cation-faujasites suggest distinct adsorption behavior and associated interaction energy.

7.4.2 Energetics and iso-surface electron density

To investigate the ability of the cation exchanged FAUs to capture NO_x, several adsorption modes were considered, and the most stable ones were selected (Figure 7.4). Calculated energies ΔE_{int} (kJ/mol), together with their associated dispersion contribution ΔE_{disp} (kJ/mol) are reported Table 7.3.

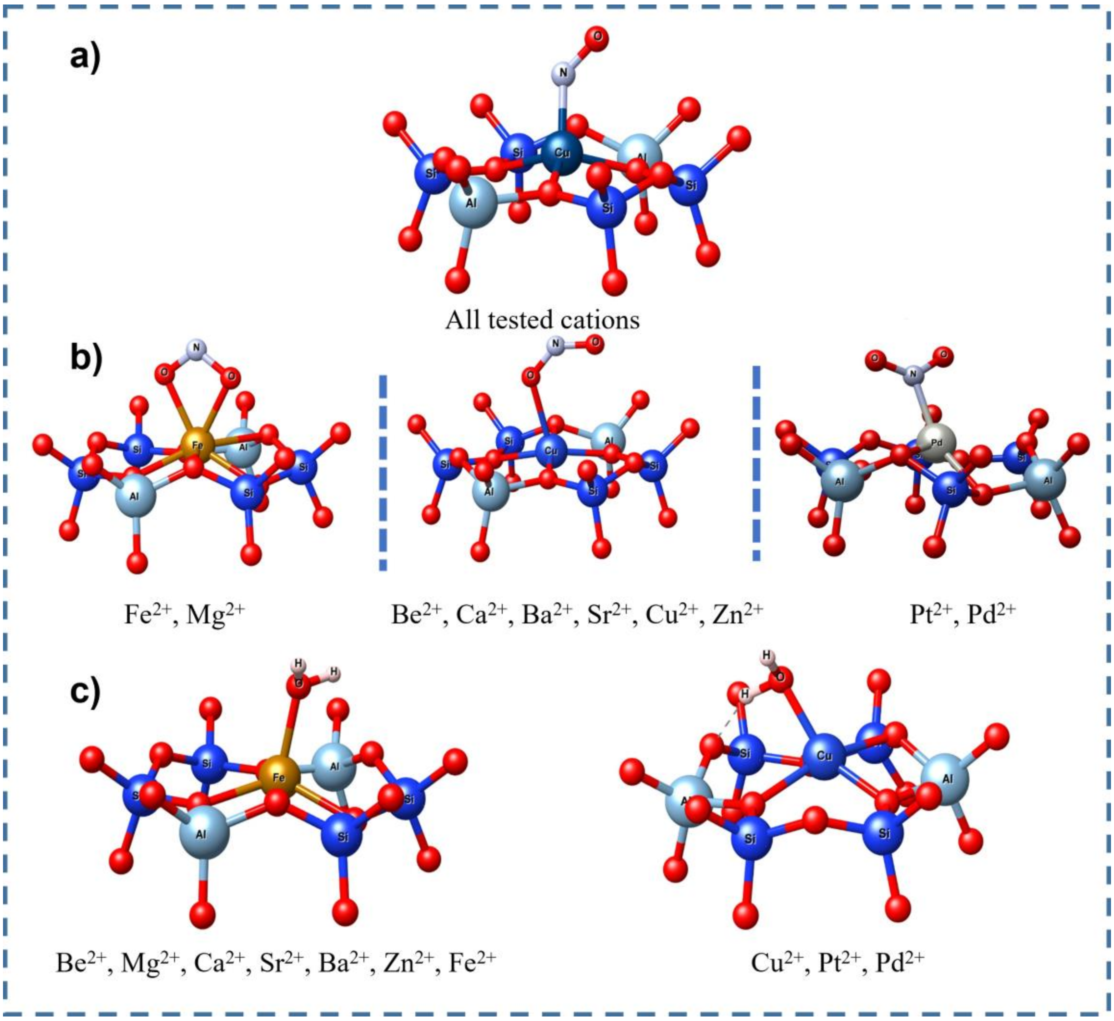

Figure 7.4: Different adsorption modes for a) NO, b) NO_2 and c) H_2O, in FAU exchanged with divalent cations.

Figure 7.4 shows that NO is adsorbed through its nitrogen atom, whereas NO_2 displays three different adsorption modes depending on whether it interacts through nitrogen, or through one or two oxygen atoms. Moreover, water adsorbs preferentially through its oxygen atom although an additional interaction can occur with one of its hydrogen atoms.

Table 7.3: Interaction energies ΔE_{int} (kJ/mol) and in brackets, dispersion energies ΔE_{disp} (kJ/mol), calculated at the PBE+TS/HI theory level for NO, NO_2 and H_2O molecules.

	Be^{2+}	Mg^{2+}	Ca^{2+}	Sr^{2+}	Ba^{2+}	Zn^{2+}	Cu^{2+}	Fe^{2+}	Pd^{2+}	Pt^{2+}
NO	−37.6 (-11.8)	−44.5 (-10.2)	−39.0 (-10.9)	−35.0 (-11.1)	−26.6 (-10.7)	−48.7 (-10.3)	−107.8 (-9.9)	−155.5 (-9.1)	−168.7 (-16.3)	−145.6 (-15.9)
NO_2	−33.8 (-16.6)	−53.2 (-12.7)	−49.9 (-13.6)	−42.4 (-12.5)	−21.8 (-12.9)	−42.1 (-13.3)	−27.2 (-14.4)	−53.7 (-14.2)	−74.2 (-13.0)	−84.7 (-15.4)

H_2O	−114.8 (-10.8)	−112.0 (-7.7)	−98.9 (-8.6)	−88.7 (-8.6)	−74.6 (-7.3)	−105.3 (-9.1)	−81.6 (-8.8)	−56.3 (-9.4)	−48.2 (-19.0)	−33.2 (-16.7)

7.4.2.1 Adsorption of NO

7.4.2.1.a Alkaline earth metals Be^{2+}, Mg^{2+}, Ca^{2+}, Sr^{2+}, Ba^{2+}.

Among the three adsorbates, NO shows the weakest affinity for the alkaline earth-exchanged faujasite with a calculated interaction energy for beryllium predicted to be −37.6 kJ/mol, including −11.8 kJ/mol vdW contribution i.e., 31% of the total interaction energy (Table 3). Furthermore, NO interaction energy decreases progressively from −44.5 kJ/mol with Mg^{2+} to −26.6 kJ/mol with Ba^{2+}, including an average of −10 kJ/mol vdW contribution i.e., 27%. These low values indicate a decrease in the interaction force between NO and the alkaline earth series, which is correlated with an increase in the ionic radius of this group of metals. Such results indicate that rising the electro positivity of the charge-compensating cation leads to weaker adsorption.

7.4.2.1.b Transition metals Zn^{2+}, Fe^{2+}, Cu^{2+}, Pd^{2+} and Pt^{2+}.

The interaction energy of NO significantly increases from Zn^{2+} exchanged faujasite to Pt^{2+} exchanged faujasite (Table 3). Values of Zn^{2+} exchanged faujasites are close to those observed for faujasites exchanged with alkaline earth metals. Higher interaction energies, e.g. −107.8 kJ/mol, −155.5 kJ/mol, −168.7 kJ/mol and −145.6 kJ/mol have been calculated for Cu^{2+}, Fe^{2+}, Pd^{2+} and Pt^{2+}, respectively. Corresponding dispersion contributions are −9.9 kJ/mol, −9.1 kJ/mol, −16.3 kJ/mol and −15.9 kJ/mol, respectively, representing an average of only 7% of the total interaction energy. These results are in line with those of Kanougi al.[393] who computed an interaction energy of –112.6 kJ/mol for NO in ZSM-5 exchanged with Pd^{2+}.

Similar findings were also reported by Wang et al.[394] and Sun et al.[395] for the adsorption of NO and N_2O on Fe-BEA and H-BEA zeolites on the one hand, and NO and CO on Fe/ZSM-5 on the other. Wang et al. revealed that Fe (III) exchanged BEAs show the highest affinity for NO with an interaction energy of –123 kJ/mol very close to the value we found for Fe(II)-FAU. However, Sun et al. obtained a much higher energy of –258 kJ/mol for the ZSM-5 exchanged with Fe (II) most probably due to the location of the Fe (II) on the 8MR site. Many studies reported that cations located in the 8MR sites lead to higher interaction energies compared to the cations located in the 6MR site.[396,397] Furthermore, these previous studies revealed that in all investigated zeolites, NO molecules preferentially adsorb via their nitrogen rather than their oxygens, in agreement with our finding reported in Figure 7.4.

Figure 7.5 represents negative and positive iso-surfaces between Ba-NO and Pt-NO. The high electrostatic interactions between nitrogen and Pt^{2+} were confirmed through the high charge transfer, together with the Bader method based computed ΔQ (0.14e; −0.17e) for Pt and N respectively. It is not the case with Ba cation where its Bader charge was almost unaffected by the adsorption of NO. The calculated distance between Pt atom and N atom of NO ($d_{Pt\text{-}N} = 1.92$ Å) confirmed this result, Indicating a chemical bond formation between the cations and the nitrogen atom of NO, with the formation of complexes.[398,399]

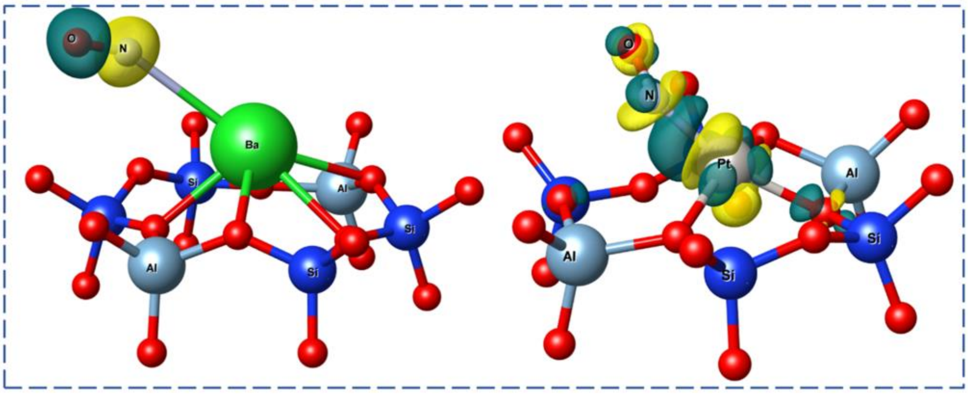

Figure 7.5: Iso-surface electron density for two cations: first, with a weak interaction energy between Ba^{2+} and NO, and second, with a strong interaction energy between Pt^{2+} and NO. Yellow and blue colors represent negative and positive iso-surfaces corresponding to +0.003 and -0.003 electron/Å^{-3}, respectively.

7.4.2.2 Adsorption of NO_2

7.4.2.2.a Alkaline earth metals Be^{2+}, Mg^{2+}, Ca^{2+}, Sr^{2+}, Ba^{2+}

The NO_2 interaction energy varies between −53.2 kJ/mol and −21.8 kJ/mol from Mg^{2+} to Ba^{2+} (Table 7.3). This relatively weak interaction is in line with the absence of charge transfer between Ba^{2+} and NO_2 (Figure 6a). The significant decrease of the interaction energy along this family of cations follows the decrease in the cation's hardness, leading to weaker interaction with hard base molecules i.e., HSAB theory (Hard Soft Bases and Acids) introduced by Parr Pearson.[92]

7.4.2.2.b Transition metals Zn^{2+}, Fe^{2+}, Cu^{2+}, Pd^{2+} and Pt^{2+}

For faujasites exchanged with transitions metals, Table 7.3 shows that NO_2 is less strongly adsorbed as compared with NO and preferentially interacts through its oxygen atoms for most of the cations as shown in Figure 4b. The total interaction energy reaches a maximum of −53.7 kJ/mol for Fe^{2+}, which is similar to the value observed for Mg^{2+} (−53.2 kJ/mol), reflecting the same interaction mode of NO_2 with these two cations. Zinc and Copper show the lowest interaction values of −42, −27 kJ/mol with NO_2, respectively.

Benco[400] used DFT to study the adsorption of a set of diatomic and triatomic probe molecules on $[Zn\text{-}Zn]^{2+}$ particles in a ferrierite zeolite. The NO and H_2O molecules were found to interact with a single Zn atom, resulting in interaction energies of – 48.8 and –100 kJ/mol, respectively, very similar to our findings (Table 3). However, the NO_2 molecule was found to interact with both Zn atoms of the $[Zn\text{-}Zn]^{2+}$ particle, explaining the 54 kJ/mol higher adsorption as compared to our results.

Pt^{2+} and Pd^{2+} are the only cations that interact with NO_2 through its nitrogen atom and thus again, they revealed the highest adsorption values of −84.7 and −74.2 kJ/mol, respectively. The corresponding vdW contribution was estimated to −15.4 kJ/mol for Pt^{2+}. The strong interactions of NO_2 with the Pt cation was confirmed by the iso-surface electron density presented in Figure 7.6b.

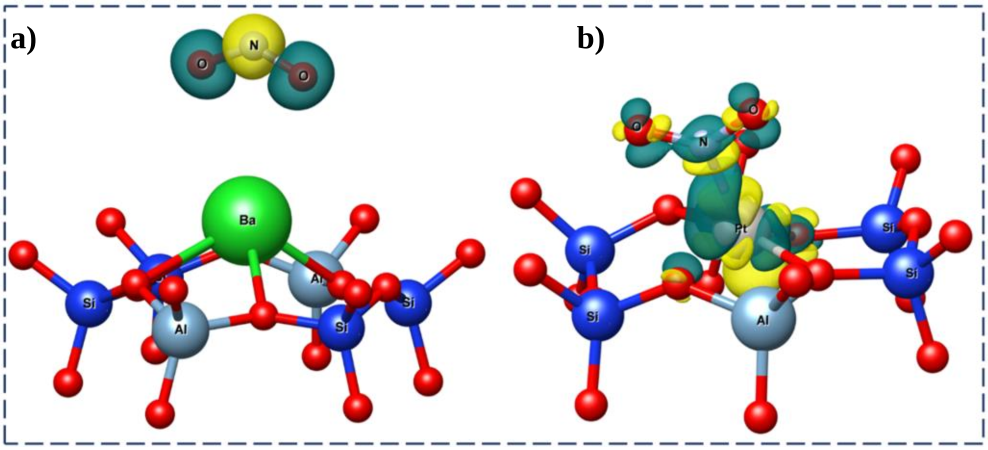

Figure 7.6 : Iso-surface electron density for NO_2 interaction with Ba-FAU (a), and for the most stable configuration of NO_2 interaction with Pt-FAU (b). Yellow and blue colors stand for negative and positive iso-surfaces mapped from +0.003 to -0.003 electron/$Å^{-3}$, respectively.

7.4.2.3 Adsorption of H_2O

7.4.2.3.a Alkaline earth metals Be^{2+}, Mg^{2+}, Ca^{2+}, Sr^{2+}, Ba^{2+}

As shown by their high interaction energy with water around –98 kJ/mol (Table 3), all studied cations display a high affinity for this guest, with a vdW contribution of 9%. According to the HSAB theory[92], alkaline earth metals are considered as hard acids, showing a high affinity for hard bases such as H_2O, which is confirmed by the iso-surface electron-density (Figure 7a). These results are in accordance with the theoretical work of Benco and Tunega[391] on mordenite.

7.4.2.3.b Transition metals Zn^{2+}, Fe^{2+}, Cu^{2+}, Pd^{2+} and Pt^{2+}

With interactions values of −105.3 kJ/mol and −81.6 kJ/mol, Zn^{2+} and Cu^{2+} display the strongest interactions with water (Table 7.3). These values are close to those calculated for alkaline earth metals (Table 7.3). Considering the HSAB theory, Zn^{2+} and Cu^{2+} are the hardest acids amongst all transition metals tested.

On the other hand, Pd^{2+} and Pt^{2+} exhibit weak interactions with water as indicated by the low interaction energies observed, of −48.2 kJ/mol and −33.2 kJ/mol, respectively. Indeed, located below Zn^{2+} and Cu^{2+} in the periodic table, Pd^{2+} and Pt^{2+} are softer cations. The iso-surface electron-density representation (Figure 7b) confirms the weak interaction between Pt and water.

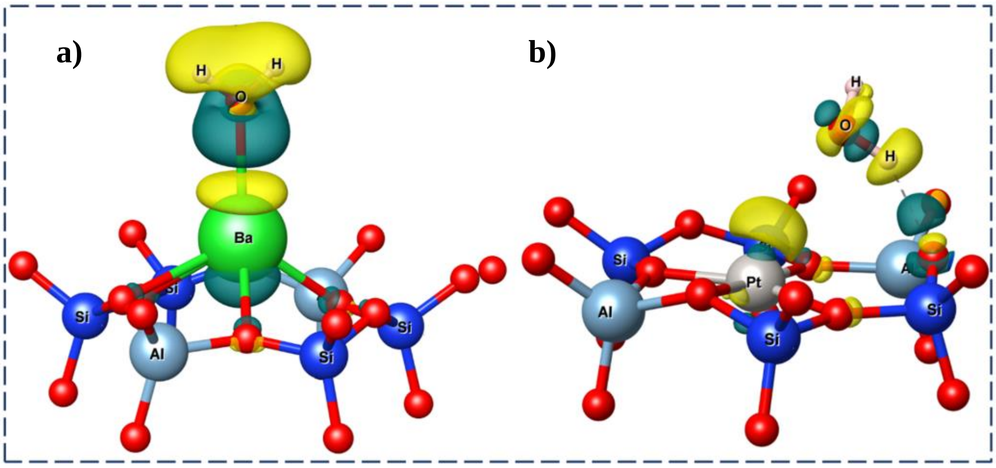

Figure 7.7: Iso-surface electron density for the most stable configuration of water adsorption on Ba-FAU (a) and Pt-FAU (b). Yellow and green colors represent negative and positive iso-surfaces corresponding to +0.003 and -0.003 electron/Å^{-3}, respectively.

Recently, Mandal et al.[401] provided insights into the molecular structure of Pd cations in SSZ-13 zeolites and their interaction with H_2O and NO using experimental and computational analyses. The most stable position of Pd was found to be equal to the site II used here (Figure 7.1), in which the six-membered ring has two aluminum atoms on opposite sides. Once again, the interaction energies of –42 and –123 kJ/mol for H_2O and NO_2 molecules, respectively, agree with the values listed in Table 3.

7.4.3 Selection of the most effective cation to selectively capture NO_x

7.4.3.1 Thermodynamic selectivity of cation-exchanged faujasites

Here our objective was to identify the most effective charge-compensating cation for the selective trapping of NO_x in presence of water by comparing the interaction energies for NO, NO_2 and H_2O

in the different cation-exchanged faujasite zeolites (Figure 8). Knowing that in diesel exhaust gas, concentrations in NO_x (300-1000 ppm) [346,347] are much lower than that of water (10 000 ppm),[306] the adsorbent will have to show a much higher affinity for NO and NO_2 than for water.

Be^{2+}, Mg^{2+}, Ca^{2+}, Sr^{2+}, Ba^{2+} Zn^{2+}, and Cu^{2+}– exchanged FAU, exhibit a higher or equivalent affinity for water than for NO_x (Figure 8), NO and NO_2 have almost the same interaction energy on a given cation, their interaction decreases in absolute value from Mg^{2+} (49 kJ/mol) to Ba^{2+} (23.5kJ/mol). This indicates that these materials will be poor sorbents for NO_x, and unsuitable for the intended pollution control application.

As shown in Figure 7.8, Fe^{2+}– exchanged FAU exhibits a similar affinity for water and NO_2 (–56.3, –53.7 kJ/mol, respectively), but much higher affinity for NO (–155 kJ/mol). This means that water is expected to play a detrimental role on the NO_2 adsorption. However, NO_2 molecule appears to be highly reactive with water in zeolites, leading to NO formation,[313] therefore Fe^{2+} could be an appropriate cation for selectively trapping NO_x in the presence of water owing to its high affinity for NO.

Palladium and Platinum are the only cations showing a higher affinity for NO and NO_2 compared to water (Figure 7.8 - Table 7.3). NO shows a high affinity for both cations (–145.6 and –168.7 kJ/mol, respectively) followed by NO_2 (–84.7 and –74.2 kJ/mol). These interaction energies are significantly higher than for water (–33.2 and –48.2 kJ/mol, for Pd^{2+} and Pt^{2+}, respectively). Therefore, water is not expected to play a detrimental role on the NO_x adsorption in these zeolites. These results reveal that in terms of thermodynamic selectivity, the Pd^{2+}, Pt^{2+} and in a lesser extend Fe^{2+} forms are clearly the most interesting faujasites for the selective capture of NO_x from water.

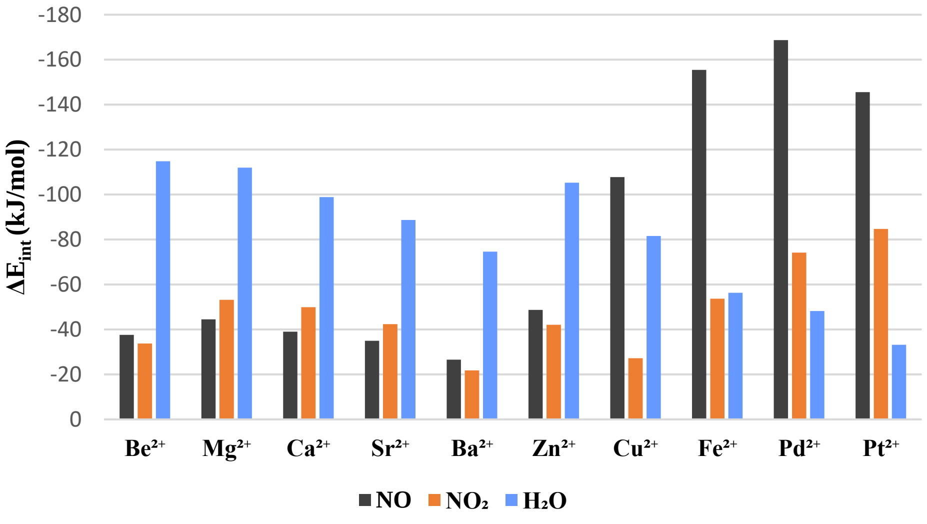

Figure 7.8: The total interaction energies of NO, NO_2, and H_2O with divalent cation-exchanged faujasite, calculated using the PBE + TS/HI level of theory.

7.4.3.2 Regeneration of the faujasites

One further requirement of the adsorbent is to prevent chemical reactions and by-products development that would limit the reliability of the trapping process and the regeneration of the sorbent.[402,403] This can be performed by a full comparative analysis of bond lengths before and after adsorption, the less the bond is activated (i.e., stretched) the more the cation-faujasite is efficient for our purpose.

For alkaline earth cations, bond length analysis for the pristine and loaded faujasites (Figure 9) revealed that the NO bond length slightly decreases (from 0.006 to 0.008 Å for most cations). The "N-O1" bond length with the first oxygen atom in NO_2 is almost unaffected but the "N-O2" bond with the second oxygen is stretched with an average variation of 0.02 Å. Concerning H_2O, the distances of the two water bonds (O-H) are barely changed. In terms of regeneration, alkaline earth cations can safely be used for NO removal. However, NO_2 may develop undesirable by-products formation by chemically reacting with these cations and other molecules. One additional observation in Figure 9 is that beryllium has the most noticeable differences in bond lengths (both stretched and retracted); this may be attributed to its small ionic radius (Table 7.1). Therefore, we can suggest that the smaller the radius, the higher the probability of activating the bond length becomes.

Looking at transition metals, all five cations can be safely used to trap NO, as their (N-O) bond lengths become shorter than in the gas phase (Figure 7.9). For NO_2, significant activation of both N-O1 and N-O2 bonds occurs for Fe^{2+}, Cu^{2+} and Zn^{2+}, while only a slight variation in bond length from 0.004 and 0.005 Å is observed for Pd^{2+} and Pt^{2+}, respectively. These variations are too small for affecting the regeneration process and are therefore negligible. Concerning water adsorption, a minor variation in H-O bond length was observed for all cations, except for zinc and copper where the variation in the O-H bond of water was significant (Figure 7.9).

Indeed, the analysis of the bond activation shows that only Pd^{2+} and Pt^{2+} can be effectively used for NO_x trapping. In the following, we will evaluate the potential of Pt^{2+}, which is less costly than Pd^{2+}, when embedded in a realistic faujasite Y structure characterized by a Si/Al ratio of 2.4.

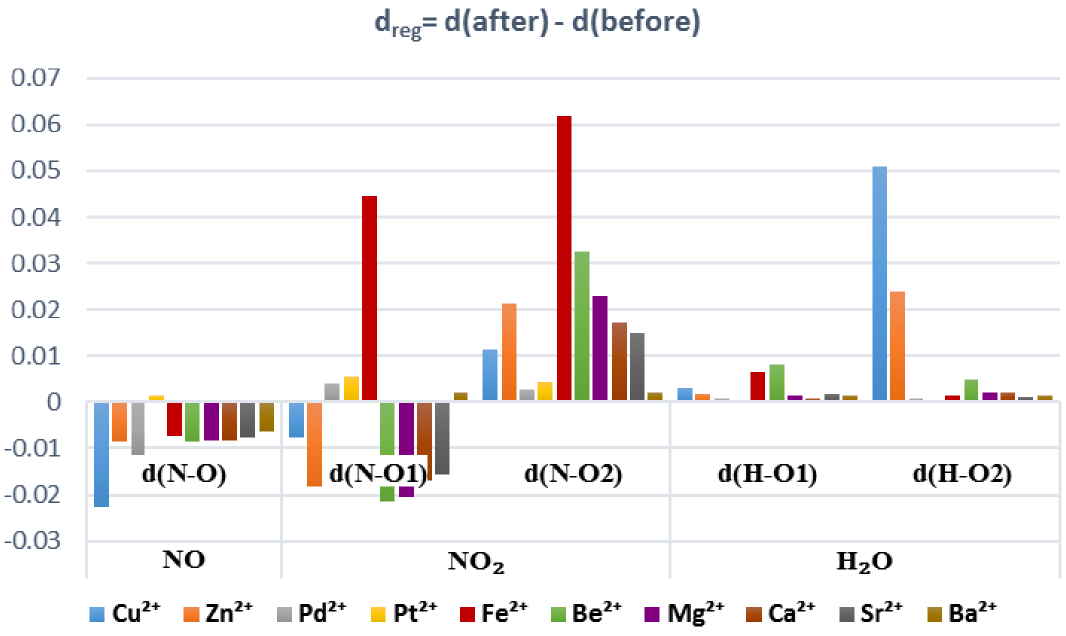

Figure 7.9: Variation of the molecules bond lengths between the gas phase and once adsorbed in the faujasites. N-O (in the NO molecule); N-O1 with the first oxygen atom, and N-O2 with the second oxygen atom (in the NO_2 molecule) and O-H1 and O-H2 (in water).

7.4.4 Evaluation of Pt(II)-NaY for NO_x capture

To obtain a Pt(II)-NaY structure (Si/Al ratio =2.4), 14 Si atoms were substituted by 14 Al atoms in the primitive cell (Figure 7.10). The distribution of platinum cations in the zeolitic Y-structure may have an impact on the adsorption mechanisms of NO_x. Numerous experimental and, more recently, simulation methods have been reported on the location of cations in Faujasite. Frising and Leflaive,[381] have gathered and presented in an extensive review, all the different results that have been published in the literature over the years.

For platinum, only one reference was found where Na-Y zeolite was partially Pt-exchanged.[404] Therefore, the molecular formula of the investigated cell is $Pt_4Na_6Al_{14}Si_{34}O_{96}$. In this cell, unexchanged Na^+ cations seem to prefer site II (supercage) followed by site I (at the center of the hexagonal prism), while Pt^{2+} cations tend to occupy site II and site I' (In the sodalite cage) (Figure 10).

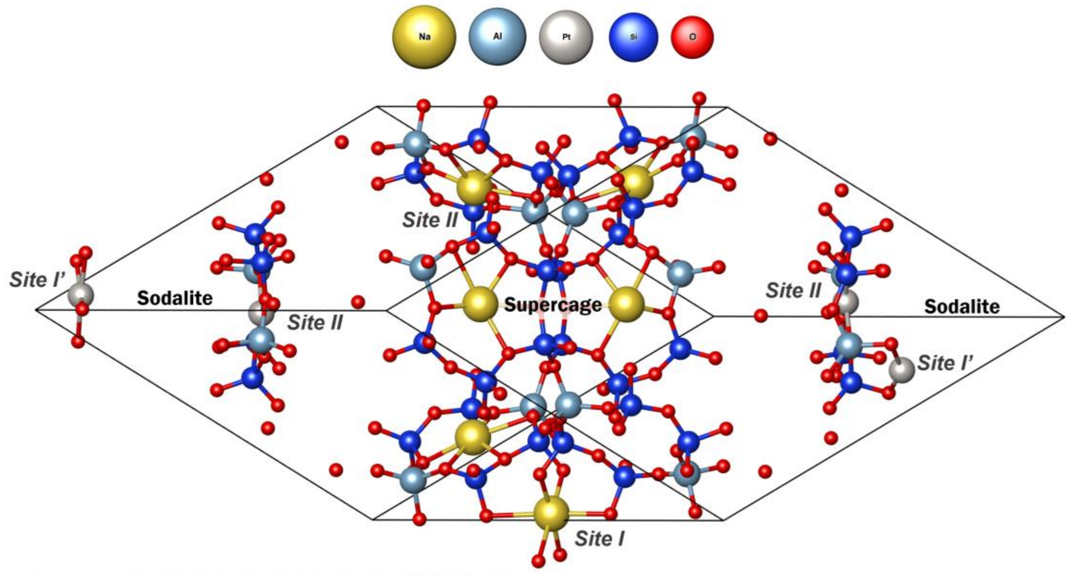

Figure 7.10: The Pt-NaY zeolite primitive cell displayed in ball and stick cell, with three accessible sites. Site II (Supercage), site I (Hexagonal Prism) and site I'(Sodalite cage).

7.4.4.1 Thermodynamic selectivity of cation-exchanged faujasites.

The interaction energies calculated for NO, NO_2 and H_2O in Pt-Y zeolites (Figure 11) follow the same trend that presented above for USY (Figure 8). NO_x molecules interact strongly with the zeolite with an associated interaction energies of –269.0 kJ/mol and –199.8 kJ/mol for NO and NO_2 respectively which are higher than the value obtained for H_2O (–38.4 kJ/mol). Therefore, upon increasing of Pt concentration (i.e., Si/Al ratio = 2.4), the affinity towards NO_x molecules enhances, while the adsorption of water molecule shows no change related to the concentration of the cation.

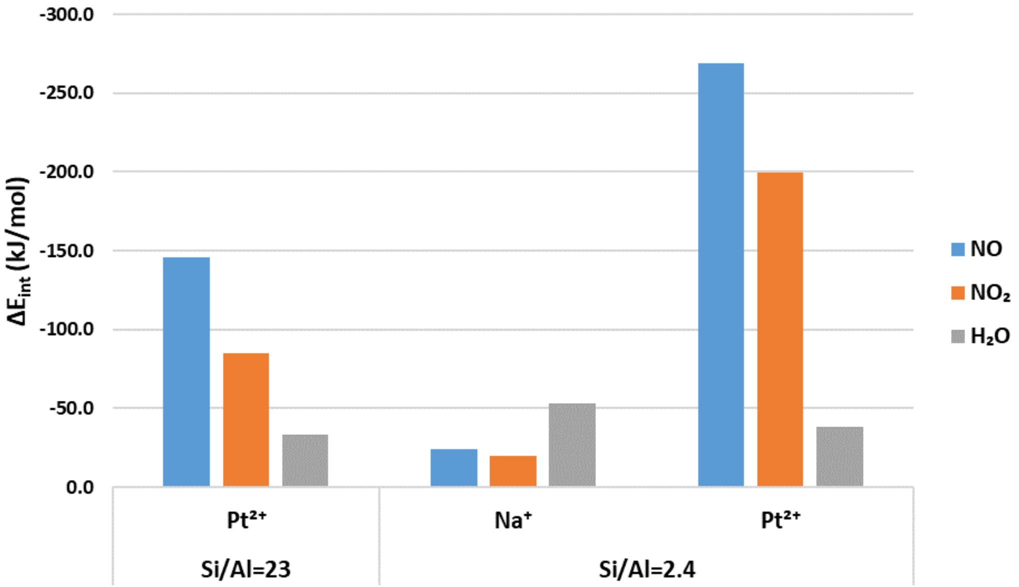

Figure 7.11: The total interaction energies of NO, NO_2, and H_2O with platinum exchanged Na-Y zeolite, calculated using the PBE + TS/HI level of theory.

By contrast, the difference in interaction energies for NO_x by increasing the cation concentration is surprisingly relatively high, especially since in both cases the adsorption takes place on the same cation position (site II). These observations tend to be driven by the location stability of the cation.

Comparing the [Pt-O] distance between the Pt (II) cation and the D6R oxygens on both Si /Al ratio, it was found that for the pristine bare zeolite, the platinum cation located on the D6R plane binds strongly to four oxygens, with an average distance of 2.07 Å. Upon adsorption, Pt on zeolite Y was found to be more sensitive to NO_x adsorption. The platinum in zeolite Y is displaced from its original position and slightly elevated from the D6R plane with 2.04 Å (Figure 13e,f) compared to 1.08 Å for USY (Figure 5).

This higher mobility of the Pt cations in zeolite Y compared to zeolite USY seems to be related to the influence of neighboring cations in the sodalite cage. As can be seen in the Figure 7.12, the sodalite cage is strongly perturbed upon NO_x adsorption, the site II Pt cation is pulled out from its original position, subsequently followed by a displacement of the site I' Pt cation towards this vacant site II. This cation confinement effect leads to a greater exposure of the site II Pt cation to the probe molecule compared to the USY zeolite.

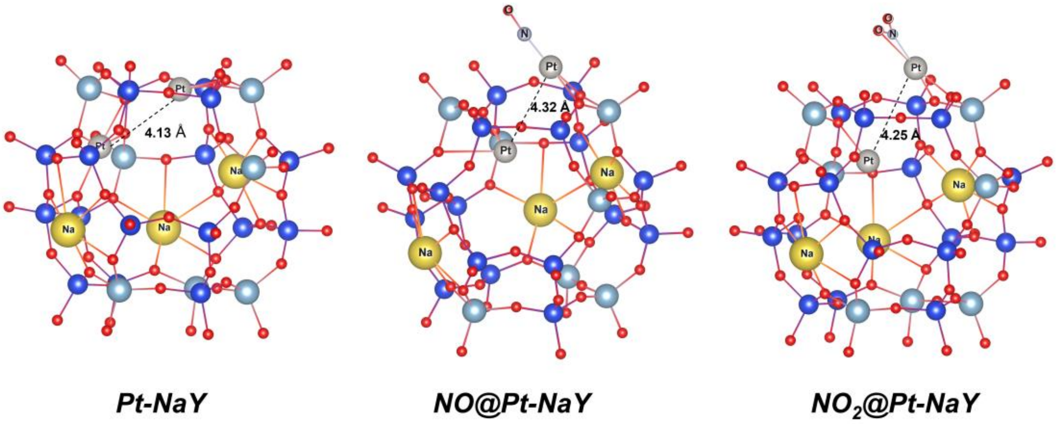

Figure 7.12: Displacement of site I' and site II Pt cations upon NO_x adsorption in Y-type zeolites.

The migration of cations from site II to the supercage in zeolite Y, has been discussed in many works: Typically, some of us [405] demonstrated by molecular dynamics combined with complex impedance spectroscopy measurements that methanol perturbs Na-Y zeolite, moving cations from site II to the center of the supercage, followed by hopping of SI' cations from the sodalite cage into the supercage to fill the vacant SII sites. Klier[406] also mentioned that a CO molecule induces the displacement of Cu(I) from less accessible to more accessible positions in Y-type zeolites.

As a result, this leads to a higher interaction energy along with 0.21 and 0.19 |e| charge transfer (Eq.4) for Pt-NO and Pt-NO_2 respectively (Figure 13e,f), compared to 0.14 and 0.09 |e| (Eq.4) found previously for the USY zeolite. In contrast, a slight perturbation of the Pt position is observed upon H_2O adsorption, explaining the low interaction energy and charge transfer of 0.05 |e| (Eq.4) (Figure 13g).

Similarly, the presence of residual sodium from the partially exchanged zeolite may affect our NO_x trapping and should therefore be investigated. Adsorption of NO_x on these cations revealed very low interaction energies of −24 and −20 kJ/mol for NO and NO_2, respectively (Figure 11). While a strong affinity towards water has been achieved, at an interaction energy of −55 kJ/mol (Figure 11) in agreement with the HSAB principle.[92] These results indicate that the NO_x trapping efficiency would improve in tandem with a high Pt exchange in the Na-Y.

The reported high NO_x interaction energies with Pt cations along with the low interaction energies for Na cations can be understood by studying the differences in electron density ($\Delta\rho$) induced by adsorption. In this context, we found that the interactions between N and Pt atoms display a significant electron transfer (Figure 13 e,f), the green density around the NO_x molecules reflecting the loss of charges towards the yellow area of the Pt cation. For the Na cations a poor charge transfer can be observed upon adsorption of NO_x (Figure 13a,b), the water molecule, however showed a higher charge transfer but mainly in the form of hydrogen bonding with the D6R oxygen atom (Figure 13c).

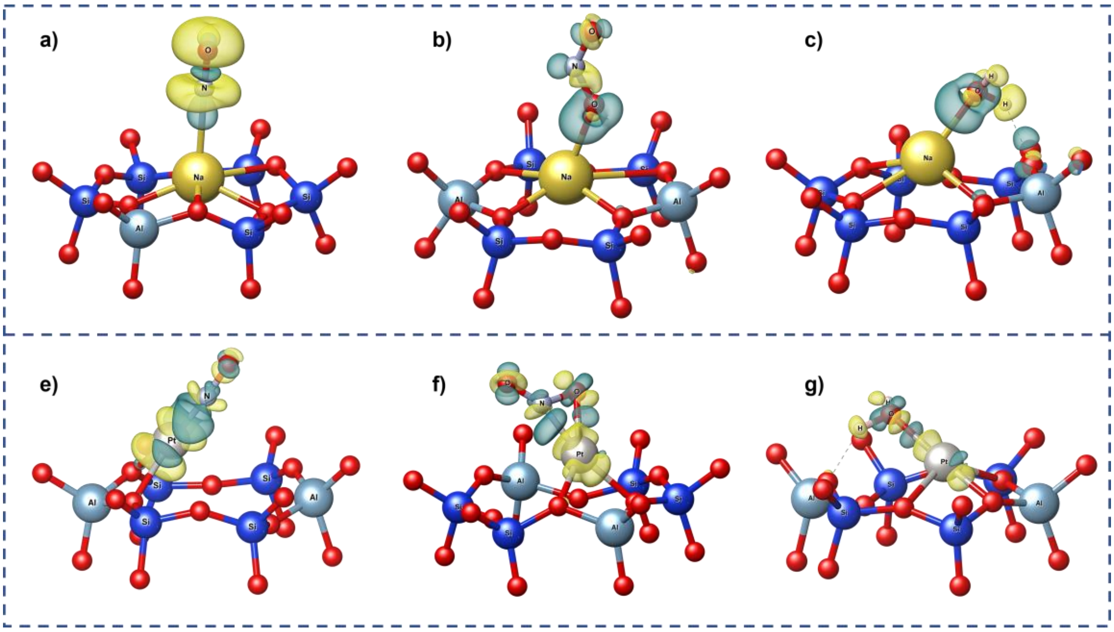

Figure 7.13: Iso-surface electron density for the most stable configuration of NO, NO_2 and H_2O adsorption on Na-Y (a-c) and Pt-NaY (e-g). Yellow and green colors represent negative and positive iso-surfaces corresponding to +0.01/+0.003 and -0.01/-0.003 electron/Å^{-3} for Pt and Na respectively.

7.4.4.2 Regeneration of Pt(II)-NaY faujasite

A comprehensive comparative analysis of bond lengths for the pristine and loaded zeolites has been achieved.

As for USY (Figure 4a), the NO molecule was found to be adsorbed by its nitrogen atom on the Y zeolite (Figure 13e). This adsorption configuration maintained the same bond length, preventing it from activation (Figure 14), similarly to what has been observed on USY (Figure 9).

For NO_2, due to the large displacement of the cation position, π interactions were observed between the Pt of the Y zeolite and the molecule (Figure 13f). This adsorption configuration led to a significant stretching of the non-interactive (N-O) bond (Figure 14). In contrast, for the USY, the NO_2 molecule was adsorbed only via its nitrogen (Figure 4b), resulting in no change in its bond length (Figure 14).

Concerning water, due to the weak hydrogen bonding that occurred during adsorption (Figure 13g), the bond length of the molecule was negligibly stretched (Figure 14).

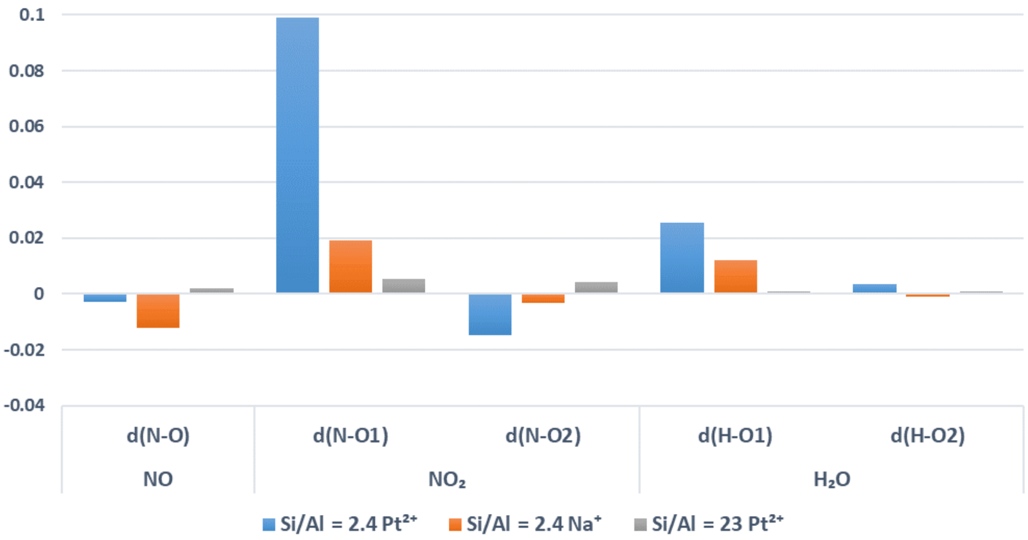

Figure 7.14: Variation of the molecules bond lengths before the adsorption on cation-exchange faujasites (gas phase) and after the adsorption. N-O (in the NO molecule); N-O1 with the first oxygen atom, and N-O2 with the second oxygen atom (in the NO_2 molecule) and O-H1, O-H2 (in water).

To summarize, the binding analysis shows that Pt(II)-NaY can be safely used for NO removal in presence of water. However, because of the significant lengthening of NO_2 bond lengths, Pt(II)-NaY appears to be not usable for NO_2 removal, as it can lead to the formation of undesirable by-products, resulting from the dissociation and the chemical reaction of NO_2 with platinum and other molecules. In addition, the revealed high interactions between NO_x and Pt may leave the latter difficult to regenerate. Therefore, future work is needed to investigate the desorption properties of the most promising zeolites to determine the optimal regeneration temperature.

7.5 Conclusion

In summary, in the context of the prevention of harmful emissions from diesel engines, DFT simulations using van der Waals correction have been conducted to study the effect of water on the NO_x capture by cations containing faujasites. Several divalent cations (alkaline earths (Be^{2+}, Mg^{2+}, Ca^{2+}, Sr^{2+}, Ba^{2+}) and transition metals (Fe^{2+}, Cu^{2+}, Zn^{2+}, Pd^{2+}, Pt^{2+})) exchanged faujasite were tested to identify the most selective sorbents toward NO and NO_2 contaminants.

Overall, when considering thermodynamic selectivity criteria, our interaction energy calculations show that alkaline earth metals, as well as Cu^{2+} and Zn^{2+}, exhibit a higher affinity for water than NO_x, indicating their unsuitability for the target application, whereas the remaining charge-compensating cations (Fe^{2+}, Pd^{2+} and Pt^{2+}) behave more efficiently, since all of them show a greater affinity for NO, leaving water with no expected detrimental effect on NO_x adsorption, with the exception of Fe^{2+} that presents a similar affinity for water and NO_2.

Nevertheless, the bond activation analysis discarded Fe^{2+} from the suitable cations list, since a significant activation of the N-O1 and N-O2 bonds is observed for the adsorption of NO_2 on Fe^{2+}, resulting in undesired by-product formation, whereby a negligible variation in bond length is observed for Pd^{2+} and Pt^{2+}.

The Pt^{2+}cation was then incorporated and studied within Y zeolite (Si/Al = 2.4). The results highlight that the Pt^{2+} Faujasite Y is an interesting material for the removal of NO_x from diesel engine exhaust.

This screening method transferable to the adsorption study of other contaminants by zeolite sorbents, including ammonia gas and formaldehyde among others is expected to guide the experimental effort towards the synthesis of the optimum sorbents to avoid tedious and time-consuming trial-error approach.

Chapter 8

UiO-66 nano-porous Metal-Organic Framework functionalized by metal(II)-catecholate for effective NOx capture

The studies summarized in this Chapter have been published as:

A Computational Exploration of Metal (II) Catecholate Functionalized UiO-66 Nanoporous Metal-Organic Framework for Effective NOx Capture

Karuppasamy Gopalsamy, Mohammad Wahiduzzaman, **Ayoub Daouli**, Michael Badawi[‡] and Guillaume Maurin

ACS Applied Nano Materials Article ASAP
DOI: 10.1021/acsanm.2c03284

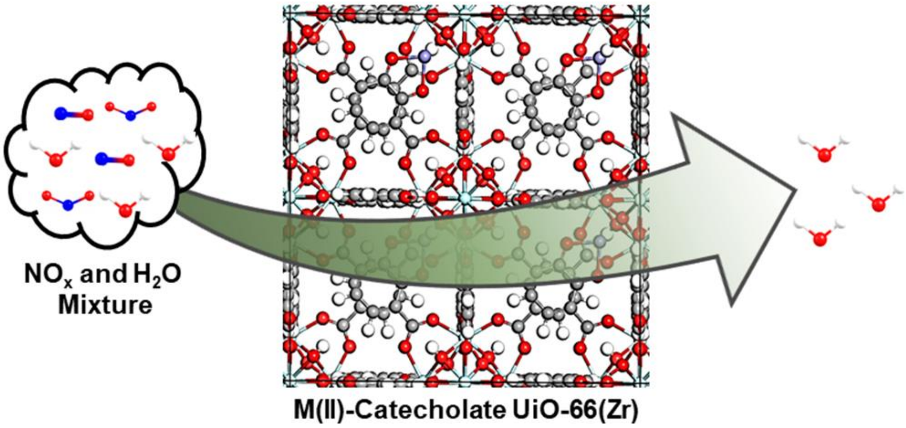

8.1 Abstract

Metal-organic frameworks (MOFs) have attracted much attention for the effective capture of contaminants from air. Herein, density functional theory (DFT) calculations and grand canonical Monte-Carlo (GCMC) simulations were combined to systematically assess the adsorption performance of the cage-like UiO-66 nanoporous MOF functionalized by metal(II)-catecholate (CatM(II), where M(II) = Mg(II), Mn(II), Fe(II), Co(II), Ni(II), Cu(II), Zn(II), Pd(II) and Pt(II)) with respect to NO_x potentially present at very low concentration (from ppm to ppb levels). The adsorption modes and energetics of NO_x towards the metal(II)-catecholate functions

were first examined systematically using cluster DFT-calculations in order to determine the optimum metal(II) for an effective NO_x capture. The best CatFe(II) was further incorporated in the crystal structure of UiO-66 and force field parameters to accurately describe the specific interactions between Fe(II) and both NO_x were derived from periodic DFT calculations and further implemented in a GCMC scheme to predict the adsorption isotherms in a whole range of gas pressure. These calculations revealed that UiO-66-CatFe(II) exhibit steep-adsorption isotherms for both NO_x, leading to excellent adsorption uptakes at very low gas pressure (from 10^{-9} to 10^{-4} bar). This finding complements the portfolio of nano porous materials that have been so far almost exclusively tested in operation conditions at much higher NO_x concentration (> 1000 ppm).

8.2 Introduction

Fossil fuels (coal, oil, and gas) are still the main energy resource for various chemical industries, power plants and automotive sectors. Almost 80% of the world energy requirements are derived from fossil fuels by combustion processes[407] that produce a wide array of pollutants, such as nitrogen oxides (NO_x), carbon oxides (CO_x), sulphur oxides (SO_x) and various volatile organic compounds (VOCs) that contribute to degrade air quality.[408-409]Among them, NO_x are considered as life threatening toxic gases present in the atmosphere, with NO_2 showing even a higher level of toxicity than NO.[408] Exhaust from transport vehicles is the primary source of NO_2 emission.[4] Exposure to NO_2 alters the respiratory paths and can cause death even at the ppm level of concentration.[409] Therefore, NO_2 capture is of key importance due the high reactivity and toxicity of this molecule as well as its impact on global warming. Industries currently rely on the energy intensive selective catalytic reduction (SCR) technique to remove NO_2 from flue gas emission.[410] However, this process requires very high operational temperature (>300 °C) to reduce NO_x by ammonia or urea in the presence of V_2O_5-supported catalyst.[411] In addition to NO_2, capturing of NO is also pay more attention due to it is important biological applications in wound healing, antibacterial, antithrombotic, neurotransmitter and neuromodulator in the central nervous system, etc.[412-413]

Physisorption Physisorption-based NO_x adsorption with the use of efficient sorbents is a promising alternative strategy.[408] Among the family of porous materials, activated carbons (ACs)[414] and diverse zeolites including mordenite, ZSM-5 and faujasite have been revealed as potential candidates for NO_x capture,[415-416] however with some limitations due the high reactivity and acidic nature of NO_x that led to either a collapse of the porous structures or regeneration issues. More recently, Nanoporous metal-organic framework[417-418] structures have been proposed as alternative solution for NO_x capture at low pressure owing to the large variety of NO_x specific adsorption sites that can be incorporated in their pore walls. Besides MFM-300[417-419] and MFM-520[420] that were found to exhibit high NO_2 adsorption capacity at low pressure, the presence of accessible metal sites either in the inorganic nodes or grafted to the organic linker of the MOF framework has been demonstrated to be a key for the selective adsorption of highly polar molecules such as NO_x.[417-418] Typically, the MOF-74 architectures containing open metal sites in the inorganic nodes have been found attractive for NO capture in a relatively broad range of gas pressures 0.1 - 1 bar.[421] while PCN-250 with Fe(III) partially substituted by Co(II), Mn(II), and Zn(II) was predicted to exhibit a high binding energy for NO_2 of importance for sensing applications.[418] Nanoporous MOF-808(Zr) incorporating various functionalized ligands was also evoked as a promising candidate with attractive NO_2 uptake under dry and humid conditions.[422] The prototypical Zr-cage like MOF UiO-66 in its pristine and $-NH_2$ ligand functionalized form have been also reported as good candidates for NO_2 adsorption.[422] Alternatively, ligand-defective UiO-66 MOFs incorporating oxalic acid ligand (labelled as UiO-66-ox), through a solvent-assisted ligand incorporation procedure was also shown to exhibit a high NO_2 storage capacity however associated with a chemisorption process or a substantial electronic transfer with the MOF wall that makes the regeneration questionable.

Herein, we envisage the incorporation of metal(II)-catecholates (CatM(II)) grafted to the carboxylate linker of the nanoporous Zr-MOF UiO-66 with the objective to substantially boost the adsorption performance of this family of cage-like MOF owing to the specific interactions between the exposed M(II) sites and the NO_x molecules. The incorporation of metal-catecholate functional groups in MOFs has been already envisaged in the literature. From a theoretical standpoint, Stoneburner and Gagliardi explored the O_2/N_2 separation ability of a series of redox-active transition metal catecholates by means of DFT calculations revealing the Fe(II) and Zn(II) substituted metal-catecholates units as the most promising candidates implying moderate binding energy.[423] Another computational study reported by Dimer et al. computationally screened by Monte Carlo techniques the O_2/N_2 separation performance of 5109 MOFs from the CoreMOF database and incorporated metal catecholate units in the most promising MOF candidates. They evidenced that the Cd(II)-catecholates incorporated in UiO-66, MOF-5 and IRMOF-14 enable an effective separation of O_2 over N_2.[424] Snurr *et al* extensively studied a variety of divalent s-block and d-block metals substituted catecholates for the adsorption of various small molecules such as H_2, H_2O, NO, CO, CO_2, NH_3, PH_3, AsH_3 and CH_3Br using DFT-cluster calculations.[425]-[426] More recently, the same group performed high-throughput Monte Carlo screening of 2736 metal-catecholate functionalized Zr-MOFs for room temperature hydrogen storage.[426]

Li *et al.* reported a series of two-dimensional Cu(II)-catecholate MOF (M = Cu(II), Ni(II) or (Co(II) with H_6HHTP (2,3,6,7,10,11-hexahydroxytriphenylene) as linker using a cathodic synthesis approach.[427] Zhang *et al.* prepared copper-catecholate functionalized UiO-68 MOFs using de novo mixed-linker strategy with attractive catalytic activity for cyclohexane oxidation.[428] Weston et al. synthesized various catecholate and metal-catecholate-functionalized porous organic polymers (POPs) with Cu(II), Mg(II), Mn(II), and Zn(II) using post-synthetic metalation strategies of interest for trapping a range of airborne toxic chemicals such as NH_3, ClCN and SO_2.[429]-[430] More recently, Daliran *et al* synthesized porphyrin catecholate iron(II)-based MOFs and studied their photocatalytic performance for the one-pot selective oxidation of benzyl alcohol.[431] Cohen *et al* successfully prepared various metal(III)-catecholates (Fe(III), Cr(III), and Ga(III)) functionalized UiO-66 MOFs for the catalytic reduction of CO_2 and oxidation of alcohols.[432]-[433]

Indeed, all these previous experimental and theoretical studies emphasized that the incorporation of metal(II)-catecholate functions in the MOFs backbone is feasible. This encouraged us to first systematically explore the affinity of NO and NO_2 as well as H_2O in a series of metal catecholate (CatM(II): M = Mg(II), Mn(II), Fe(II), Co(II), Ni(II), Cu(II), Zn(II), Pd(II) and Pt(II)) models using cluster-based Density Functional Theory (DFT) calculations. The objective of this preliminary step (Figure 8.1-step 1) was to identify the metal(II)-catecholate showing the highest affinity to NO and NO_2 vs H_2O. Among these best metal(II)-catecholates, the Fe(II)-derivative was introduced as partially-substituted linker in the UiO-66(Zr) framework (Figure 8.1-step 2). Further periodic DFT calculations on the resulting UiO-66-CatFe(II) structure were performed to derive specific Morse-potential force field parameters in order to accurately describe the interactions between the Fe(II) accessible sites and both NO and NO_2 that cannot be achieved with the current generic force fields (Figure 8.1-step 3). These newly-derived force fields were then implemented in a Grand-Canonical Monte Carlo (GCMC) scheme to predict the single component NO_x adsorption isotherms in a wide range of pressure from 10^{-9} to 1 bar to assess the performances of these functionalized materials in different working conditions (Figure 8.1-step 4) and beyond to deliver an *in-depth* understanding of the microscopic adsorption mechanism in play. These findings revealed that UiO-66-CatFe(II) is highly effective for NO_x capture in the very low domain of pressure, exceeding the adsorption uptakes of the other porous solids reported so far under this working condition. This makes this material a very promising adsorbent for the sorption of NO_x traces at the ppm and even ppb levels.

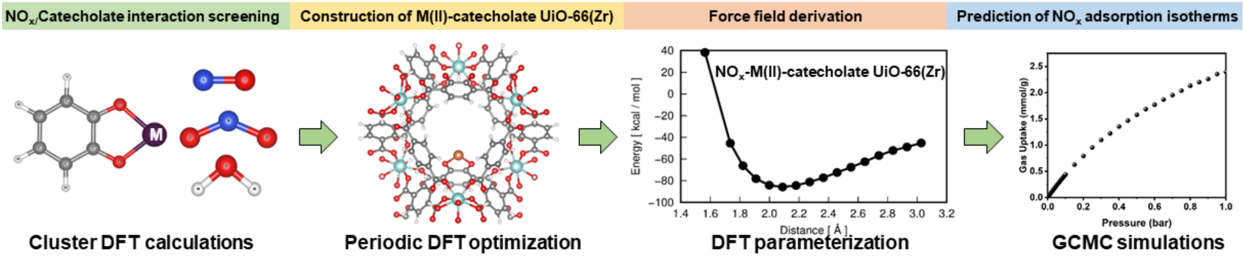

Figure 8.1: Overview of the overall computational strategy with step 1: cluster-DFT calculations to assess the interaction energy between NOx and a series of metal-catecholate cluster models incorporating a systematic change of the nature of the divalent metals: M = Mg(II), Mn(II), Fe(II), Co(II), Ni(II), Cu(II), Zn(II), Pd(II) and Pt(II); step 2: incorporation of the best catecholates as ligand in the periodic crystal structure of UiO-66 further DFT-optimized; step 3: Derivation of the NOx/Metal catecholate UiO-66(Zr) force field parameters for the most promising catecholate functionalized UiO-66(Zr) by periodic DFT-calculations and, step 4: GCMC predictions of their adsorption isotherms. Color codes: red (oxygen), blue (nitrogen), gray (carbon), white (hydrogen), cyan (zirconium) and brown (iron).

8.3 Computational methods

8.3.1 Cluster-DFT Calculations

DFT calculations were first carried out to explore the interaction mode and energetics of NO_x and H_2O towards the Metal(II) catecholate CatM(II) [where M = Mg(II), Mn(II), Fe(II), Co(II), Ni(II), Cu(II), Zn(II), Pd(II) and Pt(II)] using representative catecholate linker cluster models (Figure 8.1-step 1) in similarity to previous works.[425] Several starting configurations were considered for each guest/cluster system. All these calculations were performed with the Gaussian09 software[434] using the PBE-D3(BJ)[435] functional with def2-TZVPP[436] basis set except for Pd(II) and Pt(II), for which we employed the LANL2DZ[437] (effective core potential) basis set. Spin multiplicities for all these systems are described in Table S8.1. Vibrational frequency analysis enabled to check the absence of negative frequencies for all these DFT-optimized structures thereby confirming that they correspond to energy minima. The interaction energies (IEs) of NO, NO_2 and H_2O for each CatM(II) complex were then calculated using the following energy expression (Eq 8.1):

$$\mathbf{IE} = \mathbf{E_{cluster-guest}} - (\mathbf{E_{cluster}} + \mathbf{E_{guest}}) \qquad \text{Eq 8.1}$$

where IE represents the cluster/guest interaction energy, $E_{cluster-guest}$ is the total energy of the CatM(II)/guest complex, $E_{cluster}$ and E_{guest} are the energies of the isolated CatM(II) cluster and guest molecule respectively. These interaction energy values were corrected with the basis set superposition error (BSSE) using the counterpoise (CP) procedure.[438] In order to understand further the interaction nature of NO_x in the metal substituted catecholate units (CatM(II)), the projected density of states (pDOS) were calculated using the PBE-D3(BJ)[439] functional as implemented in the Vienna ab initio simulation package (VASP).[440]

8.3.2 Periodic DFT Calculations on NO_x/ UiO-66-CatFe(II) and Force Field Parameterization

A single Fe(II)-catecholate linker was incorporated in the periodic structure of UiO-66 (Figure 8.1-step 2). The corresponding UiO-66-CatFe(II) model (primitive cell) (Figure 8.1) and its NO- and NO_2-loaded forms were fully geometry optimized at the DFT-level using the same PBE-D3(BJ)[439] functional as implemented in VASP.[440] On site Hubbard U corrections (U = 4.0 eV) were employed to account for the electronic correlation of the unpaired d electrons of Fe(II).[441] The core and valence electrons of the interacting elements were treated with projector-augmented wave potentials (PAW)[442] and plane-wave basis sets. Gamma point mesh for sampling Brillouin zone were used along a plane wave kinetic energy cutoff of 600 eV. The total energy and ionic forces convergence criteria were set to 10^{-6} eV and 0.02 eV/Å, respectively. The UiO-66-CatFe(II)-NO and UiO-66-CatFe(II)-NO_2 interaction energy curves were constructed from periodic single point energy calculations performed for 15 UiO-66-CatFe(II)-NO and UiO-66-CatFe(II)-NO_2 configurations associated with different NO_x-CatFe(II) separating distances while maintaining the same orientation as obtained for the DFT-optimized structure. These interaction energy curves were fitted by an analytical function combining van der Waals (vdW) and Coulombic terms (equation 2). The atomic partial charges for the MOF atoms were derived with the DDEC (Density-Derived Electrostatic and Chemical charges) method from the DFT-optimized structure using the DDEC6 program.[443] The vdW interactions between NO_x and all atoms of the UiO-66-CatFe(II) framework except the open metal Fe(II) sites were treated by the standard 12-6 Lennard-Jones (LJ) pairwise interaction potential (equation 2). The LJ parameters for all MOF atoms were taken from the Universal force field (UFF)[444] while NO and NO_2 were described by previously reported two and three LJ charged models respectively (Table S8.2 and S8.3).[445] The cross- LJ terms were calculated using the Lorentz Berthelot combination rules. The interactions between NO_x and the open metal Fe(II) sites were described by a Morse potential with D, α and r_0 parameters were derived using the General Utility Lattice Program (GULP)[446] by minimizing the difference between the DFT interaction energy and the analytical function given in equation 2.

$$E(r_{ij}) = \sum_{i,j} 4\,\varepsilon_{ij}\left[\left(\frac{\sigma_{ij}}{r_{ij}}\right)^{12} - \left(\frac{\sigma_{ij}}{r_{ij}}\right)^{6}\right] + \sum_{i,j} D\left[\left(1 - e^{-\alpha * (r_{ij} - r_0)}\right)^2 - 1\right] + \sum_{i,j} \frac{q_i q_j}{4\pi\varepsilon_0\, r_{ij}} \qquad \text{Eq 8.2}$$

i, j: all MOF atoms except Fe(II) and all NO_x atoms — i: Fe(II) and j: all NO_x atoms — i, j: all MOF atoms and all NO_x atoms

Lennard-Jones Term — Morse Term — Coulombic Term

where r_{ij} is the distance between the interacting atoms i and j, ε_{ij} and σ_{ij} are the associated LJ interatomic potential parameters, ε_0 is the permittivity of vacuum while, D α and r_0 are the Morse potential parameters for the interactions between Fe(II) and NO_x.

8.3.3 Monte Carlo Simulations

The NO and NO_2 single component adsorption isotherms for both UiO-66 and UiO-66-CatFe(II) were calculated by grand canonical Monte-Carlo (GCMC) simulations implementing the force field discussed above (equation 2) using CADSS software.[447] Both pristine UiO-66 and UiO-66-CatFe(II) incorporating four CatFe(II) units per unit cell (corresponding to a Zr/Fe metalation ratio of 1:0.17 similar to the value 1:0.21 reported previously for the analogue UiO-66-CatFe(III)-OCH_3[432]) were DFT-geometry optimized. A simulation box consisting of eight-unit cells (2×2×2) was considered for both MOFs and the atomic positions of the MOF frameworks were held fixed, during the adsorption and trial moves for the guest molecules included i.e., translational, rotational, creation and deletion. The host-guest non bonded LJ interactions were computed in real space using a cutoff of 12.0 Å. The long-range electrostatic interactions were calculated using Ewald summation technique[448] with an accuracy of 1×10^{-6}. For each pressure point, 2×10^{7} Monte-Carlo production steps were considered. Peng−Robinson equation of state was used to determine the gas phase fugacity for both NO_x molecules.[449] Radial distribution functions (RDF) for all MOF / NO_x atoms pairs were averaged over the MC steps at different pressure ranges. The NO_x adsorption enthalpy was calculated for both MOFs at infinite dilution using the Widom insertion method.[450]

8.4 Results and discussion

8.4.1 Interaction Mode and Energetics of NO_x and H_2O Towards CatM(II)

The optimized geometries of the NO_x/CatM(II) complexes are shown in Figure 8.2a and 8.2b, respectively alongside the corresponding interaction energies listed in Table 8.1. The corresponding complexes for H_2O can be found in Figure S8.1.

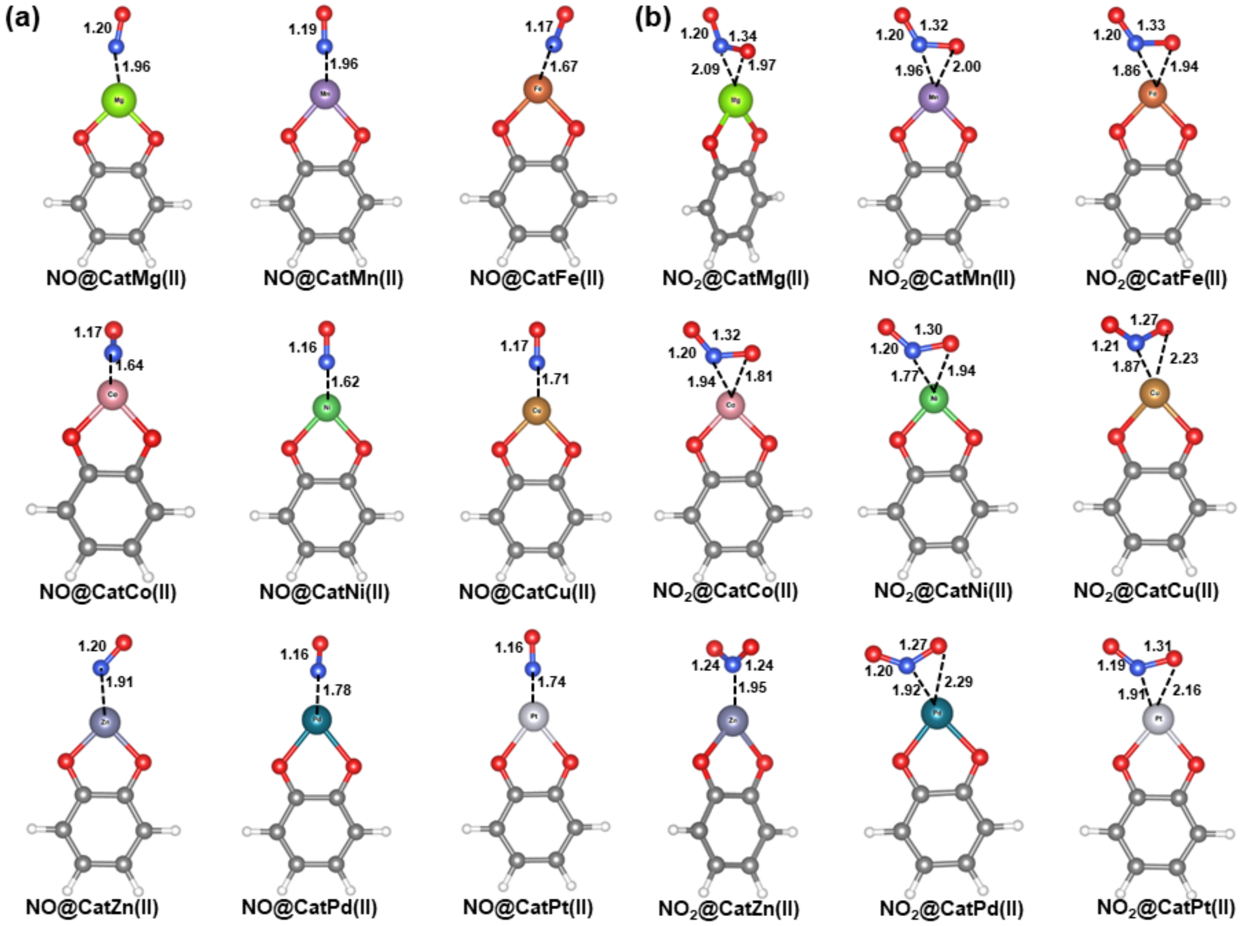

Figure 8.2: DFT-optimized geometries of (a) NO@CatM(II) and (b) NO_2@CatM(II) complexes. The characteristic distances are reported in Å. Color codes: red (oxygen), blue (nitrogen), gray (carbon) and white (hydrogen).

These calculations showed that NO preferentially interacts with the CatM(II) metal centers via its N-atom forming an end-on geometry with M(II)···N(NO) separating distances ranging from 1.62 Å (Ni(II)) to 1.96 Å (Mg(II)) (Figure 8.2a), in line with the simulated data reported previously for some of these M(II)-catecholate. Pt(II), Fe(II), Ni(II), Co(II) and Mn(II) catecholates are identified as the most attractive metal sites for NO as revealed by their higher interaction energies with NO as compared to the other Metals (II) (Table 8.1).

Table 8.1: DFT-calculated interaction energies (in kcal/mol) for NO, NO_2 and H_2O in the various CatM(II).

Complexes	**NO**	**NO_2**	**H_2O**
CatMg(II)	-50.3	-90.9	-29.6
CatMn(II)	-69.3	-76.0	-26.5
CatFe(II)	-73.0	-72.2	-26.5
CatCo(II)	-72.0	-67.9	-25.6

CatNi(II)	-72.9	-67.1	-26.1
CatCu(II)	-49.4	-46.5	-24.9
CatZn(II)	-44.6	-63.3	-26.2
CatPd(II)	-62.3	-53.7	-17.8
CatPt(II)	-90.1	-78.9	-28.4

The high NO affinity towards certain Metal-catecholates was previously demonstrated to be due to π-back-bonding from the d orbitals on the metal into the π^* orbitals of the NO.[425] Regarding NO_2, except for Zn(II) which interacts preferentially with its N atom, side-on interactions are observed with one of the N–O arms invariably lying parallel to the M(II) centers. This results into a dual interaction between metal (II) and both oxygen and nitrogen atoms of NO_2. Table 8.1 shows that in addition to Pt(II), Fe(II), Ni(II), Co(II) and Mn(II), Mg(II) equally exhibits strong interactions with NO_2. Interestingly, all these Metal(II)-catecholates exhibit a much lower affinity for H_2O (Table 8.1) that make them attractive for the capture of NO_x even in the presence of humidity. Analysis of the pDOS calculated typically for the NO_x@CatFe(II) scenario evidences that these high affinities come from an overlap between the d-orbitals of the metal center and the π^* orbitals of the NO_x molecules, which is (electron transfer) further visually confirmed by the charge density difference analysis as illustrated in Figure S8.2a and S8.2b for the corresponding NO_x@CatFe(II) system.

8.4.2 NO_x/UiO-66-CatFe(II) and Force Field Parameterization

Among the M(II) catecholates showing the highest affinity for both NO and NO_2 from the preliminary cluster calculations described above, CatFe(II) was incorporated in the nanoporous UiO-66 MOF structure. This structure model was loaded with either 1 NO molecule or 1 NO_2 molecule and further DFT-geometry optimized to identify the preferential siting of both guests in the MOF cages prior generating the interaction energy curves. The corresponding optimized structures along with the geometric features of the NO_x/catecholate adducts are provided in Figure 8.3a, and Figure 8.3b. One observes that while the end-on and side-on preferential geometries for UiO-66-CatFe(II)-NO (IE is -57.5 kcal/mol) and UiO-66-CatFe(II)-NO_2 (IE is -85.7 kcal/mol) respectively are globally in line with the cluster calculations reported in Figure 8.2, the separating host/guest distances for both NO_x and the orientations for NO_2 significantly differ due to the confinement environment of the MOF cage. This emphasizes the critical need to consider periodic DFT calculations to derive reliable force field parameters for the guest/CatFe(II) interactions rather than relying on cluster calculations.

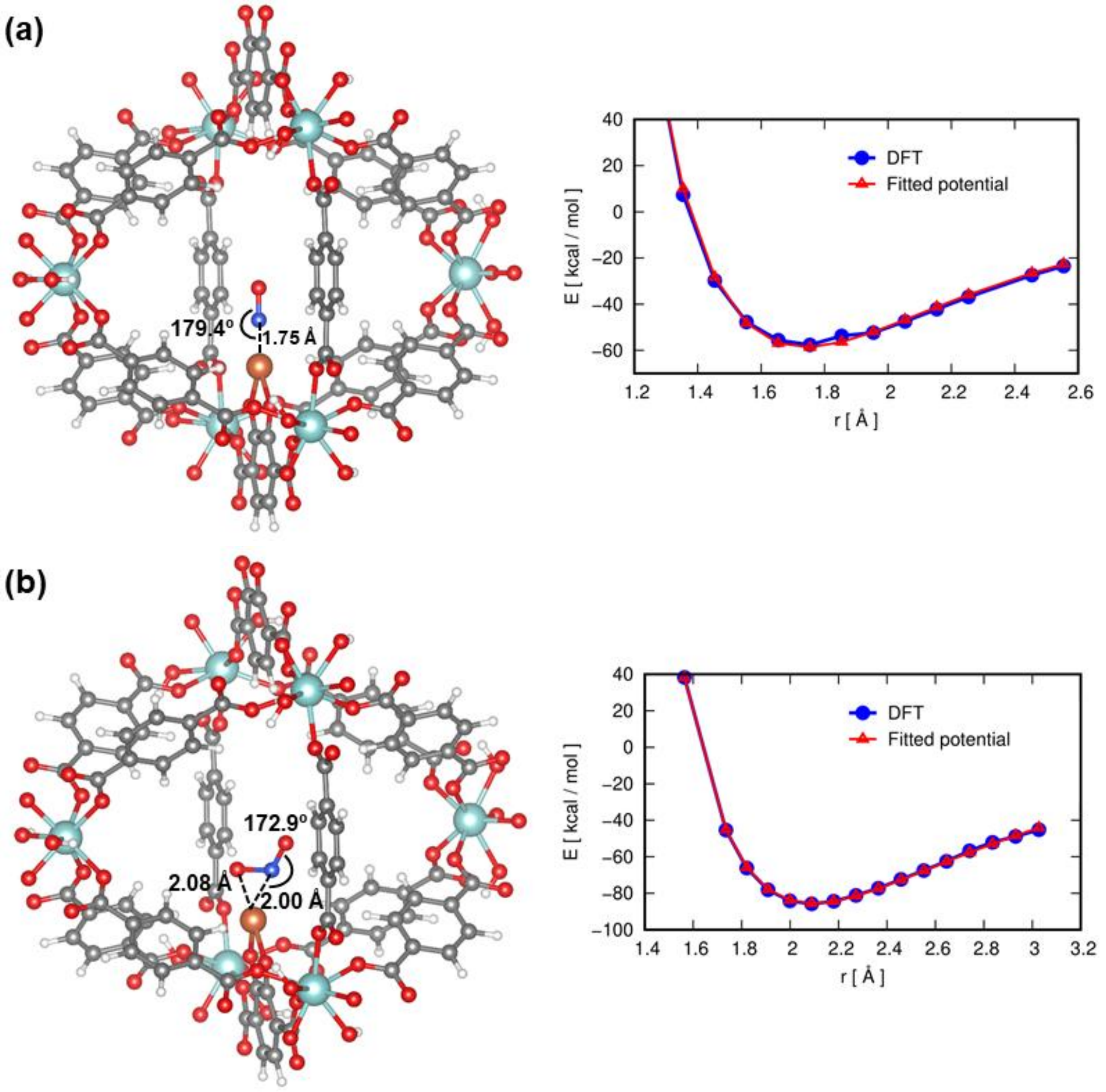

Figure 8.3: Periodic DFT optimized structures of (a) NO@UiO-66-CatFe(II), (b) NO2@ UiO-66-CatFe(II) and corresponding DFT-derived (blue) and fitted force-field interaction energy curves plotted as a function of the Fe(II)···N distance in both cases. The characteristic distances and angles are reported while color codes are the same than in Figure2.

Figures 8.3a and 8.3b equally report the DFT-derived NO$_x$/UiO-66-CatFe(II) interaction energy curves. One observes that these DFT curves can be accurately fitted by the analytical function as introduced in equation 2, the corresponding Morse force field parameters being summarized in Table 8.2.

Table 8.2: Periodic DFT-derived Morse force field parameters for the NOx/Fe interactions in the UiO-66-CatFe(II)-NOx systems.

Pair	**D (kcal/mol)**	**α**	**r_0 (Å)**
Fe(II)---N_{NO}	24561	6.682	1.741
Fe(II)---O_{NO}	4508.8	11.292	2.925
Fe(II)---N_{NO_2}	19463.8	4.435	2.100

Fe(II)---O1$_{NO_2}$	12766.6	7.457	1.999
Fe(II)---O2$_{NO_2}$	10366.3	7.523	3.300

8.4.3 NO$_x$ Adsorption Isotherms

Figure 8.4a and Figure 8.4b report the GCMC simulated NO and NO$_2$ single component adsorption isotherms for both pristine UiO-66 and UiO-66-CatFe(II) at 298 K. One observes that the introduction of metal-catecholate linker substantially increases the adsorption uptake of both NO$_x$ in the whole range of pressure up to 1 bar. Typically, the predicted NO$_2$ and NO uptakes at 1 bar are more than 4 times higher in UiO-66-CatFe(II) (NO$_2$: 10.6 mmol.g^{-1}, NO: 5.7 mmol.g^{-1}) compared to UiO-66 (NO$_2$: 2.4 mmol.g^{-1}, NO: 1.4 mmol.g^{-1}) that make this functionalized material among the best MOF sorbents for NO$_2$ capture at 1 bar along with MFM-300(Al); 14.1 mmol.g^{-1},[417] MFM-300(V);13.0 mmol.g^{-1},[419] and MFM-520(Zn); 4.5 mmol.g^{-1},[420] The same observation remains true for NO at 1 bar with attractive performance as compared to HKUST-1; 3.8 mmol.g^{-1},[428] Cu-SIP-3; 1.1 mmol.g^{-1},[451] Fe$_2$(dobdc); 6.2 mmol.g^{-1},[421] MIL-88-A; 2.5 mmol.g^{-1},[452] and MIP-177; 3.0 mmol.g^{-1},[453].

Decisively, the catecholate functionalization enables to achieve a very steep-adsorption isotherm at very low pressure, in line with the simulated adsorption enthalpies at low coverage for both NO (15.5 kcal/mol) and NO$_2$ (29.7 kcal/mol) in UiO-66-CatFe(II) that largely exceed the corresponding values (4.4 and 5.4 kcal/mol, respectively) in UiO-66. This adsorption behavior is of key importance for the capture of traces of NO$_x$ at the ppm levels and even below. Indeed, UiO-66-CatFe(II) can already adsorbs 2.2 mmol.g^{-1} and 2.3 mmol.g^{-1} of NO and 3.8 mmol.g^{-1} and 5.4 mmol.g^{-1} of NO$_2$ at 10^{-9} bar (i.e. 1 ppb) and 10^{-6} bar (i.e. 1 ppm) respectively. This level of performance makes these MOFs rather unique for NO$_x$ capture at the trace levels since the large majority of MOFs reported so far has been not able to adsorb NO$_2$ in this very low domain of pressure (Table S8.4). Moreover, the predicted NO$_2$ uptake at 0.001 bar (1000 ppm) and 0.01 bar (10000 ppm) of about 7.2 mmol.g^{-1} and 7.3 mmol.g^{-1} respectively largely exceeds the best MOF reported so far in the same pressure conditions, i.e. MFM-300(Al)[417] with 0.1 mmol.g^{-1} and 1.4 mmol.g^{-1} and MFM-520(Zn)[420] with 1.3 mmol.g^{-1} and 4.2 mmol.g^{-1}. All these comparative results highlight that the incorporation of metal-catecholate units in the UiO-66 structure leads to an excellent NO$_2$ adsorption efficiency even at 1 ppm level.

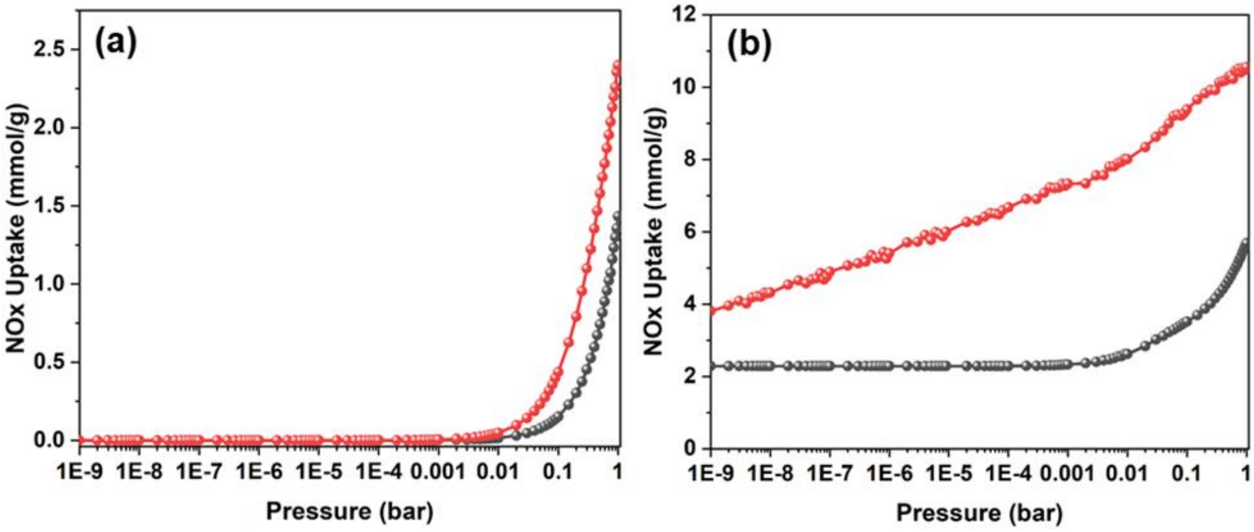

Figure 8.4: Simulated NOx single component adsorption isotherms (NO in black and NO2 in red color) for (a) unfunctionalized UiO-66 and (b) UiO-66-CatFe(II) at 298 K with pressure ranging from 10-9 bar to 1 bar.

8.4.4 NO_x Microscopic Adsorption Mechanisms

A careful analysis of the GCMC configurations generated in the whole gas pressure range enabled to shed light on the adsorption mechanism in play for both NO_x. At the initial stage of adsorption (10^{-9} bar), NO molecules are located in the vicinity of the CatFe(II) site (Figure 8.5a) with a separating N(NO)-Fe(II) distance of 1.85 Å as shown in the corresponding RDF (Figure 8.6a). A maximum of four NO molecules were found to be adsorbed on the metal site (Figure 8.5a). At higher pressure, NO molecules start to adsorb in a second coordination sphere before populating the whole pore volume when the pressure gradually increases up to 1 bar.

As like NO molecule, at very low pressure (10^{-9} bar) NO_2 molecules were found to be preferentially adsorbed over Fe(II) with a maximum of five molecules in its first coordination shell adopting a side-on conformation (Figure 8.5b) associated with a N(NO_2)-Fe(II) separating distance of 2.51 Å (see RDF for the corresponding pairs) (Figure 8.6b). When pressure increases up to 0.1 bar, NO_2 molecules populate gradually the MOF cage up to occupy the entire porosity at 1 bar (see Figures 8.5b).

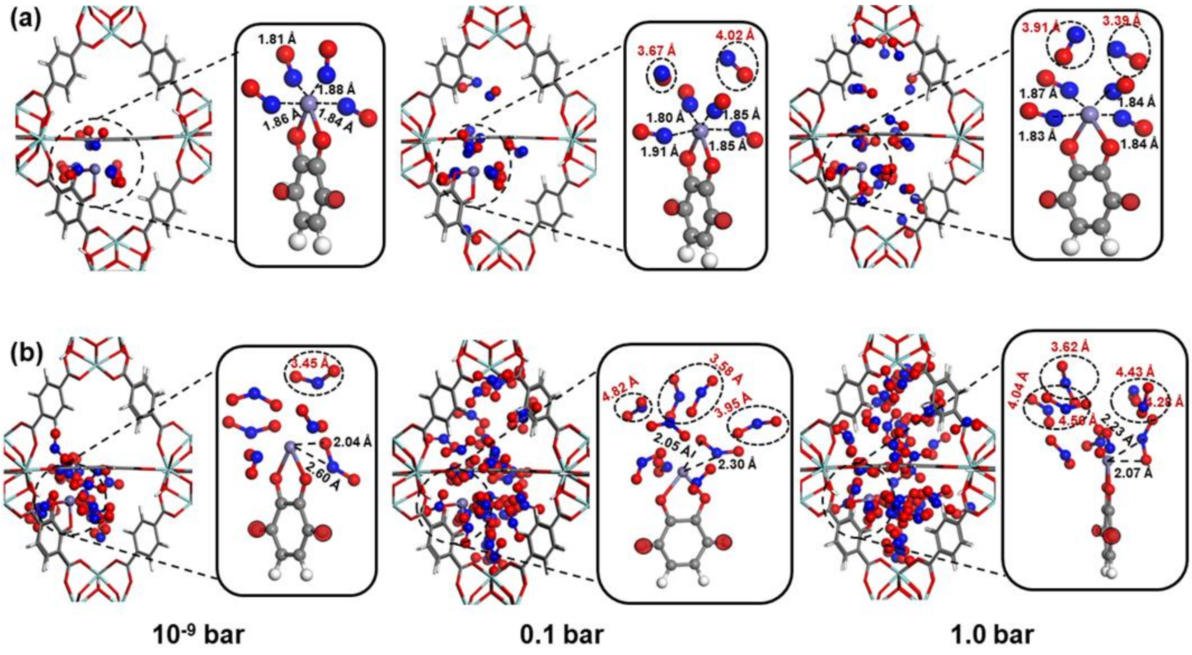

Figure 8.5: GCMC simulated snapshots of the (a) NO and (b) NO2 loaded UiO-66-CatFe(II) at 298 K and 10-9 bar, 0.1 bar, and 1.0 bar. NO and NO2 molecules located in the second coordination shells are marked with dotted black color circles.

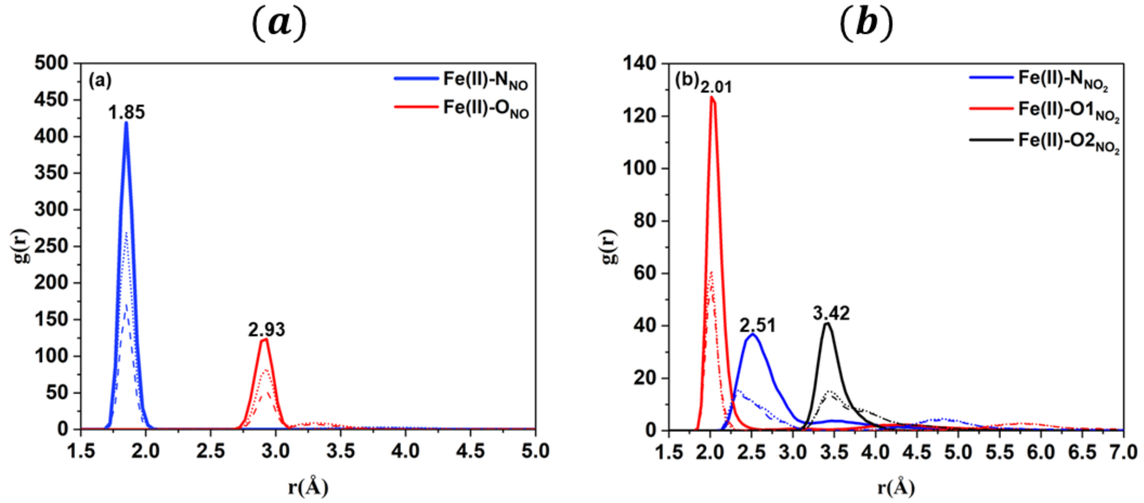

Figure 8.6: 6. Radial distribution functions calculated for the (a) NO (NNO, ONO) and Fe(II)UiO-66-CatFe(II) and (b) (a) NO2 (N$_{NO2}$, O1$_{NO2}$, O2$_{NO2}$) and Fe(II)UiO-66-CatFe(II) atom pairs averaged over the GCMC simulated configurations obtained at 298 K and 10-9 bar (solid line), 0.1 bar (dotted line), and 1.0 bar (dashed line).

As a further step, we carried out Bader charge analysis[454-455]on the periodic DFT UiO-66-CatFe(II) MOF structure to assess the charge transfer between Fe(II) and NO$_x$ upon adsorption. We found that the charge transfer is more pronounced in the case of NO$_2$ (0.24 electrons) adsorption compared to NO (0.12 electrons) in line with a higher interaction energy simulated for NO$_2$. Notably, these electron transfers of similar magnitude than the values previously reported for other MOFs and zeolites with exposed metal sites remain rather limited as summarized in

Table S8.6. This later observation strongly suggests a relatively easy regeneration of UiO-66-CatFe(II) upon sorption cycles.

8.5 Conclusions

DFT quantum calculations were carried to first identify the optimum Metal-catecholate linker for an effective NO_x capture prior to its incorporation in the cage-like UiO-66. GCMC simulations implementing a newly derived NO_x/MOF force field were further carried out to assess the adsorption performance of the corresponding functionalized MOF and in-depth understand the microscopic mechanism in play. Remarkably, this computational work anticipates nanoporous UiO-66-CatFe(II) as an excellent sorbent for NO_x capture even at the ppm level (a NO_x concentration that already can cause severe health damages) owing to strong host/guest interactions that lead to very steep adsorption isotherms for both NO_x. This MOF showing attractive adsorption behavior at very low NO_x concentration complements the portfolio of porous materials that have been so far almost exclusively tested in operation conditions encompassing higher NO_x concentration (> 1000 ppm). This is expected to guide the elaboration of UiO-66-CatFe(II) for further adsorption testing.

General Conclusion:

The main objective of this thesis was to investigate the adsorption of harmful gases by solid materials, regarding two specific applications, trapping and detection of radioactive species (I_2, ICH_3) and the trapping of highly toxic NO_x species emissions, aiming at protecting the health of humans and ecosystems.

For this purpose, based on molecular scale simulation methods that provide a fundamental understanding of the observed phenomena, providing in-depth knowledge at the atomic level that is often difficult to obtain by experimental methods. Density function theory (DFT) calculations and grand canonical Monte Carlo (GCMC) simulations have been adopted to identify promising materials for the detection and capture of gaseous molecules.

Following that, several classes of materials have been implemented, namely Graphene monolayers (defected and doped Ag and Cu) together with 2D carbonaceous materials (BC_3, C_3N, BCN_6-2), for the detection of iodinated species. Secondly, radioactive iodine sorbents, Metal Organic Frameworks (MOFs) have been examined in order to avoid any risk of propagation of radioactive products in the environment and to avoid any probability of contamination. In the case of capturing NO_x. Zeolites were selected as one of the most widely used materials for gas adsorption.

Our results revealed that: In the presence of iodine adsorption inhibitors (contaminants) present in air (CO, H_2O, O_2), PG (Pristine graphene), Cu_PG (Copper-decorated pristine graphene), and to a lesser extent Ag_MG (Silver-doped pristine graphene) are clearly the most interesting graphene monolayers for selective detection of iodine species among all the formulations studied. Using Ab initio molecular dynamics simulations to determine thermal stability, we were able to show that the planar structure of graphene is well maintained and no atomic shift in the z-direction is observed, which indicates the thermal stability of the three graphene monolayers at room temperature. In the same perspective, an adsorption of I_2, ICH_3, CO and H_2O molecules on 2D materials BC_3, borophene, BC_6N-2 and C_3N has been performed. Our investigations revealed that results of adsorption on C3N seem very promising in so far, the difference between the adsorption energies of (I_2, ICH_3) vs (CO, H_2O) is very significant. These findings have been further strengthened by simulations at finite temperatures (300K). In addition, to a discussion of electronic structure calculations.

Based on these results, C_3N, PG, Cu_PG and Ag_MG can be strongly suggested as an effective sensors for the envisaged application.

Our work on MOFs for stable trapping of iodine species showed that after a systematic evaluation of the adsorption performance of M-MOF-74 where M = Mg, Zn, Cu, Fe, Co, Ni and Mn to determine the optimal metal (II) for a selective capture of I_2 and ICH_3. Copper (Cu) and iron (Fe) are the only metal sites in MOF-74 showing a higher affinity for I_2 and ICH_3 than for H_2O and CO. From a thermodynamic point of view, these results reveal that Fe-MOF-74 and Cu-MOF-74 are clearly the most interesting MOF-74 structures for the selective capture of iodinated compounds from carbon monoxide and water.

The best series were later altered by replacing their linkers ("dobdc") with a smaller molecule ("dhfuma") to improve the affinity of the metal site for the adsorbed iodine compounds. The calculated interaction energies of I_2, ICH_3, H_2O and CO on the new MOF material M_2(dhfuma) were on average 18.2, 6.0, 3.0 and 2.9 kJ/mol higher than on M_2(dobdc). On the other hand, the copper affinity was further improved using this alternative linker and highlighted the MOF Cu_2(dhfuma) structure as a promising material. The interaction of I_2 on Mn- and Fe-MOF is on average 62 and 83 kJ/mol stronger than that of H_2O and CO, interestingly higher than that already reported on M_2(dobdc). From a practical point of view, the strong chemoadsorption demonstrated by Fe and Mn will be extremely useful in the fields of handling harmful materials (e.g., nuclear power plants) by providing additional protection, but it may prevent the reuse of the MOF structure, since the molecule is completely integrated into the MOF structure and its chemical identity cannot be recovered. On the other hand, the Cu interaction is mainly controlled by the long-range dispersion, which offers the possibility of a regenerable iodine capture material that can be very interesting as a chemical pre-concentrator for iodine gas detection.

For our second application, which involves the capture of harmful NO_x gases, with a Si/Al=23 ratio, the FAU exchanged by Be^{2+}, Mg^{2+}, Ca^{2+}, Sr^{2+}, Ba^{2+}, Zn^{2+}, and Cu^{2+}, exhibit a higher or equivalent affinity for water than for NO_x. FAU exchanged by Fe^{2+} has a similar affinity for water and NO_2 (-56.3, -53.7 kJ/mol, respectively), but a much higher affinity for NO (-155 kJ/mol). Palladium and platinum are the only cations showing a higher affinity for NO and NO2 than for water. These results reveal that in terms of thermodynamic selectivity, the Pd^{2+}, Pt^{2+}, and to a lesser extent Fe^{2+} forms are clearly the most interesting faujasites for the selective capture of NO_x in the presence of water. Nevertheless, bond activation analysis excluded Fe^{2+} from the list of suitable cations, as significant activation of N-O1 and N-O2 bonds is observed for NO_2 adsorption on Fe^{2+}, leading to the formation of undesirable co-products, whereas negligible variation in bond length is observed for Pd^{2+}, and Pt^{2+}. Subsequently, the cation Pt^{2+}, was incorporated and studied in Y zeolite (Si/Al = 2.4). The results show that Faujasite Y-Pt^{2+}, is an interesting material for the removal of NO_x from diesel engine emissions.

For a rational and specific continuation of this zeolite study, these same cations were integrated as metals into the catecholate ligand for efficient NO_x capture before incorporation into the cage-like UiO-66. GCMC simulations implementing a NO_x/MOF force field were then performed to evaluate the adsorption performance of MOFs. Remarkably, this computational work predicts nanoporous UiO-66-CatFe(II) as an excellent sorbent for NO_x capture, even at the ppm level due to strong Fe(II)/NO_x interactions. Our resulted functionalized UIO-66 MOF, exhibits interesting adsorption behavior at a very low NO_x concentration, complements the portfolio of porous materials that have, until now, been almost exclusively tested under operating conditions involving higher NO_x concentration (>1000 ppm). This should guide the development of UiO-66-CatFe(II) for additional adsorption testing.

Appendices

Supporting Information (SI) of Chapter 8 (S8)

Calculated spin and multiplicity of guest, host and host-guest complexes (Table S8.1), LJ potential parameters for the framework atoms and adsorbate molecules (Table S8.2 and S8.3), NO_x adsorption isotherms in various MOFs at 1bar (Table S8.4), comparison of NO_2 uptake amount at PPM level (Table S8.5), calculated bader charge transfer values (Table S8.6), DFT optimized geometries of H_2O@CatM(II) complexes (Figure S8.1), calculated charge density and pDOS (Figure S8.2),

Table S8.1: Spin and Multiplicities used for the isolated guest (NO_x and H_2O), Host (CatM(II)) and Host-Guest (NOx@CatM(II)) complexes in DFT-cluster models calculations

Pristine systems	Unpaired electrons	Multiplicity	Complex systems	Unpaired electrons	Multiplicity
NO	1	2	-	-	-
NO_2	1	2	-	-	-
H_2O	0	1	-	-	-
CatMg(II)	0	1	NO_x@CatMg(II)	1	2
CatMn(II)	5	6	NO_x@CatMn(II)	4	5
CatFe(II)	4	5	NO_x@CatFe(II)	3	4
CatCo(II)	3	4	NO_x@CatCo(II)	2	3
CatNi(II)	2	3	NO_x@CatNi(II)	1	2
CatCu(II)	1	2	NO_x@CatCu(II)	0	1
CatZn(II)	0	1	NO_x@CatZn(II)	1	2
CatPd(II)	2	3	NO_x@CatPd(II)	1	2
CatPt(II)	2	3	NO_x@CatPt(II)	1	2

* For H_2O@CatM(II) complexes, bare CatM(II) complexes multiplicities were used

Table S8.2: Table S2. LJ Potential Parameters for the atoms of UiO-66 and UiO-66-CatFe(II) MOFs taken from UFF.[444]

MOFs	Atom	σ (Å)	ε/k_B (K)
UiO-66 & UiO-66-CatFe(II)	H	2.57	22.14
	C	3.43	52.84
	O	3.12	30.19
	Zr	2.78	34.72
	Fe	2.59	6.54

Table S8.3: LJ Potential Parameters and electrostatic charges for the NO and NO2 models taken from the literature.[445]

Molecules	Site	σ (Å)	ε/k_B (K)	Q
NO	N_NO	3.014	79.500	0.0288
	O_NO	2.875	96.945	-0.0288
NO_2	N_NO_2	3.224	50.360	0.146
	O_NO_2	2.930	62.510	-0.073

Table S8.4: Comparison of simulated UiO-66-CatFe(II) MOFs NOx Uptake (in mmol/g) at 298 K with 1 bar.

MOF	NO	Reference
HKUST-1	3.8	[456]
Cu-SIP-3	1.1	[451]
Fe_2(dobdc)	6.2	[421]
MIL-88-A	2.5	[452]
MIP-177	3.0	[453]
UiO-66	1.4	This work
UiO-66-CatFe(II)	5.7	This work
	NO_2	
MFM-300(Al)	14.1	[417]
MFM-300(V)	13.0	[419]
MFM-520(Zn)	4.5	[420]
UiO-66	2.4	This work
UiO-66-CatFe(II)	10.6	This work

Table S8.5: NO2 Uptake (in mmol/g) simulated for UiO-66-CatFe(II) MOF at 298 K and various ppm level.

MOF	1 ppm	10 ppm	100 ppm	1000 ppm	10000 ppm	Reference
UiO-66-CatFe(II)	5.4	6.2	6.7	7.2	7.3	This work
MFM-300(Al)	-	-	-	0.1	1.4	[417]
MFM-520(Zn)	-	-	-	1.3	4.2	[420]
MFM-300(V)	-	-	-	-	1.1	[419]

Table S8.6: Comparison of calculated Bader charge transfer values from the Fe(II) to NOx molecules in UiO-66-CatFe(II) systems.

		Charge Transfer (e)		
System	**Metal**	**M(II)•••NO**	**M(II)•••NO_2**	**Reference**
UiO-66-CatFe(II)	Fe(II)	0.12	0.24	This Work
Ti-MOF-74	Ti(IV)	0.36	--	[457]
M-HKUST-1	Fe(II)	0.10	0.45	[458]
Faujasite Y	Pt(II)	0.14	--	[459]
Rh-BN Sheet	Rh_{atom}	0.23	0.41	[460]

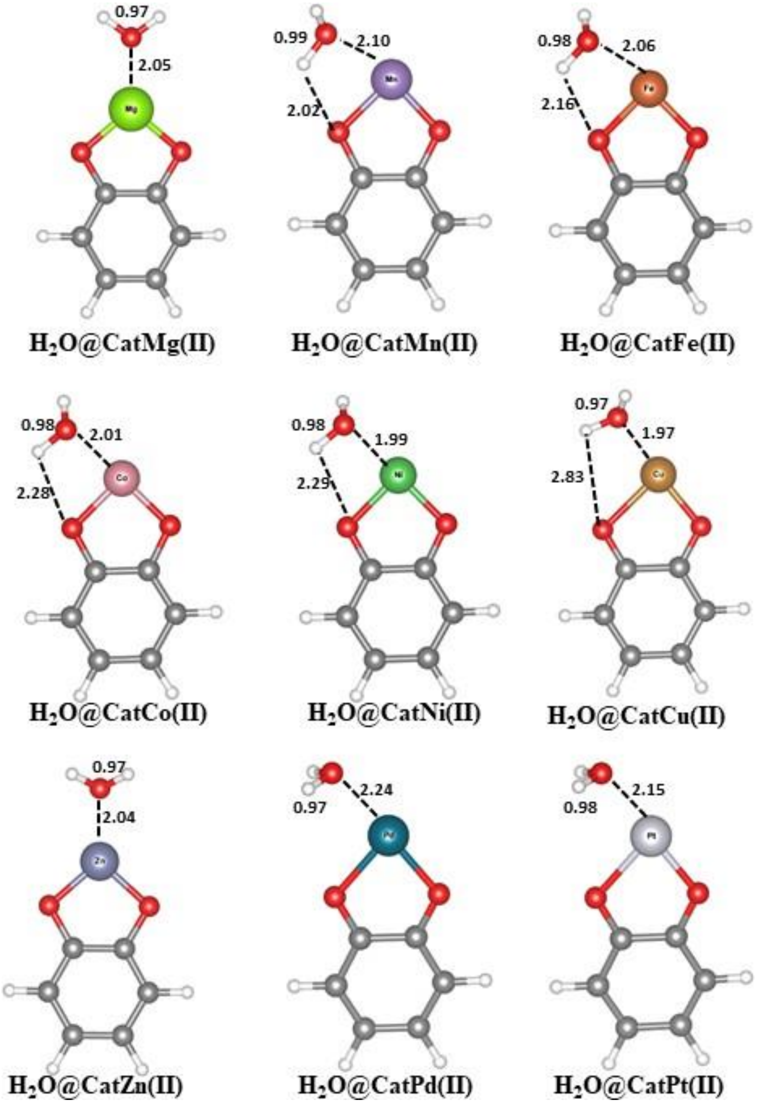

H_2O@CatMg(II) H_2O@CatMn(II) H_2O@CatFe(II)

H_2O@CatCo(II) H_2O@CatNi(II) H_2O@CatCu(II)

H_2O@CatZn(II) H_2O@CatPd(II) H_2O@CatPt(II)

Figure S8.1: DFT-optimized geometries of H_2O@CatM(II) complexes. The characteristic distances are reported in Å. Colors code: red (oxygen), gray (carbon), white (hydrogen).

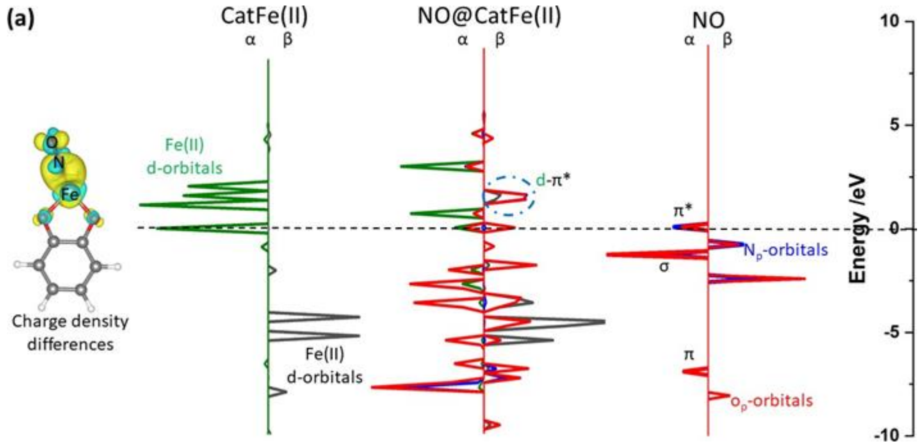

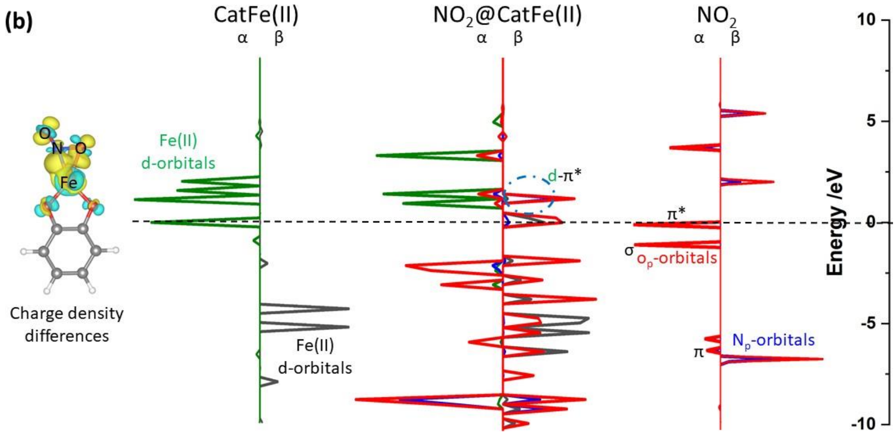

Figure S8.2: DFT-derived charge density differences ($\delta\rho = \rho_{CatFe(II)+NO2} - \rho_{CatFe(II)} - \rho_{NO2}$; Cyan stands for holes and yellow for electrons with the isosurface values ranging from +0.006 to -0.06e/Å^3) and projected electronic densities of states (pDOS) of CatFe(II), guest@CatFe(II) and guest for NO (a) and NO$_2$ (b).

Bibliography:

1 A. Liebard, C. Nahon and M. Auzet, *Worldwide electricity production from renewable energy sources - Fifteenth Inventory, Edition 2013*, France, 2013.

2 D. F. Birol, 81.

3 La consommation d'électricité en chiffres | EDF FR, https://www.edf.fr/groupe-edf/espaces-dedies/l-energie-de-a-a-z/tout-sur-l-energie/l-electricite-au-quotidien/la-consommation-d-electricite-en-chiffres, (accessed September 25, 2022).

4 L. Mathilde, Les sources d'énergie pour obtenir de l'électricité, https://www.killmybill.be/fr/sources-energie/, (accessed September 26, 2022).

5 F. Bergé, *Dans 15 pays d'Europe, l'électricité est moins chère qu'en France*, 2018.

6 G. Marta M., *Dans un contexte de crises, le nucléaire a contribué à la sécurité énergétique en augmentant la production d'électricité en 2021*, IAEA, 2022.

7 Le nucléaire en chiffres | EDF FR, https://www.edf.fr/groupe-edf/espaces-dedies/l-energie-de-a-a-z/tout-sur-l-energie/produire-de-l-electricite/le-nucleaire-en-chiffres, (accessed September 26, 2022).

8 Statistical Review of World Energy | Energy economics | Home, https://www.bp.com/en/global/corporate/energy-economics/statistical-review-of-world-energy.html, (accessed October 31, 2022).

9 *Production – Production totale : RTE Bilan électrique 2020*, .

10 Institut de radioprorection et de surete nucleaire(IRSN), Base de connaissance du cycle du combustible nucleaire, https://www.irsn.fr/FR/connaissances/Installations_nucleaires/cycle_combustible/cycle/Pages/sommaire.aspx#.Y1_G6HbMJEY.

11 M. Nilsson, Harvesting usable fuel from nuclear waste – and dealing with the last chemical troublemakers, http://theconversation.com/harvesting-usable-fuel-from-nuclear-waste-and-dealing-with-the-last-chemical-troublemakers-35284, (accessed October 22, 2022).

12 OCDE and Agence pour l'énergie nucléaire, *La sûreté du cycle du combustible nucléaire - Troisième édition*, OECD, 2005.

13 T. Higashi, T. Kudo and S. Kinuya, *Ann. Nucl. Med.*, 2012, **26**, 99–112.

14 N. R. Soelberg, T. G. Garn, M. R. Greenhalgh, J. D. Law, R. Jubin, D. M. Strachan and P. K. Thallapally, *Sci. Technol. Nucl. Install.*, 2013, **2013**, e702496.

15 M. V. Ramana, *WIREs Energy Environ.*, 2018, **7**, e289.

16 M. Stojanovska, V. M. Petruševski and B. Šoptrajanov, *Educ. Quím.*, 2012, **23**, 171–174.

17 LibreTexts chemistry, Group 17: General Properties of Halogens, https://chem.libretexts.org/Bookshelves/Inorganic_Chemistry/Supplemental_Modules_and_Websites_(Inorganic_Chemistry)/Descriptive_Chemistry/Elements_Organized_by_Block/2_p-Block_Elements/Group_17%3A_The_Halogens/0Group_17%3A_Physical_Properties_of_the_Halogens/Group_17%3A_General_Properties_of_Halogens.

18 E. B. Silberstein, *Semin. Nucl. Med.*, 2012, **42**, 164–170.

19 J. Timar, Z. Elekes and B. Singh, *Nucl. Data Sheets*, 2014, **121**, 143–394.

20 B. Bartoníček, V. Plaček and V. Hnát, *Radiat. Phys. Chem.*, 2007, **76**, 857–863.

21 J. C. Wren, J. M. Ball and G. A. Glowa, *Nucl. Technol.*, 1999, **125**, 337–362.

22 P. Darnowski, E. Skrzypek, P. Mazgaj, K. Świrski and P. Gandrille, *Nucl. Eng. Des.*, 2015, **289**, 8–18.

23 S. M. Friedman, *Bull. At. Sci.*, 2011, **67**, 55–65.

24 communauté des physiciennes et physiciens, L'iode de Tchernobyl, https://laradioactivitefr.gatsbyjs.io/energie_nucleaire/liodedetchernobyl.

25 CAHIER PARTENAIRE IRSN / POUR LA SCIENCE décembre 2020, https://www.irsn.fr/FR/Larecherche/publications-documentation/aktis-lettre-dossiers-thematiques/cahier-partenaire-Pour-la-science/Pages/Cahier-partenaire-PLS-n4-iode.aspx, (accessed September 26, 2022).
26 Japon: les techniciens “perdent la course” à Fukushima - L’Express, https://www.lexpress.fr/actualite/monde/japon-les-techniciens-perdent-la-course-a-fukushima_977667.html, (accessed September 26, 2022).
27 M. Balonov and A. Bouville, in *Encyclopedia of Environmental Health (Second Edition)*, ed. J. Nriagu, Elsevier, Oxford, 2013, pp. 448–459.
28 UARGA - Le site de retraités et d’anciens du nucléaire, https://www.uarga.org/nucleaire/rejets_nucleaire.php, (accessed September 26, 2022).
29 Retraitement du combustible nucléaire, https://www.connaissancedesenergies.org/fiche-pedagogique/retraitement-du-combustible-nucleaire-use, (accessed September 26, 2022).
30 J. M. López-Gutiérrez, M. García-León, Ch. Schnabel, M. Suter, H.-A. Synal, S. Szidat and R. García-Tenorio, *Sci. Total Environ.*, 2004, **323**, 195–210.
31 Gazette Nucléaire: La Hague - Nord Cotentin, https://gazettenucleaire.org/2000/181_Hague.html, (accessed October 10, 2022).
32 A. Aldahan, E. Englund, G. Possnert, I. Cato and X. L. Hou, *Appl. Geochem.*, 2007, **22**, 637–647.
33 H. Reithmeier, V. Lazarev, W. Rühm and E. Nolte, *Sci. Total Environ.*, 2010, **408**, 5052–5064.
34 Orano | Acteur majeur de l'énergie et du combustible nucléaire, https://www.orano.group/fr/orano-accueil, (accessed September 26, 2022).
35
36
37 A. de sûreté nucléaire, Réacteurs 1 et 2 Rejets d’effluents gazeux radioactifs sans filtration, https://www.asn.fr/l-asn-controle/actualites-du-controle/installations-nucleaires/avis-d-incident-des-installations-nucleaires/reacteurs-1-et-2-rejets-d-effluents-gazeux-radioactifs-sans-filtration, (accessed October 5, 2022).
38 V. Balasubramani, S. Chandraleka, T. S. Rao, R. Sasikumar, M. R. Kuppusamy and T. M. Sridhar, *J. Electrochem. Soc.*, 2020, **167**, 037572.
39 A. K. Farquhar, G. S. Henshaw and D. E. Williams, *ACS Sens.*, 2021, **6**, 1295–1304.
40 P. Zuo, R. Wang, F. Li, F. Wu, G. Xu and W. Niu, *Talanta*, 2021, **233**, 122539.
41 E.-B. Lee, I.-S. Hwang, J.-H. Cha, H.-J. Lee, W.-B. Lee, J. J. Pak, J.-H. Lee and B.-K. Ju, *Sens. Actuators B Chem.*, 2011, **153**, 392–397.
42 R.-J. Wu, X.-M. Tian, Z.-Q. Hua, N. Lu and P. Wang, *Chin. J. Anal. Chem.*, 2021, **49**, 63–68.
43 H. Li, R. Wu, H.-B. Liu, L.-Y. Han, W.-J. Yuan, Z.-Q. Hua, S.-R. Fan and Y. Wu, *Chin. J. Anal. Chem.*, 2021, **49**, 93–101.
44 J. Hodgkinson and R. P. Tatam, *Meas. Sci. Technol.*, 2012, **24**, 012004.
45 J. Li, H. Yan, H. Dang and F. Meng, *Opt. Laser Technol.*, 2021, **135**, 106658.
46 E. L. W. Gardner, A. De Luca, T. Vincent, R. G. Jones, J. W. Gardner and F. Udrea, in *2019 IEEE SENSORS*, 2019, pp. 1–4.
47 G. Korotcenkov, in *Handbook of Gas Sensor Materials: Properties, Advantages and Shortcomings for Applications Volume 1: Conventional Approaches*, ed. G. Korotcenkov, Springer, New York, NY, 2013, pp. 307–328.
48 X. Jiang, K. Kim, S. Zhang, J. Johnson and G. Salazar, *Sensors*, 2014, **14**, 144–169.
49 P. Hamacher, P. Boeker, P. Schulze Lammers and A. Yuwono, *ODOUR POLLUTION IN THE ENVIRONMENT: DEVELOPMENT OF A MEASURING SYSTEM*, 2001.
50 J. Tong, Y. Wang, S. Wang, W. Wang, Y. Jia and X. Liu, *Appl. Sci.*, 2017, **7**, 755.
51 A. Tricoli, M. Righettoni and A. Teleki, *Angew. Chem. Int. Ed.*, 2010, **49**, 7632–7659.

52 M. V. Nikolic, V. Milovanovic, Z. Z. Vasiljevic and Z. Stamenkovic, *Sensors*, 2020, **20**, 6694.
53 A. Dey, *Mater. Sci. Eng. B*, 2018, **229**, 206–217.
54 C. Muhire, A. Tesfay Reda, D. Zhang, X. Xu and C. Cui, *Chem. Eng. J.*, 2022, **431**, 133816.
55 Y.-F. Sun, S.-B. Liu, F.-L. Meng, J.-Y. Liu, Z. Jin, L.-T. Kong and J.-H. Liu, *Sensors*, 2012, **12**, 2610–2631.
56 aeml4735, Development of gas sensors based on metal oxide semiconductors for potential diagnosis of diseases, https://www.skku-aeml.com/post/온라인-커뮤니티-구축, (accessed October 12, 2022).
57 W. Yang, K. R. Ratinac, S. P. Ringer, P. Thordarson, J. J. Gooding and F. Braet, *Angew. Chem. Int. Ed.*, 2010, **49**, 2114–2138.
58 E.-M. Kirchner and T. Hirsch, *Mikrochim. Acta*, 2020, **187**, 441.
59 G. D. Pirngruber, P. Raybaud, Y. Belmabkhout, J. Čejka and A. Zukal, *Phys. Chem. Chem. Phys.*, 2010, **12**, 13534–13546.
60 M. Yi and Z. Shen, *J. Mater. Chem. A*, 2015, **3**, 11700–11715.
61 J.-O. Carlsson and P. M. Martin, in *Handbook of Deposition Technologies for Films and Coatings (Third Edition)*, ed. P. M. Martin, William Andrew Publishing, Boston, 2010, pp. 314–363.
62 Y. Xu, H. Cao, Y. Xue, B. Li and W. Cai, *Nanomaterials*, 2018, **8**, 942.
63 N. Mishra, J. Boeckl, N. Motta and F. Iacopi, *Phys. Status Solidi A*, 2016, **213**, 2277–2289.
64 V. Agarwal and P. B. Zetterlund, *Chem. Eng. J.*, 2021, **405**, 127018.
65 K. S. Novoselov, V. I. Fal′ko, L. Colombo, P. R. Gellert, M. G. Schwab and K. Kim, *Nature*, 2012, **490**, 192–200.
66 T. Geng, L. Ma, G. Chen, C. Zhang, W. Zhang and Q. Niu, *Environ. Sci. Pollut. Res.*, 2020, **27**, 20235–20245.
67 X. Dong, Q. He, M. Li, X. Wang, Y. Wang and W. Zhang, *Dalton Trans.*, 2021, **50**, 15567–15575.
68 F. Pena-Pereira, N. Capón, I. de la Calle, I. Lavilla and C. Bendicho, *Sens. Actuators B Chem.*, 2019, **299**, 126979.
69 C.-X. Jiao, Q. Shen, S.-Y. Huan, G.-L. Shen and R.-Q. Yu, *Anal. Chim. Acta*, 2005, **528**, 229–234.
70 E. Cho, A. Perebikovsky, O. Benice, S. Holmberg, M. Madou and M. Ghazinejad, *Sensors*, 2018, **18**, 1486.
71 L. J. Small, J. L. Krumhansl, D. X. Rademacher and T. M. Nenoff, *Microporous Mesoporous Mater.*, 2019, **280**, 82–87.
72 L. J. Small and T. M. Nenoff, *ACS Appl. Mater. Interfaces*, 2017, **9**, 44649–44655.
73 L. J. Small, R. C. Hill, J. L. Krumhansl, M. E. Schindelholz, Z. Chen, K. W. Chapman, X. Zhang, S. Yang, M. Schröder and T. M. Nenoff, *ACS Appl. Mater. Interfaces*, 2019, **11**, 27982–27988.
74 Y.-Q. Hu, M.-Q. Li, Y. Wang, T. Zhang, P.-Q. Liao, Z. Zheng, X.-M. Chen and Y.-Z. Zheng, *Chem. – Eur. J.*, 2017, **23**, 8409–8413.
75 B. J. Riley, J. D. Vienna, D. M. Strachan, J. S. McCloy and J. L. Jerden, *J. Nucl. Mater.*, 2016, **470**, 307–326.
76 Daryl Haefner, *Methods of Gas Phase Capture of Iodine from Fuel Reprocessing Off-Gas: A Literature Survey*, 2007.
77 R. T. Jubin, P. Printed, C. Microfiche and R. T. Jubin, .
78 P. Paviet-Hartmann, W. Kerlin and S. Bakhtiar, 12.
79 W. Hebel and G. Cottone, .
80 Porous sorbents for the capture of radioactive iodine compounds: a review - RSC Advances (RSC Publishing), https://pubs.rsc.org/en/content/articlelanding/2018/ra/c8ra04775h, (accessed October 5, 2022).

81 M. Chebbi, C. Monsanglant-Louvet, P. Parent, C. Gerente, L. Le Coq and B. M. Mokili, *Carbon Trends*, 2022, **7**, 100164.

82 B. Li, X. Dong, H. Wang, D. Ma, K. Tan, S. Jensen, B. J. Deibert, J. Butler, J. Cure, Z. Shi, T. Thonhauser, Y. J. Chabal, Y. Han and J. Li, *Nat. Commun.*, 2017, **8**, 485.

83 C. M. González-García, J. F. González and S. Román, *Fuel Process. Technol.*, 2011, **92**, 247–252.

84 G.-I. Park, I.-T. Kim, J.-K. Lee, S.-K. Ryu and J.-H. Kim, *Carbon Lett.*, 2001, **2**, 9–14.

85 Iodine adsorption on silver-exchanged titania-derived adsorbents | SpringerLink, https://link.springer.com/article/10.1007/s10967-014-3252-5, (accessed October 2, 2022).

86 Pence: In 12th AEC Air Cleaning Conference, CONF 720823 - Google Scholar, https://scholar.google.com/scholar_lookup?title=Proceedings+of+the+12th+AEC+Air+Cleaning+Conference,+Conf.+720823&author=J.+G.+Wilhelm&author=H.+Schuttelkopf&author=M.+W.+First&publication_year=1972&, (accessed October 2, 2022).

87 N. Mnasri, C. Charnay, L.-C. de Ménorval, Y. Moussaoui, E. Elaloui and J. Zajac, *Microporous Mesoporous Mater.*, 2014, **196**, 305–313.

88 J. H. Yang, Y.-J. Cho, J. M. Shin and M.-S. Yim, *J. Nucl. Mater.*, 2015, **465**, 556–564.

89 M. Chebbi, 2016.

90 J. Matyáš, E. S. Ilton and L. Kovařík, *RSC Adv.*, 2018, **8**, 31843–31852.

91 B. J. Riley, J. O. Kroll, J. A. Peterson, J. Matyáš, M. J. Olszta, X. Li and J. D. Vienna, *ACS Appl. Mater. Interfaces*, 2017, **9**, 32907–32919.

92 R. G. Pearson, *J. Chem. Educ.*, 1968, **45**, 581.

93 Polyacrylonitrile-Chalcogel Hybrid Sorbents for Radioiodine Capture | Environmental Science & Technology, https://pubs.acs.org/doi/10.1021/es405807w, (accessed October 2, 2022).

94 D. Chen, Y. Fu, W. Yu, G. Yu and C. Pan, *Chem. Eng. J.*, 2018, **334**, 900–906.

95 B. J. Riley, S. Chong, J. Schmid, J. Marcial, E. T. Nienhuis, M. K. Bera, S. Lee, N. L. Canfield, S. Kim, M. A. Derewinski and R. K. Motkuri, *ACS Appl. Mater. Interfaces*, 2022, **14**, 18439–18452.

96 J. Zhou, T. Lan, T. Li, Q. Chen, P. Bai, F. Liu, Z. Yuan, W. Zheng, X. Luo, W. Yan and T. Yan, *Sep. Purif. Technol.*, 2022, **290**, 120895.

97 J. Zhou, Q. Chen, T. Li, T. Lan, P. Bai, F. Liu, Z. Yuan, W. Zheng, W. Yan and T. Yan, *Inorg. Chem.*, 2022, **61**, 7746–7753.

98 B. Azambre, M. Chebbi and A. Hijazi, *Chem. Eng. J.*, 2020, **379**, 122308.

99 B. Azambre and M. Chebbi, *ACS Appl. Mater. Interfaces*, 2017, **9**, 25194–25203.

100 K. W. Chapman, P. J. Chupas and T. M. Nenoff, *J. Am. Chem. Soc.*, 2010, **132**, 8897–8899.

101 T. M. Nenoff, M. A. Rodriguez, N. R. Soelberg and K. W. Chapman, *Microporous Mesoporous Mater.*, 2014, **200**, 297–303.

102 E. R. Vance and D. K. Agrawal, *J. Mater. Sci.*, 1982, **17**, 1889–1894.

103 B. S. Choi, G. I. Park, J. H. Kim, J. W. Lee and S. K. Ryu, *Adsorption*, 2001, **7**, 91–103.

104 Y. Nan, L. L. Tavlarides and D. W. DePaoli, *AIChE J.*, 2017, **63**, 1024–1035.

105 M. Li, D. Li, M. O'Keeffe and O. M. Yaghi, *Chem. Rev.*, 2014, **114**, 1343–1370.

106 Y. Kang, F. Wang, J. Zhang and X. Bu, *J. Am. Chem. Soc.*, 2012, **134**, 17881–17884.

107 W.-G. Lu, C.-Y. Su, T.-B. Lu, L. Jiang and J.-M. Chen, *J. Am. Chem. Soc.*, 2006, **128**, 34–35.

108 T. Li, J. E. Sullivan and N. L. Rosi, *J. Am. Chem. Soc.*, 2013, **135**, 9984–9987.

109 A. J. Howarth, Y. Liu, P. Li, Z. Li, T. C. Wang, J. T. Hupp and O. K. Farha, *Nat. Rev. Mater.*, 2016, **1**, 1–15.

110 C. Pettinari, F. Marchetti, N. Mosca, G. Tosi and A. Drozdov, *Polym. Int.*, 2017, **66**, 731–744.

111 A. Li, R. Bueno-Perez, S. Wiggin and D. Fairen-Jimenez, *CrystEngComm*, 2020, **22**, 7152–7161.

112 Y. Huo, S. Liu, Z. Gao, B. Ning and Y. Wang, *Microchim. Acta*, 2021, **188**, 168.

113 T. D. Bennett and A. K. Cheetham, *Acc. Chem. Res.*, 2014, **47**, 1555–1562.
114 J. J. P. Iv, J. A. Perman and M. J. Zaworotko, *Chem. Soc. Rev.*, 2009, **38**, 1400–1417.
115 A. K. Cheetham, C. N. R. Rao and R. K. Feller, *Chem. Commun.*, 2006, 4780–4795.
116 W. Cai, J. Wang, C. Chu, W. Chen, C. Wu and G. Liu, *Adv. Sci.*, 2019, **6**, 1801526.
117 N. L. Rosi, J. Kim, M. Eddaoudi, B. Chen, M. O'Keeffe and O. M. Yaghi, *J. Am. Chem. Soc.*, 2005, **127**, 1504–1518.
118 W. L. Queen, M. R. Hudson, E. D. Bloch, J. A. Mason, M. I. Gonzalez, J. S. Lee, D. Gygi, J. D. Howe, K. Lee, T. A. Darwish, M. James, V. K. Peterson, S. J. Teat, B. Smit, J. B. Neaton, J. R. Long and C. M. Brown, *Chem. Sci.*, 2014, **5**, 4569–4581.
119 L. J. Wang, H. Deng, H. Furukawa, F. Gándara, K. E. Cordova, D. Peri and O. M. Yaghi, *Inorg. Chem.*, 2014, **53**, 5881–5883.
120 W. Zhou, H. Wu and T. Yildirim, *J. Am. Chem. Soc.*, 2008, **130**, 15268–15269.
121 K. S. Lim, W. R. Lee, H. G. Lee, D. W. Kang, J. H. Song, J. Hilgar, J. D. Rinehart, D. Moon and C. S. Hong, *Inorg. Chem.*, 2017, **56**, 7443–7448.
122 H. Deng, S. Grunder, K. E. Cordova, C. Valente, H. Furukawa, M. Hmadeh, F. Gándara, A. C. Whalley, Z. Liu, S. Asahina, H. Kazumori, M. O'Keeffe, O. Terasaki, J. F. Stoddart and O. M. Yaghi, *Science*, 2012, **336**, 1018–1023.
123 A. M. Fracaroli, H. Furukawa, M. Suzuki, M. Dodd, S. Okajima, F. Gándara, J. A. Reimer and O. M. Yaghi, *J. Am. Chem. Soc.*, 2014, **136**, 8863–8866.
124 D. J. Xiao, J. Oktawiec, P. J. Milner and J. R. Long, *J. Am. Chem. Soc.*, 2016, **138**, 14371–14379.
125 T. Xiao and D. Liu, *Microporous Mesoporous Mater.*, 2019, **283**, 88–103.
126 R. Freund, O. Zaremba, G. Arnauts, R. Ameloot, G. Skorupskii, M. Dincă, A. Bavykina, J. Gascon, A. Ejsmont, J. Goscianska, M. Kalmutzki, U. Lächelt, E. Ploetz, C. S. Diercks and S. Wuttke, *Angew. Chem. Int. Ed.*, 2021, **60**, 23975–24001.
127 K. S. Park, Z. Ni, A. P. Côté, J. Y. Choi, R. Huang, F. J. Uribe-Romo, H. K. Chae, M. O'Keeffe and O. M. Yaghi, *Proc. Natl. Acad. Sci.*, 2006, **103**, 10186–10191.
128 D. F. Sava, M. A. Rodriguez, K. W. Chapman, P. J. Chupas, J. A. Greathouse, P. S. Crozier and T. M. Nenoff, *J. Am. Chem. Soc.*, 2011, **133**, 12398–12401.
129 J. T. Hughes, D. F. Sava, T. M. Nenoff and A. Navrotsky, *J. Am. Chem. Soc.*, 2013, **135**, 16256–16259.
130 T. Assaad and B. Assfour, *J. Nucl. Mater.*, 2017, **493**, 6–11.
131 D. Banerjee, X. Chen, S. S. Lobanov, A. M. Plonka, X. Chan, J. A. Daly, T. Kim, P. K. Thallapally and J. B. Parise, *ACS Appl. Mater. Interfaces*, , DOI:10.1021/acsami.8b02651.
132 W. Xie, D. Cui, S.-R. Zhang, Y.-H. Xu and D.-L. Jiang, *Mater. Horiz.*, 2019, **6**, 1571–1595.
133 D. S. Sholl and J. A. Steckel, *Density Functional Theory: A Practical Introduction | Wiley*, 2009.
134 T. Ayadi, M. Badawi, L. Cantrel and S. Lebègue, *Mol. Syst. Des. Eng.*, 2022, **7**, 422–433.
135 M. Chebbi, S. Chibani, J.-F. Paul, L. Cantrel and M. Badawi, *Microporous Mesoporous Mater.*, 2017, **239**, 111–122.
136 S. Chibani, M. Chebbi, S. Lebègue, T. Bučko and M. Badawi, *J. Chem. Phys.*, 2016, **144**, 244705.
137 H. Jabraoui, E. P. Hessou, S. Chibani, L. Cantrel, S. Lebègue and M. Badawi, *Appl. Surf. Sci.*, 2019, **485**, 56–63.
138 M. Leloire, C. Walshe, P. Devaux, R. Giovine, S. Duval, T. Bousquet, S. Chibani, J.-F. Paul, A. Moissette, H. Vezin, P. Nerisson, L. Cantrel, C. Volkringer and T. Loiseau, *Chem. – Eur. J.*, 2022, **28**, e202104437.
139 L. Wang, T. Li, X. Dong, M. Pang, S. Xiao and W. Zhang, *Chem. Eng. J.*, 2021, **425**, 130578.
140 S. Chibani, F. Chiter, L. Cantrel and J.-F. Paul, *J. Phys. Chem. C*, 2017, **121**, 25283–25291.

141 M. L. Díaz-Ramírez, B. Vargas, J. R. Álvarez, B. Landeros-Rivera, M. Rivera-Almazo, C. Ramos, J. G. Flores, E. Morales, R. Vargas, J. Garza, E. González-Zamora, A. Martínez, D. Solís-Ibarra and I. A. Ibarra, *Dalton Trans.*, 2020, **49**, 6572–6577.
142 F. Hassani and H. Tavakol, *Sens. Actuators B Chem.*, 2014, **196**, 624–630.
143 H. Tavakol and F. Hassani, *Struct. Chem.*, 2015, **26**, 151–158.
144 C. Cramer, *Essentials of Computational Chemistry: Theories and Models, 2nd Edition | Wiley*, 2004.
145 P. Deák, T. Frauenheim and M. R. Pederson, Eds., *Computer simulation of materials at atomic level*, Wiley-VCH, Berlin ; Chichester, 2000.
146 B. Smit and F. Daan, *Understanding Molecular Simulation - 2nd Edition*, Elsevier, 2001.
147 D. Marx and J. Hutter, *Ab Initio Molecular Dynamics: Basic Theory and Advanced Methods*, Cambridge University Press, Cambridge, Reprint edition., 2012.
148 R. Y. Rubinstein and D. P. Kroese, *Simulation and the Monte Carlo Method*, Wiley, 3rd edition., 2016.
149 J. M. Haile, *Molecular Dynamics Simulation: Elementary Methods*, Wiley-Interscience, New York, NY, 1st edition., 1997.
150 E. Schrödinger, *Phys. Rev.*, 1926, **28**, 1049–1070.
151 M. Born and R. Oppenheimer, *Ann. Phys.*, 1927, **389**, 457–484.
152 M. Moshinsky, *Am. J. Phys.*, 1968, **36**, 52–53.
153 E. R. Johnson and A. D. Becke, *J. Chem. Phys.*, 2005, **123**, 024101.
154 L. H. Thomas, *Math. Proc. Camb. Philos. Soc.*, 1927, **23**, 542–548.
155 P. Hohenberg and W. Kohn, *Phys. Rev.*, 1964, **136**, B864–B871.
156 W. Kohn and L. J. Sham, *Phys. Rev.*, 1965, **140**, A1133–A1138.
157 L. J. Sham and W. Kohn, *Phys. Rev.*, 1966, **145**, 561–567.
158 J. P. Perdew and K. Schmidt, *AIP Conf. Proc.*, 2001, **577**, 1–20.
159 J. P. Perdew, K. Burke and M. Ernzerhof, *Phys. Rev. Lett.*, 1996, **77**, 3865–3868.
160 T. Bučko, J. Hafner, S. Lebègue and J. G. Ángyán, *J Phys Chem A*, 2010, **114**, 11814–11824.
161 S. Grimme, J. Antony, S. Ehrlich and H. Krieg, *J. Chem. Phys.*, 2010, **132**, 154104.
162 S. Grimme, S. Ehrlich and L. Goerigk, *J. Comput. Chem.*, 2011, **32**, 1456–1465.
163 T. Bučko, S. Lebègue, J. Hafner and J. G. Ángyán, *Phys. Rev. B*, 2013, **87**, 064110.
164 A. Tkatchenko and M. Scheffler, *Phys. Rev. Lett.*, 2009, **102**, 073005.
165 R. J. Maurer, C. Freysoldt, A. M. Reilly, J. G. Brandenburg, O. T. Hofmann, T. Björkman, S. Lebègue and A. Tkatchenko, *Annu. Rev. Mater. Res.*, 2019, **49**, 1–30.
166 T. Bučko, S. Lebègue, T. Gould and J. G. Ángyán, *J. Phys. Condens. Matter*, 2016, **28**, 045201.
167 W. J. Kim, M. Kim, E. K. Lee, S. Lebègue and H. Kim, *J. Phys. Chem. Lett.*, 2016, **7**, 3278–3283.
168 B. Himmetoglu, A. Floris, S. de Gironcoli and M. Cococcioni, *Int. J. Quantum Chem.*, 2014, **114**, 14–49.
169 S. A. Tolba, K. M. Gameel, B. A. Ali, H. A.Almossalami and N. K. Allam, *The DFT+U: Approaches, Accuracy, and Applications*, IntechOpen, 2018.
170 F. Bloch, *Z. Für Phys.*, 1929, **52**, 555–600.
171 P. E. Blöchl, O. Jepsen and O. K. Andersen, *Phys. Rev. B*, 1994, **49**, 16223–16233.
172 G. Kresse and J. Hafner, *J. Phys. Condens. Matter*, 1994, **6**, 8245–8257.
173 G. Kresse and J. Furthmüller, *Comput. Mater. Sci.*, 1996, **6**, 15–50.
174 G. Kresse and J. Hafner, *Phys Rev B*, 1993, **47**, 558–561.
175 J. J. Jorgensen and G. L. W. Hart, *Model. Simul. Mater. Sci. Eng.*, 2021, **29**, 065014.
176 R. P. Feynman, *Phys. Rev.*, 1939, **56**, 340–343.
177 J. E. Moran, S. Oktay, P. H. Santschi and D. R. Schink, *Environ. Sci. Technol.*, 1999, **33**, 2536–2542.

178 C. M. Grossman, W. E. Morton and R. H. Nussbaum, *Arch. Environ. Health Int. J.*, 1996, **51**, 175–176.
179 J. R. Goldsmith, C. M. Grossman, W. E. Morton, R. H. Nussbaum, E. A. Kordysh, M. R. Quastel, R. B. Sobel and F. D. Nussbaum, *Environ. Health Perspect.*, 1999, **107**, 303–308.
180 G. Levey and J. E. Willard, *J. Chem. Phys.*, 1956, **25**, 904–907.
181 H. Ji, W. Zeng and Y. Li, *Nanoscale*, 2019, **11**, 22664–22684.
182 A. K. Geim and K. S. Novoselov, *Nat. Mater.*, 2007, **6**, 183–191.
183 W. Yuan and G. Shi, *J. Mater. Chem. A*, 2013, **1**, 10078–10091.
184 F. Schedin, A. K. Geim, S. V. Morozov, E. W. Hill, P. Blake, M. I. Katsnelson and K. S. Novoselov, *Nat. Mater.*, 2007, **6**, 652–655.
185 G. Ko, H. Y. Kim, J. Ahn, Y. M. Park, K. Y. Lee and J. Kim, *Curr. Appl. Phys.*, 2010, **10**, 1002–1004.
186 N. Tit, K. Said, N. M. Mahmoud, S. Kouser and Z. H. Yamani, *Appl. Surf. Sci.*, 2017, **394**, 219–230.
187 G. Lee, G. Yang, A. Cho, J. W. Han and J. Kim, *Phys. Chem. Chem. Phys.*, 2016, **18**, 14198–14204.
188 N. Ghaderi and M. Peressi, *J. Phys. Chem. C*, 2010, **114**, 21625–21630.
189 O. V. Yazyev and L. Helm, *Phys. Rev. B*, 2007, **75**, 125408.
190 Y. Zhang, T.-T. Tang, C. Girit, Z. Hao, M. C. Martin, A. Zettl, M. F. Crommie, Y. R. Shen and F. Wang, *Nature*, 2009, **459**, 820–823.
191 R. Quhe, J. Zheng, G. Luo, Q. Liu, R. Qin, J. Zhou, D. Yu, S. Nagase, W.-N. Mei, Z. Gao and J. Lu, *NPG Asia Mater.*, 2012, **4**, e6–e6.
192 X. Wang, G. Sun, P. Routh, D.-H. Kim, W. Huang and P. Chen, *Chem. Soc. Rev.*, 2014, **43**, 7067–7098.
193 A. K. Singh, R. S. Singh and A. K. Singh, *Adv. Eng. Mater.*, **n/a**, 2200259.
194 J. Huve, A. Ryzhikov, H. Nouali, V. Lalia, G. Augé and T. Jean Daou, *RSC Adv.*, 2018, **8**, 29248–29273.
195 H. E. Shim, J. E. Yang, S.-W. Jeong, C. H. Lee, L. Song, S. Mushtaq, D. S. Choi, Y. J. Choi and J. Jeon, *Nanomaterials*, 2018, **8**, 660.
196 M. Chebbi, B. Azambre, L. Cantrel, M. Huvé and T. Albiol, *Microporous Mesoporous Mater.*, 2017, **244**, 137–150.
197 M. del Rio, M. Villar, S. Quesada, G. Turnes Palomino, L. Ferrer and C. Palomino Cabello, *Appl. Mater. Today*, 2021, **24**, 101130.
198 J. Zhou, T. Lan, T. Li, Q. Chen, P. Bai, F. Liu, Z. Yuan, W. Zheng, X. Luo, W. Yan and T. Yan, *Sep. Purif. Technol.*, 2022, **290**, 120895.
199 P. Puschnig, P. Amiri and C. Draxl, *Phys. Rev. B*, 2012, **86**, 085107.
200 P. Miró, M. Audiffred and T. Heine, *Chem. Soc. Rev.*, 2014, **43**, 6537–6554.
201 G. Henkelman, A. Arnaldsson and H. Jónsson, *Comput. Mater. Sci.*, 2006, **36**, 354–360.
202 E. Sanville, S. D. Kenny, R. Smith and G. Henkelman, *J. Comput. Chem.*, 2007, **28**, 899–908.
203 W. Tang, E. Sanville and G. Henkelman, *J. Phys. Condens. Matter*, 2009, **21**, 084204.
204 K. Momma and F. Izumi, *J. Appl. Crystallogr.*, 2011, **44**, 1272–1276.
205 S. Nosé, *J. Chem. Phys.*, 1984, **81**, 511–519.
206 W. G. Hoover, *Phys. Rev. A*, 1985, **31**, 1695–1697.
207 W. Wang, Y. Zhang, C. Shen and Y. Chai, *AIP Adv.*, 2016, **6**, 025317.
208 S. U. D. Shamim, D. Roy, S. Alam, A. A. Piya, M. S. Rahman, Md. K. Hossain and F. Ahmed, *Appl. Surf. Sci.*, 2022, **596**, 153603.
209 Y. Ma, P. O. Lehtinen, A. S. Foster and R. M. Nieminen, *New J. Phys.*, 2004, **6**, 68–68.
210 P. Rani and R. Bhandari, in *International Conference on Advanced Nanomaterials Emerging Engineering Technologies*, 2013, pp. 237–239.

211 M. Amft, S. Lebègue, O. Eriksson and N. V. Skorodumova, *J. Phys. Condens. Matter*, 2011, **23**, 395001.
212 D. Düzenli, *J. Phys. Chem. C*, 2016, **120**, 20149–20157.
213 A. N. Rudenko, F. J. Keil, M. I. Katsnelson and A. I. Lichtenstein, *Phys. Rev. B*, 2010, **82**, 035427.
214 K. W. Chapman, P. J. Chupas and T. M. Nenoff, *J. Am. Chem. Soc.*, 2010, **132**, 8897–8899.
215 J. Troyano, F. Zamora and S. Delgado, *Chem. Soc. Rev.*, 2021, **50**, 4606–4628.
216 H. Yang, Z. Wang, H. Ye, K. Zhang, X. Chen and G. Zhang, *Appl. Surf. Sci.*, 2018, **459**, 554–561.
217 S. Peng, K. Cho, P. Qi and H. Dai, *Chem. Phys. Lett.*, 2004, **387**, 271–276.
218 S. V. Selvi, N. Nataraj, T.-W. Chen, S.-M. Chen, P. Balu and X. Liu, *J. Environ. Chem. Eng.*, 2022, **10**, 107182.
219 N. Baig, A.-N. Kawde and A. Elgamouz, *Biosens. Bioelectron. X*, 2022, **11**, 100205.
220 Y.-T. Li, L.-L. Qu, D.-W. Li, Q.-X. Song, F. Fathi and Y.-T. Long, *Biosens. Bioelectron.*, 2013, **43**, 94–100.
221 B. Clement, L. Cantrel, G. Ducros, F. Funke, L. Herranz, A. Rydl, G. Weber and C. Wren, .
222 Daryl Haefner, *Methods of Gas Phase Capture of Iodine from Fuel Reprocessing Off-Gas: A Literature Survey*, 2007.
223 B. Xerri, S. Canneaux, F. Louis, J. Trincal, F. Cousin, M. Badawi and L. Cantrel, *Comput. Theor. Chem.*, 2012, **990**, 194–208.
224 A. J. González, *Health Phys.*, 2007, **93**, 571–592.
225 L. J. Small and T. M. Nenoff, *ACS Appl. Mater. Interfaces*, 2017, **9**, 44649–44655.
226 M. L. Díaz-Ramírez, B. Vargas, J. R. Álvarez, B. Landeros-Rivera, M. Rivera-Almazo, C. Ramos, J. G. Flores, E. Morales, R. Vargas, J. Garza, E. González-Zamora, A. Martínez, D. Solís-Ibarra and I. A. Ibarra, *Dalton Trans.*, 2020, **49**, 6572–6577.
227 M. Xu, T. Wang, L. Zhou and D. Hua, *J. Mater. Chem. A*, 2020, **8**, 1966–1974.
228 P. Dariyal, S. Sharma, G. Singh Chauhan, B. Pratap Singh and S. R. Dhakate, *Nanoscale Adv.*, 2021, **3**, 6514–6544.
229 I. Raya, H. H. Kzar, Z. H. Mahmoud, A. Al Ayub Ahmed, A. Z. Ibatova and E. Kianfar, *Carbon Lett.*, 2022, **32**, 339–364.
230 Q. Tang, Z. Zhou and Z. Chen, *WIREs Comput. Mol. Sci.*, 2015, **5**, 360–379.
231 R. Kumar, J. Mittal and M. Jaiswal, *Diam. Relat. Mater.*, 2021, **120**, 108551.
232 E. Cho, A. Perebikovsky, O. Benice, S. Holmberg, M. Madou and M. Ghazinejad, *Sensors*, 2018, **18**, 1486.
233 M. Kim, W. J. Kim, E. K. Lee, S. Lebègue and H. Kim, *Int. J. Quantum Chem.*, 2016, **116**, 598–607.
234 A. J. A. Price, K. R. Bryenton and E. R. Johnson, *J. Chem. Phys.*, 2021, **154**, 230902.
235 M. Arabieh and Y. T. Azar, *Appl. Surf. Sci.*, 2018, **434**, 604–612.
236 S. Beniwal, J. Hooper, D. P. Miller, P. S. Costa, G. Chen, S.-Y. Liu, P. A. Dowben, E. C. H. Sykes, E. Zurek and A. Enders, *ACS Nano*, 2017, **11**, 2486–2493.
237 B. Mortazavi, M. Shahrokhi, M. Raeisi, X. Zhuang, L. F. C. Pereira and T. Rabczuk, *Carbon*, 2019, **149**, 733–742.
238 H. Tanaka, Y. Kawamata, H. Simizu, T. Fujita, H. Yanagisawa, S. Otani and C. Oshima, *Solid State Commun.*, 2005, **136**, 22–25.
239 S. Yang, W. Li, C. Ye, G. Wang, H. Tian, C. Zhu, P. He, G. Ding, X. Xie, Y. Liu, Y. Lifshitz, S.-T. Lee, Z. Kang and M. Jiang, *Adv. Mater.*, 2017, **29**, 1605625.
240 X. Liu, X. Ma, H. Gao, X. Zhang, H. Ai, W. Li and M. Zhao, *Nanoscale*, 2018, **10**, 13179–13186.
241 S. M. Aghaei, A. Aasi, S. Farhangdoust and B. Panchapakesan, *Appl. Surf. Sci.*, 2021, **536**, 147756.

242 V. Babar, S. Sharma and U. Schwingenschlögl, *J. Phys. Chem. C*, 2020, **124**, 5853–5860.
243 S. Mehdi Aghaei, M. M. Monshi, I. Torres, S. M. J. Zeidi and I. Calizo, *Appl. Surf. Sci.*, 2018, **427**, 326–333.
244 D. Ma, J. Zhang, X. Li, C. He, Z. Lu, Z. Lu, Z. Yang and Y. Wang, *Sens. Actuators B Chem.*, 2018, **266**, 664–673.
245 T. (Japan) Atomic Energy Society of Japan, Japan, 2014.
246 D. Jacquemain, S. Guentay, S. Basu, M. Sonnenkalb, L. Lebel, J. Ball, H. J. Allelein, B. Liebana Martinez, B. Eckardt, N. Losch, L. Ammirabile, D. Gryffroy, L. Sallus, A. Kroes, T. Rensonnet, A. Anden, S. Gyepi-Garbrah, A. Viktorov, J. Duspiva, T. Routamo, S. Guieu, A. Hotta, H. Nakamura, J. H. Song, K. S. Ha, C. Filio, M. V. Kuznetsov, L. Kubisova, T. Nemec, W. Frid, D. Loy, D. Pellini, T. Zieger, L. Herranz Puebla, A. Amri and M. Kissane, *OECD/NEA/CSNI Status Report on Filtered Containment Venting*, Nuclear Energy Agency of the OECD (NEA), 2014.
247 J. J. Foit, *Nucl. Eng. Des.*, 1997, **170**, 73–79.
248 M. Chebbi, S. Chibani, J.-F. Paul, L. Cantrel and M. Badawi, *Microporous Mesoporous Mater.*, 2017, **239**, 111–122.
249 S. Chibani, I. Medlej, S. Lebègue, J. G. Ángyán, L. Cantrel and M. Badawi, *ChemPhysChem*, 2017, **18**, 1642–1652.
250 S. Chibani, M. Chebbi, S. Lebègue, T. Bučko and M. Badawi, *J. Chem. Phys.*, 2016, **144**, 244705.
251 S. Chibani, M. Chebbi, S. Lebègue, L. Cantrel and M. Badawi, *Phys. Chem. Chem. Phys.*, 2016, **18**, 25574–25581.
252 F. R. Baptista, S. A. Belhout, S. Giordani and S. J. Quinn, *Chem. Soc. Rev.*, 2015, **44**, 4433–4453.
253 V. V. Speybroeck, K. Hemelsoet, L. Joos, M. Waroquier, R. G. Bell and C. R. A. Catlow, *Chem. Soc. Rev.*, 2015, **44**, 7044–7111.
254 B. A. De Moor, M.-F. Reyniers, O. C. Gobin, J. A. Lercher and G. B. Marin, *J. Phys. Chem. C*, 2011, **115**, 1204–1219.
255 F. Göltl, A. Grüneis, T. Bučko and J. Hafner, *J. Chem. Phys.*, 2012, **137**, 114111.
256 G. Piccini, M. Alessio, J. Sauer, Y. Zhi, Y. Liu, R. Kolvenbach, A. Jentys and J. A. Lercher, *J. Phys. Chem. C*, 2015, **119**, 6128–6137.
257 G. Kresse and J. Furthmüller, *Phys. Rev. B*, 1996, **54**, 11169–11186.
258 P. E. Blöchl, *Phys. Rev. B*, 1994, **50**, 17953–17979.
259 G. Kresse and D. Joubert, *Phys Rev B*, 1999, **59**, 1758–1775.
260 K. Zhour and A. Postnikov, *Phys. Status Solidi B*, 2021, **258**, 2100131.
261 K. Zhour, J. M. Otero-Mato, F. E. H. Hassan, H. Fahs, M. Vaezzadeh, E. López-Lago, L. J. Gallego and L. M. Varela, *J. Mol. Liq.*, 2021, **321**, 114759.
262 S. Grimme, *J Comput Chem*, 2006, **27**, 1787–1799.
263 R. F. W. Bader, *Acc. Chem. Res.*, 1985, **18**, 9–15.
264 J. Beheshtian, A. A. Peyghan and M. Noei, *Sens. Actuators B Chem.*, 2013, **181**, 829–834.
265 A. Bafekry, S. Farjami Shayesteh, M. Ghergherehchi and F. M. Peeters, *J. Appl. Phys.*, 2019, **126**, 144304.
266 H. Zhang, Y. Tang, H. Chai, W. Chen, M. Zhao and X. Dai, *Mol. Phys.*, 2019, **117**, 125–135.
267 A. Tkatchenko, R. A. DiStasio, R. Car and M. Scheffler, *Phys. Rev. Lett.*, 2012, **108**, 236402.
268 T. Bučko, S. Lebègue, J. G. Ángyán and J. Hafner, *J. Chem. Phys.*, 2014, **141**, 034114.
269 A. Bafekry, M. Neek-Amal and F. M. Peeters, *Phys. Rev. B*, 2020, **101**, 165407.
270 X. Zhou, W. Feng, S. Guan, B. Fu, W. Su and Y. Yao, *J. Mater. Res.*, 2017, **32**, 2993–3001.
271 J. Mahmood, E. K. Lee, M. Jung, D. Shin, H.-J. Choi, J.-M. Seo, S.-M. Jung, D. Kim, F. Li, M. S. Lah, N. Park, H.-J. Shin, J. H. Oh and J.-B. Baek, *Proc. Natl. Acad. Sci.*, 2016, **113**, 7414–7419.

272 M. Yu and D. R. Trinkle, *J. Chem. Phys.*, 2011, **134**, 064111.
273 O. K. Farha, I. Eryazici, N. C. Jeong, B. G. Hauser, C. E. Wilmer, A. A. Sarjeant, R. Q. Snurr, S. T. Nguyen, A. Ö. Yazaydın and J. T. Hupp, *J. Am. Chem. Soc.*, 2012, **134**, 15016–15021.
274 O. K. Farha, A. Özgür Yazaydın, I. Eryazici, C. D. Malliakas, B. G. Hauser, M. G. Kanatzidis, S. T. Nguyen, R. Q. Snurr and J. T. Hupp, *Nat. Chem.*, 2010, **2**, 944–948.
275 H. Furukawa, N. Ko, Y. B. Go, N. Aratani, S. B. Choi, E. Choi, A. Ö. Yazaydin, R. Q. Snurr, M. O'Keeffe, J. Kim and O. M. Yaghi, *Science*, 2010, **329**, 424–428.
276 B. Li, H. Wang and B. Chen, *Chem. – Asian J.*, 2014, **9**, 1474–1498.
277 H. Daglar and S. Keskin, *Coord. Chem. Rev.*, 2020, **422**, 213470.
278 K. Maity, C. K. Karan and K. Biradha, *Chem. – Eur. J.*, 2018, **24**, 10988–10993.
279 A. S. Rosen, M. R. Mian, T. Islamoglu, H. Chen, O. K. Farha, J. M. Notestein and R. Q. Snurr, *J. Am. Chem. Soc.*, 2020, **142**, 4317–4328.
280 Z. Gao, Y. Lai, L. Gong, L. Zhang, S. Xi, J. Sun, L. Zhang and F. Luo, *ACS Catal.*, 2022, **12**, 9101–9113.
281 Y. Li, X. Zhang, J. Lan, D. Li, Z. Wang, P. Xu and J. Sun, *ACS Sustain. Chem. Eng.*, 2021, **9**, 2795–2803.
282 Z. Zhai, X. Zhang, X. Hao, B. Niu and C. Li, *Adv. Mater. Technol.*, 2021, **6**, 2100127.
283 X. Chen, Y. Yu, C. Yang, J. Yin, X. Song, J. Li and H. Fei, *ACS Appl. Mater. Interfaces*, 2021, **13**, 52765–52774.
284 G.-D. Wang, Y.-Z. Li, W.-F. Zhang, L. Hou, Y.-Y. Wang and Z. Zhu, *ACS Appl. Mater. Interfaces*, 2021, **13**, 58862–58870.
285 X. Liang, P. Wang, C. Li, M. Yuan, Q. Shi and J. Dong, *Microporous Mesoporous Mater.*, 2021, **320**, 111109.
286 J. Ha, M. Jung, J. Park, H. Oh and H. R. Moon, *ACS Appl. Mater. Interfaces*, 2022, **14**, 30946–30951.
287 M. Witman, S. Ling, A. Gladysiak, K. C. Stylianou, B. Smit, B. Slater and M. Haranczyk, *J. Phys. Chem. C*, 2017, **121**, 1171–1181.
288 L. Wang, T. Maxisch and G. Ceder, *Phys. Rev. B*, 2006, **73**, 195107.
289 P. Canepa, Y. J. Chabal and T. Thonhauser, *Phys. Rev. B*, 2013, **87**, 094407.
290 J. E. Bachman, M. T. Kapelewski, D. A. Reed, M. I. Gonzalez and J. R. Long, *J. Am. Chem. Soc.*, 2017, **139**, 15363–15370.
291 A. de Oliveira, G. F. de Lima and H. A. De Abreu, *Chem. Phys. Lett.*, 2018, **691**, 283–290.
292 R. Sanz, F. Martínez, G. Orcajo, L. Wojtas and D. Briones, *Dalton Trans.*, 2013, **42**, 2392–2398.
293 K. Lee, J. D. Howe, L.-C. Lin, B. Smit and J. B. Neaton, *Chem. Mater.*, 2015, **27**, 668–678.
294 P. D. C. Dietzel, Y. Morita, R. Blom and H. Fjellvåg, *Angew. Chem. Int. Ed.*, 2005, **44**, 6354–6358.
295 P. D. C. Dietzel, B. Panella, M. Hirscher, R. Blom and H. Fjellvåg, *Chem. Commun.*, 2006, 959–961.
296 R. D. Shannon, *Acta Crystallogr. Sect. A*, 1976, **32**, 751–767.
297 T. Pham, K. A. Forrest, J. Eckert and B. Space, *Cryst. Growth Des.*, 2016, **16**, 867–874.
298 Y. Liao, L. Zhang, M. H. Weston, W. Morris, J. T. Hupp and O. K. Farha, *Chem. Commun.*, 2017, **53**, 9376–9379.
299 E. D. Bloch, M. R. Hudson, J. A. Mason, S. Chavan, V. Crocellà, J. D. Howe, K. Lee, A. L. Dzubak, W. L. Queen, J. M. Zadrozny, S. J. Geier, L.-C. Lin, L. Gagliardi, B. Smit, J. B. Neaton, S. Bordiga, C. M. Brown and J. R. Long, *J. Am. Chem. Soc.*, 2014, **136**, 10752–10761.
300 L. Valenzano, B. Civalleri, S. Chavan, G. T. Palomino, C. O. Areán and S. Bordiga, *J. Phys. Chem. C*, 2010, **114**, 11185–11191.
301 W. You, Y. Liu, J. D. Howe and D. S. Sholl, *J. Phys. Chem. C*, 2018, **122**, 8960–8966.

302 R. G. Pearson, *J. Am. Chem. Soc.*, 1963, **85**, 3533–3539.
303 Y. Li, X. Wang, D. Xu, J. D. Chung, M. Kaviany and B. Huang, *J. Phys. Chem. C*, 2015, **119**, 13021–13031.
304 B. Vlaisavljevich, J. Huck, Z. Hulvey, K. Lee, J. A. Mason, J. B. Neaton, J. R. Long, C. M. Brown, D. Alfè, A. Michaelides and B. Smit, *J. Phys. Chem. A*, 2017, **121**, 4139–4151.
305 P. Kumar, C.-Y. Sung, O. Muraza, M. Cococcioni, S. Al Hashimi, A. McCormick and M. Tsapatsis, *Microporous Mesoporous Mater.*, 2011, **146**, 127–133.
306 İ. A. Reşitoğlu, K. Altinişik and A. Keskin, *Clean Technol. Environ. Policy*, 2015, **17**, 15–27.
307 Departement for transport, 2017.
308 9 out of 10 people worldwide breathe polluted air, but more countries are taking action, https://www.who.int/news/item/02-05-2018-9-out-of-10-people-worldwide-breathe-polluted-air-but-more-countries-are-taking-action, (accessed October 11, 2022).
309 A. Ghorani-Azam, B. Riahi-Zanjani and M. Balali-Mood, *J. Res. Med. Sci.*, 2016, **21**, 65.
310 A. Amaducci and J. W. Downs, in *StatPearls*, StatPearls Publishing, Treasure Island (FL), 2022.
311 Dieases & Harmful Health Effects of Air Pollution, https://www.lalpathlabs.com/blog/health-effects-of-air-pollution/, (accessed October 11, 2022).
312 Air pollution, https://www.eea.europa.eu/themes/air/health-impacts-of-air-pollution, (accessed October 11, 2022).
313 C. Guardiola, J. Martín, B. Pla and P. Bares, *Appl. Therm. Eng.*, 2017, **110**, 1011–1020.
314 Euro 6 drives early NOx improvement, https://www.emissionsanalytics.com/news/euro-6-drives-early-nox-improvement, (accessed October 11, 2022).
315 U. Asad and M. Zheng, *Appl. Energy*, 2014, **123**, 242–252.
316 J. Jordal, *Reducing Air Pollution from Ships*, Miljøstyrelsen, 2012.
317 G. H. Abd-Alla, *Energy Convers. Manag.*, 2002, **43**, 1027–1042.
318 Z. G. Liu, D. R. Berg, T. A. Swor and J. J. Schauer, *Environ. Sci. Technol.*, 2008, **42**, 6080–6085.
319 The NOx Reduction by CO on a Pt−K/Al2O3 Lean NOx Trap Catalyst | The Journal of Physical Chemistry C, https://pubs.acs.org/doi/abs/10.1021/jp106753g, (accessed October 11, 2022).
320 n-Heptane As a Reducing Agent in the NOx Removal over a Pt–Ba/Al2O3 NSR Catalyst | ACS Catalysis, https://pubs.acs.org/doi/abs/10.1021/cs500850g, (accessed October 11, 2022).
321 Detailed Characterization Studies of Vehicle and Rapid Aged Commercial Lean NOx Trap Catalysts | Industrial & Engineering Chemistry Research, https://pubs.acs.org/doi/abs/10.1021/acs.iecr.8b01468, (accessed October 11, 2022).
322 A review of NO x storage/reduction catalysts : mechanism, materials and degradation studies - Catalysis Science & Technology (RSC Publishing) DOI:10.1039/C1CY00007A, https://pubs.rsc.org/en/content/articlehtml/2011/cy/c1cy00007a, (accessed October 11, 2022).
323 Carbonate-Based Lean-Burn NOx Trap Catalysts Pt–K2CO3/ZrO2 with Large NOx Storage Capacity and High Reduction Efficiency | The Journal of Physical Chemistry C, https://pubs.acs.org/doi/abs/10.1021/jp3117598, (accessed October 11, 2022).
324 L. Lietti and L. Castoldi, *NOx Trap Catalysts and Technologies: Fundamentals and Industrial Applications*, Royal Society of Chemistry, 2018.
325 Promotional Effect of Ce-doped V2O5-WO3/TiO2 with Low Vanadium Loadings for Selective Catalytic Reduction of NOx by NH3 | The Journal of Physical Chemistry C, https://pubs.acs.org/doi/abs/10.1021/jp907109e, (accessed October 11, 2022).

326 Excellent Performance of One-Pot Synthesized Cu-SSZ-13 Catalyst for the Selective Catalytic Reduction of NOx with NH3 | Environmental Science & Technology, https://pubs.acs.org/doi/abs/10.1021/es4032002, (accessed October 11, 2022).
327 P. Chen and J. Wang, *Appl. Energy*, 2014, **122**, 310–320.
328 X. Xiao, S. Xiong, B. Li, Y. Geng and S. Yang, *Catal. Lett.*, 2016, **146**, 2242–2251.
329 Catalytic NOx Abatement Systems for Mobile Sources: From Three-Way to Lean Burn after-Treatment Technologies | Chemical Reviews, https://pubs.acs.org/doi/full/10.1021/cr100168g, (accessed October 11, 2022).
330 F. Millo and D. Vezza, in *SAE Technical Paper*, 2012.
331 Pt- and Pd-Promoted CeO2–ZrO2 for Passive NOx Adsorber Applications | Industrial & Engineering Chemistry Research, https://pubs.acs.org/doi/abs/10.1021/acs.iecr.6b03793, (accessed October 11, 2022).
332 The role of platinum on the NOx storage and desorption behavior of ceria: an online FT-IR study combined with in situ Raman and UV-vis spectroscopy - Physical Chemistry Chemical Physics (RSC Publishing), https://pubs.rsc.org/en/content/articlelanding/2021/cp/d0cp05800a/unauth, (accessed October 11, 2022).
333 Database of Zeolite Structures, http://www.iza-structure.org/databases/, (accessed January 13, 2022).
334 R. Millini and G. Bellussi, 2017, 1–36.
335 A. J. Porter and A. J. O'Malley, *J. Phys. Chem. C*, 2021, **125**, 11567–11579.
336 W. Loewenstein, *Am. Mineral.*, 1954, **39**, 92–96.
337 E. M. Flanigen, *Pure Appl. Chem.*, 1980, **52**, 2191–2211.
338 Y. Li and J. Yu, *Nat. Rev. Mater.*, 2021, **6**, 1156–1174.
339 S. Gligorovski and J. P. D. Abbatt, *Science*, 2018, **359**, 632–633.
340 IARC Working Group on the Evaluation of Carcinogenic Risks to Humans and International Agency for Research on Cancer, *Diesel and gasoline engine exhausts and some nitroarenes.*, 2014.
341 9 out of 10 people worldwide breathe polluted air, but more countries are taking action, https://www.who.int/news/item/02-05-2018-9-out-of-10-people-worldwide-breathe-polluted-air-but-more-countries-are-taking-action, (accessed December 7, 2020).
342 W. Jedrychowski, F. Perera, D. Mrozek-Budzyn, E. Mroz, E. Flak, J. D. Spengler, S. Edwards, R. Jacek, I. Kaim and Z. Skolicki, *Environ. Res.*, 2009, **109**, 447–456.
343 European Environment Agency. and European Topic Centre on Air Pollution and Climate Change Mitigation (ETC/ACM)., *Air quality in Europe: 2017 report.*, Publications Office, LU, 2017.
344 A. kumar Agrawal, S. K. Singh, S. Sinha and M. K. Shukla, *Sadhana*, 2004, **29**, 275–284.
345 H. Ahari, M. Smith, M. Zammit, K. Price, J. Jacques, T. Pauly and L. Wang, *SAE Int. J. Passeng. Cars - Mech. Syst.*, 2015, **8**, 526–530.
346 X. Wang, D. Westerdahl, J. Hu, Y. Wu, H. Yin, X. Pan and K. Max Zhang, *Atmos. Environ.*, 2012, **46**, 45–55.
347 T. Lee, J. Park, S. Kwon, J. Lee and J. Kim, *Sci. Total Environ.*, 2013, **461–462**, 377–385.
348 AVIS et RAPPORT de l'Anses relatif à l'Evaluation des méthodes de mesure de 27 substances listées en annexe de la directive (UE) n°2017/164 de la Commission du 31 janvier 2017 | Anses - Agence nationale de sécurité sanitaire de l'alimentation, de l'environnement et du travail, https://www.anses.fr/fr/content/avis-et-rapport-de-lanses-relatif-%C3%A0-levaluation-des-m%C3%A9thodes-de-mesure-de-27-substances, (accessed January 14, 2022).
349 L. Castoldi, L. Lietti, R. Bonzi, N. Artioli, P. Forzatti, S. Morandi and G. Ghiotti, *J. Phys. Chem. C*, 2011, **115**, 1277–1286.

350 J.-K. Lai and I. E. Wachs, *ACS Catal.*, 2018, **8**, 6537–6551.
351 G. Centi and S. Perathoner, *Appl. Catal. Gen.*, 1995, **132**, 179–259.
352 Z. G. Liu, D. R. Berg, T. A. Swor and J. J. Schauer, *Environ. Sci. Technol.*, 2008, **42**, 6080–6085.
353 J. Y. Yan, G.-D. Lei, W. M. H. Sachtler and H. H. Kung, *J. Catal.*, 1996, **161**, 43–54.
354 F. Delachaux, C. Vallières, H. Monnier and M.-T. Lecler, *Adsorption*, 2019, **25**, 95–103.
355 O. Monticelli, R. Loenders, P. A. Jacobs and J. A. Martens, *Appl. Catal. B Environ.*, 1999, **21**, 215–220.
356 A. Sultana, R. Loenders, O. Monticelli, C. Kirschhock, P. A. Jacobs and J. A. Martens, *Angew. Chem. Int. Ed.*, 2000, **39**, 2934–2937.
357 IZA Structure Commission, http://www.iza-structure.org/, (accessed December 7, 2020).
358 A. Myers, , DOI:10.1201/9780203911167.ch22.
359 P. A. Jacobs, E. M. Flanigen, J. C. Jansen and H. van Bekkum, *Introduction to Zeolite Science and Practice*, Elsevier, 2001.
360 *J. Am. Chem. Soc.*, 2003, **125**, 6839–6839.
361 W. M. Meier, *Z. Für Krist. - Cryst. Mater.*, 1961, **115**, 439–450.
362 United States, US3702886A, 1972.
363 C. Baerlocher, L. B. McCusker and D. H. Olson, *Atlas of Zeolite Framework Types*, Elsevier, 2007.
364 C. R. A. Catlow, R. G. Bell, J. D. Gale and D. W. Lewis, in *Studies in Surface Science and Catalysis*, eds. L. Bonneviot and S. Kaliaguine, Elsevier, 1995, vol. 97, pp. 87–100.
365 C. R. A. Catlow, B. Smit and R. A. van Santen, *Computer Modelling of Microporous Materials*, Elsevier, 2004.
366 M. Chebbi, S. Chibani, J.-F. Paul, L. Cantrel and M. Badawi, *Microporous Mesoporous Mater.*, 2017, **239**, 111–122.
367 I. Khalil, H. Jabraoui, S. Lebègue, W. J. Kim, L.-J. Aguilera, K. Thomas, F. Maugé and M. Badawi, *Chem. Eng. J.*, 2020, **402**, 126264.
368 H. Jabraoui, I. Khalil, S. Lebègue and M. Badawi, *Mol. Syst. Des. Eng.*, 2019, **4**, 882–892.
369 G. Li, S. C. Larsen and V. H. Grassian, *J. Mol. Catal. Chem.*, 2005, **227**, 25–35.
370 J. Szanyi, J. H. Kwak and C. H. F. Peden, *J. Phys. Chem. B*, 2004, **108**, 3746–3753.
371 W. Lutz, *Adv. Mater. Sci. Eng.*, 2014, **2014**, e724248.
372 United States, US3130007A, 1964.
373 E. P. Hessou, H. Jabraoui, I. Khalil, M.-A. Dziurla and M. Badawi, *Appl. Surf. Sci.*, 2021, **541**, 148515.
374 M. U. C. Braga, G. H. Perin, L. H. de Oliveira and P. A. Arroyo, *Microporous Mesoporous Mater.*, 2022, **331**, 111643.
375 A. A. Costa, P. R. S. Braga, J. L. de Macedo, J. A. Dias and S. C. L. Dias, *Microporous Mesoporous Mater.*, 2012, **147**, 142–148.
376 L. Cao, F. Xu, Y.-Y. Liang and H.-L. Li, *Adv. Mater.*, 2004, **16**, 1853–1857.
377 K. O. Sulaiman, M. Sajid and K. Alhooshani, *Microchem. J.*, 2020, **152**, 104289.
378 W. H. Baur, *Am. Mineral.*, 1964, **49**, 697–704.
379 E. Dempsey, G. H. Kuehl and D. H. Olson, *J. Phys. Chem.*, 1969, **73**, 387–390.
380 F. Porcher, M. Souhassou, Y. Dusausoy and C. Lecomte, *Eur. J. Mineral.*, 1999, 333–344.
381 T. Frising and P. Leflaive, *Microporous Mesoporous Mater.*, 2008, **114**, 27–63.
382 S. Buttefey, A. Boutin, C. Mellot-Draznieks and A. H. Fuchs, *J. Phys. Chem. B*, 2001, **105**, 9569–9575.
383 Z. Nour, D. Berthomieu, Q. Yang and G. Maurin, *J. Phys. Chem. C*, 2012, **116**, 24512–24521.
384 H. V. Thang, L. Grajciar, P. Nachtigall, O. Bludský, C. O. Areán, E. Frýdová and R. Bulánek, *Catal. Today*, 2014, **227**, 50–56.

385 P. Kumar, C.-Y. Sung, O. Muraza, M. Cococcioni, S. Al Hashimi, A. McCormick and M. Tsapatsis, *Microporous Mesoporous Mater.*, 2011, **146**, 127–133.
386 C.-Y. Sung, S. Al Hashimi, A. McCormick, M. Tsapatsis and M. Cococcioni, *J. Phys. Chem. C*, 2012, **116**, 3561–3575.
387 G. Kresse and J. Furthmüller, *Phys. Rev. B*, 1996, **54**, 11169–11186.
388 C. S, C. M, L. S, B. T and B. M, *J. Chem. Phys.*, 2016, **144**, 244705–244705.
389 T. Bučko, S. Lebègue, J. Hafner and J. G. Ángyán, *J Chem Theory Comput*, 2013, **9**, 4293–4299.
390 A. G. Petukhov, I. I. Mazin, L. Chioncel and A. I. Lichtenstein, *Phys. Rev. B*, 2003, **67**, 153106.
391 L. Benco and D. Tunega, *Phys. Chem. Miner.*, 2009, **36**, 281–290.
392 P. Kozyra, J. Załucka, M. Mitoraj, E. Brocławik and J. Datka, *Catal. Lett.*, 2008, **126**, 241–246.
393 T. Kanougi, H. Tsuruya, Y. Oumi, A. Chatterjee, A. Fahmi, M. Kubo and A. Miyamoto, *Appl. Surf. Sci.*, 1998, **130–132**, 561–565.
394 Y. Wang, Z. Lei, B. Chen, Q. Guo and N. Liu, *Appl. Surf. Sci.*, 2010, **256**, 4042–4047.
395 P. Sun, K. Fan, X. Cheng, Z. Qian, Z. Wang, L. Wang and T.-C. Jen, *Chem. Phys. Lett.*, 2021, **766**, 138344.
396 R. Zhang, J. Szanyi, F. Gao and J.-S. McEwen, *Catal. Sci. Technol.*, 2016, **6**, 5812–5829.
397 L. A. M. M. Barbosa, R. A. van Santen and J. Hafner, *J. Am. Chem. Soc.*, 2001, **123**, 4530–4540.
398 C. Lamberti, A. Zecchina, E. Groppo and S. Bordiga, *Chem. Soc. Rev.*, 2010, **39**, 4951–5001.
399 K. I. Hadjiivanov and G. N. Vayssilov, in *Advances in Catalysis*, Academic Press, 2002, vol. 47, pp. 307–511.
400 L. Benco, *Surf. Sci.*, 2017, **656**, 115–125.
401 K. Mandal, Y. Gu, K. S. Westendorff, S. Li, J. A. Pihl, L. C. Grabow, W. S. Epling and C. Paolucci, *ACS Catal.*, 2020, **10**, 12801–12818.
402 M. Brändle and J. Sauer, *J. Mol. Catal. Chem.*, 1997, **119**, 19–33.
403 C. Y. Li and L. V. C. Rees, *React. Polym. Ion Exch. Sorbents*, 1988, **7**, 89–99.
404 P. Gallezot, A. Alarcon-Diaz, J.-A. Dalmon, A. J. Renouprez and B. Imelik, *J. Catal.*, 1975, **39**, 334–349.
405 G. Maurin, D. Plant, S. Devautour-Vinot, A. Nicolas, F. Henn and J. C. Giuntini, *Eur. Phys. J. Spec. Top.*, 2007, **141**, 113–116.
406 K. Klier, *Langmuir*, 1988, **4**, 13–25.
407 D. J. Vogel, J. M. Rimsza and T. M. Nenoff, *Angew. Chem. Int. Ed.*, 2021, **60**, 11514–11522.
408 J. Lin, W. Ho, X. Qin, C.-F. Leung, V. K.-M. Au and S. Lee, *Small*, 2022, **18**, 2105484.
409 T. Islamoglu, Z. Chen, M. C. Wasson, C. T. Buru, K. O. Kirlikovali, U. Afrin, M. R. Mian and O. K. Farha, *Chem. Rev.*, 2020, **120**, 8130–8160.
410 B. Guan, H. Lin, Q. Cheng and Z. Huang, *Ind. Eng. Chem. Res.*, 2011, **50**, 5401–5413.
411 F. Rezaei, A. A. Rownaghi, S. Monjezi, R. P. Lively and C. W. Jones, *Energy Fuels*, 2015, **29**, 5467–5486.
412 P. Horcajada, R. Gref, T. Baati, P. K. Allan, G. Maurin, P. Couvreur, G. Férey, R. E. Morris and C. Serre, *Chem. Rev.*, 2012, **112**, 1232–1268.
413 C. He, D. Liu and W. Lin, *Chem. Rev.*, 2015, **115**, 11079–11108.
414 A. A. Abdulrasheed, A. A. Jalil, S. Triwahyono, M. A. A. Zaini, Y. Gambo and M. Ibrahim, *Renew. Sustain. Energy Rev.*, 2018, **94**, 1067–1085.
415 J. Grand, S. N. Talapaneni, H. A. Aleksandrov, G. N. Vayssilov and S. Mintova, *ACS Appl. Mater. Interfaces*, 2019, **11**, 12914–12919.
416 S. Smeekens, S. Heylen, N. Janssens, K. Houthoofd, J. A. Martens and C. E. A. Kirschhock, *Chem. Mater.*, 2011, **23**, 4606–4611.

417 X. Han, H. G. W. Godfrey, L. Briggs, A. J. Davies, Y. Cheng, L. L. Daemen, A. M. Sheveleva, F. Tuna, E. J. L. McInnes, J. Sun, C. Drathen, M. W. George, A. J. Ramirez-Cuesta, K. M. Thomas, M. Schröder and S. Yang, *Nat. Mater.*, , DOI:10.1038/s41563-018-0104-7.

418 M. W. Khan, M. M. Sadiq, K. Gopalsamy, K. Xu, A. Jannat, B. Y. Zhang, M. Mohiuddin, M. Haris, R. Ou, S. Afrin, T. Alkathiri, S. Loomba, X. Mulet, N. Mahmood, R. Babarao and J. Z. Ou, *J. Colloid Interface Sci.*, 2022, **610**, 304–312.

419 X. Han, Y. Hong, Y. Ma, W. Lu, J. Li, L. Lin, A. M. Sheveleva, F. Tuna, E. J. L. McInnes, C. Dejoie, J. Sun, S. Yang and M. Schröder, *J. Am. Chem. Soc.*, 2020, **142**, 15235–15239.

420 J. Li, X. Han, X. Zhang, A. M. Sheveleva, Y. Cheng, F. Tuna, E. J. L. McInnes, L. J. McCormick McPherson, S. J. Teat, L. L. Daemen, A. J. Ramirez-Cuesta, M. Schröder and S. Yang, *Nat. Chem.*, 2019, **11**, 1085–1090.

421 E. D. Bloch, W. L. Queen, S. Chavan, P. S. Wheatley, J. M. Zadrozny, R. Morris, C. M. Brown, C. Lamberti, S. Bordiga and J. R. Long, *J. Am. Chem. Soc.*, 2015, **137**, 3466–3469.

422 X. Wang, Z. Xu, L. Li, Y. Zhao, R. Su, G. Liang, B. Yang, Y. Miao, W. Meng, Z. Luan, K. Li, H. Xi and R. Zou, *ACS Appl. Nano Mater.*, 2020, **3**, 11442–11454.

423 S. J. Stoneburner and L. Gagliardi, *J. Phys. Chem. C*, 2018, **122**, 22345–22351.

424 H. Demir, S. J. Stoneburner, W. Jeong, D. Ray, X. Zhang, O. K. Farha, C. J. Cramer, J. I. Siepmann and L. Gagliardi, *J. Phys. Chem. C*, 2019, **123**, 12935–12946.

425 S. J. Stoneburner, V. Livermore, M. E. McGreal, D. Yu, K. D. Vogiatzis, R. Q. Snurr and L. Gagliardi, *J. Phys. Chem. C*, 2017, **121**, 10463–10469.

426 H. Chen and R. Q. Snurr, *J. Phys. Chem. C*, 2021, **125**, 21701–21708.

427 P. Li, X. Shi, Y. Wu, M. Song, Y. Lai, H. Yu and G. Lu, *CrystEngComm*, 2021, **23**, 1828–1835.

428 X. Zhang, N. A. Vermeulen, Z. Huang, Y. Cui, J. Liu, M. D. Krzyaniak, Z. Li, H. Noh, M. R. Wasielewski, M. Delferro and O. K. Farha, *ACS Appl. Mater. Interfaces*, 2018, **10**, 635–641.

429 M. H. Weston, O. K. Farha, B. G. Hauser, J. T. Hupp and S. T. Nguyen, *Chem. Mater.*, 2012, **24**, 1292–1296.

430 M. H. Weston, G. W. Peterson, M. A. Browe, P. Jones, O. K. Farha, J. T. Hupp and S. T. Nguyen, *Chem. Commun.*, 2013, **49**, 2995–2997.

431 S. Daliran, M. Khajeh, A. R. Oveisi, H. García and R. Luque, *ACS Sustain. Chem. Eng.*, 2022, **10**, 5315–5322.

432 H. Fei, J. Shin, Y. S. Meng, M. Adelhardt, J. Sutter, K. Meyer and S. M. Cohen, *J. Am. Chem. Soc.*, 2014, **136**, 4965–4973.

433 H. Fei, S. Pullen, A. Wagner, S. Ott and S. M. Cohen, *Chem. Commun.*, 2015, **51**, 66–69.

434 M. J. Frisch, G. W. Trucks, H. B. Schlegel, G. E. Scuseria, M. A. Robb, J. R. Cheeseman, G. Scalmani, V. Barone, G. A. Petersson and H. Nakatsuji, *Gaussian 16 Revis. B*.

435 S. Grimme, J. Antony, S. Ehrlich and H. Krieg, *J. Chem. Phys.*, 2010, **132**, 154104.

436 F. Weigend and R. Ahlrichs, *Phys. Chem. Chem. Phys.*, 2005, **7**, 3297–3305.

437 P. J. Hay and W. R. Wadt, *J. Chem. Phys.*, 1985, **82**, 270–283.

438 S. F. Boys and F. Bernardi, *Mol. Phys.*, 1970, **19**, 553–566.

439 S. Grimme, S. Ehrlich and L. Goerigk, *J. Comput. Chem.*, 2011, **32**, 1456–1465.

440 G. Kresse and J. Hafner, *Phys. Rev. B*, 1993, **48**, 13115–13118.

441 Heterometallic Metal Organic Frameworks for Air Separation: A Computational Study | Industrial & Engineering Chemistry Research, https://pubs.acs.org/doi/abs/10.1021/acs.iecr.0c02449, (accessed October 23, 2022).

442 G. Kresse and D. Joubert, *Phys. Rev. B*, 1999, **59**, 1758–1775.

443 T. A. Manz and N. Gabaldon Limas, *RSC Adv.*, 2022, **12**, 14384–14384.

444 A. K. Rappe, C. J. Casewit, K. S. Colwell, W. A. I. Goddard and W. M. Skiff, *J. Am. Chem. Soc.*, 1992, **114**, 10024–10035.

445 L. Ding and A. Ö. Yazaydin, *J. Phys. Chem. C*, 2012, **116**, 22987–22991.

446 J. D. Gale and A. L. Rohl, *Mol. Simul.*, 2003, **29**, 291–341.
447 S. Nandi, S. Wang, M. Wahiduzzaman, V. Yadav, K. Taksande, G. Maurin, C. Serre and S. Devautour-Vinot, *ACS Appl. Mater. Interfaces*, 2021, **13**, 20194–20200.
448 P. P. Ewald, *Ann. Phys.*, 1921, **369**, 253–287.
449 D.-Y. Peng and D. B. Robinson, A New Two-Constant Equation of State, https://pubs.acs.org/doi/pdf/10.1021/i160057a011, (accessed October 23, 2022).
450 B. Widom, *J. Chem. Phys.*, 1963, **39**, 2808–2812.
451 B. Xiao, P. J. Byrne, P. S. Wheatley, D. S. Wragg, X. Zhao, A. J. Fletcher, K. M. Thomas, L. Peters, J. S. O. Evans, J. E. Warren, W. Zhou and R. E. Morris, *Nat. Chem.*, 2009, **1**, 289–294.
452 A. C. McKinlay, J. F. Eubank, S. Wuttke, B. Xiao, P. S. Wheatley, P. Bazin, J.-C. Lavalley, M. Daturi, A. Vimont, G. De Weireld, P. Horcajada, C. Serre and R. E. Morris, *Chem. Mater.*, 2013, **25**, 1592–1599.
453 R. V. Pinto, S. Wang, S. R. Tavares, J. Pires, F. Antunes, A. Vimont, G. Clet, M. Daturi, G. Maurin, C. Serre and M. L. Pinto, *Angew. Chem. Int. Ed.*, 2020, **59**, 5135–5143.
454 S.-R. G. Christopoulos, N. Kuganathan and A. Chroneos, *Sci. Rep.*, 2020, **10**, 7459.
455 W. Tang, E. Sanville and G. Henkelman, *J. Phys. Condens. Matter*, 2009, **21**, 084204.
456 B. Xiao, P. S. Wheatley, X. Zhao, A. J. Fletcher, S. Fox, A. G. Rossi, I. L. Megson, S. Bordiga, L. Regli, K. M. Thomas and R. E. Morris, *J. Am. Chem. Soc.*, 2007, **129**, 1203–1209.
457 S. Jensen, K. Tan, L. Feng, J. Li, H.-C. Zhou and T. Thonhauser, *J. Am. Chem. Soc.*, 2020, **142**, 16562–16568.
458 S. Zong, Y. Zhang, N. Lu, P. Ma, J. Wang and X.-R. Shi, *Nanomaterials*, 2018, **8**, 958.
459 A. Daouli, E. P. Hessou, H. Monnier, M.-A. Dziurla, A. Hasnaoui, G. Maurin and M. Badawi, *Phys. Chem. Chem. Phys.*, 2022, **24**, 15565–15578.
460 J. Zhang, J. Tian, Q. Zhang, Y. Lu, L. Li and Y. Xu, *ChemistrySelect*, 2021, **6**, 13609–13615.